Chemical Thermodynamics of Water Soluble Organic Compounds Found in Aqueous Atmospheric Aerosols: Modeling and Microfluidic Measurements

A Thesis

SUBMITTED TO THE FACULTY OF THE GRADUATE SCHOOL OF THE UNIVERSITY OF MINNESOTA

BY

Lucy Nandy

IN PARTIAL FULFILLMENT OF THE REQUIREMENTS FOR THE DEGREE OF DOCTOR OF PHILOSOPHY

Professor Cari S. Dutcher, *advisor*

June, 2018

Acknowledgements

I would like to thank my colleagues, friends and family for all their support and motivation in the success of my doctoral thesis during the past four years. Throughout the PhD program, I have interacted with several great minds and have gained wonderful experiences. I feel it is important to acknowledge all of them who have always come forward to help me whenever I needed.

First of all, I owe my understanding of the field, atmospheric aerosols, to my PhD advisor, Professor Cari Dutcher. I thank her for all the support and encouragement, and a good working environment that she has provided during these years. I thank her for her valuable comments, excellent suggestions and inputs during revision of the thesis drafts, article drafts for publication, and oral presentations. It has been a privilege to work with Cari, as she has taught me how we as scientists, are responsible to take the discipline in the right direction. She is a dedicated and an enthusiastic teacher.

I thank my PhD thesis examining committee members, Professors Chris Hogan, Dylan Millet, Sungyon Lee and David Pui for their guidance when the thesis was taking shape and during the thesis proposal defense. In particular, I thank Professor Chris Hogan for his insightful ideas on my career path. I sat-in his advanced aerosols lectures, that were helpful in my research. I also thank Professor Dylan Millet for letting me sit-in his lectures on atmospheric processes. The lectures provided me with a broad perspective of my

research area. Lastly, I thank Professor Sungyon Lee for her helpful suggestions on my conference and job talks.

I gratefully acknowledge Professors Lynn Walker and Shelley Anna at Carnegie Mellon University, Professor Siva A. Vanapalli at Texas Tech University for their useful insights on the microfluidic experimental work, and Professor Kevin Dorfman for use of his laboratory and equipment for fabrication of the PDMS microfluidic devices. Part of the microfluidic work was carried out in the College of Science and Engineering Minnesota Nano Center, University of Minnesota, which receives partial support from National Science Foundation (NSF) through the National Nanotechnology Infrastructure Network (NNIN) program. The material in this dissertation is based upon work supported by the NSF under Grant No. 1554936.

I thank my collaborators, Professor Jonathan P. Reid and Professor Andrew P. Ault who have helped me along the way. Working with them and their groups was a pleasure, which aided me in understanding various aspects of aerosol measurement studies. I would also like to thank my mentors from India, Professor G. K. Roy and Professor Sunando DasGupta, who have helped me throughout my research career. I also thank my former colleagues from Tata Steel India who have encouraged me throughout my graduate tenure.

I must also thank Noro Andriamanalina (PhD), Director of Academic and Professional Development, for her practical suggestions and best wishes whenever we met. I appreciate the conversations we have had over the years.

I thank my colleagues from the Dutcher group for all their help and support during the years. I thank Andrew Metcalf, Hallie Boyer, Shweta Narayan and Shihao Liu for the experimental support with microfluidics. I especially thank Hallie Boyer and Nikolas Wilkinson for their motivation during my initial years of graduate school. I also thank Peter Ohm, Eric Ruud, Athena Metaxas, Ellie Raethke, Tom Neumiller, Priyatanu Roy and Archit Dani for being wonderful lab-mates. I loved all the fun we had over our group outings, especially the summer picnics and Dutcher group holiday parties. Special thanks to my friends at the university for sharing coffee breaks with me.

Finally, I have to thank my parents for their immense support, and for encouraging me to shape my career as I wanted. I thank them, my parents-in-law and my husband for their understanding and patience throughout. I also thank my sister and brother-in-law, Merlin didi & Dilip bhai, my brother, Benjamin (Pul), and my cousin, Kitty didi, who have always been supportive no matter what; my sister-in-law, Marua for her generosity when I needed it the most during my final phase of studies. I thank my other relatives and friends (biggest stress relievers), both in India and United States, for their continuous support and friendship; special thanks to Prahit for his visions, which made the whole process much easier than I expected. I thank the organizations, Council of International Graduate Students, Global Minnesota, and Boynton Health, that I have been associated with for other activities. I also thank my tennis playing partners and Shu Lee for all the tennis practices, that have helped me maintain a balance between work and life all these years. Most importantly, I thank Jyoti, my husband (still trying to understand what I was working on),

who has provided me with whatever I needed to achieve my goals and made my stay in the United States fun and thrilling.

Dedication

“Karma-yoga is a supreme secret indeed.”

- *Bhagavad Gita*

This thesis is dedicated to my parents, Mummy & Baba, for their constant support. They have taught me the value of hard work, and have always inspired me to have a work-life balance.

Abstract

Atmospheric aerosols, suspensions of tiny particulates in atmosphere, are known to have a major impact on Earth's climate. Due to the highly chemically and physically complex nature of aerosol particles, large uncertainty in climate modeling arises when attempting to predict the aerosol effect. This dissertation comprises of (1) development of thermodynamic statistical mechanics models to predict solute and water content in aqueous aerosols, and (2) development of an experimental microfluidics approach to measure water loss and study liquid-liquid phase separation. The research effort will significantly advance understanding of aerosol particle thermodynamics by assessing the water content of multiphase particles containing soluble organic compounds, and reduce uncertainty in climate modeling associated with aerosol properties and dynamics.

The specific objectives attained in this dissertation research are as follows.

I. Aqueous Solution Thermodynamic Model Development: Thermodynamic analytic predictive models using statistical mechanics were developed for multicomponent systems across the entire range of equilibrium relative humidity (RH - 0 to 100%). The models predicted solute activity for a wide range of compounds consisting of partially dissociating organic and inorganic acids, fully dissociating symmetric and asymmetric electrolytes, and neutral organic compounds to capture their chemical behavior.

II. Model Applications: (1) pH of aerosols was evaluated in a collaborative work, which is of significant interest due to its effect on the environment. (2) Hygroscopicity was

estimated in a collaborative work, which has effects on the optical properties of aerosol particles.

III. Experimental Microfluidics: The thermodynamic model was parameterized and validated with measurements of water uptake of multicomponent aerosol particles. The influence of relative humidity on phase behavior to assess the effects on water loss properties was studied for improved understanding of liquid-liquid morphologies. Hydrodynamic trapping of atmospheric aerosol chemical mimics in microfluidic channels was used to perform the experiments, that also represented supersaturated solutions.

The efforts in this dissertation together will enhance understanding of atmospheric aerosol phase, solid/liquid/gas partitioning, and liquid-liquid morphologies found in the troposphere. Additionally, the measurements and modeling performed here are useful to any application that requires thermodynamic predictions of water content in complex fluids, like emulsions.

Table of Contents

List of Tables

List of Figures

List of Abbreviations

GHGs – greenhouse gases

LLPS – liquid-liquid phase separation

AS – ammonium sulfate

CCN – cloud condensation nuclei

RK – Redlich-Kister

O/C – elemental oxygen to carbon ratio

SRH – separation relative humidity

OIR – organic-to-inorganic dry mass ratio

VOCs – volatile organic compounds

DRH – deliquescence relative humidity

SOA – secondary organic aerosol

SSA – sea spray aerosol

MSE – mean square error

NRTL – nonrandom two-liquid

EDB – electrodynamic balance

CK-EDB – comparative kinetics electrodynamic balance

RH – relative humidity

UNIFAC – Universal Quasichemical Functional Group Activity Coefficients

EDH – extended Debye-Hückel

MFS – mass fraction of solute

MA – maleic acid

SVOC – semi-volatile organic compound

PSC – Pitzer, Simonson, Clegg

EMF – electromagnetic field

IN – ice nucleation

H-TDMA – Hygroscopic Tandem Differential Mobility Analyzer

E-AIM – extended-aerosol inorganics model

MRH – mixing relative humidity

RI – refractive index

PDMS – poly(dimethylsiloxane)

CAD – computer-aided design

3MGA – 3-methyl glutaric acid

3MAA – 3-methyl adipic acid

ERH – efflorescence relative humidity

IEPOX – isoprene-epoxydiol

SOAS – Southern Oxidant and Aerosol Study

2MG – 2-methyl glyceric acid

2MT – 2-methyl tetrol

FIGAERO – filter inlet for gas and aerosol

OS – organosulfate

SML – sea surface microlayer

2MG OS – 2-methyl glyceric acid organosulfate

2MT OS – 2-methyl tetrol organosulfate

SSW – synthetic sea water

Chapter 1

Introduction

1.1 Relevance of Aerosols in Earth's Atmosphere

There has been a substantial variation in the Earth's climate in recent years due to both natural and human causes. It is mainly because of radiative forcing, i.e. disruption in the balance between the incoming energy from the Sun and the outgoing energy from the Earth's surface and atmosphere. The major factors causing the discrepancy in the energy balance are air pollutants such as greenhouse gases (GHGs) and aerosols,[1] both of which are important components of the atmosphere. They alter climate through perturbations in temperature, natural precipitation, and atmospheric circulation.[2] The GHGs are known to have a warming effect on the Earth's surface and atmosphere, i.e. positive radiative forcing, whereas the aerosols are known to have a cooling effect although there is much more uncertainty in the magnitude of their effect than for GHGs.[3]

The Earth's atmosphere is composed of water vapor, oxygen, nitrogen, carbon dioxide and methane originated by a series of dynamic and complex processes. Other trace atmospheric gases are SO_2, NO_2 and organic compounds. The lowest layer of the atmosphere, the troposphere, is where most of the weather phenomena take place, and the thermodynamic properties of air in this layer are determined largely by its contact with the surface of the Earth.[4] Generally, the temperature decreases linearly with increasing altitude in the troposphere, and there is substantial variation of atmospheric water vapor.

Atmospheric aerosols are fine solid or liquid particles suspended in the atmosphere that significantly alter our climate, and have a major impact on air quality and health. They are created by natural and anthropogenic processes, such as sea-spray, volcanic eruptions, and combustion, and also by new particle formation, or nucleation, which occurs when gas phase species nucleate to form new particles, i.e. gas-to-particle conversion. Nucleation of aerosols is significant in the troposphere, and studies suggest that sulfuric acid, ammonia and water are the key precursors in the nucleation process of new atmospheric aerosol particles.[5–7]

Aerosols typically consist of a mixture of inorganic compounds (ammonium sulfates, nitrates, sea salt), organic compounds (primary and secondary organic material), and the components of wind-blown dust, volcanoes and plant material.[8] Numerous studies on thermodynamic properties have been done for inorganic species as they consist of a limited number of ions, whereas uncertainty for organic compounds remains, as they are known to be chemically complex. Aerosols are commonly composed of an aqueous phase, one or more hydrophobic phases of mostly organic material, and multiple solid phases. The

aerosol components equilibrate between the two or more liquid phases as well as with the gas phase. Compounds can also dissociate (e.g. organic acids) in either or both phases, depending on temperature and relative humidity.

Atmospheric aerosol particles have a major impact on global climate,[9] aerosol optical properties,[10] visibility[11] and human health.[9] The effect on the Earth's climate is through reflection and absorption of solar radiation (direct effect) and through aerosol – cloud interactions (indirect effect).[12] A large contribution to the uncertainty in climate modeling is associated with aerosol properties and dynamics. The uncertainty arises from the highly varied nature of aerosol particles, which range in size from 1 nm to 10 μm in diameter and contain hundreds to thousands of dissolved salt and water-soluble organic chemical compounds. In addition, changes in relative humidity and temperature in the atmosphere affect the size and phases of aerosol particles.

1.2 Chemical Thermodynamics of Aqueous Atmospheric Aerosols

Aerosol particles take up moisture at high ambient relative humidities, and form aqueous solutions of inorganic and organic compounds that typically consist of a mixture of ammonium sulfates, nitrates, sea salt, and primary and secondary organic material. Water uptake is governed by particle size, chemical composition, condensation, and thermodynamic equilibria. This dissertation focuses on liquid aqueous droplets containing sulfates and organic acids. Sulfate particles are known to be widespread in the atmosphere, particularly in particles "activated" by condensation of organics[13] or in phase-separated particles containing an organic coating.[14]

Typically, hygroscopic particles show water uptake/loss behavior with respect to changing relative humidities, leading to changes in aerosol composition. The water uptake/loss causes particles to deliquesce (suddenly take-up water from a crystalline state) or effloresce (crystallize), which significantly influences light scattering properties of aerosol particles. Further, presence of an organic phase in equilibrium with an aqueous inorganic phase, in phase-separated particles, may significantly affect gas-to-particle partitioning.[15,16] Therefore, to understand chemical composition and phase, thermodynamic modeling and measurements are required.

The point when a particle transitions from a solid to a dissolved state as a function of solute solubility is known as the deliquescence point, i.e. when the Gibbs free energy for the dissolved droplet is less than the Gibb's free energy for the dry particle, making the process thermodynamically favorable.[17,18] Conversely, the efflorescence point is when a liquid droplet crystallizes with decreasing relative humidities. However, the deliquescence and efflorescence points for the same particle might be different which leads to a hysteresis effect. For example, ammonium sulfate deliquesces at a relative humidity ~80% (DRH) and effloresces at ~ 35-40% (ERH) relative humidity.[19–21] It means that the liquid droplet may remain in a supersaturated, metastable state even at low relative humidities depending on the particle history.

Ultimately, the supersaturated droplet will crystallize at a low enough relative humidity. A lower ERH than DRH is due to the kinetic barrier to nucleation, and depends on the probability of the formation of a solid nucleus of the thermodynamically favored solid state.[18] In addition, for ternary mixtures containing both inorganic and organic

compounds, the deliquescence and efflorescence relative humidities of the salts are different compared to single salt binary aqueous solutions alone. Therefore, a thermodynamic model is required to predict the concentrations of each component in the solution.

A more complex behavior might occur in organic-inorganic mixtures due to the non-ideal interactions between ions and organic compounds during atmospheric humidity cycles leading to liquid-liquid phase separation (LLPS).[22] LLPS is often caused by the salting-out effect, which reduces the water activity of the organic compound with increase in the salt mole fraction in the solution. In addition, it has recently been found that liquid-liquid phase separation may also occur in particles containing some types of secondary organic material (such as those derived from α-pinene), even in the absence of inorganic salts.[23] Therefore, the aerosol particle phase for organic-inorganic mixtures can vary from liquid, solid and LLPS, with a significant impact on gas-to-particle partitioning.[15]

Particles take up water from the atmosphere until they reach a thermodynamic equilibrium state between the gas and the particle, i.e. chemical potential of water in the liquid droplet phase is same as in the gas phase. Water content in an aerosol particle at equilibrium can be calculated using thermodynamic models. Due to solution non-idealities, activity coefficients are calculated to predict the chemical composition in the aerosol particle at equilibrium with the ambient air. The water content in the particle phase (solution) depends on the relative humidity, and the amount of salts and organic compounds in the solution.

For aqueous solutions or droplets in equilibrium with the gas phase in contact with them, the relative humidity is equivalent to the water activity,[24] which is the independent variable in the model described in this dissertation. Thermodynamic equilibrium solution properties such as osmotic coefficient and solute activities in multicomponent solutions can be predicted to understand the water uptake by compounds. Chemical activity is the measure of the chemical effectiveness of a component in a solution. The activity of the solute, a_j, is defined as:

$$\mu_j = \mu_j^o + kT\ln a_j \quad (1.\ 1)$$

Where subscript j is the solute species, μ_j is the chemical potential, μ_j^o is the chemical potential at a given reference state, k is Boltzmann's constant, and T is absolute temperature. The ratio between the chemical activity and the mole fraction of species j is known as the activity coefficient, given by:

$$\gamma_j = a_j/x_j \quad (1.\ 2)$$

The activity coefficient indicates how much the real solution deviates from an ideal solution. If the activity coefficient is equal to unity, then the activity exactly equals the concentration, an ideal relationship known as Raoult's Law. In addition to the activity coefficient, the osmotic coefficient is defined by:

$$\varphi = \frac{-\ln(a_w)}{M_w m_j v_j} \quad (1.\ 3)$$

where a_w is the water activity of the aqueous solution, M_w is the molar mass of water, m_j is the molality of solute j in solution, and ν_j is the number of moles of ions into which one mole of solute disassociates (ν_j = 1 for organics). The osmotic coefficient allows more sensitive parameterization of activity coefficient models than activity alone, and is frequently used in this work.

1.3 Scientific Background and Motivation for Modeling and Measurements.

This dissertation particularly focuses on thermodynamic properties of water-soluble organic acid and sulfate aqueous solutions in order to better understand water uptake and phase of organic-inorganic aqueous systems. Key aqueous solution thermodynamic properties depend upon the type and concentration of solute molecules, and the temperature and relative humidity conditions. Predictive models for thermodynamic properties are governed by the molecular scale interactions of the organic, inorganic, and water molecules.

Water-soluble organic compounds are important in aerosols. Field measurements of aerosol particles and time-of-flight mass spectrometric measurements show that both organic and water-soluble inorganic compounds (aqueous ammonium and sulfate are a significant fraction) are important.[24–26] It is found that substantial amounts of dicarboxylic acids are present in the water-soluble organic fraction of aerosol particles in the atmosphere.[27] Collected aerosol samples have been analyzed by gas chromatography[28], and C_2 – C_{10} dicarboxylic acids have been detected in these samples. Phase transitions have been both measured[19,29–31] and thermodynamically modeled[32–37] in binary ammonium

sulfate (AS) ($(NH_4)_2SO_4/H_2O$) system and ternary organic/$(NH_4)_2SO_4/H_2O$ system as a function of RH. Liquid-liquid phase separation has also been studied in mixed organic/inorganic atmospheric aerosol particles.[38–40] Thermodynamic calculations suggest that mixed solutions separate into organic- and inorganic-rich phases, increasing organic partitioning into the condensed phase by 50%.[16,41]

Organic acids make up an important fraction of atmospheric aerosol composition. The total amount of organic carbon in aerosol particles has been estimated to account for anywhere between 10 and 65% of the total aerosol mass.[42] Dicarboxylic acids and other organic acids represent a major component of the total organic carbon mass in the atmosphere and are integral to many of the processes of atmospheric aerosol formation and growth as well as the properties expressed by the aerosols. For example, for cloud condensation nuclei (CCN) in the atmosphere, dicarboxylic acids are potentially as important as sulfates.[43] Studies have shown that dicarboxylic acids can reduce the surface tension and hygroscopic property of CCN, affecting cloud formation and optical properties.[44] The most abundant dicarboxylic acids found in atmospheric aerosols are oxalic acid (C2), malonic acid (C3), and succinic acid (C4) that comprise more than 80% of the total diacid concentrations. Measurable amounts of acids having higher carbon numbers, e.g., C5, C6, are also present in atmospheric aerosols.[28,45–47]

Given the abundance and importance of organic acids in atmospheric aerosols, measurements and models of thermodynamic properties of the organic species in solution are essential for accurate predictions of the gas/particle partitioning and aerosol size distribution and composition.[48] Experimental thermodynamic studies include

investigations into vapor pressure measurements and hygroscopic properties.[48–55] Soonsin et al.[48] reported that organic acids with an even number of carbon molecules (“even acids”, e.g., succinic acid) are less soluble in water and have lower vapor pressures than odd acids. In a study of growth factor of hygroscopic acids such as malonic acid, citric acid, and malic acid, Peng et al.[49] found that these water-soluble organic acids at low concentrations contribute less than inorganics to the hygroscopicity of atmospheric aerosols. Extended to ternary systems, Beyer et al.[50–53] and Pearson and Beyer[54] studied thermodynamic properties of dicarboxylic acids/ammonium sulfate/water mixtures using differential scanning calorimetry and infrared spectroscopy of thin films. They have reported water activities and solid/liquid ternary phase diagrams for systems having dicarboxylic acids like malonic, glutaric, maleic, and succinic acids below 300 K. Bilde et al.[55] have reviewed experimental measurements of equilibrium vapor pressures from evaporation rate of straight-chain dicarboxylic acids with water and inorganics. They found that for estimation of equilibrium vapor pressure, knowledge of the phase state of mixed organic-inorganic particles, is essential.

1.3.1 Modeling of aqueous aerosol activity and water content.

Predicting activities of aqueous solutions to understand thermodynamics of aerosol particles is important. In this dissertation, the equilibrium solution properties of aqueous droplets that mimic chemical components in atmospheric aerosols, mainly sulfates and organic acids, are predicted.

Thermodynamic models allow estimation of equilibrium solution properties such as osmotic coefficient and activity of organic solute compounds. Fully predictive models,

like UNIFAC, can predict activity coefficients with moderate success based on parametrization that describes the energetic interactions between individual functional groups.[56] Due to the absence of a separate structure group for CH_2, Peng et al.[49] modified the standard UNIFAC parameter set by fitting the model with measured water activity data of dicarboxylic acid aqueous solutions. It is important to note that UNIFAC and UNIFAC-Peng models assume nondissociation for dicarboxylic acids. The more accurate Redlich-Kister (RK) expansion equation[57] is used to predict osmotic coefficients and activities of aqueous binary dicarboxylic acids at 298.15 K and also of aqueous mixtures of acids and salts for both nondissociating and dissociating acids, however, with an increased number of adjustable binary and ternary parameters.[33,34]

Recently, adsorption isotherm models using statistical mechanics were used to model thermodynamic properties of solutions with very low water content. In this framework, solutes were the adsorbents, which were "hydrated" by water molecules in multilayer lattice formation.[58,59] The framework consisted of two main energetic interaction terms: long range Debye-Hückel and short-range adsorption. Debye-Hückel theory describes non-ideal behavior by the Coulomb potential of the hard charged spherical ions in a continuous dielectric medium, such as water.[60] It is also used in other available thermodynamic models for Gibb's energy[61,62] consisting of the excess Gibbs-Margules expansion for short range forces and Debye-Hückel terms, which successfully predict water activity of inorganic aqueous electrolyte solutions. In the adsorption isotherm model, however, the short-range adsorption interaction is used, versus a more empirical Margules expansion. For the adsorption treatment, an associated energy parameter for each sorption

layer was initially determined by an empirical power law model (for various electrolytes, organics and mixtures),[63] and then by a more accurate short range Coulombic interactions model (for symmetric 1-1 electrolytes and various organics),[64] reducing the number of model parameters. The advantage of the Coulombic model is that it provides physical interpretations of the model parameters by relating them to structure properties.

1.3.2 Measurements of aqueous droplet phase.

In addition to predicting activities of aqueous solutions, this dissertation also advances understanding in aerosol phase through experimental microfluidics. In this dissertation, droplets that mimic atmospheric aerosols to determine their compositions at varied RH until solidification (efflorescence) are also studied. Direct measurements of water loss properties allow estimation of phase behavior of atmospheric aerosol particles with respect to ambient RH.

Using fluorescence microscopy, it has been shown that liquid-liquid phase separation (LLPS) occurs in samples of ambient aerosol particles.[40] In particular, LLPS is known to occur in mixtures of organic and inorganic compounds, as shown by laboratory studies of particles composed of inorganic salts mixed with organic species.[38,65–68] The studies have provided information on the dependence of phase separation on the elemental oxygen to carbon ratio (O/C) ranging from 0.3 to 1.33, and the number of organic species.[65] Liquid-liquid phase separation was always observed for organic species having O/C values less than 0.5, never for values greater than 0.8, and for some species $0.5 < O/C < 0.8$ depending on the type of functional group. Results also suggested that the number of organic species in a single particle does not affect phase separation significantly.[65]

A recent study of single aerosol droplets trapped using optical tweezers coupled with Raman spectroscopy[69–71] sheds light on the separation relative humidity (SRH) and morphology of phase-separated particles. SRH of aqueous aerosol droplets with PEG-400/AS and C6-dicarboxylic acids/AS were measured using optical tweezers for organic-to-inorganic dry mass ratios (OIR) ranging from 0.11 to 9.[72] Phase separation was observed for the PEG system at intermediate OIR, and for the diacids system at OIR 0.2 and 0.5. SRH for the diacids system was significantly lower than the PEG system, and the different morphologies in both the systems observed were core-shell, core-shell with inclusions and partial engulfment.

Experimental thermodynamic measurements for estimating water activities, evaporation rates and hygroscopic growth of diacid – salt systems have also been reported.[22,73,74] Physical states of atmospheric aerosol particles have been studied using electrodynamic balance and optical microscopy.[75–77] It was found that, for mixed organic/AS aqueous solution, efflorescence (of the AS phase) always occurred in systems that first underwent liquid-liquid phase separation. In contrast, efflorescence was not necessarily observed for systems where LLPS did not first occur. Therefore, it is suggested that LLPS facilitates efflorescence of a mixed organic/AS solution.[30] Complex mixtures of C5 – C7 dicarboxylic acids having varied O/C mixed with AS using optical microscopy and Raman spectroscopy have been studied showing different behavior of phases.[68] The studies report that liquid-liquid phase separation occurs for compounds that have O/C ratios < 0.7 in mixed tropospheric aerosols.

Finally, in addition to dicarboxylic acids that are produced in the atmosphere by biomass burning and photochemical chain reactions or photooxidation of organic precursors,[28,45,46,78,79] volatile organic compounds (VOCs), for example isoprene (2-methyl-1,3-butadiene, a biogenic non-methane hydrocarbon emitted into the atmosphere),[80] act as precursors and oxidize to yield secondary organic aerosol (SOA).[81–85] Likewise, sea spray aerosols play a significant role in forming complex mixture particles (e.g. composition, structure) in the atmosphere.

1.4 Scope of this Dissertation.

The aim of this dissertation is to study and predict thermodynamic properties of aqueous aerosol particles in the atmosphere over the entire range of relative humidity, for a wide range of inorganic and organic compounds that totally dissociate, partially dissociate, or do not dissociate. The research is motivated by the lack of accurate predictions at low relative humidities when the droplets could be at supersaturated states. The model developed in this work is based on adsorption isotherms because it yields accurate predictions at supersaturated conditions. Further, the goal of this work is to better understand the role of organic compounds in ternary mixtures containing both inorganic and organic species. Microfluidic measurements complement the model predictions and provide an advanced understanding of various aerosol phase states at atmospherically relevant conditions.

The goal of this dissertation is accomplished by model predictions and measurements as indicated in the following outline.

In Chapter 2, a Coulombic model based on multilayer adsorption has been developed for prediction of equilibrium solution thermodynamic properties such as osmotic coefficient and solute activity for water-soluble organic compounds with partial disassociation (e.g. organic acids, such as dicarboxylic acids). The model here is also extended for parameter reduction through physical interpretation. In addition, an improved reference state has been projected for ternary mixtures containing organic-inorganic species. The work presented in Chapter 2 has appeared in Nandy, L.; Ohm, P. B.; Dutcher, C. S. Isotherm-Based Thermodynamic Models for Solute Activities of Organic Acids with Consideration of Partial Dissociation. *J. Phys. Chem. A* **2016**, *120* (24), 4147–4154. The Coulombic model has been extended in Chapter 3 to include asymmetric electrolytes (e.g. ammonium sulfate and sulfuric acid). Particularly for sulfate systems, sulfate partitioning is explicitly treated here by the model. The work presented in Chapter 3 has appeared in Nandy, L.; Dutcher, C. S. Isotherm-Based Thermodynamic Model for Solute Activities of Asymmetric Electrolyte Aqueous Solutions. *J. Phys. Chem. A* **2017**, *121* (37), 6957–6965.

In Chapter 4, the adsorption isotherm model is applied to single particle measurements to estimate pH of acidic particles, to study aerosol hygroscopicity, and to interpret optical tweezer measurements of gas-particle partitioning with ternary aqueous solutions of sucrose/organic acid, in collaborative studies. The modeling work presented in Chapter 4 is used to inform measurements by collaborators, and has appeared as a part of Rindelaub, J. D.; Craig, R. L.; Nandy, L.; Bondy, A. L.; Dutcher, C. S.; Shepson, P. B.; Ault, A. P. Direct Measurement of pH in Individual Particles via Raman Microspectroscopy and Variation in Acidity with Relative Humidity. *J. Phys. Chem. A*

2016, *120* (6), 911–917; Craig, R. L.; Nandy, L.; Axson, J. L.; Dutcher, C. S.; Ault, A. P. Spectroscopic Determination of Aerosol pH from Acid-Base Equilibria in Inorganic, Organic, and Mixed Systems. *J. Phys. Chem. A* **2017**, *121* (30), 5690−5699; Marsh, A.; Miles, R. E. H.; Rovelli, G.; Cowling, A. G.; Nandy, L.; Dutcher, C. S.; Reid, J. P. Influence of Organic Compound Functionality on Aerosol Hygroscopicity: Dicarboxylic Acids, Alkyl-Substituents, Sugars and Amino Acids. *Atmos. Chem. Phys.* **2017**, *17* (9), 5583–5599; Craig, R.; Peterson, P.; Nandy, L.; Lei, Z.; Hossain, M.; Camarena, S.; Dodson, R.; Cook, R.; Dutcher, C. S.; Ault, A. Direct Determination of Aerosol pH: Size-Resolved Measurements of Submicron and Supermicron Aqueous Particles. *Ana. Chem.* **2018** (under review); and Marshall, F.; Berkemeier, T.; Shiraiwa, M.; Dutcher, C. S.; Nandy, L.; Ohm, P.; Reid, J. P. Influence of Particle Viscosity on Mass Transfer and Heterogeneous Ozonolysis Kinetics in Aqueous-Sucrose-Maleic Acid Aerosol. *Phys.Chem.Chem.Phys.***2018**, 20, 15560-15573. Chapter 5 presents the ongoing and future directions of the modeling efforts, and provides an overview of temperature-based studies to better understand behavior of aerosol particles in the troposphere, and subsequent development of temperature-dependent Coulombic model.

In Chapter 6, a biphasic microfluidic approach has been used to study relative humidity dependent phase behavior (efflorescence and LLPS) and water content of aqueous mixtures of salt and organic compounds of varied ratios. The work presented here has appeared in Nandy, L.; Dutcher, C. S. Phase Behavior of Ammonium Sulfate with Organic Acid Solutions in Aqueous Aerosol Mimics Using Microfluidic Traps. *J. Phys. Chem. B* **2018** *122* (13), 3480-3490. Chapter 7 highlights preliminary results of phase

behavior with secondary organic aerosol (SOA) and sea spray aerosol (SSA) real sample experiments. Finally, Chapter 8 summarizes the conclusions of this dissertation and provides an outlook on the future scope of these studies.

Additional results from Chapters 2, 3 and 6 are shown in Appendix A, B and C respectively; the MATLAB codes for model development are in Appendix D; and the copyright permissions are stated in Appendix E.

Overall, this dissertation incorporates material from seven papers by the author.[74,86–90] Chapters 2, 3 and 6 use material from Nandy et al. 2016, Nandy and Dutcher 2017, and Nandy and Dutcher 2018 respectively. Some material from each of these three papers has also been incorporated into this introductory chapter. Finally, Chapter 4 is based on Rindelaub et al. 2016, Craig et al. 2017, 2018 (under review), Marsh et al. 2017 and Marshall et al. 2018, coauthored with researchers from Professor Andrew Ault's group and Professor Jonathan Reid's group at University of Michigan and University of Bristol, respectively.

Sulfate with Organic Acid Solutions in Aqueous Aerosol Mimics Using Microfluidic Traps. *J. Phys. Chem. B* **2018** *122* (13), 3480-3490. Copyright (2018) American Chemical Society.

Chapter 2

Isotherm-Based Thermodynamic Models for Solute Activities of Organic Acids with Consideration of Partial Dissociation†

†Adapted with permission from Nandy, L.; Ohm, P. B.; Dutcher, C. S. Isotherm-Based Thermodynamic Models for Solute Activities of Organic Acids with Consideration of Partial Dissociation. *J. Phys. Chem. A* **2016**, *120* (24), 4147–4154.

2.1 Introduction

Organic acids make up a significant fraction of the organic mass in atmospheric aerosol particles. The calculation of gas-liquid-solid equilibrium partitioning of the organic acid is therefore critical for accurate determination of atmospheric aerosol physicochemical properties and processes such as new particle formation and activation to cloud condensation nuclei. Previously, an adsorption isotherm based statistical thermodynamic model was developed for capturing solute concentration–activity relationships for multicomponent aqueous solutions over the entire concentration range,[58,59,63] with model parameters for energies of adsorption successfully related to dipole-dipole electrostatic forces in solute-solvent and solvent-solvent interactions for both electrolytes and organics.[64] However, careful attention is needed for weakly dissociating semivolatile organic acids. Dicarboxylic acids, such as malonic acid and glutaric acid are treated in this chapter as a mixture of nondissociated organic solute (HA) and dissociated solute ($H^+ + A^-$) as shown in **Figure 2. 1**. It was found that the apparent dissociation was greater than that predicted by known dissociation constants alone, emphasizing the effect of dissociation on osmotic and activity coefficient predictions. To avoid additional parametrization from the mixture approach, an expression was used to relate the Debye-Hückel hard-core collision diameter to the adjustable solute-solvent intermolecular distance. An improved reference state treatment for electrolyte-organic aqueous mixtures, such as that observed here with partial dissociation, has also been proposed. The work results in predictive correlations for estimation of organic acid and water activities for which there is little or no activity data.

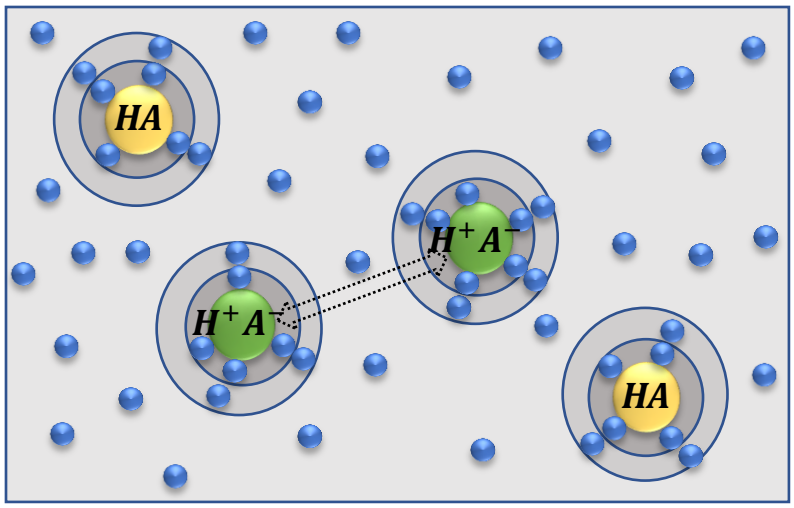

Figure 2. 1. Adsorption isotherm model framework for an organic acid treated as a mixture of nondissociated organic solute (HA) and dissociated organic solute (H+ + A-).

Recently, multilayer adsorption isotherm-based modeling was developed by Dutcher and co-workers[58,59,63] to predict osmotic coefficients and activities of binary and ternary aqueous mixtures. Previous work by Ohm et al.[64] detailed the introduction of a Coulombic interaction for determining the energy parameters for the sorption of water onto a solute molecule, reducing the number of adjustable parameters per solute to as low as two: (1) the intermolecular distance between the solute and water molecule in the first adsorption layer and (2) the solute dipole moment (organics) or Debye-Hückel closest approach parameter (electrolytes). However, the binary Coulombic isotherm model is unable to accurately predict the properties of some organic acids such as malonic or glutaric acid when the acid is treated as a neutral, nondissociating molecular solute. In this chapter, the effect caused by partial dissociation of weak acids in solutions is treated by extending the model to treat acids as a mixture of nondissociated organic solute (HA) and dissociated organic solute ($H^+ + A^-$) as shown in **Figure 2. 1**.

2.2 Theoretical Treatment of Partial Dissociation in Adsorption Isotherms

A multilayer adsorption isotherm-based model for predicting activity coefficients of aqueous solutions was derived by Dutcher et al. [58,59,63] The model parameters include the energy of adsorption parameter, $C_{j,i}$, related to the energy change from the sorption of a water molecule from the bulk water onto the respective hydration shell, *i*, of solute *j*

$$C_{j,i} = \exp\left(\frac{\Delta\varepsilon_{j,i}}{kT}\right) \tag{2. 1}$$

where $\Delta\varepsilon_{j,i}$ is the difference in energy between a sorbed water and a free water molecule in the bulk, $k = 1.38 \times 10^{-23}$ J K^{-1} (Boltzmann's constant), T is temperature. It should be noted that in the limit of $\Delta\varepsilon_{j,i} = 0$ for all layers and all solutes, meaning there is no energy change associated with the sorption of water molecules with a solute, the adsorption isotherm model reduces to the ideal mixing model on a mole fraction basis. The isotherm-based model was originally implemented using two different approaches to the determination of the energy $C_{j,i}$ parameters. The first approach was to treat each $C_{j,i}$ value as a separate fit parameter, fitting all $C_{j,i}$ values individually, resulting in moderate to good predictions with, however, a large number of fit parameters with no physicochemical interpretation. The second approach was to use a power law relationship to calculate the $C_{j,i}$ parameters, where the first $C_{j,i}$ value ($C_{j,1}$) was fit and the subsequent $C_{j,i}$ parameters were calculated using the following relationship:

$$C_{j,i} = \left(i/n_j\right)^{P_j} \tag{2. 2}$$

where P_j is a fit parameter, n_j is the number of sorption layers surrounding solute j, and $i = 2, 3, \ldots, (n_j - 1)$. The power law expression significantly reduced the number of empirical parameters in the energy calculations to three: $C_{j,1}$, P_j, and n_j. The phenomenological explanation of a power law fit is to cause the energy $C_{j,i}$ parameters to decay toward unity as the solvent molecule moves further from the solute particle. Results for model predictions using the empirical "all $C_{j,i}$" and phenomenological "power-law" expressions for the $C_{j,i}$ parameters are shown in Appendix A.

Recently, the Coulombic method for determining the energy $C_{j,i}$ parameters was derived,[64] on the basis of physicochemical solution properties. Here, the model is applied to the organic acid systems, first treating the organic acids as neutral solute with no dissociation. The models are fitted to molality-based osmotic coefficients at 298.15 K taken from the literature. Because osmotic coefficients depend on the natural logarithm of the water activity,[63] they illustrate deviations of the model from the experimental data more sensitively, versus more simple concentration–water activity (plots in Appendix A) relationships. Results are shown in **Figure 2. 2** and **Figure 2. 3**, where the use of a nondissociating Coulombic fit successfully predicted the osmotic coefficient behavior for acetic acid, butyric acid, citric acid, malic acid, and succinic acid (**Figure 2. 2**), but not for acids like malonic acid and glutaric acid (**Figure 2. 3**). Although the model accurately predicts the correct limiting values for malonic acid, the fit fails to replicate the dip and peak of the osmotic coefficient data. Likewise, the Coulombic fit for glutaric acid is unable to match the quickly decreasing osmotic coefficient at low mole fraction solute and shifts the osmotic coefficient peak into a higher mole fraction range ignoring the peak shown in

the data. In general, the drop in the osmotic coefficient at low concentrations in the data indicates electrolyte-type behavior, which cannot be predicted by treating the organic acid as a purely neutral solute.

Organic acids, such as malonic acid and glutaric acid, are known to partially dissociate into ions. Hence, a treatment incorporating the partial dissociation of organic acids should be used in the context of the Coulombic model.[64] In the Coulombic-based adsorption isotherm model,[64] the number of parameters needed to model organics is reduced to two parameters (r_{jw}, n_j). In addition, the model for electrolytes has been reduced to three parameters (r_{jw}, ρ_j, n_j), where r_{jw} is the intermolecular distance between solute *j* and solvent *w*, and parameter ρ_j can be related to the hard-core collision diameters of the solute ions. The isotherm model eqs (2. 3) – (2. 9) using Coulombic interactions for the energy parameters are as follows:[58,59,63,64]

$$\bar{m}_j^o = \frac{\left(\frac{1-\bar{a}_w}{M_w v_j \bar{a}_w}\right)\left(1-\sum_{i=1}^{n_j-1}\left((\bar{a}_w)^i\left(1-C_{j,i}\right)\prod_{k=1}^{i-1}C_{j,k}\right)\right)}{(1-\bar{a}_w)^2\sum_{p=1}^{n_j-2}\left(p(\bar{a}_w)^{p-1}\prod_{k=1}^{p}C_{j,k}\right)+\left(\left(n_j-1\right)-\left(n_j-2\right)\bar{a}_w\right)(\bar{a}_w)^{n_j-2}\prod_{k=1}^{n_j-1}C_{j,k}} \quad (2.\ 3)$$

$$\sum_j \frac{m_j}{\bar{m}_j^o} = 1 \quad (2.\ 4)$$

$$a_w = \bar{a}_w K_w^{DH} \quad (2.\ 5)$$

where M_w (kg mol^{-1}) is the molecular weight of the solvent (water), a_w is the water activity of the mixture on a mole fraction basis and is equal to the relative humidity in the gas phase

above a mixture, m_j is the molality of the solute j in solution, $\bar{m}_j^o$ is the molality of the solute j in a pure aqueous solution at the $\bar{a}_w$ of the mixture normalized by the long-range Debye-Hückel term, and K_w^{DH} is given by

$$K_w^{DH} = \exp\left(\frac{A_x {I_x}^{1/2} \sum_j \left(v_j N_j |z_{j-}| z_{j+} / \left(1 + \rho_j {I_x}^{1/2}\right)\right)}{\sum_j v_j N_j + N_w}\right) \quad (2.6)$$

where A_x is the Debye-Hückel coefficient on a mole fraction basis, equal to 2.917 at 298.15 K, I_x is the mole fraction ionic strength of the solution in terms of molalities of solutes present, defined by $I_x = \left(\frac{1}{2}\right)\frac{\sum_j v_j m_j |z_{j-}| z_{j+}}{\sum_j v_j m_j + 1/M_w}$, v_j is the stoichiometric coefficient of solute j, which is the number of moles of ions formed from 1 mol of fully dissociated solute j, N_j is the number of molecules of solute j, N_w is the number of water molecules, z_{j+} is the normalized charge on the cation of dissociated solute j, and z_{j-} is the normalized charge on the anion of dissociated solute j.

$$C_{j,i} = \exp\left(\left(\frac{\mu_j \mu_w D^2}{4\pi\varepsilon_0 \left(r_{jw} + (i-1) r_{ww}\right)^3} - \frac{\mu_w \mu_w D^2}{4\pi\varepsilon_0 (i \cdot r_{ww})^3}\right) / kT\right) \quad (2.7)$$

$$\mu_{H^+A^-} = qe\left(r_{jw}\right)/D \quad (2.8)$$

$$\mu_{HA} = \left(r_{jw}/2.023\text{Å}\right)^3 \quad (2.9)$$

where μ_j is the dipole moment of solute j, r_{ww} = 2.82 × 10^{-10} m, μ_w = 2.9, ε_o is the permittivity of free space, $4\pi\varepsilon_o$= 1.113 × 10^{-10} C^2 N^{-1} m^{-2}, D is a unit of conversion (Debye), D = 3.33564 × 10^{-30} C m, q = 1 is the charge for 1:1 electrolytes, e = 1.60218 × 10^{-19} C is

the elementary charge, subscript H^+A^- is for the dissociated solute, and subscript HA is for the neutral solute. Note that eq (2. 8) has a slightly different form than the Coulombic model in Ohm et al.[64]

If a partially dissociating organic solute is modeled as a mixture of a dissociated organic solute (modeled as an electrolyte) and a nondissociated organic solute (modeled as an organic), an additional parameter, β, that indicates the solute concentration ratio and is a function of concentration, is required. Therefore, it initially gives the model a total of six parameters: three fit parameters ($r_{jw,\mathrm{HA}}, r_{jw,\mathrm{H^+A^-}}, \rho$) and three adjustable parameters ($n_{\mathrm{HA}}, n_{\mathrm{H^+A^-}}, \beta$). Writing out eq (2. 4) for a partially dissociated organic acid gives the following

$$m_{\mathrm{HA}}\left(\frac{1}{\bar{m}^o_{\mathrm{HA}}}+\frac{\beta}{\bar{m}^o_{\mathrm{H^+A^-}}}\right)=1 \tag{2. 10}$$

where $\beta = m_{\mathrm{H^+A^-}}/m_{\mathrm{HA}}$ is the solute concentration ratio of dissociated acid to nondissociated acid.

Ideally, the known dissociation constants, K_a,[33] could be used in the determination of the solute concentration ratio, β. The molality-based dissociation constant, K_a is given by

$$K_a = \frac{a_{\mathrm{H^+}}a_{\mathrm{A^-}}}{a_{\mathrm{HA}}} \tag{2. 11}$$

where a is the activity of each component on molality basis, defined by $a = \frac{m}{m_\Theta}\gamma$, m_Θ is a unit molality of 1 mol/kg and γ is the molality-based activity coefficient (calculated from

eq 30 of Dutcher et al.[63]). Assuming that the only source of hydrogen ions is from the first dissociation of the organic acid (because $K_{a2} << K_{a1}$),[33] it is found that $m_{\mathrm{H^+}} = m_{\mathrm{A^-}}$, and that the concentration of nondissociated acid, m_{HA}, is equal to the provided data concentration minus the concentration of dissociated acid. Substituting these equations for $m_{\mathrm{H^+}}$ and m_{HA} into eq (2. 11) results in a polynomial in terms of $m_{\mathrm{A^-}}$ that can be solved for each data point, giving a concentration dependent solute concentration ratio.

However, when K_a is used to determine the concentration dependent solute concentration ratio, the resultant predictions were nearly identical to the nondissociating fits in **Figure 2. 2** and **Figure 2. 3**, except at very dilute concentrations. The concentration of dissociated organic acid was too low in the limit of ideal mixing (in the order of 10^{-4}) to have any impact, indicating that the apparent dissociation is greater than the actual dissociation. Instead, a higher solute concentration ratio value is used, which, for simplicity, is considered constant for all solute concentrations. The static dissociation ratios (neutral solute concentration:dissociated solute concentration) tested here include 1:0.5 and 1:0.1 (organic:electrolyte). The dissociation constants (K_a) from literature,[33] with $\mathrm{p}K_a$ (-log K_a) values ranging from 3 to 5 (depending on the acid) were higher from dilute to high concentration range, except at extreme dilute concentrations. The range of values for pK_a with the assumption of the above two constant solute concentration ratios, 0.1 and 0.5, were found to be in the range 1 - 3. As the model is only applied to weak acids, for which $\mathrm{p}K_a$ is generally between -2 and +12,[91] the assumption made is reasonable. Note that, because β is treated as a constant, the degree of dissociation will also remain constant, which is generally defined as the ratio of concentration of the dissociated solute to the

initial concentration of the solute, i.e., $m_{\mathrm{H^+A^-}}/(m_{\mathrm{HA}} + m_{\mathrm{H^+A^-}})$. For example, for $\beta = 0.5$, the degree of dissociation is calculated to be 1/3. Similarly, for $\beta = 0.1$, the degree of dissociation is calculated to be 1/11.

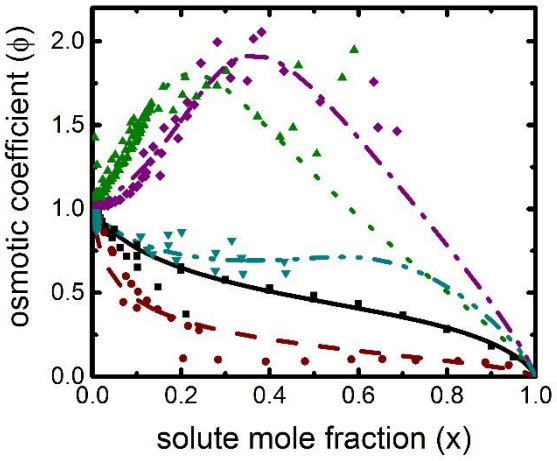

Figure 2. 2. Osmotic coefficient (φ = -ln $(a_w)/M_w \sum_j v_j m_j$), plotted against the solute mole fraction (x = $\sum_j v_j m_j/(\sum_j v_j m_j + 1/M_w)$) at 298.15 K. The model calculates the energy $C_{j,i}$ parameters using Coulombic interactions (eq (2. 3)). Lines: black solid, acetic acid; brown dash, butyric acid; green dot, citric acid; purple dash-dot, malic acid; cyan dash-dot-dot, succinic acid. Symbols: black square, acetic acid experimental data; brown circle, butyric acid experimental data; green triangle, citric acid experimental data; purple diamond, malic acid experimental data; cyan inverted triangle, succinic acid experimental data, where references for the experimental data are given in **Table 2. 1**.

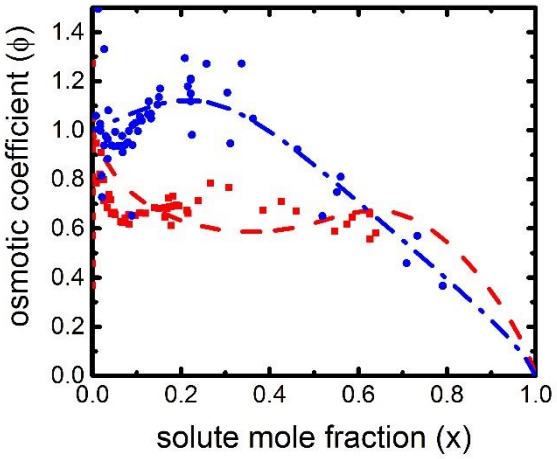

Figure 2. 3. Osmotic coefficient plotted against the solute mole fraction at 298.15 K (see caption from **Figure 2. 2**). The model calculates the energy $C_{j,i}$ parameters using Coulombic interactions (eq (2. 3)). Lines: red dash, glutaric acid; blue dash-dot, malonic acid. Symbols: red square, glutaric acid experimental data; blue circle, malonic acid experimental data, where references for the experimental data are given in **Table 2. 1**.

The partial dissociation model predictions for acetic acid, butyric acid, citric acid, malic acid, and succinic acid, shown in **Figure 2. 4** and **Figure 2. 5** are in agreement with available data across the entire concentration range, much like their equivalent Coulombic predictions. The mean square errors (MSE) are of the same order, as can be seen in **Table 2. 1**. For these organic acids, both dissociation ratios, 1:0.1 and 1:0.5, resulted in model predictions that were in agreement with the available data, with the lowest best fit dissociation ratio shown in **Figure 2. 4** and **Figure 2. 5** (dash-dot-dot lines in gold color). The partial dissociation model applied to malonic and glutaric acids (**Figure 2. 6**), shown with a 1:0.5 ratio, resulted in a remarkable improvement in predictions across the entire available data range, including the expected limiting conditions at high solute concentrations.

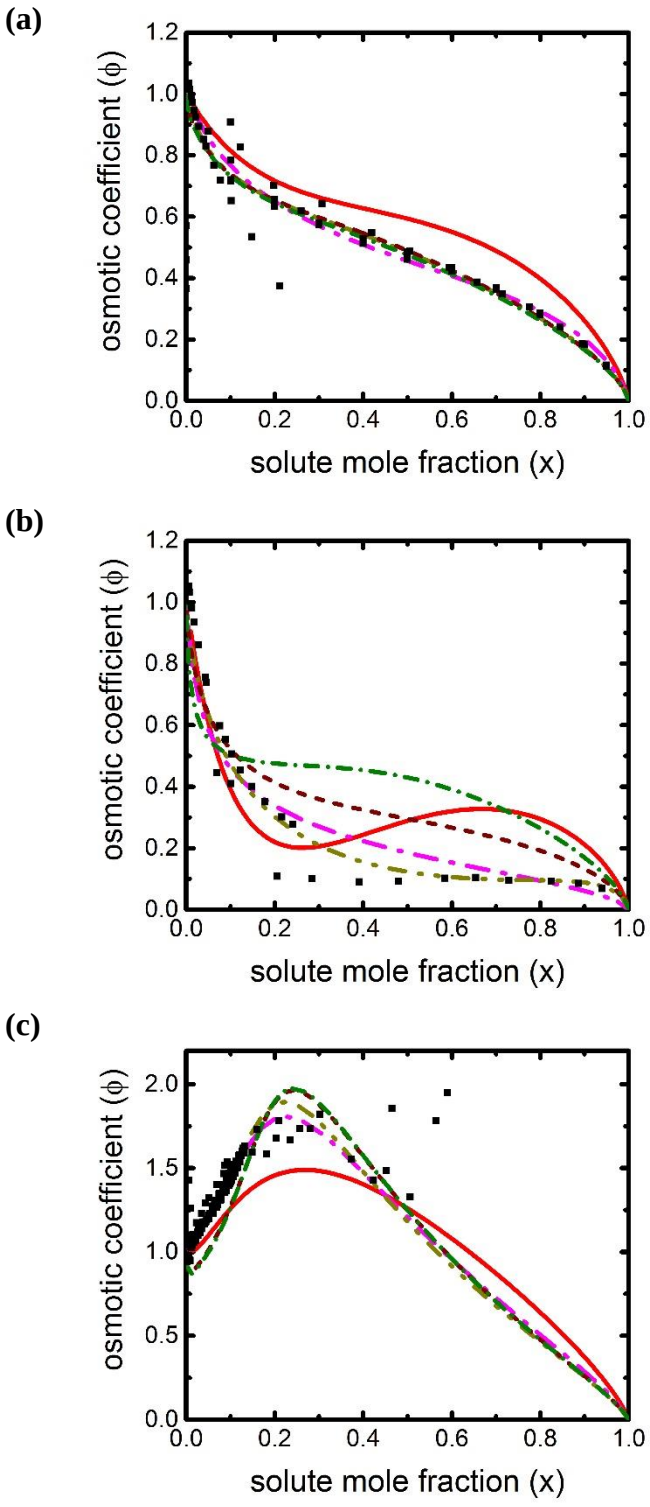

Figure 2. 4. Osmotic coefficient plotted against the solute mole fraction at 298.15 K (see caption from **Figure 2. 2**), comparing different models for (a) acetic acid, (b) butyric acid,

and (c) citric acid. Lines: red solid, UNIFAC (AIOMFAC);[92,93,252] magenta dash-dot, eq (2. 3); gold dash-dot-dot, eq (2. 10) (three-fit); maroon short-dash, eq (2. 10) (two-fit); cyan dash-dot-dash, eq (2. 10) (one-fit); black squares, experimental data, where references for the experimental data are given in **Table 2. 1**.

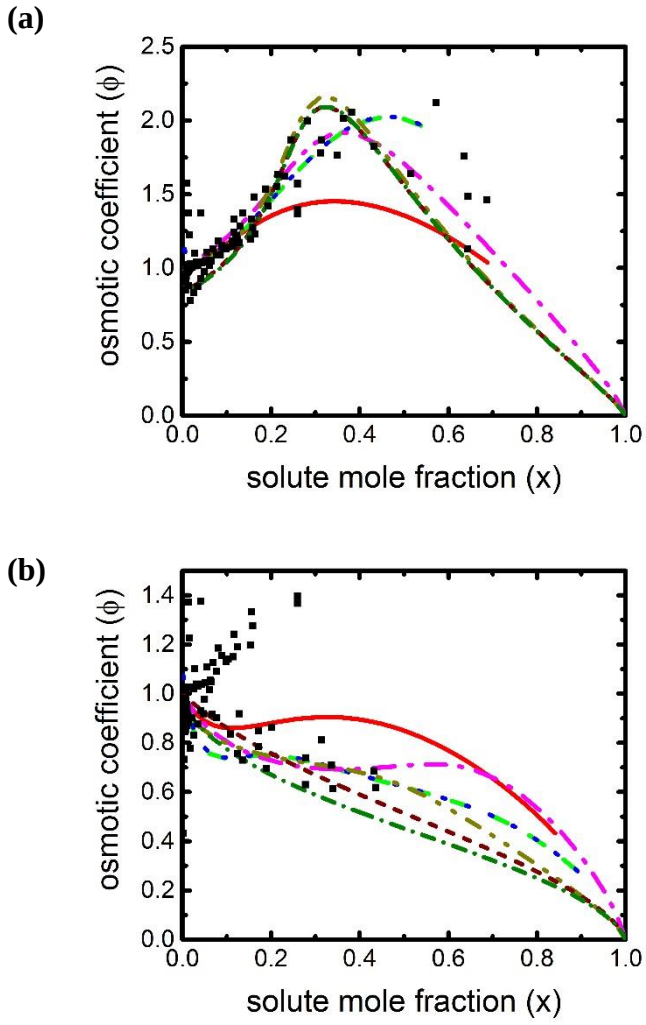

Figure 2. 5. Osmotic coefficient plotted against the solute mole fraction at 298.15 K (see caption from **Figure 2. 2**), comparing different models for (a) malic acid and (b) succinic acid. Lines: red solid, UNIFAC (Peng et al.);[49,253] green dash, E-AIM (RK)[33,253] no dissociation; blue dotted, E-AIM (RK)[34,253] dissociation; magenta dash-dot, eq (2. 3); gold dash-dot-dot, eq (2. 10) (three-fit); maroon short-dash, eq (2. 10) (two-fit); cyan dash-dot-

dash, eq (2. 10) (one-fit); black squares, experimental data, where references for the experimental data are given in **Table 2. 1**.

2.3 Model Parameter Reduction

A general trend of $r_{jw,\mathrm{H^+A^-}} = 2r_{jw,\mathrm{HA}}$ was observed when the partial dissociation was applied (cf. parameter values in **Table 2. 1**). The constraint reduces the number of fit parameters by one, and results in excellent agreement across all acid systems (**Figure 2. 4 – Figure 2. 6**) (short-dash lines in maroon color), with the exception of butyric acid and citric acid. The model agrees with the available data and with the expected limiting conditions with dissociation ratios 1:0.5. It should be noted that for glutaric acid, the constrained model fails at dissociation ratios less than 1:0.5.

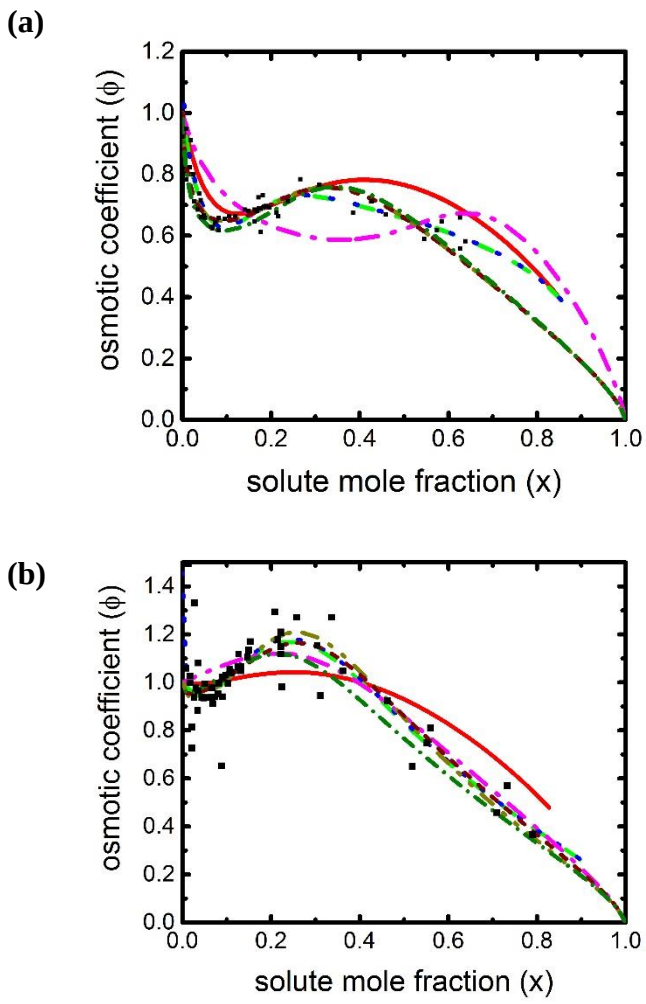

Figure 2. 6. Osmotic coefficient plotted against the solute mole fraction at 298.15 K (see caption from **Figure 2. 2**), comparing different models for (a) glutaric acid and (b) malonic acid. Lines: see caption from **Figure 2. 5**. Black squares, experimental data, where references for the experimental data are given in **Table 2. 1**.

To reduce the number of adjustable parameters further, the Debye-Hückel parameter ρ was re-examined. Up until this point, the parameter ρ has been treated as either a constant[61,62,94] or as a fit parameter, as was done in Coulombic fit.[64] A theoretical

derivation of ρ performed by Pitzer and Simonson[95] gives us the following definition of ρ in terms of the hard-core collision diameter of the solute:

$$\rho = a(2e^2 N_A d_1 / M_1 \varepsilon_0 D_1 kT)^{1/2} \quad (2.\ 12)$$

where a is the hard-core collision diameter, e is the electronic charge, k is Boltzmann's constant, T is the Temperature, ε_0 is the permittivity of free space, N_A is Avogadro's number, d_1 is the density of the solvent, M_1 is the molecular weight of the solvent, and D_1 is the dielectric constant (relative permittivity) of the solvent.

Here, the nondissociated organic radius, $r_{jw,\mathrm{HA}}$, was used as the hard-core collision diameter for the solute ion. Using $r_{jw,\mathrm{HA}}$ as the hard-core collision diameter in eq (2. 12) and forcing $r_{jw,\mathrm{H^+A^-}}$ to be twice $r_{jw,\mathrm{HA}}$, it is, for a given n_{HA}, $n_{\mathrm{H^+A^-}}$, and β, possible to obtain a model that has a single fit parameter, $r_{jw,\mathrm{HA}}$. Remarkably, even with adjustments to the model making it a "single parameter" model, the predictions for acetic and succinic acids (**Figure 2. 4**a and **Figure 2. 5**b) (dash-dot-dash lines in cyan color)) and malonic and glutaric acids (**Figure 2. 6**) remain very similar to their predictions when ρ was used as a fit parameter (two-parameter model), or even when the values for $r_{jw,\mathrm{H^+A^-}}$ and $r_{jw,\mathrm{HA}}$ were uncoupled (three-parameter model). With the approach discussed here, the reduction to a single parameter has had little effect on the predictions or MSE of the model when compared to the MSE of the partial dissociation model using three and two fit parameters.

The Coulombic model predictions for osmotic coefficient without dissociation (eq (2. 3)), and with dissociation (eq (2. 10)) are compared with those from UNIFAC (Peng et

al.),[49,253] and the extended AIM aerosol thermodynamics model, E-AIM (Redlich-Kister expansion equation).[33,34,253] As an example, it is observed for malonic acid that both the dissociation models (three- and two-parameter fit) and the E-AIM (Redlich-Kister) model were in good agreement with the osmotic coefficient data unlike UNIFAC alone, **Figure 2. 6**b. Similar comparisons for the other organic acids used in this study are given in **Figure 2. 4**, **Figure 2. 5**, and **Figure 2. 6**a.

solute	model[a]	β	$n_{\mathrm{HA}}, n_{\mathrm{H^+A^-}}$	ρ	$r_{jw,\mathrm{HA}}$ (Å)	$r_{jw,\mathrm{H^+A^-}}$ (Å)	MSE[b]	ref
acetic acid	neutral		6[c]		2.280[c]		0.0360	96–98
	mix (n_m = 3)	0.5	4,5	381.60[d]	3.939	8.715	0.0278	
	mix (n_m = 2)	0.5	4,5	14.567	4.234	8.468[e]	0.0294	
	mix (n_m = 1)	0.5	4,5	10.310[e]	4.200	8.400[e]	0.0317	
butyric acid	neutral		3[c]		11.57[c]		2.3430	96,97
	mix (n_m = 3)	0.5	3,3	0.8500	0.526	7.619	2.5043	
	mix (n_m = 2)	0.5	3,3	4.48×10^{-13} [d]	4.088	8.176[e]	2.7362	
	mix (n_m = 1)	0.5	3,3	11.440[e]	4.663	9.326[e]	5.4590	
citric acid	neutral		9[c]		5.000[c]		0.0297	73
	mix (n_m = 3)	0.1	8,3	144.01[d]	6.216	6.732	0.0343	
	mix (n_m = 2)	0.1	8,3	405.66[d]	6.650	13.30[e]	0.0473	
	mix (n_m = 1)	0.1	8,3	16.460[e]	6.710	13.42[e]	0.0491	
malic acid	neutral		4[c]		4.080[c]		0.0149	49,99–101
	mix (n_m = 3)	0.1	4,5	207.52[d]	9.281	8.490	0.0493	
	mix (n_m = 2)	0.1	4,5	11672[d]	9.030	18.06[e]	0.0557	
	mix (n_m = 1)	0.1	4,5	22.300[e]	9.090	18.18[e]	0.0571	
succinic acid	neutral		10[c]		1.690[c]		0.0059	49,99,100,102
	mix (n_m = 3)	0.5	3,3	1.9×10^{-5} [d]	8.235	6.988	0.0047	
	mix (n_m = 2)	0.5	3,3	4279.9[d]	3.628	7.256[e]	0.0117	

	mix (n_m = 1)	0.5	3,3	8.9100[e]	3.629	7.258[e]	0.0219	
glutaric acid	neutral		7[c]		1.040[c]		0.0263	49,99,101
	mix (n_m = 3)	0.5	7,8	40.680	5.061	10.48	0.0072	
	mix (n_m = 2)	0.5	7,8	22.390	5.150	10.30[e]	0.0072	
	mix (n_m = 1)	0.5	7,8	12.860[e]	5.240	10.48[e]	0.0088	
malonic acid	neutral		3[c]		7.090[c]		0.0990	49,99–101
	mix (n_m = 3)	0.5	4,6	0.5500	3.944	6.292	0.0890	
	mix (n_m = 2)	0.5	4,6	5.5500	3.220	6.440[e]	0.0891	
	mix (n_m = 1)	0.5	4,6	8.2000[e]	3.342	6.684[e]	0.0903	

Table 2. 1. Fitted Parameters at 298.15 K. [a]"neutral" model refers to eq (2. 3). "mix" model refers to eq (2. 10), where the organic acid is treated as a mixture of neutral solute (HA) and dissociated solute (H^+A^-). n_m is equal to the number of fit parameters. [b]MSE is a normalized mean-square error, equal to $\left(\frac{1}{n_p}\right)\sum_{i=1}^{n_p}((m_{model,i} - m_{data,i})/(m_{model,i}))^2$, where n_p is the number of data points. [c]Neutral model is not dissociated, so only one n and r_{jw} value. [d]Unrealistic value. [e]Calculated value.

2.4 Fused Salt Reference State for Mixed Charge Type Solutions

It was observed that using equations from the activity model,[63] the solute activities were calculated to be greater than unity at the hypothetical pure liquid solute for certain mixed charge type solutions, which is not accurate. One explanation for this occurrence is the treatment of the reference state in the combined adsorption isotherm-Debye-Hückel model. The ionic strength of a ternary solution on a mole fraction basis over all solutes *j* consisting of ionic species in terms of molalities of solutes present[63,103] is defined by

$$I_x = \left(\frac{1}{2}\right)\frac{\sum_j v_j N_j |z_{j-}| z_{j+}}{\sum_j v_j N_j + N_w} = \left(\frac{1}{2}\right)\frac{\sum_j v_j m_j |z_{j-}| z_{j+}}{\sum_j v_j m_j + 1/M_w} \quad (2.\ 13)$$

A fused salt reference state can be found at the limit of pure (*single*) solute (fused salt state) on a mole fraction basis for a given solute *j*. The ionic strength is then given by

$$I_{x,j}^{ref} = \lim_{N_w \to 0} I_{x,j} = \left(\frac{1}{2}\right)|z_{j-}| z_{j+} \quad (2.\ 14)$$

The Debye-Hückel contribution for electrolyte solute *j* in a mixture uses the reference state ionic strength for the solute *j* and is given by[63]

$$K_j^{DH} = \left(\exp\left[-A_x |z_{j-}| z_{j+} \left\{ \frac{2}{\rho_j} \ln\left(\frac{1 + \rho_j I_x^{\frac{1}{2}}}{1 + \rho_j (I_{x,j}^{ref})^{\frac{1}{2}}} \right) + \left(\frac{1 - \frac{2I_x}{z_{j-} z_{j+}}}{\sum_k (v_k N_k) + N_w} \right) \sum_k \frac{v_k N_k |z_{k-}| z_{k+}}{2 I_x^{\frac{1}{2}} \left(1 + \rho_k I_x^{\frac{1}{2}}\right)} \right\} \right] \right)^{v_j} \quad (2.\ 15)$$

for an electrolyte solute *j* and

$$K_j^{DH} = \exp\left(\frac{A_x I_x{}^{\frac{1}{2}} \sum_k \frac{v_k N_k |z_{k-}| z_{k+}}{\left(1+\rho_k I_x{}^{\frac{1}{2}}\right)}}{\sum_k (v_k N_k) + N_w}\right) \tag{2. 16}$$

for a nonelectrolyte solute *j* in a solution containing electrolytes. Expressions (2. 15) and (2. 16) are used in calculations of activities and activity coefficients at the fused salt reference state.[61,63]

However, in a ternary mixture solution, the ionic strength *of the mixture* of a fixed solute molar ratio at fused salt state could instead be given as

$$I_{x,mix}^{FS} = \lim_{N_w \to 0} I_{x,mix} = \left(\frac{1}{2}\right) \frac{\sum_j v_j N_j |z_{j-}| z_{j+}}{\sum_j v_j N_j} = \left(\frac{1}{2}\right) \frac{\sum_j \alpha_j v_j |z_{j-}| z_{j+}}{\sum_j \alpha_j v_j} \tag{2. 17}$$

where α_j is the fraction of moles of solute *j* to the total number of moles of solutes in the mixture. Note that for fixed solute molar ratios, $I_{x,mix}^{FS}$ is a constant value. For example, for a partially dissociating organic acid as treated here, $I_{x,mix}^{FS} = \left(\frac{1}{2}\right) \frac{\alpha_{H^+A^-} v_{H^+A^-}}{\alpha_{H^+A^-} v_{H^+A^-} + \alpha_{HA}} = \left(\frac{1}{2}\right) \frac{\beta v_{H^+A^-}}{(\beta v_{H^+A^-} + 1)}$. Therefore, the ionic strength *of the mixture* at a fused salt reference state would be $I_{x,mix}^{ref} = I_{x,mix}^{FS}$, instead of $\frac{|z_{j-}| z_{j+}}{2}$.

For a system where the reference state is defined by the limit where the amount of water goes to zero, for a fixed molar ratio of solutes, the Debye−Hückel contribution[63] for

electrolyte solute *j* in a mixture can be recast by replacing $I_{x,j}^{ref}$ with $I_{x,mix}^{ref}$, and replacing $\frac{|z_{j-}|z_{j+}}{2}$ (from eq (2. 14)) with $I_{x,mix}^{FS}$ (from eq (2. 17)), yielding

$$K_j^{DH} = \left(\exp\left[-A_x |z_{j-}| z_{j+} \left\{ \frac{2}{\rho_j} \ln\left(\frac{1+\rho_j I_x^{\frac{1}{2}}}{1+\rho_j (I_{x,mix}^{ref})^{\frac{1}{2}}} \right) + \left(\frac{1-\frac{I_x}{I_{x,mix}^{FS}}}{\sum_k (v_k N_k) + N_w} \right) \sum_k \frac{v_k N_k |z_{k-}| z_{k+}}{2 I_x^{\frac{1}{2}} \left(1+\rho_k I_x^{\frac{1}{2}}\right)} \right\} \right] \right)^{v_j} \tag{2. 18}$$

where the summations are over all solutes *k* in the solution. Similarly, the Debye−Hückel term for nonelectrolyte solute *j* in a solution containing electrolytes is expressed by

$$K_j^{DH} = \exp\left(\frac{-A_x \left(I_{x,mix}^{FS} - I_x\right) \sum_k \frac{v_k N_k |z_{k-}| z_{k+}}{\left(1+\rho_k I_x^{\frac{1}{2}}\right)}}{I_x^{\frac{1}{2}} \left(\sum_k (v_k N_k) + N_w\right)} \right) \tag{2. 19}$$

Equation (2. 18) is a generalized equation where $I_{x,mix}^{ref}$can be calculated based on the two reference states, fused salt or infinite dilution. All calculations in this work are based on the pure solute (fused salt) reference state. For a reference state of infinite dilution in the solvent, $I_{x,mix}^{ref}$ = 0. In the limit of a single solute, or in the limit of mixtures of solutes of the same charge type, eqs (2. 18) and (2. 19) reduce to eqs (2. 15) and (2. 16). However, for mixed charge type aqueous mixtures with a fixed molar solute ratio, eqs (2. 18) and (2. 19) may be more appropriate for studies of varied water content, or in aerosol science, relative humidities with a fused salt reference state. Treatment of ternary mixture aqueous

solutions using the model is not specific to partially dissociating organic acids, but an alternative to treat mixture with two or more solutes having same molar ratio throughout, including at the fused salt limit.

2.5 Conclusions

By accounting for partial dissociation of organic acids, the model has been able to successfully capture the trends of osmotic coefficient of organic acids with only a small increase in the number of parameters needed for the model. The partial dissociation approach also implemented a theoretical equation for ρ, where previous models have treated it as a constant or an empirical fit parameter. The partial dissociation model, like the Coulombic binary model, has reduced the empirical dependence of the parameters by providing physical interpretations of the fit parameters.

Outside of glutaric acid and malonic acid, the other dicarboxylic and carboxylic acids modeled are capable of being modeled by the Coulombic interaction without the need to account for dissociation. The predictions for glutaric and malonic acids are greatly improved with the inclusion of partial dissociation. Despite the added complexity of including partial dissociation, the number of fit parameters does not increase, and the physicochemical relationships in the model are more accurately addressed. Compared to the Coulombic model without partial dissociation, the only parameters that are added are an additional n value and a term for the solute concentration ratio of dissociated acid to nondissociated acid as a result of partial dissociation.

Associated Content

Additional plots and tables in Appendix A - Figures of osmotic coefficient plotted versus solute mole fraction for "all energy $C_{j,i}$ parameters" fit and "power law" fit; figures of water activity plotted against the solute mole fraction, comparing different models; tables of fitted parameters at 298.15 K for each acid for "all energy $C_{j,i}$ parameters" fit and "power law" fit.

Chapter 3

Isotherm-Based Thermodynamic Model for Solute Activities of Asymmetric Electrolyte Aqueous Solutions†

†Adapted with permission from Nandy, L.; Dutcher, C. S. Isotherm-Based Thermodynamic Model for Solute Activities of Asymmetric Electrolyte Aqueous Solutions. *J. Phys. Chem. A* **2017**, *121* (37), 6957–6965.

3.1 Introduction

Adsorption isotherm-based statistical thermodynamic models can be used to determine solute concentration and solute and solvent activities in aqueous solutions. The number of

adjustable parameters in the isotherm model of Dutcher et al.[58,59,63] was reduced for neutral solutes as well as symmetric 1-1 electrolytes by using a Coulombic model to describe the solute – solvent energy interactions.[64,86] In this chapter, the Coulombic treatment for symmetric electrolytes is extended to establish improved isotherm model equations for asymmetric 1-2 and 1-3 electrolyte systems. The Coulombic model developed here results in prediction of activities and other thermodynamic properties in multicomponent systems containing ions of arbitrary charge. The model is found to accurately calculate osmotic coefficient over the entire solute concentration range with two model parameters, related to intermolecular solute-solute and solute-solvent spacing. The inorganic salts and acids treated here are generally considered to be fully dissociated. However, there are certain weak acids that do not dissociate completely, such as the bisulfate ion. In this work, partial dissociation of the bisulfate ion from sulfuric acid is treated as a mixture, with an additional model parameter which accounts for dissociation ratio of the dissociated ions to non-dissociated ions.

In Chapter 2, Coulombic interactions model for organic acids that partially dissociate into 1-1 electrolyte was used to represent activity coefficients and solute concentrations by treating the acids as a mixture of electrolyte and neutral non-dissociated organic.[86] The Coulombic isotherm model developed, when applied to salts, only treated symmetric 1-1 aqueous electrolyte solutions. However, ions common to atmospheric aerosols[104] as well as water treatment[105] and desalination,[106,107] include mixtures of both symmetric and asymmetric electrolytes. The difference in valency is important, as it produces a different effect on aqueous solutions in a variety of applications from sea salt aerosols, soil permeability, waste water treatment, rheology, drug delivery, and industrial discharge. For

example, it has been shown in a study on hygroscopic behavior[108] that NaCl-$MgCl_2$ mixture aerosol particles from sea salt particles can maintain an aqueous phase over a wider relative humidity range than the pure NaCl particles, and hence will be more susceptible to aqueous heterogeneous reactions with gas phase. Even at very low relative humidities, Mg^{2+} will more readily remain in aqueous phase having a high surface tension and viscosity than that of NaCl that crystallizes at higher relative humidity. In a study on nanoparticles from industrial discharges and disposal of wastewater treatment effluents,[109] it is shown that the presence of divalent cations promote destabilization of TiO_2 nanoparticles in aqueous solutions, which then enter natural aquatic systems and form agglomerates.[109] Finally, soil permeability studies suggest improvements in water permeability when divalent calcium and magnesium ions are in excess compared to monovalent sodium and potassium ions, due to enhanced soil flocculation, and resultant enlarged porous chemical size, in the presence of higher valency ions.[110]

In addition, crustal species like Ca^{2+} and Mg^{2+} may be in thermodynamic equilibrium with atmospheric gases as they are a major component of ambient particles from significant dust sources.[111] SCAPE2 gas-particle equilibrium model introduced these water-soluble ions that affect aerosol chemistry in dusty regions for accurate estimation of gas-aerosol equilibrium.[112] A considerable amount of the alkaline elements (Ca and Mg) is in the form of carbonate. Hence, the gas-aerosol equilibrium models need to incorporate carbonate and bicarbonate salts as well.[113] Size-resolved equilibrium model, e.g. SELIQUID for treating crustal species assuming equivalent concentrations of sodium has been developed,[114] although it introduces errors when concentrations of these species are high. Other studies have showed that gas-aerosol partitioning of volatile or semi-volatile

aerosol compounds are influenced by the concentration levels of alkaline cations.[115] Since partition prediction considering these materials is important, ISORROPIA II was introduced that could add the thermodynamics of the $Ca^{2+,}$ Mg^{2+} and SO_4^{2-} aerosol systems in addition to monovalent species.[116]

In this work, the Coulombic model has been extended to calculate thermodynamic properties of asymmetric (1-2 and 1-3) aqueous electrolyte solutions over the entire concentration range at 298.15 K. The compounds studied include Al^{3+}, Cr^{3+}, Co^{2+}, Cu^{2+}, Mn^{2+}, Ni^{2+}, Ba^{2+}, Sr^{2+}, Na^{+}, K^{+}, H^{+}, Li^{+}, NH_4^{+}, Mg^{2+}, Ca^{2+}, Cl^{-}, Br^{-}, I^{-}, SO_4^{2-}, NO_3^{-}, HSO_4^{-}, PO_4^{3-}, CO_3^{2-}. Partial dissociation of the weak acid bisulfate ion is also considered by treating the system as a mixture of dissociated ions and non-dissociated bisulfate ion. Although sulfuric acid is a strong acid, the bisulfate ion dissociates partially. Several studies have considered partial dissociation of electrolytes in their model. Activity coefficients have been derived using excess Gibb's energy from infinite dilution in solvent to electrolyte saturation, where both long range and short range interactions have been considered to account for partial dissociation into ions at high electrolyte concentrations.[117] The aqueous electrolyte nonrandom two-liquid (NRTL) model is used to represent ionic activity coefficients for study of partial dissociation of weak electrolytes.[118] A recent model predicts thermodynamic and volumetric properties of a partially ionized aqueous electrolyte along with estimation of degree of dissociation at varying concentrations.[119] The approach has applications in the hydrothermal and geothermal processes where understanding of electrolyte solution concentrations at high temperatures is required. The model can predict properties in a wide range of temperatures, pressures, and concentrations to represent nonidealities of aqueous electrolyte solutions. However, the model has more

limited accuracy for some systems at very high electrolyte concentrations, which could be especially important for atmospheric aerosols.

The work in this chapter successfully makes accurate model calculations of thermodynamic properties for the entire range of electrolyte aqueous solution concentrations containing ions of arbitrary charge. The development of the model treatment for the energy parameters with asymmetric electrolytes is given in Section 3.2. Resultant parameterizations in Sections 3.3 and 3.4 shed new insights on interactions between solute and solvent, and between partially dissociated and non-dissociated ions.

3.2 Theoretical Development

Solution molality and solute activity are determined by previous models using lattice adsorption isotherm-based statistical mechanics and long-range electrostatic interactions.[58,59,63] The model can incorporate an arbitrary number of hydrated layers, each characterized by a sorption energy parameter that is determined by a power-law empirical relationship.[63] The short-range sorption energy parameter $C_{j,i}$ is given by

$$C_{j,i} = \exp\left(\left(\frac{\mu_j \mu_w D^2}{4\pi\varepsilon_0\left(r_{jw} + (i-1)r_{ww}\right)^3} - \frac{\mu_w \mu_w D^2}{4\pi\varepsilon_0 (i \cdot r_{ww})^3}\right)/kT\right) \quad (3.1)$$

where, j is the solute, i is the hydration layer, μ_j is the dipole moment of solute j, μ_w = 2.9, r_{ww} = 2.82 × 10^{-10} m, ε_o is the permittivity of space, $4\pi\varepsilon_o$ = 1.113 × 10^{-10} $C^2N^{-1}m^{-2}$, D is a unit of conversion (Debye), D = 3.33564 × 10^{-30} Cm, r_{jw} is the intermolecular distance between solute j and solvent w (here water), k = 1.38 × 10^{-23} JK^{-1} (Boltzmann's constant), T is temperature. It is assumed that all molecules, both solute and solvent are modeled as

apparent dipoles, and that the adsorbed species is a ternary cation-water-anion cluster. It is also assumed that the sorption energies are due to short-range dipole-dipole electrostatic forces at the molecular level.[64]

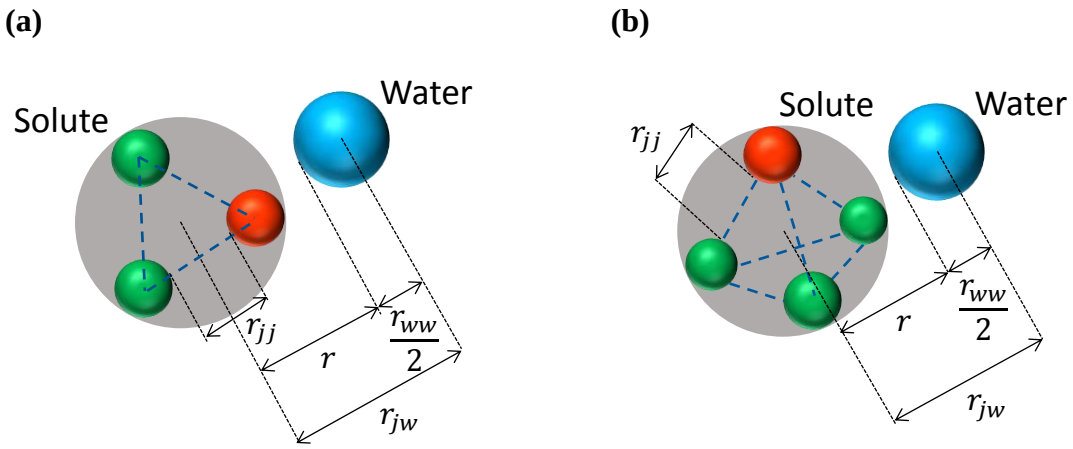

Figure 3. 1. (a) Schematic of a solute-solvent lattice model spacing for a 1-2 electrolyte (2 single-charged cations+1 double-charged anion or 1 double-charged cation+2 single-charged anions). The solute is assumed to have ions arranged by an equilateral triangle of side 'a' = r_{jj}+ r_{j+} + r_{j-}. Height of the triangle = $r = \frac{\sqrt{3}}{2}a$ = $\frac{\sqrt{3}}{2}$ [r_{jj}+ r_{j+} + r_{j-}], and therefore, r_{jw} = r + $\frac{r_{ww}}{2}$ and μ_j = r ($\frac{qe}{D}$) where q = 2. (b) Schematic of a solute-solvent lattice model spacing for a 1-3 electrolyte (3 cations+1 anion or 1 cation+3 anions). The solute is assumed to have ions arranged by a regular tetrahedron of side 'a' = r_{jj}+ r_{j+} + r_{j-}. Height of the tetrahedron = $r = \frac{\sqrt{6}}{3}a$ = $\frac{\sqrt{6}}{3}$[r_{jj}+ r_{j+} + r_{j-}], and therefore, r_{jw} = r + $\frac{r_{ww}}{2}$ and μ_j = r ($\frac{qe}{D}$) where q = 3.

Here, for a 1-2 or 1-3 electrolyte, the apparent dipole moment is calculated by considering the electrolyte as a solvent-separated ion cluster, given by

$$\mu_j = r\left(\frac{qe}{D}\right) \qquad (3.\ 2)$$

where, q is the charge, valency of each side of the cluster separated by a characteristic intermolecular distance r. In the case of 1-2 electrolytes q has a value of 2, and for 1-3 electrolytes it has a value of 3, e is the elementary charge, e = 1.60218 × 10^{-19} C. For example, a 1-2 electrolyte may have two single-charged cations (2 Na^+) and a double-charged anion (SO_4^{2-}); so q will be 2. The characteristic cluster distance r is related to r_{jw} by the following expression

$$r_{jw} = r + \frac{r_{ww}}{2} \tag{3. 3}$$

r is obtained by assuming different ionic geometry for the 1-2 and 1-3 electrolytes as shown in **Figure 3. 1**a and b, respectively, and is related to the total center-to-center distance between the ions, $a = r_{jj} + r_{j+} + r_{j-}$. r_{jj} is the interspatial distance between cation and anion, and r_{j+} and r_{j-} are the effective radii of the cation and anion, respectively. Note that r_{jj} represents the distance between ions, r represents the distance between center of ion cluster and water, and r_{jw} represents the center-to-center distance between solute and water.

To apply this framework to the model, once the energy parameters (Eq (3. 1)) are determined for the system, the same governing equations for asymmetric electrolytes are used as were done for symmetric (1-1) electrolytes (eqs 27 and 28 of Dutcher et al. 2013)[63]. The equations, given below as equations (3. 4) and (3. 5), give the solution molality and the solute activity of j in a pure aqueous solution at water activity of the mixture, $\bar{a}_w$ normalized by long-range Debye-Hückel term.

$$\bar{m}_j^o = \frac{\left(\frac{1-\bar{a}_w}{M_w v_j \bar{a}_w}\right)\left(1-\sum_{i=1}^{n_j-1}\left((\bar{a}_w)^i\left(1-C_{j,i}\right)\prod_{k=1}^{i-1}C_{j,k}\right)\right)}{(1-\bar{a}_w)^2\sum_{p=1}^{n_j-2}\left(p(\bar{a}_w)^{p-1}\prod_{k=1}^{p}C_{j,k}\right)+\left(\left(n_j-1\right)-\left(n_j-2\right)\bar{a}_w\right)(\bar{a}_w)^{n_j-2}\prod_{k=1}^{n_j-1}C_{j,k}} \quad (3.\ 4)$$

$$\bar{a}_j^o = \frac{(1-\bar{a}_w)}{\left(1-\sum_{i=1}^{n_j-1}\left((\bar{a}_w)^i\left(1-C_{j,i}\right)\prod_{k=1}^{i-1}C_{j,k}\right)\right)^{v_j}} \quad (3.\ 5)$$

where M_w (kg mol^{-1}) is the molecular weight of the solvent (water), v_j is the stoichiometric coefficient of solute *j*. It is the number of moles of ions formed from 1 mole of fully dissociated solute *j*. For a multicomponent system with arbitrary number of solutes, the molality m_j in the mixture can be found by using the following mixing model.[63]

$$\sum_j \frac{m_j}{\bar{m}_j^o} = 1 \quad (3.\ 6)$$

3.3 Model Parameterization and Results

The thermodynamic modeling has been applied to thirty-eight 1-2 electrolytes and five 1-3 electrolytes, to determine osmotic and activity coefficients in aqueous solutions at 298.15 K. Incorporating equations (3. 1) and (3. 4) in the asymmetric electrolyte model, there are four unknown model parameters ρ, n_j, r_{jw} and μ_j, where n_j is the number of hydration layers and ρ is a fitting parameter.[64] Treating n_j as a constant, the number of fit parameters are three. Finally, employing equations (3. 2) and (3. 3) for μ_j and r_{jw} respectively, the number of parameters are reduced to two, i.e. ρ, and r_{jj}. Special treatment for sulfate and bisulfate ions are given in the next section.

solute	n_j	ρ^a	r_{j+} (Å)[120–122]	r_{j-} (Å)[120–122]	r_{jj} (Å)[a]	r_{jw} (Å)[b]	$\mu_j{}^b$	MSE[c]	Ref
$CaBr_2$	6	28.98	1.00	1.88	2.64	6.19	45.93	8.21×10^{-4}	[123]
$CaCl_2$	4	59.60	1.00	1.72	4.06	7.28	56.36	3.52×10^{-3}	[123]
CaI_2	8	34.00	1.00	2.10	4.16	7.70	60.41	2.86×10^{-4}	[123]
$Ca(NO_3)_2$	3	21.26	1.00	1.79	4.65	7.85	61.89	3.78×10^{-5}	[124]
$CoBr_2$	6	46.08	1.25	1.88	4.52	8.03	63.63	1.06×10^{-3}	[125]
$CoCl_2$	6	26.97	1.25	1.72	5.80	9.00	72.95	1.69×10^{-4}	[125]
CoI_2	9	36.23	1.25	2.10	3.73	7.54	58.87	6.32×10^{-4}	[125]
$Co(NO_3)_2$	5	26.49	1.25	1.79	4.88	8.27	65.88	3.40×10^{-4}	[125]
$CuBr_2$	6	35.42	0.73	1.88	7.00	9.74	79.97	5.50×10^{-4}	[126]
$CuCl_2$	4	25.74	0.73	1.72	6.39	9.07	73.55	3.65×10^{-4}	[126]
$Cu(NO_3)_2$	4	32.63	0.73	1.79	4.96	7.89	62.26	7.20×10^{-4}	[126]
$FeCl_2$	8	19.62	0.70	1.72	7.55	10.0	82.91	2.34×10^{-5}	[125]
$MgBr_2$	9	14.78	0.72	1.88	4.00	7.12	54.87	2.66×10^{-3}	[123]
$MgCl_2$	5	91.51	0.72	1.72	4.09	7.07	54.33	2.74×10^{-3}	[123]
MgI_2	9	57.70	0.72	2.10	2.33	5.87	42.84	7.93×10^{-4}	[123]
$Mg(NO_3)_2$	5	39.74	0.72	1.79	5.35	8.22	65.39	6.59×10^{-4}	[124]
$MnBr_2$	6	39.00	0.70	1.88	5.66	8.55	68.54	8.72×10^{-4}	[126]
$MnCl_2$	4	38.18	0.70	1.72	5.64	8.39	67.06	1.29×10^{-3}	[126]
$NiBr_2$	7	35.06	0.70	1.88	5.24	8.19	65.08	5.09×10^{-4}	[125]
$NiCl_2$	5	38.10	0.70	1.72	5.48	8.25	65.72	1.21×10^{-3}	[125]
$Ni(NO_3)_2$	5	32.16	0.70	1.79	5.40	8.24	65.63	4.47×10^{-4}	[125]
H_2SO_4	2	23.44	0.21	2.58	2.71	6.17	45.74	2.50×10^{-2}	[127]
K_2SO_4	2	11.83	1.38	2.58	3.28	7.68	60.22	8.94×10^{-5}	[128,129]
Na_2SO_4	3	8.040	1.02	2.58	4.34	8.28	66.01	4.00×10^{-3}	[128,129]
$(NH_4)_2SO_4$	2	11.51	1.37	2.58	2.95	7.39	57.43	1.37×10^{-3}	[130–133]
Li_2SO_4	3	15.73	0.76	2.58	4.30	8.02	63.53	5.30×10^{-5}	[129]
Rb_2SO_4	2	13.47	1.52	2.58	2.94	7.51	58.59	5.36×10^{-6}	[128]
Cs_2SO_4	4	13.53	1.67	2.58	5.53	9.88	81.32	1.15×10^{-5}	[128]

$BaBr_2$	5	25.02	1.33	1.88	2.02	5.93	43.47	1.75×10^{-4}	[123]
$BaCl_2$	7	17.43	1.33	1.72	7.51	10.6	87.82	5.69×10^{-5}	[123]
BaI_2	9	26.78	1.33	2.10	6.54	10.0	82.89	1.05×10^{-4}	[123]
$Pb(NO_3)_2$	2	8.310	1.19	1.79	4.50	7.89	62.26	2.83×10^{-4}	[126]
$SrBr_2$	9	19.32	1.18	1.88	7.09	10.2	84.45	1.18×10^{-4}	[123]
$SrCl_2$	5	24.61	1.18	1.72	5.14	8.37	66.87	2.32×10^{-4}	[123]
SrI_2	10	24.92	1.18	2.10	6.81	10.2	83.94	5.58×10^{-5}	[123]
$Cd(NO_3)_2$	6	21.60	0.95	1.79	7.25	10.1	83.12	3.26×10^{-5}	[134]
$Zn(NO_3)_2$	4	56.49	0.74	1.79	4.58	7.57	59.18	5.46×10^{-3}	[134]
Na_2CO_3	2	13.60	1.02	1.79	4.02	7.32	56.73	3.19×10^{-4}	[128]

Table 3. 1. Two-Parameter Fit for Aqueous 1-2 Electrolyte Solutions at 298.15 K. [a]Fitted value. [b]Calculated value. [c]MSE is a normalized mean-square error, equal to $\left(\frac{1}{n_p}\right)\sum_{i=1}^{n_p}((m_{model,i} - m_{data,i})/(m_{model,i}))^2$, where n_p is the number of data points.

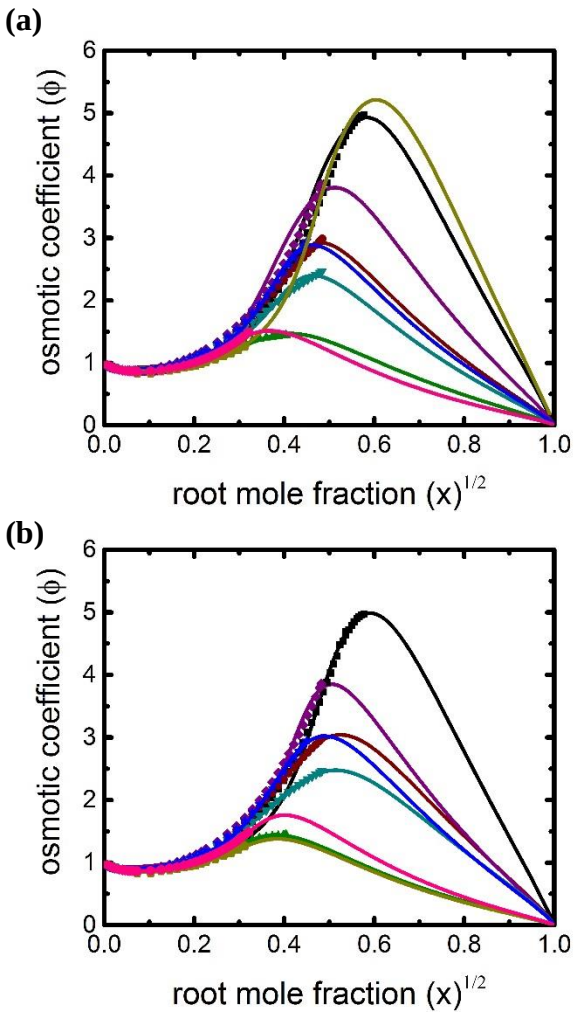

Figure 3. 2. Bromides. (a) Fitting two parameters ρ and r_{jj}. (b) Fitting three parameters ρ, r_{jj} and μ_j. Osmotic coefficient (φ = -ln $(a_w)/M_w \sum_j v_j m_j$), plotted against the square root of the solute mole fraction ($x = \sum_j v_j m_j/(\sum_j v_j m_j + 1/M_w)$) of bromides at 298.15 K. Lines (model calculations): black solid, $CaBr_2$; brown solid, $CoBr_2$; green solid, $CuBr_2$; purple solid, $MgBr_2$; cyan solid, $MnBr_2$; blue solid, $NiBr_2$; dark yellow solid, $BaBr_2$; magenta solid, $SrBr_2$. Symbols: black square, $CaBr_2$ experimental data; brown circle, $CoBr_2$ experimental data; green triangle, $CuBr_2$ experimental data; purple diamond, $MgBr_2$ experimental data; cyan inverted triangle, $MnBr_2$ experimental data; blue star, $NiBr_2$ experimental data; dark yellow pentagon, $BaBr_2$ experimental data; magenta hexagon, $SrBr_2$ experimental data, where references for the experimental data are given in **Table 3. 1** for two parameter fitting, and in **Table 3. 2** for three parameter fitting.

The results of two- and three- parameter fitting are given in Tables 3.1 and 3.2 for 1-2 electrolytes, and in Tables 3.3 and 3.4 for 1-3 electrolytes, respectively. For the two-parameter model (Tables 3.1 and 3.3), the parameters ρ and r_{jj} are fit to data. For the three-parameter model (Tables 3.2 and 3.4), the parameters ρ, r_{jj} and μ_j are fit to data, whereas r_{jw} is calculated by using equation (3. 3). The accuracy of the fitting model was calculated using a normalized mean square error (MSE), and the tables show the MSEs and the data sources. It should be noted that in **Table 3. 2**, a negative r_{jj} resulted for H_2SO_4 and $(NH_4)_2SO_4$, possibly due to the physical arrangement of the molecular ions suggesting overlap. Also, note that Li_2SO_4 and K_3PO_4 did not yield reasonable fits with the three-parameter model approach. **Figure 3. 2** (a and b) shows plots of calculated osmotic coefficients by two-parameter fitting and three-parameter fitting, respectively, with experimental literature data for family of bromides of divalent cations over the entire concentration range. Note that though both the models fit well with $BaBr_2$ data, they have peaks in osmotic coefficient at different concentrations. The bromide family of curves is representative of the accuracy of the model calculations of 1-2 electrolytes with univalent anions; complete plots of chlorides, iodides and nitrates are shown in Appendix B (Figures B1 – B3) for both two- and three- parameter fitting models.

solute	n_j	ρ^a	r_{j+} (Å)[120–122]	r_{j-} (Å)[120–122]	r_{jj} (Å)[a]	r_{jw} (Å)[b]	$\mu_j{}^a$	MSE[c]	Ref
$CaBr_2$	5	48.67	1.00	1.88	2.500	6.070	44.00	1.53×10^{-3}	[123]
$CaCl_2$	6	27.20	1.00	1.72	1.930	5.440	26.48	2.32×10^{-4}	[123]
CaI_2	8	26.24	1.00	2.10	22.70	23.76	696.0	4.81×10^{-5}	[123]
$Ca(NO_3)_2$	3	20.94	1.00	1.79	17.17	18.70	691.4	2.55×10^{-5}	[124]
$CoBr_2$	9	32.53	1.25	1.88	2.070	5.920	31.28	1.88×10^{-4}	[125]
$CoCl_2$	5	28.96	1.25	1.72	39.99	38.61	3517	2.92×10^{-4}	[125]
CoI_2	8	42.99	1.25	2.10	4.040	7.810	64.05	8.90×10^{-4}	[125]
$Co(NO_3)_2$	5	29.40	1.25	1.79	3.520	7.090	45.18	3.94×10^{-4}	[125]
$CuBr_2$	6	29.53	0.73	1.88	34.44	33.49	1877	1.95×10^{-4}	[126]
$CuCl_2$	5	23.94	0.73	1.72	2.580	5.760	21.58	2.78×10^{-4}	[126]
$Cu(NO_3)_2$	6	26.40	0.73	1.79	0.990	4.450	14.52	1.72×10^{-4}	[126]
$FeCl_2$	7	19.74	0.70	1.72	15.82	17.20	316.4	2.56×10^{-5}	[125]
$MgBr_2$	6	51.14	0.72	1.88	4.690	7.720	65.66	1.64×10^{-3}	[123]
$MgCl_2$	5	62.29	0.72	1.72	5.940	8.670	86.18	1.78×10^{-3}	[123]
MgI_2	10	45.58	0.72	2.10	2.140	5.700	40.49	4.38×10^{-4}	[123]
$Mg(NO_3)_2$	6	31.86	0.72	1.79	3.800	6.870	39.88	3.35×10^{-4}	[124]
$MnBr_2$	12	27.75	0.70	1.88	2.160	5.510	24.09	1.07×10^{-4}	[126]
$MnCl_2$	15	22.80	0.70	1.72	0.910	4.290	11.69	9.88×10^{-5}	[126]
$NiBr_2$	8	33.61	0.70	1.88	3.640	6.790	42.81	3.58×10^{-4}	[125]
$NiCl_2$	9	23.92	0.70	1.72	2.300	5.500	23.74	5.24×10^{-5}	[125]
$Ni(NO_3)_2$	5	30.03	0.70	1.79	7.430	10.00	104.9	3.40×10^{-4}	[125]
H_2SO_4	5	9.680	0.21	2.58	-0.42[d]	3.460	7.830	8.77×10^{-3}	[127]
K_2SO_4	2	11.88	1.38	2.58	2.360	6.880	43.31	8.88×10^{-5}	[128,129]
Na_2SO_4	3	8.110	1.02	2.58	3.230	7.320	47.02	3.98×10^{-3}	[128,129]
$(NH_4)_2SO_4$	3	9.600	1.37	2.58	-1.64[d]	3.410	5.440	4.90×10^{-4}	[130–133]
Rb_2SO_4	2	13.50	1.52	2.58	2.460	7.090	49.13	5.82×10^{-6}	[128]
Cs_2SO_4	4	13.46	1.67	2.58	18.04	20.71	592.9	9.59×10^{-6}	[128]
$BaBr_2$	6	21.02	1.33	1.88	24.70	25.58	919.3	4.73×10^{-5}	[123]

$BaCl_2$	6	19.55	1.33	1.72	4.490	7.940	46.34	1.46×10^{-5}	[123]
BaI_2	7	27.60	1.33	2.10	53.25	50.50	5212	1.20×10^{-4}	[123]
$Pb(NO_3)_2$	2	8.310	1.19	1.79	2.760	6.380	32.85	2.82×10^{-4}	[126]
$SrBr_2$	6	23.41	1.18	1.88	36.10	35.32	2314	7.37×10^{-6}	[123]
$SrCl_2$	7	20.36	1.18	1.72	2.350	5.950	26.99	6.57×10^{-5}	[123]
SrI_2	8	26.45	1.18	2.10	11.67	14.35	203.9	1.77×10^{-5}	[123]
$Cd(NO_3)_2$	5	22.53	0.95	1.79	26.27	26.54	1114	3.92×10^{-5}	[134]
$Zn(NO_3)_2$	6	34.15	0.74	1.79	1.540	4.940	19.74	5.00×10^{-3}	[134]
Na_2CO_3	2	13.63	1.02	1.78	3.150	6.570	40.85	3.20×10^{-4}	[128]

Table 3. 2. Three-Parameter Fit for Aqueous 1-2 Electrolyte Solutions at 298.15 K. [a]Fitted value. [b]Calculated value. [c]MSE is a normalized mean-square error, equal to $\left(\frac{1}{n_p}\right)\sum_{i=1}^{n_p}((m_{model,i} - m_{data,i})/(m_{model,i}))^2$, where n_p is the number of data points. [d]Unrealistic value.

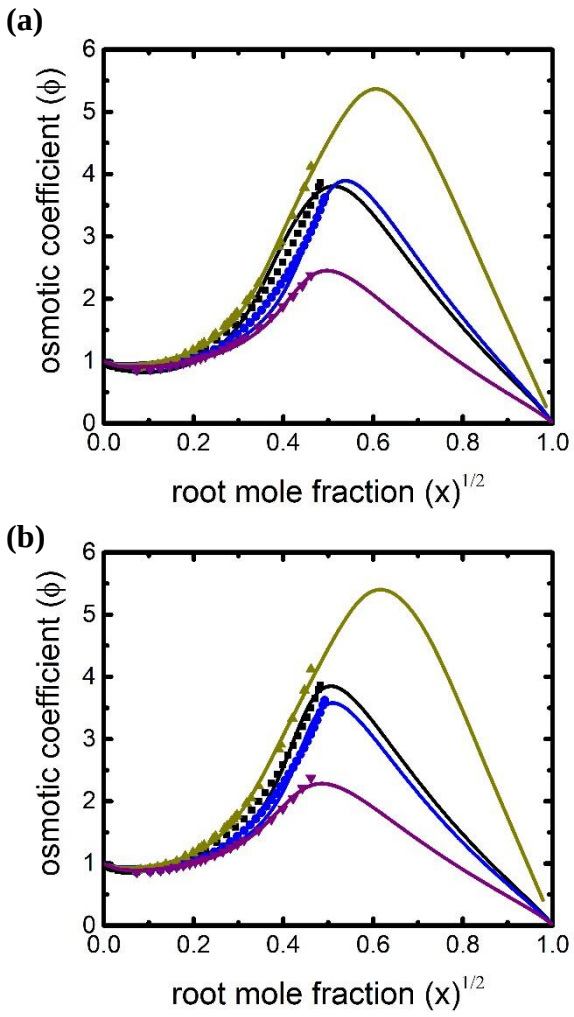

Figure 3. 3. Magnesium. (a) Two-parameter model. (b) Three-parameter model. Osmotic coefficient plotted against the square root of the solute mole fraction of magnesium at 298.15 K (see caption from **Figure 3. 2**). Lines (model calculations): black solid, $MgBr_2$; purple solid, $Mg(NO_3)_2$; blue solid, $MgCl_2$; dark yellow solid, MgI_2. Symbols: black square, $MgBr_2$ experimental data; purple inverted triangle, $Mg(NO_3)_2$ experimental data; blue circle, $MgCl_2$ experimental data; dark yellow triangle, MgI_2 experimental data, where references for the experimental data given in **Table 3. 1** for two parameter fitting, and in **Table 3. 2** for three parameter fitting.

Figure 3. 3 shows results of the model calculations for magnesium electrolytes with univalent anions, which, like bromide, is also representative of other systems of 1-2 and 2-

1 electrolytes. Complete plots of calcium family with univalent anions, and sulfates family with univalent cations are shown in Appendix B (Figures B4 and B5) for both two- and three- parameter fitting models. It is seen that the calculated osmotic coefficients of sulfuric acid do not follow the trend of available data, and hence has been treated separately in section 3.4. **Figure 3. 4** shows results for 1-3 electrolytes containing trivalent ions of aluminium, chromium and phosphate. There is agreement between the model calculations and the experimental data for all 1-2 and 1-3 solutes except sulfuric acid due to partial dissociation of the bisulfate ion. The model calculations by three-parameter fit are seen to be improved, and μ_j can be related to r_{jj} by the following equation by power fit as shown in **Figure 3. 5** for 1-2 electrolytes.

$$\mu_j = (0.3225.a)^{2.095}\left(\frac{qe}{D}\right) \qquad (3.\ 7)$$

where $a = r_{jj} + r_{j+} + r_{j-}$. In addition to the plots for the family of salts, a complete set of osmotic coefficient plots for the individual salts addressed in this paper are shown in the Appendix B (Figures B7 – B46).

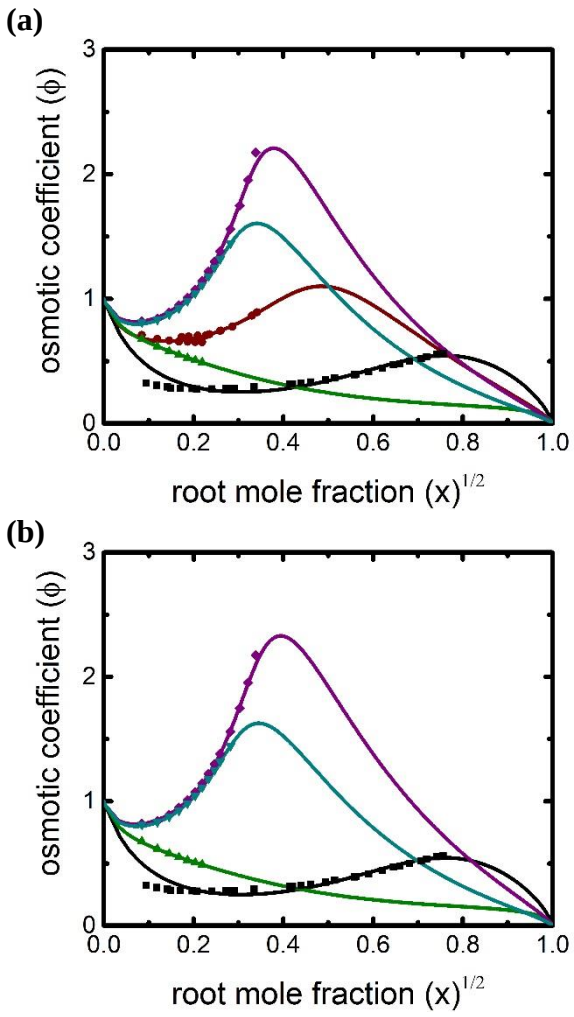

Figure 3. 4. 1-3 Electrolytes. (a) Fitting two parameters ρ and r_{jj} (b) Fitting three parameters ρ, r_{jj} and μ_j. Osmotic coefficient plotted against the square root of the solute mole fraction of 1-3 electrolytes at 298.15 K (see caption from **Figure 3. 2**). Lines (model calculations): black solid, H_3PO4; brown solid, K_3PO4; green solid, Na_3PO4; purple solid, $AlCl_3$; cyan solid, $CrCl_3$. Symbols: black square, H_3PO_4 experimental data; brown circle, K_3PO_4 experimental data; green triangle, Na_3PO_4 experimental data; purple diamond, $AlCl_3$ experimental data; cyan inverted triangle, $CrCl_3$ experimental data, where references for the experimental data given in **Table 3. 3** for two parameter fitting, and in **Table 3. 4** for three parameter fitting.

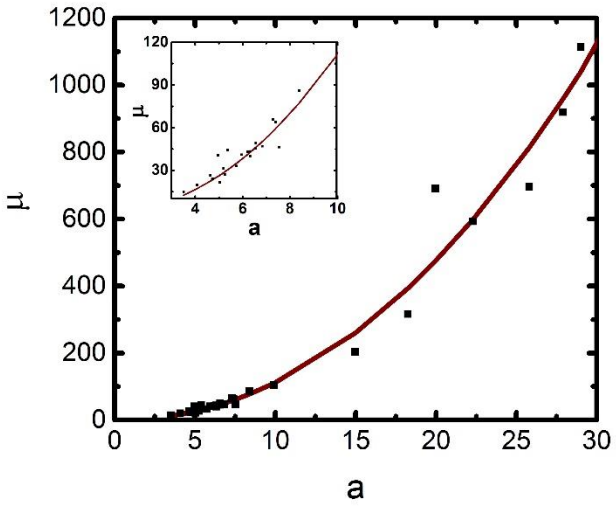

Figure 3. 5. Fit parameter μ plotted against a, where $a = r_{jj} + r_{j+} + r_{j-}$ and r_{jj} is the fit parameter. Solid brown line is eq (3. 7) and black square symbols are parameter values for 1-2 electrolytes.

solute	n_j	ρ^a	r_{j+} (Å)$^{120}_{-122}$	r_{j-} (Å)$^{120}_{-122}$	r_{jj} (Å)^a	r_{jw} (Å)^b	$\mu_j{}^b$	MSE^c	ref
H_3PO_4	2	7.640	0.21	2.38	6.880	9.140	111.38	3.67 x 10^{-2}	135
K_3PO_4	4	16.84	1.38	2.38	8.960	11.80	149.64	6.61 x 10^{-4}	136,137
Na_3PO_4	2	19.55	1.02	2.38	8.110	10.81	135.43	3.07 x 10^{-5}	136
$AlCl_3$	9	29.30	0.53	1.72	11.75	12.84	164.69	8.66 x 10^{-5}	124
$CrCl_3$	10	25.48	0.62	1.72	13.33	14.20	184.30	2.38 x 10^{-5}	124

Table 3. 3. Two-Parameter Fit for Aqueous 1-3 Electrolyte Solutions at 298.15 K. [a]Fitted value. [b]Calculated value. [c]MSE is a normalized mean-square error, equal to $\left(\frac{1}{n_p}\right)\sum_{i=1}^{n_p}((m_{model,i} - m_{data,i})/(m_{model,i}))^2$, where n_p is the number of data points.

solute	n_j	ρ^a	r_{j+} (Å)$^{120}_{-122}$	r_{j-} (Å)$^{120}_{-122}$	r_{jj} (Å)^a	r_{jw} (Å)^b	$\mu_j{}^a$	MSE^c	ref
H_3PO_4	2	7.650	0.21	2.38	2.960	5.940	30.57	3.69×10^{-2}	[135]
Na_3PO_4	2	18.99	1.02	2.38	7.060	9.950	106.8	3.47×10^{-5}	[136]
$AlCl_3$	10	28.90	0.53	1.72	8.210	9.950	91.78	4.97×10^{-5}	[124]
$CrCl_3$	10	26.09	0.62	1.72	11.69	12.87	148.0	1.28×10^{-5}	[124]

Table 3. 4. Three-Parameter Fit for Aqueous 1-3 Electrolyte Solutions at 298.15 K. [a]Fitted value. [b]Calculated value. [c]MSE is a normalized mean-square error, equal to $\left(\frac{1}{n_p}\right)\sum_{i=1}^{n_p}((m_{model,i} - m_{data,i})/(m_{model,i}))^2$, where n_p is the number of data points.

The adsorption isotherm model framework is based on the mole fraction basis with a pure solute reference state. However, it is essential to mention that the model can be analytically recast[63] to a molality basis with an infinite dilution reference state that is more standard for some fields. Additionally, model calculations for solute activity coefficients at infinite dilution reference state on a molality basis are comparable to the RMSE of the model calculations for osmotic coefficient as shown here.

3.4 Treatment of Sulfuric Acid

Sulfuric acid is known as a strong acid (first ionization) completely dissociating in aqueous solution with pK_a ($-\log_{10} K_a$) = -3 (dissociation constant, $K_a > 1$), and the bisulfate ion is known as a weak acid (second ionization) at 298.15 K because it does not dissociate completely and has a pK_a value of 1.92 ($K_a < 1$).[91] The dissociation of H_2SO_4 is described below as two steps, where step I is the total dissociation and step II is the partial dissociation. Hence, our model can treat aqueous H_2SO_4 solution considering it as a

mixture of two electrolytes (similar to treating a partially dissociated dicarboxylic acid as a mixture of an electrolyte and an organic in Chapter 2).[86]

$$H_2SO_4 \rightleftharpoons HSO_4^- + H^+ \quad \text{(I)}$$

$$HSO_4^- \rightleftharpoons SO_4^{2-} + H^+ \quad \text{(II)}$$

Moreover, there is an additional parameter that accounts for the ratio of dissociated ions to non-dissociated acid ion, defined as the dissociation ratio, β. It is a parameter that indicates the dissociated to non-dissociated solute ratio, i.e. the ratio of 1-2 electrolyte ($SO_4^{2-} + 2H^+$) to 1-1 electrolyte ($HSO_4^- + H^+$), and is known to be a function of the concentrations of both solutes. However, for simplicity, β is treated as a fixed adjustable parameter. Note that the van't Hoff factor (i), often related to degree of dissociation for osmotic coefficients, depends on the degree of dissociation, and is related to β by the following equation.

$$i = 1 + \frac{\beta(n-1)}{1+\beta} \quad (3.8)$$

where, n = number of dissociated ions.

Solute	Model[a]	β	n_{BS}, n_S	ρ_{BS}	ρ_S	$r_{jj,BS}$ (Å)	$r_{jj,S}$ (Å)	MSE[b]
H_2SO_4	n_m = 4	0.3	7,3	6.612	1.6e-4[c]	0.898	6.608	3.60 x 10^{-3}
	n_m = 3			2.437[d]	2.437[d]	0.736	6.927	3.81 x 10^{-3}
	n_m = 2			14.14[e]	38.63[e]	1.560	13.76	9.23 x 10^{-2}
	n_m = 4	0.5	3,8	4.014	4.014	2.769	3.094	5.96 x 10^{-4}
	n_m = 3			4.016[d]	4.016[d]	2.400	3.094	5.99 x 10^{-4}
	n_m = 2			18.00[e]	16.17[e]	3.133	3.188	1.58 x 10^{-2}
	n_m = 4	0.55	3,13	3.246	3.246	2.981	3.135	4.47 x 10^{-4}
	n_m = 3			3.287[d]	3.287[d]	2.616	3.036	4.48 x 10^{-4}
	n_m = 2			19.52[e]	17.35[e]	3.754	3.745	8.10 x 10^{-3}
	n_m = 4	0.8	9,7	2.786	2.786	3.649	3.773	1.32 x 10^{-3}
	n_m = 3			2.770[d]	2.770[d]	3.273	3.912	1.34 x 10^{-3}
	n_m = 2			23.09[e]	18.68[e]	5.209	4.371	1.58 x 10^{-2}
	n_m = 4	1.0	7,5	4.362	4.362	3.451	4.470	2.33 x 10^{-3}
	n_m = 3			4.357[d]	4.357[d]	3.079	4.523	2.34 x 10^{-3}
	n_m = 2			21.47[e]	18.91[e]	4.547	4.481	2.10 x 10^{-2}
	n_m = 4	1.5	4,3	8.334	8.334	2.503	4.246	5.57 x 10^{-3}
	n_m = 3			8.331[d]	8.331[d]	2.133	4.246	5.61 x 10^{-3}
	n_m = 2			16.94[e]	18.16[e]	2.700	4.126	2.01 x 10^{-2}

Table 3. 5. Fitted Parameters for H_2SO_4 at 298.15 K. [a]n_m is equal to the number of fit parameters. [b]MSE is a normalized mean-square error, equal to $\left(\frac{1}{n_p}\right)\sum_{i=1}^{n_p}((m_{model,i} - m_{data,i})/(m_{model,i}))^2$, where n_p is the number of data points, from Staples (1981).[127] [c]Unrealistic value. [d]Only one ρ is fitted, $\rho_{BS} = \rho_S$. [e]Calculated value.

Since the solute is treated as a mixture, for a given β, there are originally four parameters: ρ and r_{jj} for each electrolyte, i.e. $r_{jj,BS}$, $r_{jj,S}$, ρ_{BS}, ρ_S, where subscripts *BS* and *S* stand for bisulfate and sulfate respectively. μ_j and r_{jw} for each electrolyte are calculated

using equations (3. 2) and (3. 3). Results for six values of β for the four-parameter fit are provided in Figure B6a in Appendix B Poor agreements were found for β < 0.3 and β >= 0.8, and the model calculated unrealistic parameter values for β< 0.1. The model agreed reasonably well at β = 0.5 and 0.55, with an optimal value at β = 0.55. Interestingly, it was observed that the value of ρ for each electrolyte is approximately the same (from **Table 3. 5**). Therefore, by fitting only ρ_S and equating that to ρ_{BS}, the number of parameters could be reduced to three, i.e. r_{jj} for each electrolyte and ρ_S parameter. Figure B6b in Appendix B shows the fitting plots for all six values of β for the three-parameter fit, with only marginal change in MSE than compared to the four-parameter model. Again, the most agreeable fitting plot was found for 0.55 dissociation ratio.

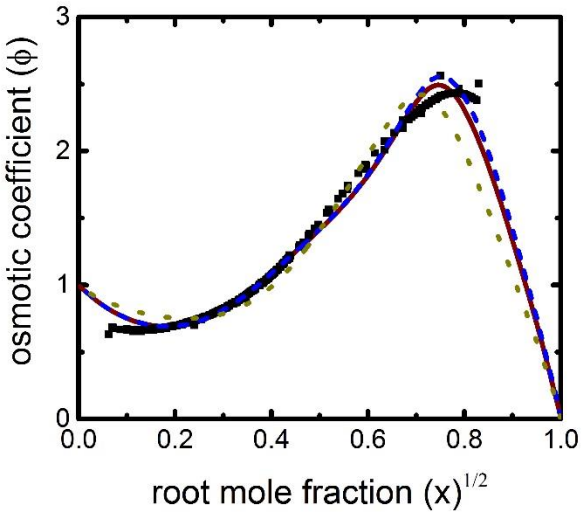

Figure 3. 6. Sulfuric acid - Osmotic coefficient plotted against the square root of the solute mole fraction of sulfuric acid at 298.15 K (see caption from **Figure 3. 2**); β = 0.55. Lines (model calculations): brown solid, four-parameter model; blue short dash, three-parameter model; dark yellow dot, two-parameter model. Symbols: black square, experimental data, where references for the experimental data and parameter values given in **Table 3. 5**.

Finally, the parameter ρ was related to the hard-core collision radius of the solute:[95]

$$\rho = a(2e^2 N_A d_1 / M_1 \varepsilon_0 DkT)^{1/2} \quad (3.9)$$

where a is the hard-core collision radius, e is the electronic charge, N_A is Avogadro's number, d_1 is the density of the solvent, M_1 is the molecular weight of the solvent, ε_0 is the permittivity of free space, D is the dielectric constant (relative permittivity) of the solvent, k is Boltzmann's constant and T is the temperature. The collision radius was assumed to be r_{jw} for each electrolyte,[86] thereby further reducing the number of parameters to two with modest accuracy. For example, r_{jj} could be fit for each electrolyte and both ρ values could be calculated using eq (3.9). Figure B6c represents the fitting plots for varying β for the two-parameter fit showing a modest agreement for solute ratio 0.55. Though the parameters do not vary significantly (**Table 3. 5**), the mean square error for the two-parameter fitting model is the highest. Results of the best fit at β =0.55 is shown in **Figure 3. 6** for each four-, three- and two- parameter model. Here, the mixture treatment of sulfuric acid resulted in an improvement at higher concentrations over the three-parameter fit of Figure B5b in Appendix B (model with total dissociation). Note that the dissociated solute is treated as a solvent-separated ion cluster, whereas the non-dissociated solute is treated as a molecular salt.

3.5 Conclusions

The electrostatic solute-solvent interaction model has been used to develop a solution thermodynamic model for accurate calculations of osmotic coefficients for a wide range of binary electrolyte solutions over the entire concentration range. The number of model

parameters is reduced to two by relating two of the parameters to the intermolecular spacing. The work calculates the energy of adsorption by parameterizing the ion-solvent and solvent-solvent bond length that represent physical structure properties. Although the intermolecular distances are fitted here, the model has potential to be fully predictive for solutes for which intermolecular spacing is known. With the known parameter values, activities can be calculated for multisolute systems.

The model works well for all the 1-2 and 1-3 electrolytes explored here, except for sulfuric acid due to two-step dissociation, allowing for inter- and extrapolation of calculations for concentrations and mixtures where data is not available. Taking partial dissociation of the bisulfate ion into account, the trends of osmotic coefficient could be well-captured with a mixture treatment of dissociated acid and non-dissociated acid as a result of partial dissociation. While the model here is developed for temperatures at 298.15 K only, it can potentially be developed for other temperatures that represent a wide range in the atmosphere. It may be done by taking into account the explicit temperature dependence in the energy parameter equation as well as in the Debye-Hückel ρ parameter equation.

Associated Content

Additional plots in Appendix B - Figures for osmotic coefficient plotted versus square root of solute mole fraction for chlorides, iodides, nitrates, sulfates and calcium families, for each individual salt for two- and three- parameter fitting model, and partial dissociation of sulfuric acid.

Chapter 4

Applications of the Thermodynamic Model to Determine pH and Hygroscopicity of Single Particles†

†Parts of this chapter were carried out in collaboration with researchers from Professor Andrew Ault's group at University of Michigan and Professor Jonathan Reid's group at University of Bristol, and were published in the following journals.

Adapted with permission from Rindelaub, J. D.; Craig, R. L.; Nandy, L.; Bondy, A. L.; Dutcher, C. S.; Shepson, P. B.; Ault, A. P. Direct Measurement of pH in Individual Particles via Raman Microspectroscopy and Variation in Acidity with Relative Humidity. *J. Phys. Chem. A* **2016**, *120* (6), 911–917. Copyright (2016) American Chemical Society.[1]

[1] The author acknowledges measurements taken by Prof. Andrew Ault's group.

Adapted with permission from Craig, R. L.; Nandy, L.; Axson, J. L.; Dutcher, C. S.; Ault, A. P. Spectroscopic Determination of Aerosol pH from Acid-Base Equilibria in Inorganic, Organic, and Mixed Systems. *J. Phys. Chem. A* **2017**, *121* (30), 5690−5699. Copyright (2017) American Chemical Society.[2]

Adapted from Marsh, A.; Miles, R. E. H.; Rovelli, G.; Cowling, A. G.; Nandy, L.; Dutcher, C. S.; Reid, J. P. Influence of Organic Compound Functionality on Aerosol Hygroscopicity: Dicarboxylic Acids, Alkyl-Substituents, Sugars and Amino Acids. *Atmos. Chem. Phys.* **2017**, *17* (9), 5583–5599. Link to the license. (Credit and License notice provided in Appendix E)[3]

Adapted from Marshall, F. H.; Berkemeier, T.; Shiraiwa, M.; Nandy, L.; Ohm, P. B.; Dutcher, C. S.; Reid, J. P. Influence of Particle Viscosity on Mass Transfer and Heterogeneous Ozonolysis Kinetics in Aqueous-Sucrose-Maleic Acid Aerosol. *Physical Chemistry Chemical Physics* **2018**, 20, 15560-15573 with permission from The Royal Society of Chemistry - Published by the PCCP Owner Societies. (Link to the article)[4]

4.1 Introduction

Atmospheric aerosol acidity impacts key multiphase processes, such as acid-catalyzed reactions leading to secondary organic aerosol formation, which impact climate and human health. However, traditional indirect methods of estimating aerosol pH often

[2] The author acknowledges measurements taken by Prof. Andrew Ault's group.

[3] The author acknowledges measurements taken by Prof. Jonathan Reid's group.

[4] The author acknowledges measurements taken by Prof. Jonathan Reid's group.

disagree with thermodynamic model predictions, resulting in aerosol acidity still being poorly understood in the atmosphere. The first part of this chapter details a collaborative study with the Ault group at the University of Michigan, which employs a method coupling Raman microspectroscopy with extended Debye−Hückel activity calculations. The method was applied to directly determine the acidity of individual particles to a range of atmospherically relevant inorganic and organic acid−base equilibria systems ($H_2SO_4/MgSO_4$, HNO_3/NO_3^-, $HC_2O_4/C_2O_4^{2-}$, CH_3COOH/CH_3COO^-, and HCO_3^-/CO_3^{2-}) covering a broad pH range (−1 to 10), as well as an inorganic−organic mixture (sulfate-oxalate). This chapter emphasizes the modeling component of the study.

The second part of the chapter includes use of the model in determining the hygroscopicity from comparative kinetics electrodynamic balance (CK-EDB) measurements in a collaborative work with the Reid group at the University of Bristol. The CK-EDB applies an electric field to trap-charged aqueous droplets in a chamber with controlled temperature and relative humidity (RH). The dual micro dispenser set-up allows for sequential trapping of probe and sample droplets for accurate determination of droplet water activities from 0.45 to > 0.99. A series of increasingly complex organic compounds, with subtle changes to molecular structure and branching, are used to rigorously assess the accuracy of predictions by Universal Quasichemical Functional Group Activity Coefficients (UNIFAC), which does not explicitly account for molecular structure. New hygroscopicity data are also reported for a selection of amino acids, alcohols and sugars and they show variable levels of agreement with predictions. In addition, the isotherm model has been used in this chapter to understand the influence of particle viscosity on mass transfer in aqueous sucrose-maleic acid aerosol. Again, the work presented in this

chapter emphasizes the modeling aspects.

4.2 Application I: Determination of pH of Single Particles

4.2.1 Method I: Raman microspectroscopy in Ault group

A direct spectroscopic method is established in the Ault group at the University of Michigan for measuring the pH of individual aerosol particles using Raman microspectroscopy. The pH of each individual particle was determined from the concentration of each anion within laboratory-generated aerosol particles based on integrated peak area and subsequent calculations for ionic strength, activity coefficients, and, ultimately, $[H^+]$. The spectroscopic approach has the potential to improve the fundamental understanding of aerosol acidity, which is currently lacking, and to eventually improve understanding of key atmospheric processes such as SOA formation and phase behavior in liquid droplets.

The spectroscopic method for determining aerosol particle pH has been applied to inorganic and organic acids with a range of pK_a values (K_a is the dissociation constant) in individual aerosol particles. These systems include nitric acid/nitrate (HNO_3/NO_3^-, pK_a −1.3), bisulfate/sulfate (HSO_4^-/ SO_4^{2-}, pK_a 2), bioxalate/oxalate ($HC_2O_4^-/ C_2O_4^{2-}$, pK_a 3.81), acetic acid/acetate (CH_3COOH/ CH_3COO^-, pK_a 4.76), and bicarbonate/carbonate (HCO_3^-/ CO_3^{2-}, pK_a 10.30).[138,139] Concentration values for each solution are provided in **Table 4. 1** and **Table 4. 2**.

Bulk Solution pH	[$MgSO_4$] (mM)	[H_2SO_4] (mM)	[Mg^{2+}]/([HSO_4^- + SO_4^{2-}])
0.44	30	360	0.08
0.89	30	198	0.13
1.15	30	54	0.36
1.64	30	18	0.63
1.99	30	4.1	0.88

Table 4. 1. Bulk solution composition for $MgSO_4$ - H_2SO_4 system.

Acid-Base System	pH	Salt	Acid	[ion]:[acid + conjugate base]
HNO_3/NO_3^-	< 0[a]	0.085-0.096 M $NaNO_3$	8.81-9.63 M HNO_3	Na^+ - ~0.01:1
$HC_2O_4/C_2O_4^{2-}$	3.63	0.272 M $(NH_4)_2C_2O_4$	0.091 M HCl	NH_4^+ - 2:1 Cl^- - 0.33:1
	3.97	0.280 M $(NH_4)_2C_2O_4$	0.065 M HCl	NH_4^+ - 2:1 Cl^- - 0.23:1
HCH_3COO/ CH_3COO^-	3.92	0.695 M $NaCH_3COO$	0.023 M HCl[b]	Cl^- - 0.03:1
HCO_3^-/CO_3^{2-}	10.47	0.038 M Na_2CO_3	0.010 M HCl	Na^+ - 2:1 Cl^- - 0.26:1
HSO_4^-/SO_4^{2-} & $HC_2O_4^-/C_2O_4^{2-}$	0.39	0.273 M $(NH_4)_2SO_4$, 0.273 M $(NH_4)_2C_2O_4$	0.795 M H_2SO_4	NH_4^+ - 0.81:1
	0.83	0.286 M $(NH_4)_2SO_4$, 0.286 M $(NH_4)_2C_2O_4$	0.476 M H_2SO_4	NH_4^+ - 1.09:1
	3.58	0.284 M $(NH_4)_2SO_4$, 0.283 M $(NH_4)_2C_2O_4$	0.057 M H_2SO_4	NH_4^+ - 1.82:1
	3.99	0.291 M $(NH_4)_2SO_4$, 0.291 M $(NH_4)_2C_2O_4$	0.033 M H_2SO_4	NH_4^+ - 1.89:1

Table 4. 2. Composition and pH of solutions used to generate particles for each acid-base system. [a]pH below measurement range of pH probe. [b]0.097 M HCH3COO also added.

Integrated peak areas of the vibrational modes corresponding to an acid (HA) and conjugate base (A^-) for each acid−base system were related to concentration using calibration curves, published in Rindelaub et al. (2016) and Craig et al. (2017).[89,90] Standard solutions of $MgSO_4$ and H_2SO_4 were used to create calibration curves relating $[SO_4^{2-}]$ and $[HSO_4^-]$ to integrated peak area of the $\nu s(SO_4^{2-})$ and $\nu s(HSO_4^-)$ modes.

The concentration of other ions present in the particle (those not directly involved in the acid − base equilibrium) were determined from the ratio of [ion]/[acid + conjugate base]. Once the concentration of all ions present was determined, ionic strength (I) was calculated using equation (4. 1), where C_i and z_i represent the concentration of each ion and its corresponding charge, respectively.

$$I = \frac{1}{2}\sum \mathrm{C}_i z_i^2 \qquad (4.\ 1)$$

Molality units were used for concentration of each species, determined by converting molarity to molality using the density of the solution mixture. The solution densities were found by using the Laliberté model,[140] and were iteratively solved during molality conversions. Since the density calculations required concentrations of each solute in the solution mixture, the equivalent concentrations of each cation and anion were found by Clegg's equivalent fraction method,[36] which assumes that all possible combinations of cation and anion are present as solute components.

Then the extended Debye−Hückel relationship (equation (4. 2)) was applied to calculate the activity coefficient for each species in the acid−base equilibrium. In the extended Debye−Hückel relationship, A and B are constants characteristic of the solvent

(water), and $å_i$ is the effective diameter of the ion in solution.[141,142] Values for the constants used in the extended Debye−Hückel relationship can be found in **Table 4. 3**. The value for *A* is 0.5085 and the value for *B* is 3.281×10^{-9}. Values for $å_i$ are listed in **Table 4. 3**.

$$-\log\gamma_i = \frac{Az_i^2\sqrt{I}}{1 + å_i B\sqrt{I}} \tag{4. 2}$$

$å_i$ x 10^8	**Ion**
2.5	NH_4^+
3.0	Cl^-, NO_3^-
4.0	Na^+, HCO_3^-, HSO_4^-, SO_4^{2-}
4.5	CO_3^{2-}, $HC_2O_4^-$, $C_2O_4^{2-}$, CH_3COO^-
9	H^+

Table 4. 3. Effective diameter ($å_i$) values.

The concentrations of acid and conjugate base, their respective activity coefficients, and the acid dissociation constant K_a were then used to calculate $[H^+]$ (equation (4. 3)) and finally pH (equation (4. 4)).

$$K_a = \frac{a_{H^+} * a_{A^-}}{a_{HA}} = \frac{([H^+] * \gamma_{H^+})([A^-] * \gamma_{A^-})}{[HA] * \gamma_{HA}} \tag{4. 3}$$

$$\text{pH} = -\log(a_{H^+}) = -\log(\gamma_{H^+} * [H^+]) \tag{4. 4}$$

Note that an iterative method is needed to solve eqs (4. 1) − (4. 3), since the value of $[H^+]$ is not known and is needed in the calculation of ionic strength and activity coefficients. As with the density calculations (discussed after eq (4. 1)), Clegg's equivalent fraction method[36] was used to find the first initial value for $[H^+]$. The value is then used to

solve for ionic strength (eq (4. 1)) and subsequently the activity coefficients (eq (4. 2)). Using the activity coefficients, eq (4. 3) is applied to calculate a new value for $[H^+]$. The initial value for $[H^+]$ is then iteratively changed until it equals that from the eq (4. 3) calculations.

Linear regressions were applied to the relationship between average aerosol particle pH and RH for each bulk solution of $MgSO_4$ - H_2SO_4 system (**Figure 4. 1**). Similar slope values for all five data sets indicate that aerosol pH increases with increasing RH at similar rates, regardless of initial pH.

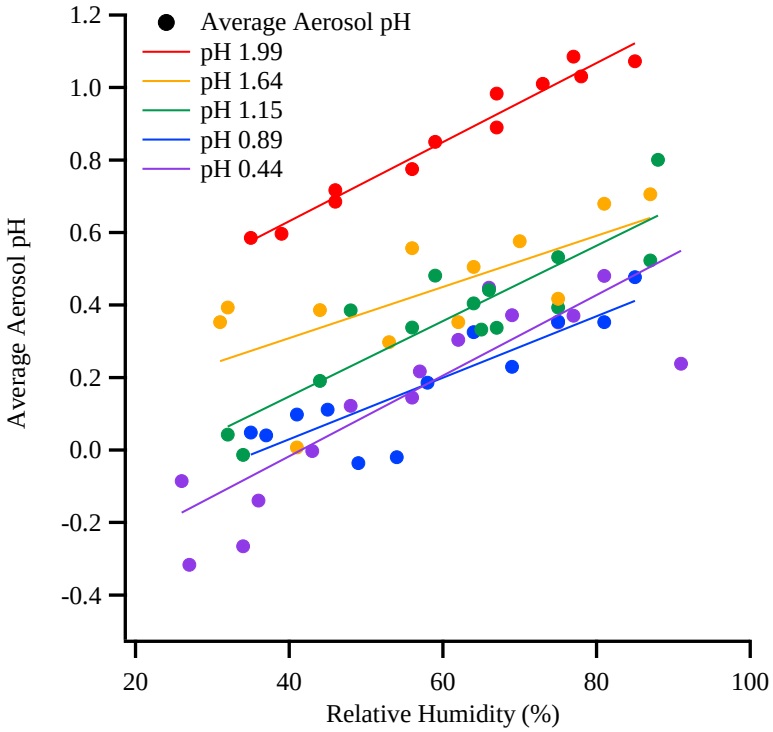

Figure 4. 1. Average aerosol pH as a function of relative humidity for each seed aerosol bulk solution for $MgSO_4$ - H_2SO_4 system. Adapted from Figure 4 (Rindelaub et al. 2016) and reproduced with permission from Rindelaub, J. D.; Craig, R. L.; Nandy, L.; Bondy, A. L.; Dutcher, C. S.; Shepson, P. B.; Ault, A. P. Direct Measurement of pH in Individual Particles via Raman Microspectroscopy and Variation in Acidity with Relative Humidity. *J. Phys. Chem. A* **2016**, *120* (6), 911–917. Copyright (2016) American Chemical Society.

Aerosol particle pH was also evaluated for each acid and conjugate base system. Since the pH was too low to be measured accurately with the pH probe, the pH of the bulk solution used to generate aerosol particles for the HNO_3/NO_3^- system was calculated to be between -1.1 and -1.4, based on the concentration of ions in solution. The pH of HNO_3/NO_3^- aerosol particles when calculated using the extended Debye-Hückel (EDH) model varied from -1.2 to 0.090, with an average of -0.48. Although the aerosol particles studied for each system were all generated from the same solution, there was some variability in particle pH. Histograms for the measured particle pH for HNO_3/NO_3^- system are given in **Figure 4. 2**.

For comparison with an alternative prediction of pH, the multilayer adsorption isotherm based model from Dutcher et al. (2013)[63] was also used to determine the molalities and activities of the solutes present, and subsequently the activity of H^+ and pH. The model includes arbitrary number of adsorbed monolayers and uses a power law relationship for aqueous solutions to determine adsorption energy parameter of water molecules with a solute by adjusting two parameters. The model (equations 27 and 28 in Dutcher et al. (2013)[63]) is used for finding the molalities and activities of the solutes present as a function of water activities. Treating fractional RH data as equivalent to water activity and using it as input to the model, the molalities and activities of the solutes are calculated. Alternatively, using both RH data and the measured (converted) molality data, the model calculated the activities of each solute present in the solution mixture. For the HNO_3/NO_3^- particles, the activity of the acid (HNO_3) is found by the model, and the activity of the conjugate base ion (NO_3^-) is found by eq (4. 5). Then, eq (4. 3) is finally used to determine the activity of the H^+, and therefore pH by eq (4. 4).

$$a_{NO3-} = \sqrt{a_{HNO3} \cdot a_{NaNO3}} \quad (4.5)$$

With the isotherm model, particle pH values were closer than the values from extended Debye-Hückel model to the calculated pH values of the HNO_3/NO_3^- bulk solution, ranging from -1.4 to -0.88, with an average pH of -1.2. The pH of the particle corresponding to the Raman spectrum was calculated with the isotherm model to be -1.17.

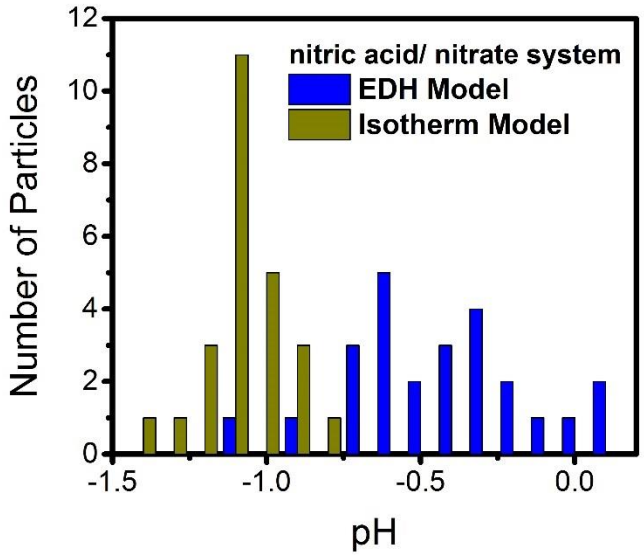

Figure 4. 2. Histogram for measured particle pH for HNO_3/NO_3^- system. Adapted from Figure S6 (Craig et al. 2017) and reproduced with permission from Craig, R. L.; Nandy, L.; Axson, J. L.; Dutcher, C. S.; Ault, A. P. Spectroscopic Determination of Aerosol pH from Acid-Base Equilibria in Inorganic, Organic, and Mixed Systems. *J. Phys. Chem. A* **2017**, *121* (30), 5690−5699. Copyright (2017) American Chemical Society.

In addition to measuring the pH of aerosol particles for each of the systems, trends were observed for H^+ activity coefficient, γ_{H+}, in relation to ionic strength and aerosol particle pH relative to the broadness of the vibrational modes analyzed. Across all the acid-base systems, there is a negative relationship for γ_{H+} as a function of ionic strength (**Figure**

4. 3), with more γ_{H+} sensitivity at lower ionic strength. However, the inorganic systems tend to have larger, more varied ionic strength with lower, less variable γ_{H+}. The inverse holds for the organic systems, which show larger, more varied γ_{H+} with smaller and less variability in ionic strength. As mentioned earlier, even though particles were generated from bulk solutions of similar pH and the $HC_2O_4^-/C_2O_4^{2-}$ system was used to determine pH, particles composed of only $HC_2O_4^-/C_2O_4^{2-}$ had lower average pH than particles of $HC_2O_4^-/C_2O_4^{2-}$ and HSO_4^-/SO_4^{2-} mixed composition (average aerosol particle pH 3.2 and 4.0, respectively). Because of the inorganic component in the $HC_2O_4^-/C_2O_4^{2-}$ and HSO_4^-/SO_4^{2-} mixed particles, their γ_{H+} was lower, thus decreasing the activity of H^+, making the particles less acidic. The observation infers that ion behavior in mixed organic and inorganic particles is dictated by contributions from all chemical species present.

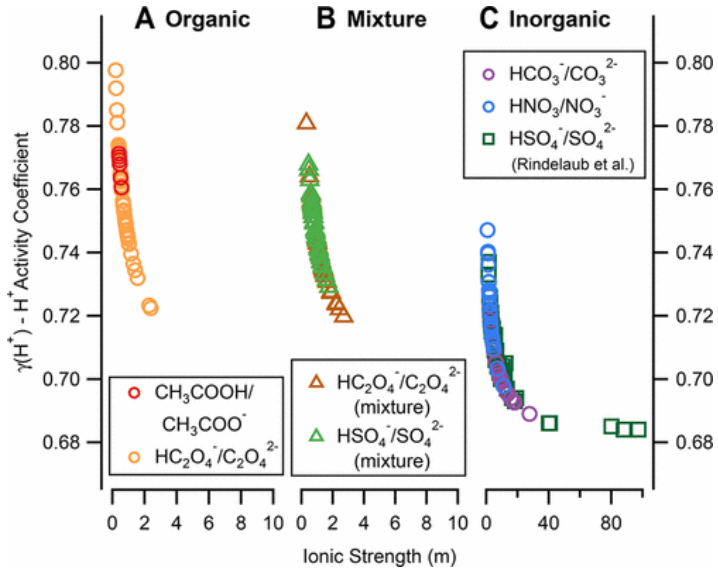

Figure 4. 3. H^+ activity coefficient (γ_{H+}) as a function of ionic strength for each organic (A), mixture (B), and inorganic (C) acid-base system. Note the differing scales for ionic strength. Reprinted with permission from Craig, R. L.; Nandy, L.; Axson, J. L.; Dutcher, C. S.; Ault, A. P. Spectroscopic Determination of Aerosol pH from Acid-Base Equilibria in Inorganic, Organic, and Mixed Systems. *J. Phys. Chem. A* **2017**, *121* (30), 5690−5699. Copyright (2017) American Chemical Society.

4.2.2 Method II: Paper-based pH measurements in Ault group

The isotherm model was also applied to the Raman microspectroscopy approach to support the measurements done using a pH indicator paper for the system, ammonium sulfate ($(NH_4)_2SO_4$) and sulfuric acid (H_2SO_4). Aerosol pH for aqueous particles was determined by colorimetric analysis of images collected on a pH indicator paper and were compared to pH probe measurements. The experimental work and comparisons with the isotherm model are under review in Craig et al., *Analytical Chemistry*, 2018.

4.3 Application II: Determination of Hygroscopicity of Single Particles

4.3.1 Experimental method in Reid group

A particle's ability to take up water from the atmosphere is described by hygroscopicity. Estimation of hygroscopicity is important in climate models because it influences the optical properties of particles that drive the amount of radiation scattering. Hygroscopicity studies are presented with measurements from a comparative kinetics technique by the Reid group at the University of Bristol. The method is applied in an electrodynamic balance (EDB) instrument (referred to as the comparative kinetics EDB, CK-EDB, below), with electrodes in a concentric cylindrical arrangement. The full experimental details for the CK-EDB have been discussed extensively in previous publications by the Reid group.[143,144] All measurements are taken at 293.15 K.

The CK-EDB can be used to probe the hygroscopic growth of aerosol particles from low to high water activities (< 0.45 to > 0.99) with a greater accuracy (< ±0.2 % error in water activity at water activities > 0.8 and ±1 % error in water activity at water activities < 0.8) than can be achieved in conventional approaches[143]. The CK-EDB employs an

electric field to trap a charged dilute aqueous droplet starting at a water activity > 0.99. The droplet evaporates towards an equilibrium composition set by the RH of the surrounding gas flow; the RH is determined accurately from an independent measurement of the evaporation profile of a probe droplet of known hygroscopic response (either a pure water droplet or an aqueous sodium chloride solution droplet). Final hygroscopicity data are averaged (binned in small steps in RH) and presented as a function of mass fraction of solute (MFS) against water activity; full hygroscopicity curves are typically the result of measurements between 30 and 80 droplets. It must be noted that the hygroscopicity parameter, κ, values are calculated using all data points.

4.3.2 Isotherm model to corroborate measurements

The isotherm model is first applied here to study hygroscopicity of amino acids. The behavior observed for different classes of chemical compounds studied (dicarboxylic acids, amino acids, sugars and alcohols) was compared and trends were observed for the value of the hygroscopicity parameter, κ, in Marsh et al.[74]

Hygroscopic response of amino acids. A selection of amino acids were chosen for their biological relevance and to represent a wide range of structures and O : C ratios. Nitrogen-containing compounds are prevalent in the atmosphere; amino acids contribute to this class of compounds due to their biological origin.[145,146] Amino acids form zwitterions in solution, which suppresses their vapor pressure and presents challenges in representing them with current thermodynamic models, with most models not allowing the inclusion of nitrogen-amine- containing groups (e.g. AIOMFAC-web). AIOMFAC-web only allows for the inclusion of organonitrate and peroxy acyl nitrate subgroups. Hence, thermodynamic model predictions for amino acids were generated using E-AIM model

III,[32] using the standard UNIFAC model, including certain modified main group interaction parameters introduced by Peng et al. (2001).[49] In addition, the isotherm model is used, as the UNIFAC predictions cannot be performed for all the amino acids examined here.

The equilibrium hygroscopic responses for glycine, DL- alanine, L-valine and L-threonine are shown in **Figure 4. 4** a. These four compounds all contain a similar glycine subunit, but include additional methyl, ethyl and hydroxyl groups. On a MFS scale, the hygroscopic response of these compounds is similar, except for L-threonine, which is less hygroscopic, an observation that is not expected given the additional hydrophilicity of the hydroxyl substituent. Compounds of the same O : C are compared in **Figure 4. 4** b with equilibrium relationships shown for L-lysine, L-histidine and L-arginine. Lysine (κ, 0.219) is more hygroscopic than histidine (κ, 0.188) and arginine (κ, 0.147), illustrating that compounds with the same O : C can have very different hygroscopic responses.

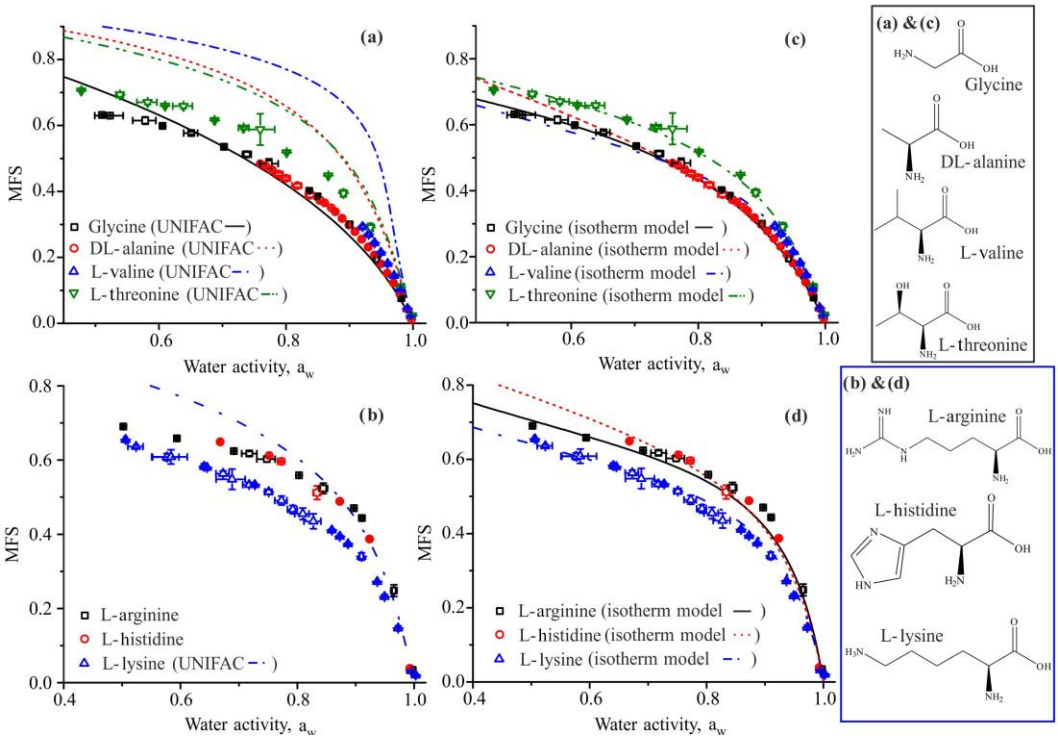

Figure 4. 4. Equilibrium hygroscopicity curves (a) for structurally similar amino acids with different substituents alongside UNIFAC predictions. (b) Equilibrium hygroscopicity curves of amino acids with the same O:C ratio (0.33), with UNIFAC predictions generated using E-AIM model III. (c, d) The same amino acids as (a, b), respectively, presented alongside thermodynamic predictions using the isotherm model discussed in Dutcher et al. (2013),[63] with coefficients available in **Table 4. 4**. Reproduced from Marsh, A.; Miles, R. E. H.; Rovelli, G.; Cowling, A. G.; Nandy, L.; Dutcher, C. S.; Reid, J. P. Influence of Organic Compound Functionality on Aerosol Hygroscopicity: Dicarboxylic Acids, Alkyl-Substituents, Sugars and Amino Acids. *Atmos. Chem. Phys.* **2017**, *17* (9), 5583–5599.

Solute	*P*	MSE
Alanine	-0.356	0.00051
Asparagine	-0.171	0.04151
Arginine	-0.993	0.04039
Glycine	-1.934	0.00321
Histidine	-0.502	0.02211
Lysine	-1.225	0.00667
Proline	-0.619	0.03764
Threonine	-0.960	0.20107
Valine	-0.892	0.00397

Table 4. 4. Fitted parameters for nine amino acids. The power law coefficient *P* is used to calculate energy parameter *C* for the first to $(n-1)$th layers, hence $C_i = (i/n)^P$, where *i* is the layer number and *n* is the total number of hydration layers, here $n = 8$ for all compounds except glycine ($n = 3$) and threonine ($n = 5$). MSE is a normalized mean-square error, equal to $\left(\frac{1}{n_p}\right)\sum_{i=1}^{n_p}((m_{model,i} - m_{data,i})/(m_{model,i}))^2$, where n_p is the number of data points. (Parameter for L-aspartic acid could not be determined due to data range available.)

For improved predictions of the amino acids measured, the multilayer adsorption isotherm-based model from Dutcher et al. (2013),[63] which includes an arbitrary number of adsorbed monolayers, is used in **Figure 4. 4** c and d to fit to the CK-EDB data. The model uses a power-law relationship for aqueous solutions to determine adsorption energy parameter, C, of water molecules with a solute by adjusting a single parameter shown in **Table 4. 4**. The model (Eq. 27 in Dutcher et al., 2013)[63] is fitted to experimental data for solute molality as a function of water activity in order to determine the adjustable model parameter. The isotherm model results in improved MFS predictions when compared to UNIFAC. However, the notable difference in accuracy between the two models is not

overly surprising: the isotherm-based model of Dutcher et al. has an adjustable parameter (**Table 4. 4**), while UNIFAC is a fully predictive model.

The general trends show that the amino acids are much more hygroscopic than is currently predicted using UNIFAC. Increased hygroscopicity with similar O : C ratios could be due to the zwitterionic nature of amino acids, with their behavior more similar to that of a salt than an organic species.

Trends in κ with O : C ratio and molecular structure. In order to efficiently represent the hygroscopic growth of aerosols in large-scale models, it is crucially important that models of low complexity are used to represent aerosol of broad-ranging source and chemical complexity. Correlations of the value of the parameter κ with surrogate measures of ambient aerosol composition such as O : C have been considered.[147,148] In **Figure 4. 5**a, the values of κ for the homologous series of dicarboxylic acids and their branched derivatives are compared. Clearly, both increased chain length and increased branching lead to greater hydrophobicity and lower hygroscopicity. Overall trends in hygroscopicity, as represented by the dependence of MFS on water activity, can be fit to the power-law model from Dutcher et al. (2013) (**Table 4. 5**), and the upper and lower bounds for compounds from each class (amino acids, organic acids, sugars and alcohols) is shown in **Figure 4. 5**b. The work clearly illustrates that the amino acids are more hygroscopic than the majority of the other compounds studied.

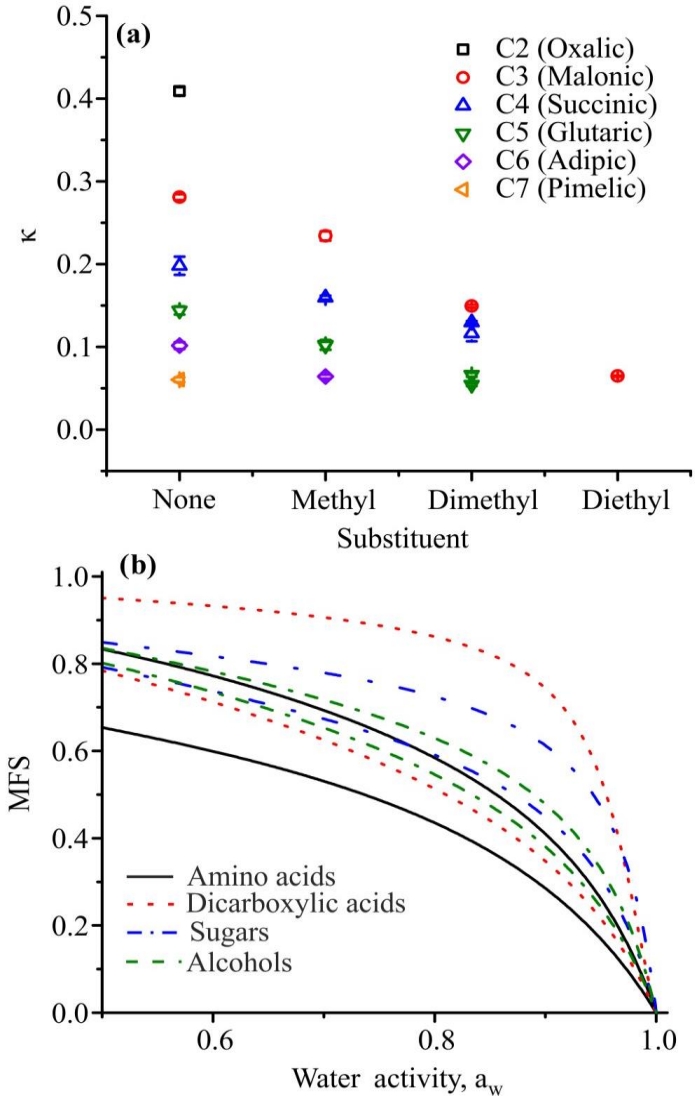

Figure 4. 5. (a) κ values at a water activity of 0.95 are plotted as a function of increasing length of substituent and carbon backbone. (b) Generalized equilibrium hygroscopicity curves are presented as a function of compound class. Upper and lower hygroscopicity limits for each compound class have been fitted using the isotherm model discussed in Dutcher et al. (2013) (coefficients available in **Table 4. 5**). Reproduced from Marsh, A.; Miles, R. E. H.; Rovelli, G.; Cowling, A. G.; Nandy, L.; Dutcher, C. S.; Reid, J. P. Influence of Organic Compound Functionality on Aerosol Hygroscopicity: Dicarboxylic Acids, Alkyl-Substituents, Sugars and Amino Acids. *Atmos. Chem. Phys.* **2017**, *17* (9), 5583–5599.

Solute	*P*	MSE
Amino acid Upper (Glycine)	-1.934	0.00321
Amino acid Lower (Asparagine)	-0.171	0.04151
Organic acid Upper (Malonic acid)	-0.212	0.00819
Organic acid Lower (2,2 dimethyl glutaric acid)	0.206	0.08315
Sugar Upper (Sorbitol)	-0.522	0.01025
Sugar Lower (Trehalose)	-0.870	0.01687
Alcohol Upper (Erythritol)	-0.238	0.01311
Alcohol Lower (PEG4)	-1.180	0.16205

Table 4. 5. Fitted parameters for upper and lower MFS vs water activity of compounds in each class, amino and organic acids, sugars and alcohols, as shown in **Figure 4. 5**b. The power law coefficient *P* is used to calculate energy parameter *C* for the first to $(n-1)$th layers, hence $C_i = (i/n)^P$, where *i* is the layer number and *n* is the total number of hydration layers, here $n = 8$ for all compounds except glycine ($n = 3$) and 2,2-dimethyl glutaric acid ($n = 16$). MSE is a normalized mean-square error, equal to $\left(\frac{1}{n_p}\right)\sum_{i=1}^{n_p}((m_{model,i} - m_{data,i})/(m_{model,i}))^2$, where n_p is the number of data points.

4.4 Application III: Mass Transfer in Viscous Aqueous Sucrose-Maleic Acid Aerosol

Mass transfer between the gas and condensed phases in aerosols can be limited by slow bulk diffusion within very viscous particles. To constrain kinetic models of the heterogeneous chemistry, measurements must provide information on as many observables as possible. In the Reid group, the ozonolysis kinetics of maleic acid (MA) in ternary aerosol particles containing water and sucrose is used as a model system. The mass ratio of sucrose to MA is varied and reactions at a wide range of relative humidity are performed for the studies.

The experimental procedure using aerosol optical tweezers has been described in detail in previous publications.[149–151] At the moment of trapping an aerosol particle, the sucrose:MA mass ratio is assumed equal to that in the starting nebulized solution, however the volatilization of MA leads to a gradual change over time. A key aspect of the work in the Reid group is to explore explicitly the relationship between the rates of evaporation of a semi-volatile organic compound (SVOC) and ozonolysis chemistry, and aerosol particle viscosity.

Compositional dependence of particle viscosity. Measurements of viscosity were performed for three initial sucrose:MA mass ratios of 10:1, 5:1 and 1:5 and the water activity dependencies of viscosity are shown in **Figure 4. 6**. Given the high uncertainty associated with the viscosity measurement, only linear fits for the dependence of the logarithm of the viscosity of RH are reported. For comparison, the linear water activity dependence of aqueous sucrose and aqueous MA droplets are shown in **Figure 4. 6**(a).[152,153] Owing to the limited solubility of MA, data are only available up to a mass fraction of MA of 0.402, corresponding to an RH of 90 %, estimated using the thermodynamic treatment of Dutcher et al. [63,64] The parameterization is extrapolated below this RH for comparison with the other data sets.

To calculate the water content as a mass fraction with varying gas phase RH and sucrose:MA ratio, the thermodynamic model of Dutcher and co-workers[58,59,63,64,149] has been used. Coulombic short range electrostatic interactions are used to determine the energy parameters for water sorption onto the hydration shell for each monolayer of the solute molecule in binary systems.[64] The multilayer adsorption isotherm model is expected to describe particularly well the compositional dependence of water content to zero solvent

activity.[58,63] The compositional dependencies on RH and activity coefficients estimated from the isotherm model for the different sucrose:MA mass ratios are shown in **Figure 4. 7**, using the model parameters given in Marshall et al.[149]

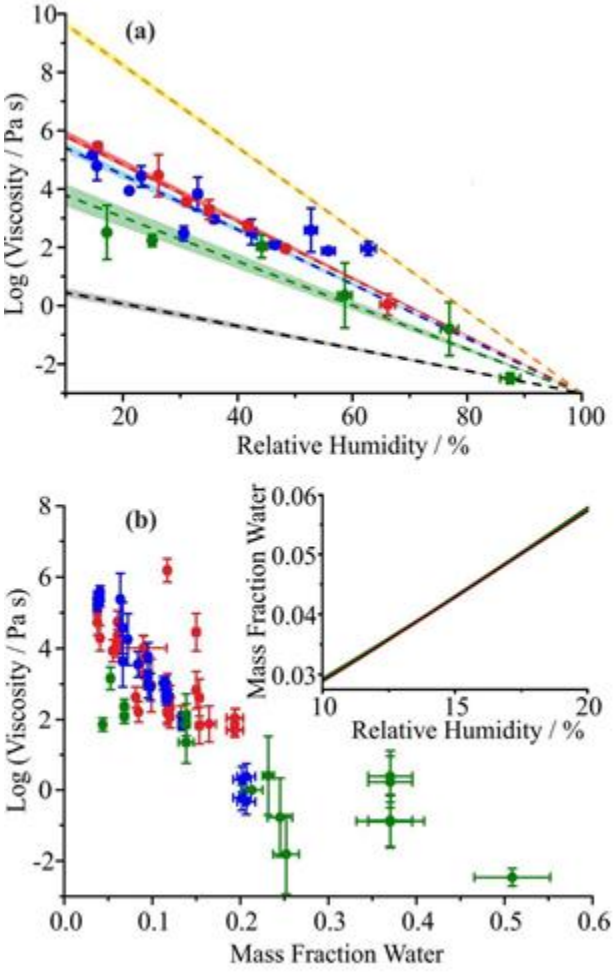

Figure 4. 6. (a) Viscosity of ternary MA/sucrose/water aerosol droplets at varying RH measured by aerosol optical tweezers. Sucrose:MA mass ratios of 10:1, 5:1 and 1:5 are indicated by the red, blue and green datasets (points and lines, top to bottom in order), respectively. The viscosity parameterizations for binary aqueous/sucrose and aqueous/MA droplets are shown by the yellow (top) and grey (bottom) lines, respectively, for comparison. (b) Mass fraction of water against viscosity for three different initial mass ratios of sucrose:MA (red 10:1, blue 5:1, green 1:5). The mass fraction of water predicted for the RH region where the largest difference in viscosities occurs are shown in the inset.

Adapted and reproduced from Marshall, F.; Berkemeier, T.; Shiraiwa, M.; Dutcher, C.; Nandy, L.; Ohm, P.; Reid, J. Influence of Particle Viscosity on Mass Transfer and Heterogeneous Ozonolysis Kinetics in Aqueous-Sucrose-Maleic Acid Aerosol. *Physical Chemistry Chemical Physics* **2018**, 20, 15560-15573 with permission from The Royal Society of Chemistry.

When the dependence of aerosol viscosity is reported in terms of mass fraction of water, **Figure 4. 6**(b), there is a consistent trend across the compositional range and spanning almost 8 orders of magnitude in viscosity. It must be recognized that the viscosity scale is shown in logarithmic form and the errors in viscosity can be as large as one order of magnitude. A closer examination of the data in **Figure 4. 6**(b) may suggest that the aerosol with higher MA fraction is marginally less viscous than the other two; conversely, the aerosol with marginally higher sucrose content may be more viscous, consistent with MA having a minor plasticizing effect on the particle viscosity. The mass fraction of water in **Figure 4. 6**(b) is calculated from the coalescence relative humidity using the isotherm model. The ordinate error arises from the error envelope associated with the viscosity parametrization, while the abscissa errors from the ±2 % uncertainty in the RH probe which propagates through to the error in the mass fraction of water in the particle.

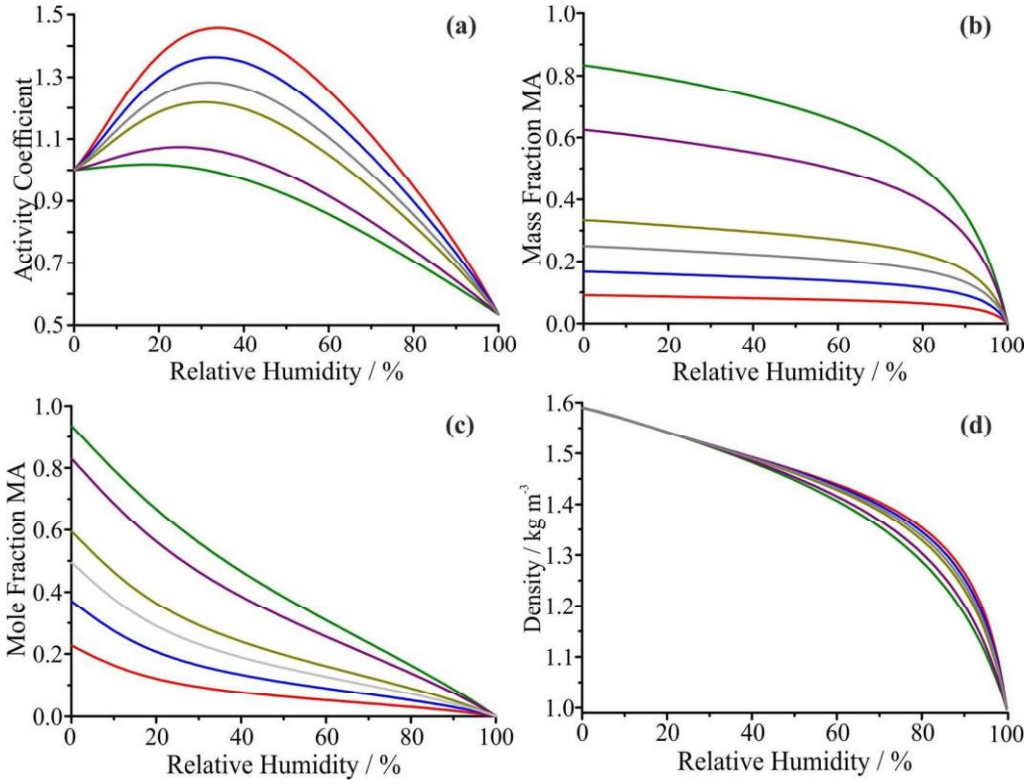

Figure 4. 7. (a) Activity coefficient of MA (mole fraction basis with a pure liquid solute reference state), (b) mass fraction of MA, (c) mole fraction of MA and (d) droplet density as functions of RH from the isotherm model. Different initial sucrose:MA mass ratios are shown: 1:5 (green), 3:5 (purple), 2:1 (mustard), 3:1 (grey), 5:1 (blue) and 10:1 (red). Reproduced from Marshall, F.; Berkemeier, T.; Shiraiwa, M.; Dutcher, C.; Nandy, L.; Ohm, P.; Reid, J. Influence of Particle Viscosity on Mass Transfer and Heterogeneous Ozonolysis Kinetics in Aqueous-Sucrose-Maleic Acid Aerosol. *Physical Chemistry Chemical Physics* **2018**, 20, 15560-15573 with permission from The Royal Society of Chemistry.

4.5 Conclusions

The multilayer adsorption isotherm model is applied in this chapter to study properties of single particles. The model is used to estimate pH of acidic particles, to study aerosol hygroscopicity of various organic compounds, and to interpret optical tweezer

measurements of gas-particle partitioning with ternary aqueous solutions of sucrose/organic acid.

In the first method of the pH study, pH was determined for individual laboratory generated aerosol particles of varying composition at ambient conditions using Raman microspectroscopic measurements of acid and conjugate base species and the extended Debye-Hückel relationship. In addition to aerosol particle pH measurements, this study explored gas-particle partitioning of volatile acid species and a few aspects of ion behavior in relation to particle pH. Nitric acid and acetic acid were found to partition from the particle to the gas phase due to increased surface-to-volume ratios and did so more than the other acid species because of their higher volatility. In terms of the impact of organic and inorganic components on ionic strength and H^+ activity, the inorganic particles had larger, more variable ionic strength with smaller, less change in the H^+ activity coefficient, while the organic particles had larger, more variable H^+ activity coefficient values with smaller, less change in ionic strength. These results show the potential for direct measurement of pH and ion behavior in individual aerosol particles and will enable future studies of more chemically complex particles, including ambient aerosol, which will improve understanding of their pH-dependent chemical processes and climate-relevant properties.

The second method of the pH study presents a simplistic method for direct measurement of pH by colorimetric analysis of aqueous aerosol samples. Comparison with direct measurement of single particle pH using the combined spectroscopic method and the isotherm model validated these results. Fundamental acidity studies of aerosol particles

provide an increased understanding of pH-dependent multiphase chemical processes, that affect human health and the environment.

In the hygroscopicity study in section 4.3, the equilibrium hygroscopic data for various organic compounds, majorly amino acids, with different O:C ratios are presented. Amino acid UNIFAC thermodynamic model predictions are not in agreement with experimental observations, while the isotherm model is. The discernible differences in hygroscopicity for different compound classes offer the potential for future modeling methods to be built on relationships between compound classes and O:C and N:C ratios. Predictive tools considering these very general and smooth relationships would be much less computationally expensive than current group contribution methods and thus could be incorporated into climate models.

In the mass transfer study in section 4.4, a comprehensive set of viscosity measurements for particles at steady state compositions has been presented, i.e. various mass ratios of sucrose:MA and with varying moisture content. From these data, a clear suppression in the rate of volatilization is apparent with increasing particle viscosity, i.e. increasing sucrose fraction and decreasing moisture content. The measured kinetics of the ozonolysis of MA, for particles with varying MA:sucrose mass ratio and at varying RH are also reported. The study illustrates the need for more refined measurements of multiple experimental parameters if the kinetic models are to be more fully constrained.

Chapter 5

Temperature Dependent Activity Coefficient Model toward Better Understanding of Thermal-Chemical Aerosol Processes

5.1 Introduction

Water uptake and loss by atmospheric aerosol particles is an important phenomenon, the effects of which are changing global climate,[9] aerosol optical properties,[10] visibility[11] and human health.[9] It is caused by changes in the ambient relative humidity and temperature. Therefore, it is essential to study the dependence of thermodynamic properties on the relative humidity as well as temperature. The effect of

relative humidity (RH) has been the focus of this dissertation. Thermodynamic models for calculating the chemical concentration and chemical potential as a function of RH has been detailed in Chapters 2 and 3. The calculations were then used in Chapter 4 to find the hygroscopic growth of particles that affects cloud condensation nuclei changing cloud properties.[74,154–156] The results were also used in Chapter 4 to determine the acidity of atmospheric aerosol particles, for improved understanding of aerosol chemical processes related to climate change and human health.[90,157] These recent theoretical developments focusing on aerosol aqueous droplets relevant to climate models include predictions of bulk solution thermodynamic properties of complex multicomponent solutions over the entire relative humidity range. However, the model so far has been developed for a temperature of 298.15 K only for a wide range of salts, organics and ternary mixtures. The model needs to be extended for a wide range of atmospheric temperatures.

In order to study atmospheric cloud and aerosol properties at a range of temperatures, data for a wide range of temperature is required for a variety of chemical systems. For example, frozen nitric acid and sulfuric acid droplets are important components in the coldest region of the Earth's stratosphere.[158] Activity coefficients have been calculated as a function of temperature (223.15 to 393.15 K) for 0 – 100% nitric acid[159,160] using Pitzer's model.[95] Ammonium sulfate is also an important component of aqueous atmospheric aerosols.[24,161] Water activities of ammonium sulfate have been measured using electrodynamic balance from 278.15 to 313.15 K,[130] Furthermore, isopiestic measurements of aqueous ammonium sulfate, sulfuric acid, and their mixtures have been made at 298.15 K and 323.15 K, and used for thermodynamic modeling of pure aqueous ammonium sulfate from freezing points to boiling points of the solutions.[133] To

cover temperatures from lower troposphere to stratosphere, the PSC (Pitzer, Simonson, Clegg) equations[61,95] have been used to develop a model that includes NH_4^+, SO_4^- and NO_3^-.[162] The model is effective for concentrations from infinite dilution to only saturation valid for temperatures 263 – 330 K. Other well-studied systems include ternary sodium chloride-sodium sulfate-water for industrial applications subject to large temperature changes, and activity coefficients from electromagnetic field (EMF) measurements have been determined at different temperatures.[163]

However, these systems are only a limited subset of needed chemical compositions. Indeed, the effect of RH on water uptake and chemical potential is far better understood than temperature dependence. Towards incorporation of temperature dependence in the model, this chapter provides a first step by reviewing the temperature dependence of atmospheric processes. Section 5.2 presents a review of the literature to study temperature dependent nucleation in new particle formation, ice nucleation, crystal nucleation, cloud condensation nucleation, and glass transition and liquid-liquid phase separation in atmospheric aerosols at tropospheric temperatures. Section 5.3 presents the development of the Coulombic model to study dependence of temperature on the model parameters, including intermolecular distance between solute and solvent, and the dipole moment of the solute.

5.2 Review of Thermal-Chemical Dependent Aerosol Processes/Nucleation

Nucleation is significant in the troposphere, which is the lowest layer of the atmosphere with an average global temperature of 288K. Studies suggest that the nucleation process of new atmospheric aerosol particles drives climate change and governs

radiative properties of Earth's atmosphere. There can be two major instances of atmospheric nucleation – condensation of the gas phase to form small aqueous solution droplets (new particle formation), and liquid to ice particles (ice nucleation). The nucleation process in the absence of foreign substances is known as homogeneous nucleation, i.e. solid or liquid particles are formed from pure supersaturated vapor, and ice particles are formed at low temperature inside a uniform solution droplet. Whereas, the nucleation process is heterogeneous when it is enabled by the presence of foreign particles/surfaces. The studies discussed here are summarized in **Table 5. 1**.

process	temperature range (K)	chemical compounds	reference
new particle formation	160 – 180	water-nitric acid	[164]
	198 - 223	sulfate particles	[165]
ice nucleation	200 - 300	alcohols and dicarboxylic acids	[166]
	263 - 293	ammonium sulfate, sodium chloride, ammonium nitrate	[167,168]
	278 – 323	potassium chloride, sodium sulfate, sodium nitrate	[169]
	243 - 298	ammonium bisulfate -water	[170]
	213 - 233	ammonium sulfate, ammonium bisulfate, sulfuric acid	[171]
crystal nucleation	210 – 298	ammonium sulfate, ammonium sulfate-calcium carbonate	[172]
	250 - 273	sodium chloride	[173]
	278 - 308	ammonium sulfate, sodium nitrate, potassium chloride	[174]
glass transition	140 - 300	glucose, sulfuric acid, ammonium nitrate, ammonium sulfate	[175]
	206.5 - 291	alpha-pinene secondary organic aerosol	[176]
liquid-liquid phase separation	244 – 290	mixed organic species and ammonium sulfate	[177]

Table 5. 1. Summary of temperature dependence studies for various aerosol processes.

5.2.1. New particle formation

New particle formation is a phenomenon which occurs when the gas phase species form new particles in the atmosphere. Vehkamäki and Riipinen (2012) show in **Figure 5. 1**a, how a particle nucleus is created by molecular collision to form a stable cluster, and condensation of the supersaturated vapor on an existing particle.[178] A thermodynamic scheme has been developed to incorporate temperature dependence to study its impact on sulfuric acid-organics nucleation rates.[179] The results suggest that a 10 K increase in temperature may reduce the nucleation rate by ~1 order of magnitude. Yet, with decreasing temperature, the nucleation rate constant (obtained from freezing point measurements of a submicron aerosol particle containing water-nitric acid in 2:1 ratio by Fourier transform infrared extinction spectroscopy) increases between 180 – 175 K, whereas decreases between 175 – 160 K.[164] The decrease in rate constant is because this temperature range represents the glass temperature, i.e. when the viscosity becomes high. There have been studies of possibility of formation of new sulfate (SO_4^{2-}) particles through homogeneous nucleation at -75 to -50 ^oC, which reveal that the nucleation rate increases by orders of magnitude with decrease in temperature at extremely low temperatures.[165] The results also suggest that the possibility of homogeneous nucleation over heterogeneous nucleation is increased with decrease in temperature at such stratospheric temperatures.

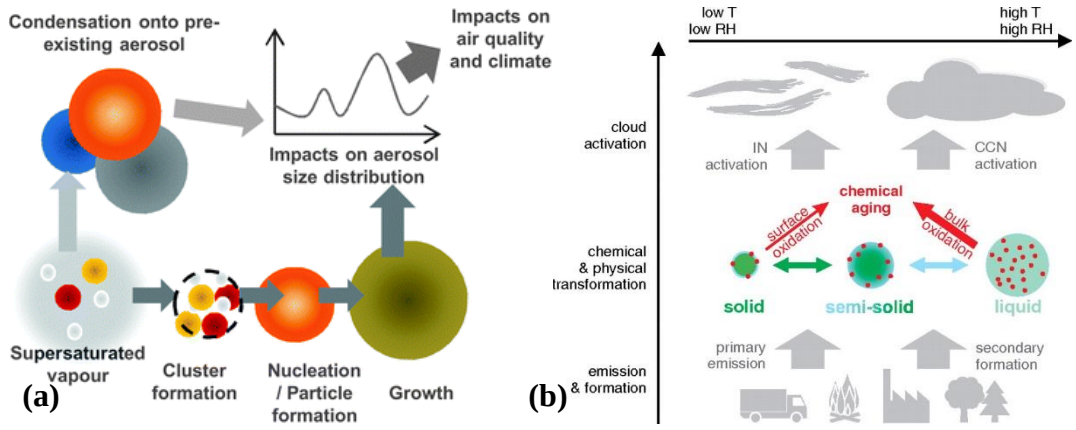

Figure 5. 1. (a). Gas-to-particle conversion processes and growth. Reproduced from Vehkamäki, H.; Riipinen, I. Thermodynamics and Kinetics of Atmospheric Aerosol Particle Formation and Growth. *Chem. Soc. Rev.* **2012**, *41*, 5160 with permission from The Royal Society of Chemistry. (b). Aerosol processes in the atmosphere with respect to ambient relative humidity and temperature.[180] Shiraiwa, M.; Ammann, M.; Koop, T.; Poschl, U. Gas Uptake and Chemical Aging of Semisolid Organic Aerosol Particles. *Proc. Natl. Acad. Sci.* **2011**, *108* (27), 11003–11008. Reprinted with permission from PNAS.

5.2.2. Ice nucleation (IN)

One place where temperature dependence affects ice nucleation is the water activity. The change in water activity with temperature describes the freezing point depression resulting from solute effect. However, it may indicate freezing temperature for only some aqueous solutions (examples of ammonium sulfate and sulfuric acid in **Figure 5. 2 s**how that sulfuric acid aerosol has a lower freezing temperature).[181] Swanson (2009) shows the homogeneous freezing temperature data in **Figure 5. 2** for ammonium sulfate and sulfuric acid solution aerosols, published previously over the last decade in blue open circles, and from his study in red solid circles.[181] Since the effect of change in water activity on temperature depends on the specific nature of the solute, the relationship with solution composition must be well understood. The concentration-water activity relationship

depends not only on the chemical nature of the solute, but also on the temperature. Particularly at low temperatures of the upper troposphere, water activity of many solutions is unknown. The gap limits understanding of nucleation and phase change in the atmosphere.[4] Hence, freezing point and melting point curves as a function of water activity and/or concentration are required to be measured/modeled.

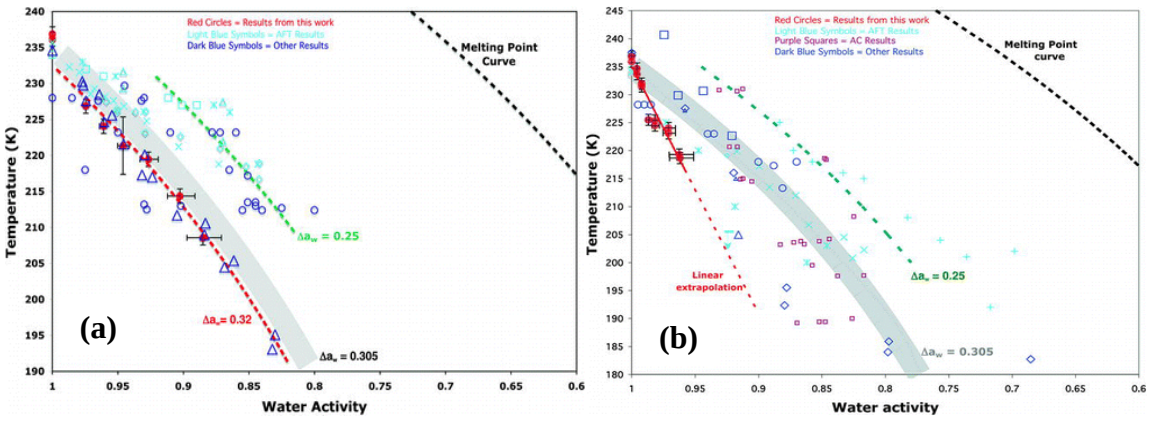

Figure 5. 2. (a). Ammonium sulfate-water solution freezing. (b). Sulfuric acid-water solution freezing. The solid red circles and the dashed red lines represent the freezing curves. Reproduced from Swanson, B. D. How Well Does Water Activity Determine Homogeneous Ice Nucleation Temperature in Aqueous Sulfuric Acid and Ammonium Sulfate Droplets? *J. Atmos. Sci.* **2009**, *66* (3), 741–754. ©American Meteorological Society. Used with permission.

In some cases, the temperature effect has been found to be subtle or even negligible. Experimental measurements of melting and freezing points, and hygroscopicity data of single aerosol particles of aqueous organic solutions have been made for various concentrations. These measurements are made by using an electrodynamic balance and differential scanning calorimetry for relative humidities, 10 - 90% and temperatures, 200 - 300 K to study effect of temperature dependence on water activity at tropospheric conditions.[166] Hygroscopic growth and deliquescence relative humidities of aerosol

particles have been measured by Hygroscopic Tandem Differential Mobility Analyzer (H-TDMA) at temperatures -10 to 20 ^{o}C, and it was found that there was negligible temperature dependence of the water activity in the solutions of ammonium sulfate, sodium chloride, and ammonium nitrate.[167,168] Water activities, osmotic and activity coefficients have also been determined by hygrometric method for aqueous solutions of potassium chloride, sodium sulfate and sodium nitrate for different concentrations and temperatures 278 – 323 K, and found that variation of water activity with temperature is less than 0.2%.[169] However, with increasing concentrations, the temperature dependence increases, shown with sucrose solutions.[182]

Laboratory measurements have been performed for ammonium bisulfate-water system from -30 to 25 ^{o}C, and found that the ice equilibrium freezing temperature obtained by Clausius-Clapeyron equation reduces with decreasing water activity,[170] agreeing well with the Clegg et al. low-temperature model for ammonium sulfate-sulfuric acid-water system.[32] Using thermodynamic models, water activity is determined above the ice melting point, and then extrapolated at supercooled temperatures.[183–187] However, it is assumed to not change significantly with decreasing temperature when data/model is unavailable.[188]

Homogeneous formation of ice in aerosol particles of ammonium sulfate, ammonium bisulfate and sulfuric acid has been studied under upper tropospheric conditions (-60 to -40 ^{o}C) with a continuous flow thermal diffusion chamber, and found that ice supersaturation increases with decreasing temperature, and the water activity decreases with decreasing temperature.[171] Berkemeier et al. (2014)[189] show that the nucleation (freezing) temperatures of solution droplets decrease with decreasing water activity, and that the heterogeneous nucleation temperature curve has higher temperatures

than the homogeneous temperature curve (schematic shown in **Figure 5. 3**).[190,191,189] For example, organic surfactants forming a shell on aqueous droplets, or presence of mineral dust may prompt ice nucleation at warmer temperatures than homogeneous freezing temperatures.[188] In addition, decrease in cooling rate and increase in ice nucleation surface area also increase the droplet freezing temperature.[192] In the study,[192] a water activity based immersion freezing model is introduced to investigate effects of changing surface area and cooling rates on the freezing.

5.2.3. Crystal nucleation

In addition to formation of a new particle and formation of *ice* as nucleation processes, there are other phase transitions that may occur e.g. formation of solute *crystals* from aqueous droplets by efflorescence. Electrodynamic trap experiments have been performed to study temperature dependent heterogeneous nucleation (efflorescence) of internally mixed single microparticles of ammonium sulfate/calcium carbonate within a temperature range 210 – 298 K.[172] The study reports that both homogeneous (ammonium sulfate nucleation) and heterogeneous efflorescence relative humidities only slightly increased with decreasing temperature. Small amount of calcium carbonate in ammonium sulfate solution has a significant effect on the kinetics of crystallization, and the results suggest that the temperature dependence of this heterogeneous efflorescence depends on the surface area and efficiency of the catalytic substance, and the temperature dependence of homogeneous nucleation as well.

In addition to temperature dependence, the concentration at which phase transition occurs, e.g. efflorescence or liquid-liquid phase separation, in mixed systems may be altered depending on the size of the particle.[193] At 298 K, an aqueous ammonium sulfate

droplet is regarded as molten state in the study[193] when the ammonium sulfate:water molar ratio increases with decreasing droplet size. The critical diameter, defined as the diameter below which droplets are expected to be in homogeneous liquid state at ambient temperature, decreases as the bulk transition temperature is reduced for sodium chloride and ammonium sulfate solutions. It has been found from electrodynamic balance and Raman microscopy experiments[173] that formation of sodium chloride dihydrate by heterogeneous nucleation of sea-salt aerosol particles strongly depends on the temperature. At temperatures higher than 273 K, anhydrous sodium chloride is more stable, whereas at temperatures lower than 250 K, sodium chloride dihydrate is more stable. Another study with electrodynamic balance experiments in the temperature range 5 – 35 ºC for ammonium sulfate, sodium nitrate and potassium chloride particles showed that the deliquescence relative humidity increased with decreasing temperatures.[174]

5.2.4. Glass transition of aqueous solution droplets

Another important behavior in aerosol particles at low tropospheric temperatures is that they form glasses, i.e. highly viscous liquids. When this occurs, the molecular motion becomes slow, and at the glass transition temperature, the particles form amorphous substances instead of crystallization (shown in **Figure 5. 3**).[194,195] Berkemeier et al. (2014) show in **Figure 5. 3**[189] how the phase state changes with ambient relative humidity, and that upon drying, the phase transitions to a glassy state. In a study by Zobrist et al. (2008),[175] for an aqueous glucose solution, as the solution concentration is increased, the homogeneous ice nucleation temperature decreases, but the glass transition temperature, T_g, increases. The increase in T_g is stronger for organics than inorganics in the temperature range 160 to 280 K. For example, the increase in T_g is higher for a glucose solution, and

the glass transition temperature (T_g) increases from 140 to 300 K with decreasing water activity from 1 to 0 (increasing concentration). On the other hand, for inorganics, e.g. a sulfuric acid, ammonium nitrate or ammonium sulfate solution, the glass transition temperature increases from 140 to 180 K. Therefore, in the atmosphere, it is most likely for the organic-rich aerosols to be present in glassy state at ambient conditions above 180 K. In addition, glass transition temperatures are higher for multicomponent solutions containing organics than inorganic solutions at the same concentrations.[175] The study also suggests that T_g increases with presence of more hydrophobic molecules, and lifetime of the glassy aerosol particles increases due to the inhibition of the chemical reactions and water uptake.

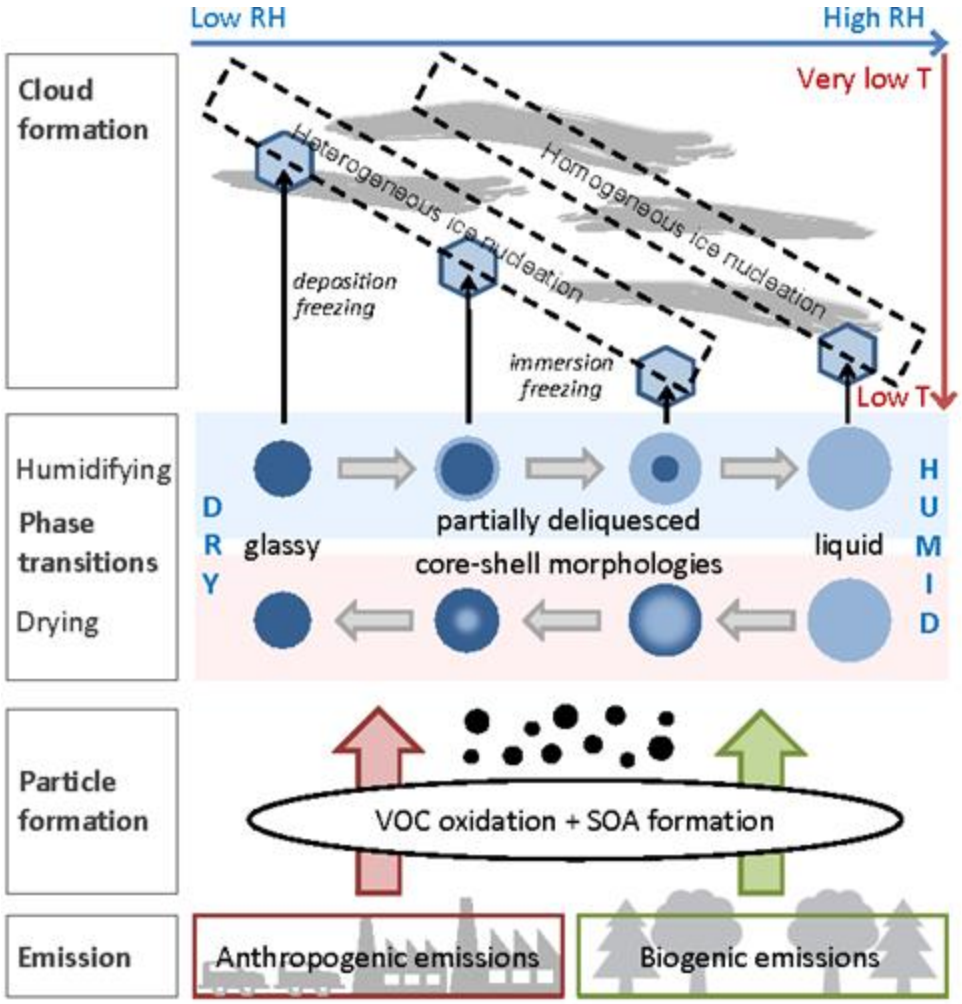

Figure 5. 3. Atmospheric processes in aerosol particles depending on temperature and humidity.[189] Reproduced from Berkemeier, T.; Shiraiwa, M.; Pöschl, U.; Koop, T. Competition between Water Uptake and Ice Nucleation by Glassy Organic Aerosol Particles. *Atmos. Chem. Phys.* **2014**, *14* (22), 12513–12531.

In a study with alpha-pinene secondary organic aerosol (SOA), it was observed that water diffusion is high at temperatures above 220 K, and that it does not deter water uptake as it is not strictly associated with T_g.[176] The study involves water diffusion measurements with respect to temperature and water activity by double-ring electrodynamic balance (EDB) to study its effect on particles to act as cloud condensation nucleus (CCN) and ice

nucleus (IN) between 206.5 and 291 K. The study also provides results from model simulations to show that the condensed-phase water diffusion does not affect the homogeneous ice nucleation rate.

5.2.5 Liquid-liquid phase separation (LLPS)

There is a possibility of another process, i.e. liquid-liquid phase separation, at a certain range of ambient relative humidity. Studies have shown that liquid-liquid phase separation (LLPS) might be affected by a change in temperature, due to its influence on the thermodynamics and kinetics of liquid-liquid phase transitions (example of core-shell morphology in **Figure 5. 3**). In a study with particles containing mixed organic species and ammonium sulfate, influence of temperature was studied for a range 244 – 290 K.[177] The study showed that LLPS relative humidity does not strongly depend on the temperature, agreeing with other studies;[38,196] there was only a slight decrease in the LLPS relative humidity with decreasing temperatures. In addition, LLPS may not even occur at extremely low temperatures due to kinetic barrier by diffusion limitations. In a separation study to yield pure alcohol from water-alcohol-entrainer (organics) mixtures, the organic phase becomes richer in alcohol with increasing temperatures.[197] In other studies with polymer blends, it has been found that LLPS might alter the rate of crystallization depending on the glass transition temperatures.[198]

5.2.6 Cloud condensation nuclei (CCN) activation

Finally, the concentration of cloud condensation nuclei (CCN), a major factor of aerosol indirect effect on the climate by modifying cloud properties and precipitation, is dependent on the new particle formation in the atmosphere (**Figure 5. 1**b by Shiraiwa et al. 2011[180]). Studies have shown that the CCN formation rate increases with decrease in

temperature in the troposphere.[199] Hence, the CCN concentrations are comparatively lower in the summer,[179] indicating that CCN activity decreases at higher temperatures.[200] There has been a study to show the influence of temperature-dependent surface tension on the CCN activity.[201] The study reports that surface tension increases with decreasing temperature, resulting in a higher saturation vapor pressure, thus increasing the critical supersaturation required to activate an aerosol particle into a cloud droplet. Yet in another study, for same supersaturation, CCN activity for larger inorganic particles is higher at higher temperatures.[202]

5.3 Temperature Dependence in Coulombic Model

5.3.1. Model description

Towards improved prediction of thermodynamic properties of aerosol particles as a function of temperature, in this section, the explicit (kT in equation (5. 1)) and implicit (model parameters including intermolecular distance, dipole moment) temperature dependence in the model equation are taken into consideration. The adsorption model presented here is extended to include a temperature-dependent model for ammonium sulfate, ammonium nitrate and nitric acid for which experimental data is available at different temperatures. The model equation (5. 1) for the Coulombic energy has the following dependency on temperature:

$$C_{j,i} = \exp\left(\frac{\Delta\varepsilon_{j,i}}{kT}\right) \tag{5. 1}$$

where $C_{j,i}$ is the adsorption energy parameter that is related to the change in energy, $\Delta\varepsilon_{j,i}$, of the free solvent in the bulk from the bound solvent to the respective monolayer, i, of the

solute, j, $k = 1.38 \times 10{-}23$ JK^{-1} (Boltzmann's constant), T is the temperature.[64] The explicit temperature dependence is taken into account when calculating the energy parameters using the Coulombic model. The model parameters r_{jj} (the interspatial distance between a cation and anion in the solute) and ρ_j (long-range interaction Debye-Hückel parameter) for the electrolytes and r_{jw} (the intermolecular distance between solute j and solvent w) for the organic acid are fit to the data-set at respective temperatures. The model may be used to treat the temperature dependence on the Debye-Hückel, ρ parameter using:

$$\rho = a(2e^2 N_A d_1 / M_1 \varepsilon_0 DkT)^{1/2} \qquad (5.\ 2)$$

where, a is the hard-core collision diameter of the solute, e is the charge, N_A is Avogadro's number, d_1 is the density of the solvent, ε_0 is the permittivity of free space, M_1 is the molecular weight of the solvent and D is the dielectric constant or relative permittivity of the solvent. Note, while T appears explicitly in equation (5. 2), both density and permittivity also have a temperature dependence.

5.3.2 Results and discussion

The temperature dependent Coulombic model has been applied to ammonium sulfate, ammonium nitrate and nitric acid to determine solution properties - osmotic coefficient and activity coefficient at various temperatures. The model now includes the temperature parameter as a variable, unlike a fixed temperature in Chapters 2 and 3. The results for the model with fitting parameters r_{jj}, μ_j and ρ for ammonium sulfate are shown in **Figure 5. 4**, and the model parameters are provided in **Table 5. 2**. The model fits to experimental literature data available for temperatures between 278 – 313 K and calculates osmotic coefficients. However, due to limitations in data availability at different

temperatures for more compounds, the model is fit to values extracted from an existing aerosol thermodynamic model, extended-aerosol inorganics model (E-AIM), in the temperature range 220 – 323 K. The fitting is done to understand the effect of temperature on the model parameters, intermolecular distance, r_{jw}, dipole moment, μ_j, and the Debye-Hückel parameter, ρ.

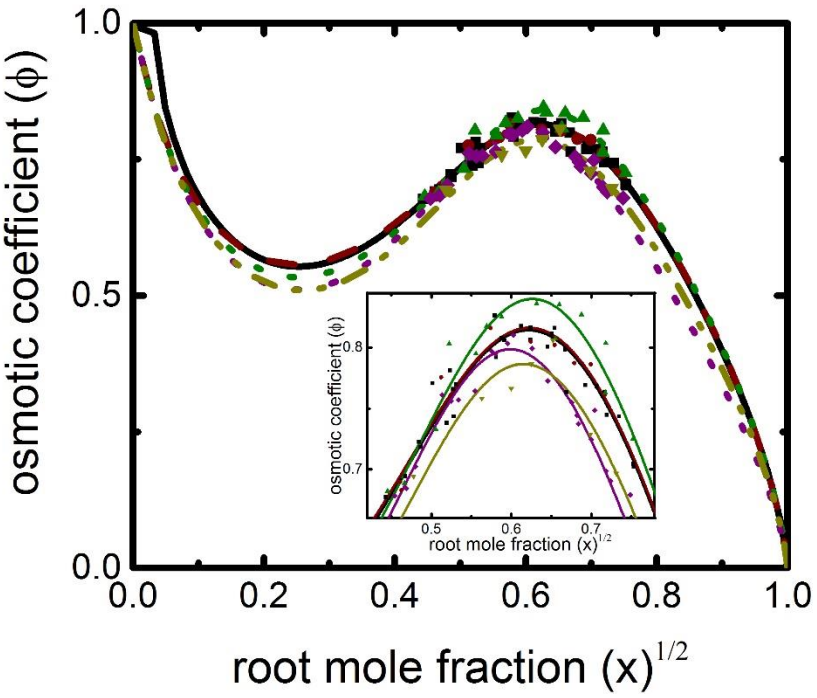

Figure 5. 4. Three-parameter model for ammonium sulfate: fitting parameters - ρ, r_{jj} and μ_j. Osmotic coefficient (φ = -ln $(a_w)/M_w \sum_j v_j m_j$), plotted against the square root of the solute mole fraction (x = $\sum_j v_j m_j/(\sum_j v_j m_j + 1/M_w)$). Lines (model calculations): black, 278 K; brown, 283 K; green, 288 K; purple, 308 K; dark yellow, 313 K. Symbols: black, 278 K experimental data; brown, (283 K) experimental data; green, 288 K experimental data; purple, 308 K experimental data; dark yellow, 313 K, where references for the experimental data given in **Table 5. 2**. The subplot represents model fitting to the data; predictions shown in solid lines.

n_j	T (K)	ρ^a	r_{jj} (Å)^a	r_{jw} (Å)^b	$\mu_j{}^a$	MSE^c	ref
	278	6.89	-1.023	3.944	8.43	2.73 x 10^{-4}	
	283	6.99	-1.051	3.921	8.30	1.89 x 10^{-4}	
3	288	6.39	-0.880	4.069	9.34	4.37 x 10^{-4}	130–133
	308	5.81	-0.501	5.264	19.06	6.02 x 10^{-4}	
	313	5.92	-0.397	4.487	12.28	4.30 x 10^{-4}	

Table 5. 2. Fitted parameters for $(NH_4)_2SO_4$ at various temperatures. [a]Fitted value. [b]Calculated value. [c]MSE is a normalized mean-square error, equal to $\left(\frac{1}{n_p}\right)\sum_{i=1}^{n_p}((m_{model,i} - m_{data,i})/(m_{model,i}))^2$, where n_p is the number of data points.

The model is fitted to the E-AIM calculated values as shown in **Figure 5. 5 - Figure 5. 7** for ammonium sulfate, ammonium nitrate and nitric acid respectively, and the variation in model parameters as a function of temperature is presented in **Figure 5. 8**. The change in solute-solvent intermolecular distance, r_{jw} and the change in dipole moment, μ_j for ammonium sulfate was not significant, although both r_{jw} and μ_j had higher values above 300 K. The Debye-Hückel parameter, ρ showed an increase at lower temperatures and a decrease at higher temperatures. For ammonium nitrate, r_{jw} slightly decreased with increasing temperatures, and the decrease was somewhat greater for nitric acid. The dipole moment, μ_j showed a slightly decreasing trend for ammonium nitrate, but an increasing trend for nitric acid with increasing temperatures. Finally, for both ammonium nitrate and nitric acid, ρ showed a steep increase with increasing temperatures.

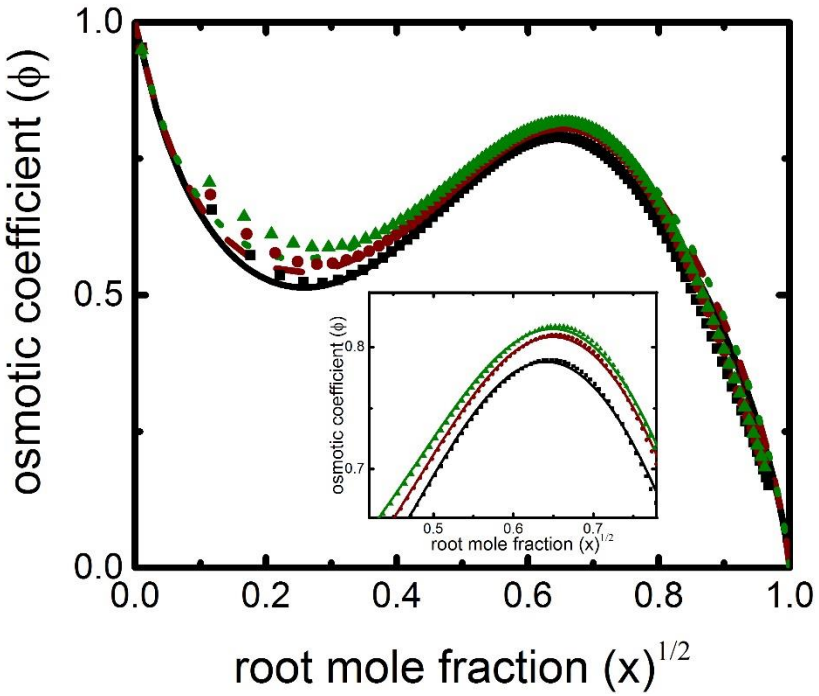

Figure 5. 5. Three-parameter model for ammonium sulfate: fitting parameters - ρ, r_{jj} and μ_j. (See caption from **Figure 5. 4**). Lines (model calculations): black, 220 K; brown, 240 K; green, 260 K. Symbols: black, 220 K E-AIM data; brown, 240 K E-AIM data; green, 260 K E-AIM data, where the data-points are calculated values extracted from E-AIM, reference given in **Table 5. 3**. The subplot represents model fitting to the data; predictions shown in solid lines.

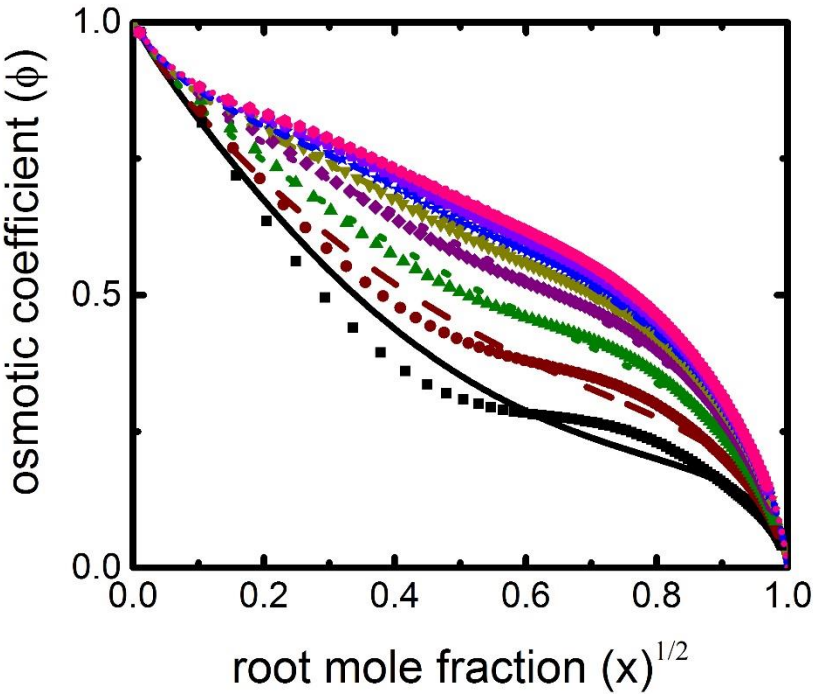

Figure 5. 6. Three-parameter model for ammonium nitrate: fitting parameters - ρ, r_{jj} and μ_j. (See caption from **Figure 5. 4**). Lines (model calculations): black, 220 K; brown, 240 K; green, 260 K; purple, 280 K; dark yellow, 293 K; blue, 303 K; violet, 313 K; magenta, 323 K. Symbols: black, 220 K E-AIM data; brown, 240 K E-AIM data; green, 260 K E-AIM data; purple, 280 K E-AIM data; dark yellow, 293 K E-AIM data; blue, 303 K E-AIM data; violet, 313 K E-AIM data; magenta, 323 K E-AIM data, where the data-points are calculated values extracted from E-AIM, reference given in **Table 5. 3**.

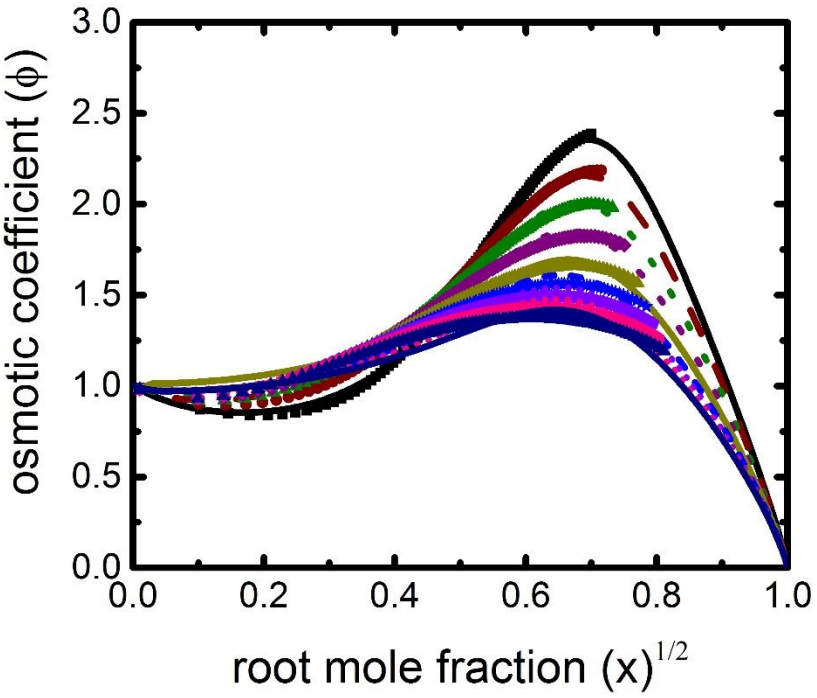

Figure 5. 7. Three-parameter model for nitric acid: fitting parameters - ρ, r_{jj} and μ_j. (See caption from **Figure 5. 4**). Lines (model calculations): black, 200 K; brown, 220 K; green, 240 K; purple, 260 K; dark yellow, 280 K; blue, 293 K; violet, 303 K; magenta, 313 K; navy, 323 K. Symbols: black, 200 K E-AIM data; brown, 220 K E-AIM data; green, 240 K E-AIM data; purple, 260 K E-AIM data; dark yellow, 280 K E-AIM data; blue, 293 K E-AIM data; violet, 303 K E-AIM data; magenta, 313 K E-AIM data; navy, 323 K E-AIM data, where the data-points are calculated values extracted from E-AIM, reference given in **Table 5. 3**.

solute	n_j	T (K)	ρ^a	r_{jj} (Å)^a	r_{jw} (Å)^b	$\mu_j{}^a$	MSE^c	ref
$(NH_4)_2SO_4$	4	220	6.00	-1.90	3.19	4.53	7.38 x 10^{-2}	32,61, 62,162, 185–187, 203
		240	6.67	-1.97	3.12	5.31	3.59 x 10^{-2}	
		260	7.27	-2.00	3.10	4.25	4.88 x 10^{-2}	
		273	7.20	-1.99	3.11	4.27	9.15 x 10^{-2}	
		278	7.37	-1.97	3.12	4.34	1.28 x 10^{-1}	
		283	7.57	-1.97	3.12	4.35	2.01 x 10^{-1}	
		288	7.74	-1.96	3.14	4.39	3.23 x 10^{-1}	
NH_4NO_3	2	220	4.70	3.11	6.24	28.57	3.29 x 10^{-2}	
		240	4.94	3.07	6.19	28.85	1.99 x 10^{-2}	
		260	6.26	3.06	6.18	29.07	9.47 x 10^{-3}	
		280	8.15	3.05	6.17	29.22	4.53 x 10^{-2}	
		293	9.54	3.04	6.17	29.30	3.02 x 10^{-3}	
		303	10.64	3.04	6.16	29.35	2.35 x 10^{-3}	
		313	11.72	3.04	6.16	29.39	1.93 x 10^{-3}	
		323	12.69	3.03	6.16	29.43	1.72 x 10^{-3}	
HNO_3	4	200	6.05	1.05	3.39	6.40	1.23 x 10^{-4}	
		220	16.76	1.00	3.34	6.08	1.97 x 10^{-4}	
		240	40.62	0.97	3.31	5.86	3.30 x 10^{-4}	
		260	56.63	0.96	3.30	5.75	4.29 x 10^{-4}	
		280	65.84	0.93	3.27	5.58	6.95 x 10^{-4}	
		293	60.73	0.92	3.26	5.48	1.00 x 10^{-3}	
		303	74.68	0..89	3.23	5.30	1.19 x 10^{-3}	
		313	79.41	0.86	3.20	5.11	1.39 x 10^{-3}	
		323	68.96	0.82	3.16	4.89	1.54 x 10^{-3}	

Table 5. 3. Fitted parameters for ammonium sulfate, ammonium nitrate and nitric acid at various temperatures. [a]Fitted value. [b]Calculated value. [c]MSE is a normalized mean-square error, equal to $\left(\frac{1}{n_p}\right)\sum_{i=1}^{n_p}((m_{model,i}-m_{data,i})/(m_{model,i}))^2$, where n_p is the number of data points. Ref: http://www.aim.env.uea.ac.uk/aim/aim.php.[32,61,62,162,185–187,203]

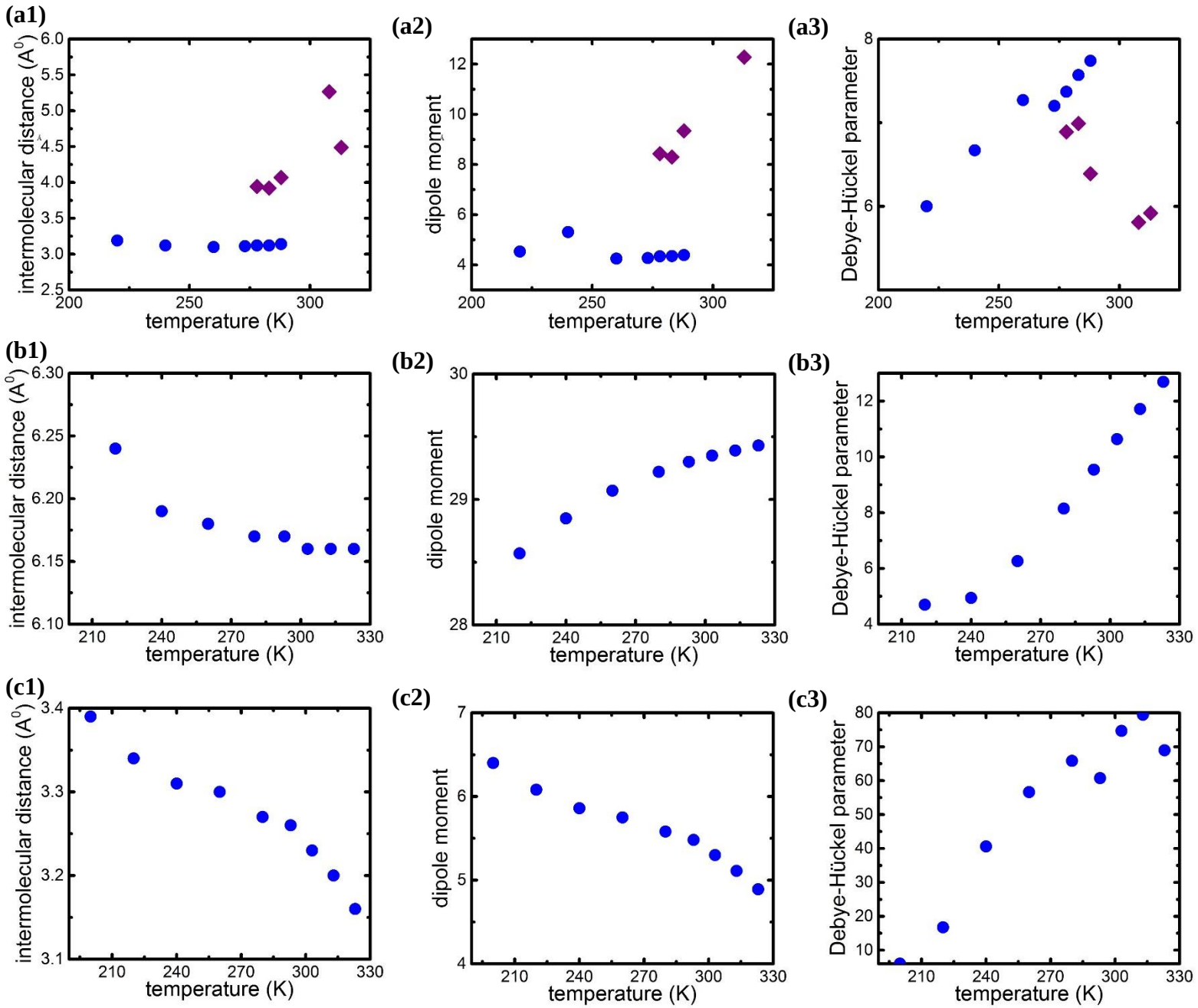
(a1)
intermolecular distance (A^0)
temperature (K)
(a2)
dipole moment
temperature (K)
(a3)
Debye-Hückel parameter
temperature (K)
(b1)
intermolecular distance (A^0)
temperature (K)
(b2)
dipole moment
temperature (K)
(b3)
Debye-Hückel parameter
temperature (K)
(c1)
intermolecular distance (A^0)
temperature (K)
(c2)
dipole moment
temperature (K)
(c3)
Debye-Hückel parameter
temperature (K)

Figure 5. 8. Temperature dependence on (a1, b1, c1) intermolecular distance between solute and solvent, (a2, b2, c2) dipole moment, (a3, b3, c3) Debye-Hückel parameter, for (a1-a3) ammonium sulfate. (b1-b3) ammonium nitrate. (c1-c3) nitric acid. Symbols: blue circle, model fitted to E-AIM calculated values; purple diamond, model fitted to experimental literature data.

5.4 Conclusions

For aerosol studies in the troposphere, considering the temperature dependence is essential. The chapter provides a review of different aerosol phase-change processes, and how the temperature influences such processes. The model presented in the second part of this chapter, takes into account the temperature dependence of the model parameters by extending parameterization at different temperatures for which data is available. The model is developed over the entire concentration range, that also provides an insight on the effect of temperature on water activity.

Chapter 6

Microfluidic Experiments to Study Liquid-Liquid Phase Separation in Organic Acids-Ammonium Sulfate Aqueous Aerosol Solution Mimics†

†Adapted with permission from Nandy, L.; Dutcher, C. S. Phase Behavior of Ammonium Sulfate with Organic Acid Solutions in Aqueous Aerosol Mimics Using Microfluidic Traps. *J. Phys. Chem. B* **2018** *122* (13), 3480-3490. Copyright (2018) American Chemical Society.

6.1 Introduction

Water-soluble organic acids such as dicarboxylic acids are known to form a significant fraction of organic aerosol mass, yet the chemical composition and interactions between components in an organic acid–inorganic salt mixed particle remain unclear. In this chapter, phase behavior of different mixing ratios of the salt and organic acids, here 3-methyl glutaric acid and 3-methyl adipic acid, are investigated with respect to their water activity. A microfluidic pervaporation approach is used to study different phase transitions of internally mixed aqueous droplets. Single droplets of varied compositions are trapped and stored in microfluidic wells until dehydration, where both the water content and the solution volume of the droplet decrease slowly with time as shown in **Figure 6. 1**. The volume is calculated by imaging techniques and correlated with the initial known concentration of the solution to determine concentrations at each time interval. The phase transitions of the droplets with changing concentrations are also observed under an inverted microscope. The study will help determine the concentration at which a mixture droplet, mimicking organic and inorganic atmospheric aerosols, changes phase.

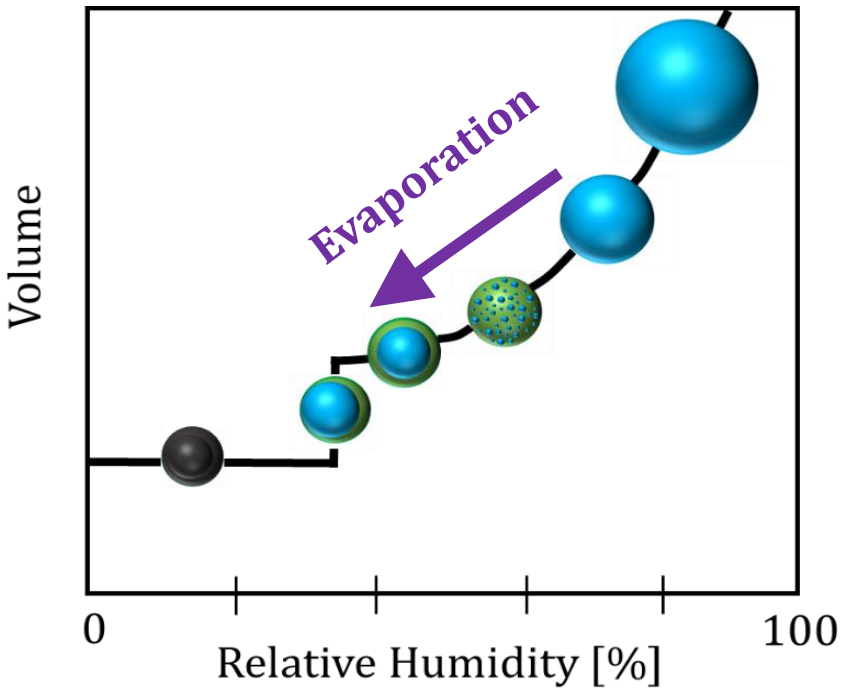

Figure 6. 1. Schematic to show reduction in volume of a ternary aqueous organic-inorganic mixture aerosol droplet upon evaporation. Droplet starts as a homogeneously mixed solution at high relative humidity which subsequently depicts different phase behavior as it loses water. Relative humidity on the x-axis is equivalent to the water activity of the solution droplet.

In previous studies, deliquescence, efflorescence and separation relative humidities of mixed ammonium sulfate and organic compound particles have been measured in laboratory using a combination of optical microscopy and flow-cells, and are reported along with different morphologies observed for the particles.[38,66,67,204] The studies suggest that core-shell and partially engulfed structures exist in tropospheric aerosols. Functional groups such as hydroxyls, dicarboxylic acids and oxidized aromatic compounds have been studied with AS for liquid-liquid phase separation with OIR 2:1, 1:2 and 1:6, that also reported dependence of O/C.[205] They found that liquid-liquid phase separation occurred for $0.56 < O/C < 0.8$, and that it depended on the composition of the functional group.

Moreover, studies on effect of pH on the SRH have also been investigated leading to hysteresis between the SRH on lowering RH and the mixing relative humidity (MRH) on increasing RH.[206] The studies suggest that the shift in SRH of the bulk solution is due to the changes in its protonation states. Some studies have linked hygroscopic growth of aerosols to their optical properties,[10] and found that change in water content with respect to ambient RH affects size, refractive index (RI), and phase of atmospheric aerosols. Studies on water content in aerosols, in turn, enhances understanding of solar radiation and aerosols interaction.[207]

In this chapter, multiphase microfluidics is used to trap aqueous droplets of different organic acids and salt mixtures that mimic atmospheric aerosols to study phase behavior and water loss properties. The systems studied here are meant to mimic atmospheric aerosol aqueous droplet dynamics. For actual atmospheric aerosols, the water activity in the droplet phase is equal to the ambient relative humidity.[2] For this reason, the calculated water activities found here are also reported as relative humidities (RH) for use in aerosol science applications. Mixtures of dicarboxylic acids with ammonium sulfate of different concentrations and organic-to-inorganic ratios are studied to determine the concentrations of efflorescence or crystallization as well as liquid-liquid phase separation. The study will shed insights on phase transition processes as a function of RH and aerosol concentrations that affect weather and climate.[208]

6.2 Experimental Method and Materials

To measure concentrations of aerosol chemical mimics with respect to the ambient relative humidity and to study liquid-liquid phase separation and efflorescence points, a

microfluidic device is fabricated with traps for two-phase fluid flow.[209–211] The microfluidic devices are fabricated in poly(dimethylsiloxane) (PDMS, Sylgard 184 Silicone Elastomer, Dow Corning Corporation) using soft lithography techniques.[212,213] A computer-aided design (CAD) based software, DraftSight (Dassault Systèmes), is used to design and draw a mask, and using standard photolithography in a clean-room facility, a master mold silicon wafer is prepared from the printed mask.[214] PDMS is then poured, degassed and cured to yield devices which are then cut out as individual chips from the wafer. The PDMS chip is then punched with holes, bonded to a glass cover slide, and polyethylene tubing (BD Intramedic PE tubing, 1.52 mm OD, 0.86 mm ID) is used to deliver the fluids to the device.

An inverted microscope (Olympus IX83) with phase contrast and bright-field imaging is used to perform experiments, and images are captured by a high-speed Lumenera INFINITY2-2M (mono) camera. Image of a microfluidic device trap design is shown in **Figure 6. 2**, and image of a droplet in the trap is shown in **Figure 6. 3**a. A steady flow of the continuous phase, here hydrophobic silicone oil (Fisher Scientific, CAS 63148-62-9), acting as a carrier fluid that wets the channel walls, surrounds the dispersed phase droplets generated in the microfluidic device. The biphasic microfluidic flow is controlled by pressure-driven flow by syringe pumps (Harvard Apparatus, Massachusetts) attached with gastight syringes (Hamilton) that supply steady and constant flow rates. The flow rate of continuous phase and dispersed phase are set at 0.001 mL/min and 0.0001 mL/min respectively. The droplets are generated at the T-junction having a cross-flow structure where the two immiscible streams, continuous and dispersed phases, are fed orthogonally to produce monodisperse droplets.[215,216] The droplets of the dispersed phase shear off by

the upstream pressure exerted by the continuous phase,[211,217,218] and enter the traps. The subsequent droplets flow through the bypass channel and enter the following traps.[209,210] Each device has an array of traps where the droplets stay confined as soon as all the flows are stopped; only one droplet is imaged. Because PDMS is a highly permeable material, pervaporation (a separation mechanism that is based on the solution diffusion model to study mass transport mechanisms)[219] occurs and droplet volume reduces continuously with time. Other studies use PDMS membrane pervaporation process in microfluidic channel for solidification of material,[220] to extract the solvent of a dilute colloidal dispersion,[221] and characterize phase behavior in a range of complex systems using microfluidic wells similar to those studied here.[222]

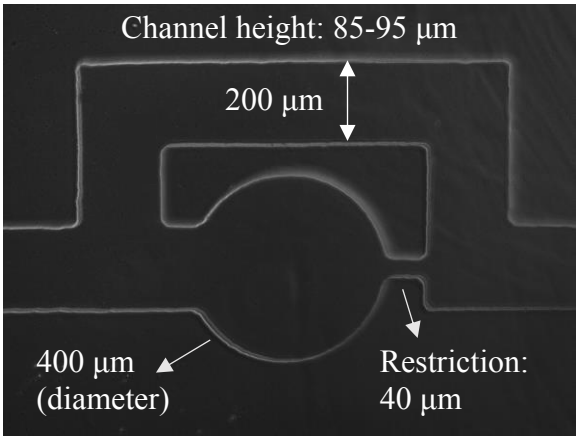

Figure 6. 2. Microfluidic trap design image; 10x magnification. Note: two different devices with channel heights 85 and 95 μm, respectively are used.

The aqueous solutions of the organic compounds of interest in this study are dicarboxylic acids – 3-methyl glutaric acid (3MGA, Sigma-Aldrich, CAS 0626-51-7) and 3-methyl adipic acid (3MAA, Sigma-Aldrich, CAS 3058-01-3). For the experiments, solutions are prepared by adding the organic acids to different concentrations of ammonium sulfate (AS, Avantor Performance Materials, CAS 7783−20−2) solutions

prepared in HPLC-grade water (Sigma-Aldrich, CAS 7732−18−8). Experiments with binary AS solution of varying concentrations are initially performed to validate the resultant ERH by comparing with that to available in the literature.[19,31] Solutions of organic-to-inorganic ratio (OIR, by dry mass) with range 0.1 to 10 are then prepared to study the influence of organic acids on the efflorescence point of AS. The solution droplets once trapped in the microfluidic devices are dehydrated in laboratory ambient conditions (23^{o}C, 21-23% RH), and images are taken every second. Selected images are analyzed using ImageJ software[223] to calculate the droplet equivalent diameters. The droplet volumes are then calculated using equations derived by Vuong and Anna.[224,225]

The two devices used for this study have channel heights of 85 and 95 μm, respectively, and a well diameter 3-4 times bigger than the channel height (measured directly using scanning electron microscopy). Therefore, the initially trapped droplet size varied from 200 to 350 μm that reduced to as low as 40 μm until dehydration. The droplet volume is calculated using a pancake-shape approximation[224,225] when the droplet diameter exceeds the channel height, as the droplet will be confined by the top and bottom walls of the microfluidic device channel. When the droplet diameter reduces to that of channel height on dehydration and subsequently lower than the channel height, the volume is calculated using the simple volume of sphere equation assuming the droplet is unbounded.

The volumes of the pancake shaped droplets (when $D > h$) are calculated using equation (6. 1), and the volumes of the subsequent smaller droplets (when $D < h$) that are assumed to be spherical are calculated using equation (6. 2).[224,225]

$$V_{pancake} = \frac{\pi h^3}{6} + \frac{\pi h}{4}\,(D_{pancake} - h)\left(\frac{\pi h}{2} + D_{pancake} - h\right) \quad (6.\ 1)$$

$$V_{sphere} = \frac{\pi {D_{sphere}}^3}{6} \quad (6.\ 2)$$

where, D is the projected diameter, h is the channel height, $D_{pancake}$ is the projected diameter when $D > h$, and D_{sphere} is the projected diameter when $D < h$.

Finally, the concentrations (molarities) are calculated using equation (6. 3) for the respective droplets for which the volumes were found using equations (6. 1) and (6. 2).

$$V_1M_1 = V_2M_2 = V_3M_3 = V_4M_4 = V_5M_5 = V_6M_6 = \ldots \quad (6.\ 3)$$

where, V is the volume of the droplet, M is the molarity concentration of the droplet, and 1, 2, 3, and so forth are the droplet images that are analyzed in the sequence of reduced droplet volume during evaporation.

Calculations are performed by assuming that only water from the aqueous droplet leaves the PDMS device, and all the solute remains in the trap. The assumption was tested and found to correctly yield the ERH for binary AS solutions as discussed later in Section 6.3.1. The mass or the number of moles of the solute remaining the same, volume (liter of solution) times molarity (moles of solute/liter of solution) remains constant. Because the initial concentration of the solution droplet is known, the concentrations are then calculated for each reduced droplet volume. The method demonstrates the evaluation of solution concentrations at different time steps during evaporation. In addition, the images from ternary solution droplet experiments reveal occurrence of liquid-liquid phase separation, for which the separation start and end concentrations are evaluated.

The ERH of the binary AS solution is determined by using the isotherm-based adsorption model[63,64,86,87] that calculates the water activities with respect to the input concentrations (molalities, moles of solute/kg of solvent). The predictive model assumes that each solute is surrounded by an arbitrary number of hydrated layers, and is developed using statistical mechanics and electrostatic relationships to determine the energy parameters for the sorption of water onto the hydration shell of solute molecule for each monolayer. Note that the unit of concentration from the experiments is molarity, whereas the adsorption model is "molality"-based. Therefore, in order to convert the units of concentration from molarity to molality input to the model, densities are required[140,226] (see Appendix C for step-by-step calculations of the densities, molalities, and relative humidities). Because the densities of ternary mixture solutions are not evaluated with respect to the concentrations in this work, the number of moles of the solute per liter of solution, i.e. the molarity is reported for the desired phase states of the ternary systems. However, the relative humidities (equivalent to water activities) are reported for binary AS aqueous solution from the model plot as shown in Figure C4 in Appendix C. The model is fit to the literature data available, and predictions are made for higher concentrations for which data is not available. Furthermore, the adsorption isotherm model can predict activities with respect to the molality concentrations for organic acids and ternary solutions as well.[86] However, in order to calculate the molalities, the densities over the full range of concentrations for these ternary solutions are required.

6.3 Results and Discussion

6.3.1 Efflorescence relative humidity (ERH) of aqueous binary ammonium sulfate (AS) solution.

Images of a droplet at different stages of dehydration are shown in **Figure 6. 3**a, and the zoomed-in images of the supersaturated droplet and the salt crystals are shown in **Figure 6. 3**b. When the droplet reaches a particular concentration, it is not visible. It happens when the refractive index (RI) of the droplet at that concentration matches with that of the continuous phase liquid surrounding it. One of the images in **Figure 6. 3**b (ii) shows the droplet with RI close to that of silicone oil (~1.4), and hence not clearly visible. The droplet images are transparent/translucent when they are in liquid phase, and therefore have a distinct boundary. The solid phase in the image sequence is distinguished when the droplet image looks opaque throughout (**Figure 6. 3**a (iv) and **Figure 6. 3**b (iv), (v)).

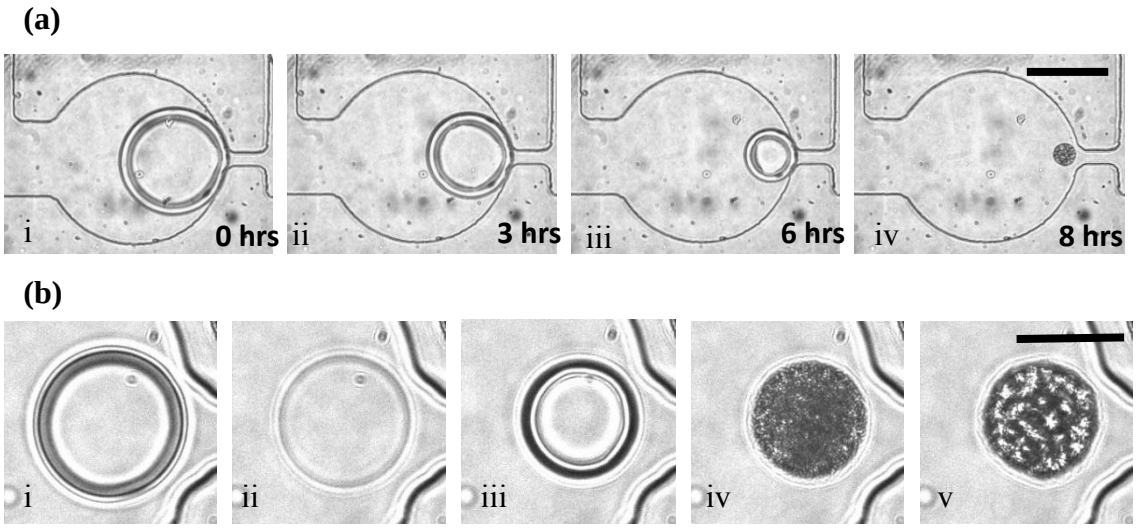

Figure 6. 3. (a) Phase contrast images of aqueous 0.25 molal AS solution droplet in silicone oil; 20x magnification. Scale bar: 200 μm. (b) Zoomed-in images of the supersaturated droplet and the solidified crystal. Scale bar: 50 μm.

The volumes of the pancake shaped droplets are calculated using equation (6. 1), and the volumes of the subsequent smaller droplets that are assumed to be spherical are calculated using equation (6. 2).[224,225] It is seen that the droplet volume reduces over time, and the rate of evaporation reduces after a certain point as shown in **Figure 6. 4**. Using equation (6. 3) which assumes that the total mass of the solute is constant, i.e. volume (L) times concentration (moles/L) in the trap remains the same, the concentration of each droplet volume is calculated. Due to pervaporation, the mass fraction of water reduces as shown in **Figure 6. 5**a.

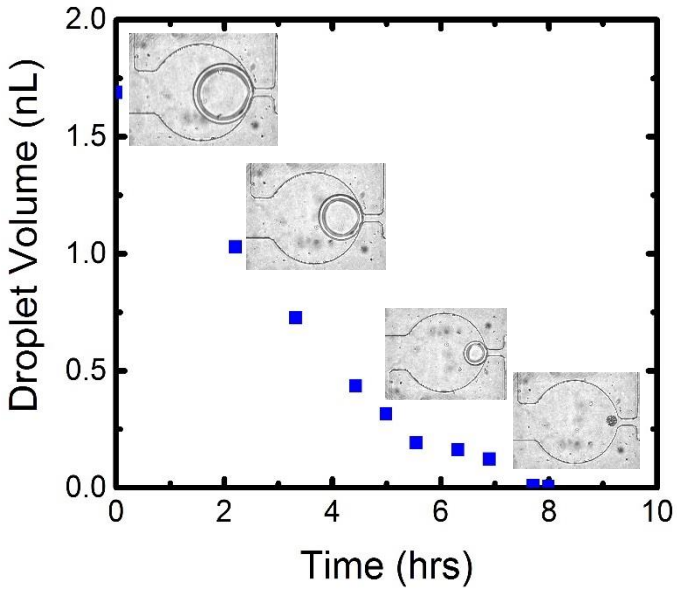

Figure 6. 4. Change in droplet volume of AS solution with time. Diameter of the well in the inset micrograph images is 400 μm.

The adsorption model[87] is then used to calculate the water activities as a function of droplet solution concentration. The water activities correspond to the relative humidities, the plot for which with change in volume is shown in **Figure 6. 5**b. The step-by-step calculations of the AS solution densities, water mass fractions, and water activities are

included in Appendix C. Results from previous work using different experimental methods and numerical models report the ERH of AS to be 30 – 40% depending on the size and concentration.[19–21,132] **Table 6. 1** shows the ERH of different starting concentrations of binary AS solution. The table also has the values of the RH at which the droplet is not visible (matched RI). The initial size of the droplets is ~300 μm, the matched RI relative humidity is ~77%, and the ERH is ~31%. A sensitivity analysis of channel height was done, and error was calculated for ±2 μm channel height. It is found that the volume calculations of droplets with low initial concentration, i.e. approximately less than 1 molar, are highly sensitive to the channel height used in the volume calculations, as the droplets shrink significantly, and take a spherical shape, by the time they crystallize. The error in final concentration for the dilute solution droplets is ~0.85% (yielding ~10% error in ERH), as compared to ~0.07% for the concentrated solution droplets (~0.86% error in ERH) that maintain the pancake shape until crystallization. Hence, it is desirable to study concentrated droplets no less than 1 molar. Model studies for refractive index predictions of various compounds with respect to their mass fraction and RH[227–229] are used to calculate the RI of the AS solution when the droplet is not visible in the experiments, and is found to be approximately between 1.369 and 1.408. The RI of silicone oil, the surrounding phase, is 1.393 – 1.403,[230] which is close to the RI of the salt solution reported here.

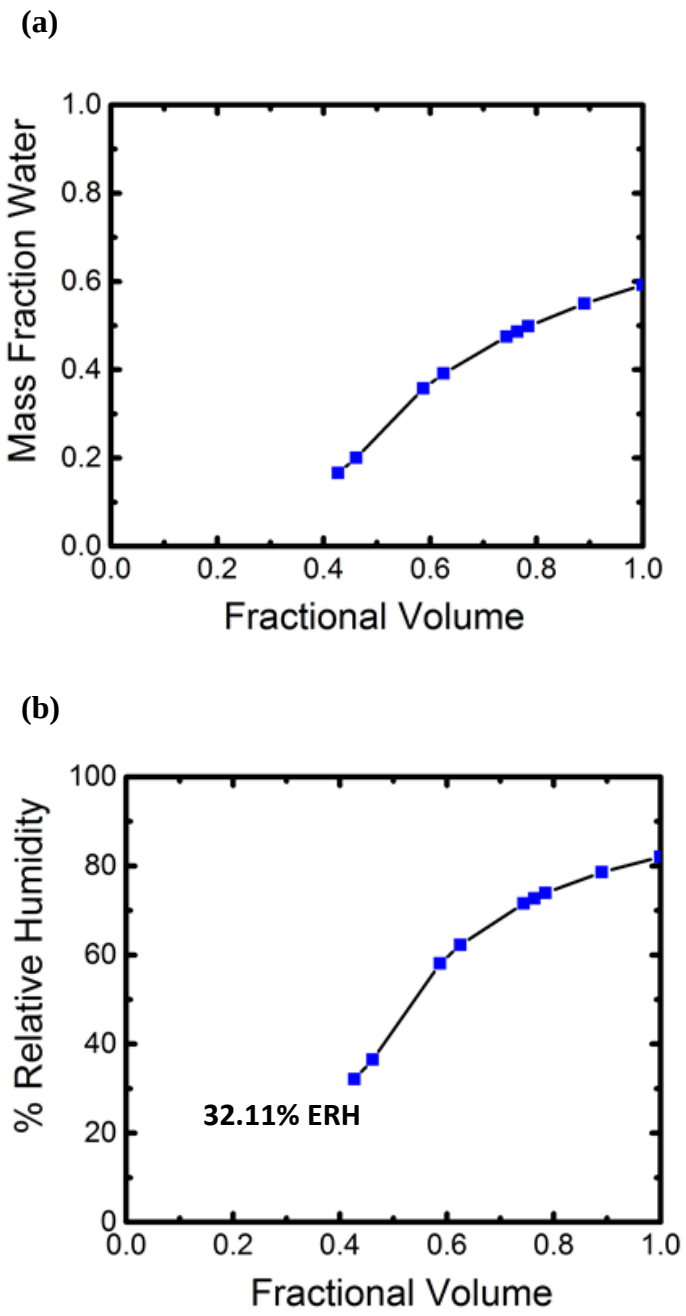

Figure 6. 5. (a) Change in mass fraction of water with droplet volume of AS solution, found using Equation (6. 3) and density calculations in SI. (b) Change in relative humidity with droplet volume of AS solution, found using Coulombic isotherm model.[63,64,86,87] Fractional volume on *x*-axis is the volume normalized by the initial volume.

initial concentration (M)	initial droplet size (μm)	matched RI concentration (M)	matched RI concentration (m)	matched RI RH (%)	final concentration (M)	final concentration (m)	ERH (%)	error (%)
0.015	208	4.540	6.80	76.59	8.953	49.10	26.13	10.58
0.104	198	4.258	6.14	78.81	8.942	48.60	26.32	10.84
0.980	299	4.707	7.21	75.24	8.491	34.72	33.33	1.530
2.504	274	4.468	6.63	77.14	8.343	31.64	35.46	0.705
3.954	308	4.657	7.09	75.62	8.346	31.70	35.41	0.353

Table 6. 1. Concentrations and relative humidities of aqueous binary ammonium sulfate solution. Channel height: 85 μm. M is moles/liter; RI is refractive index; m is moles/kg; final concentration is the concentration at which the droplet crystallizes; ERH is efflorescence relative humidity; error is calculated by ±2 μm channel height sensitivity analysis for ERH. Initial droplet volume range: 1.5 – 5.7 nl. Note – the reported "RH" values are based on the calculated water activities.

6.3.2 Final concentrations of aqueous ternary ammonium sulfate (AS)-dicarboxylic acid (3MGA or 3MAA) solution.

The experiments with binary salt solutions were performed as a method of validation. Now, the experiments are performed with ternary salt-organic acid solutions with different OIR by dry mass, ranging from 0.1 to 10, and equations (6. 1) – (6. 3) are used to calculate the volume and concentrations of each droplet. Since, the densities of these ternary solutions are not available over the full concentration range, only the molarity concentrations are reported for the studies. Liquid-liquid phase separation (LLPS) is observed for mixture solutions, as the organic phase separates from the aqueous inorganic phase. The type of phase separations observed are tiny inclusions, partially engulfed structures and core-shell structures. As an example, formation of a core-shell phase transition can be seen in **Figure 6. 6**. Two series of images showing the phase transitions of a 3-methyl adipic acid - ammonium sulfate ternary aqueous solution droplet on a glass slide and in a microfluidic well are included in Appendix C. The videos represent the same solution droplet in which the time span of the phase change differs. The difference in the phase transition behavior from the two videos implies that the lubrication layer of oil between the drop and the PDMS plays a significant role in slowing the phase change process and allows access to thermodynamically metastable states.

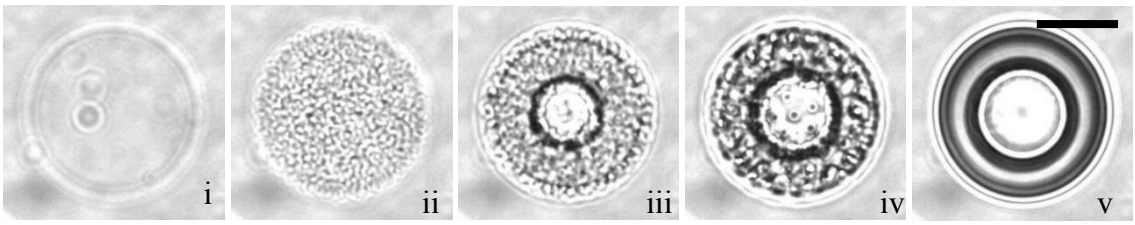

Figure 6. 6. Phase transitions observed in AS – 3MAA ternary aqueous solution; phase contrast images of the solution droplet with OIR 2:1. LLPS time span (from ii to v): ~15 minutes. Scale bar: 50 μm.

3MGA + AS. For OIR 1:10, tiny inclusions (similar to **Figure 6. 6.** Phase transitions observed in AS – 3MAA ternary aqueous solution; phase contrast images of the solution droplet with OIR 2:1. LLPS time span (from ii to v): ~15 minutes. Scale bar: 50 μm.(ii)) are not seen clearly, but a core aqueous inorganic phase tends to form. Since the amount of salt is 10 times higher than that of the acid, the core does not seem to separate fully from the organic phase as shown in **Figure 6. 7**a (ii), (iii). Both the phases share part of their surfaces with the outer oil phase. For OIR 1:5, few tiny inclusions **Figure 6. 7**b (ii), (iii) are seen to form that again mix with the aqueous inorganic phase **Figure 6. 7**a (iv) and a core tends to form that gradually shifts to a partially engulfed structure as shown in **Figure 6. 7**b. In both cases, the inorganic phase effloresces first (**Figure 6. 7**a (iv) and **Figure 6. 7**b (v) and eventually the whole droplet (**Figure 6. 7**a (v) and **Figure 6. 7**b (vi)) effloresces. For OIR 1:2, a different behavior is observed during LLPS as shown in **Figure 6. 7**c. Inclusions are seen to form in the solution droplet in **Figure 6. 7**c (ii) at supersaturated concentrations that gradually coalesce to form a core aqueous inorganic phase in **Figure 6. 7**c (v). However, the core tends to move toward the outer surface and takes up a different structure seen in **Figure 6. 7**c (vi), (vii), and finally solidifies. Note that after the spontaneous efflorescence in **Figure 6. 7**c (viii), part of the organic phase (which is still in

liquid state) separates out of the solid phase (**Figure 6. 7**c (ix)) and spreads out in the oil before dehydrating completely (**Figure 6. 7**c (x)).

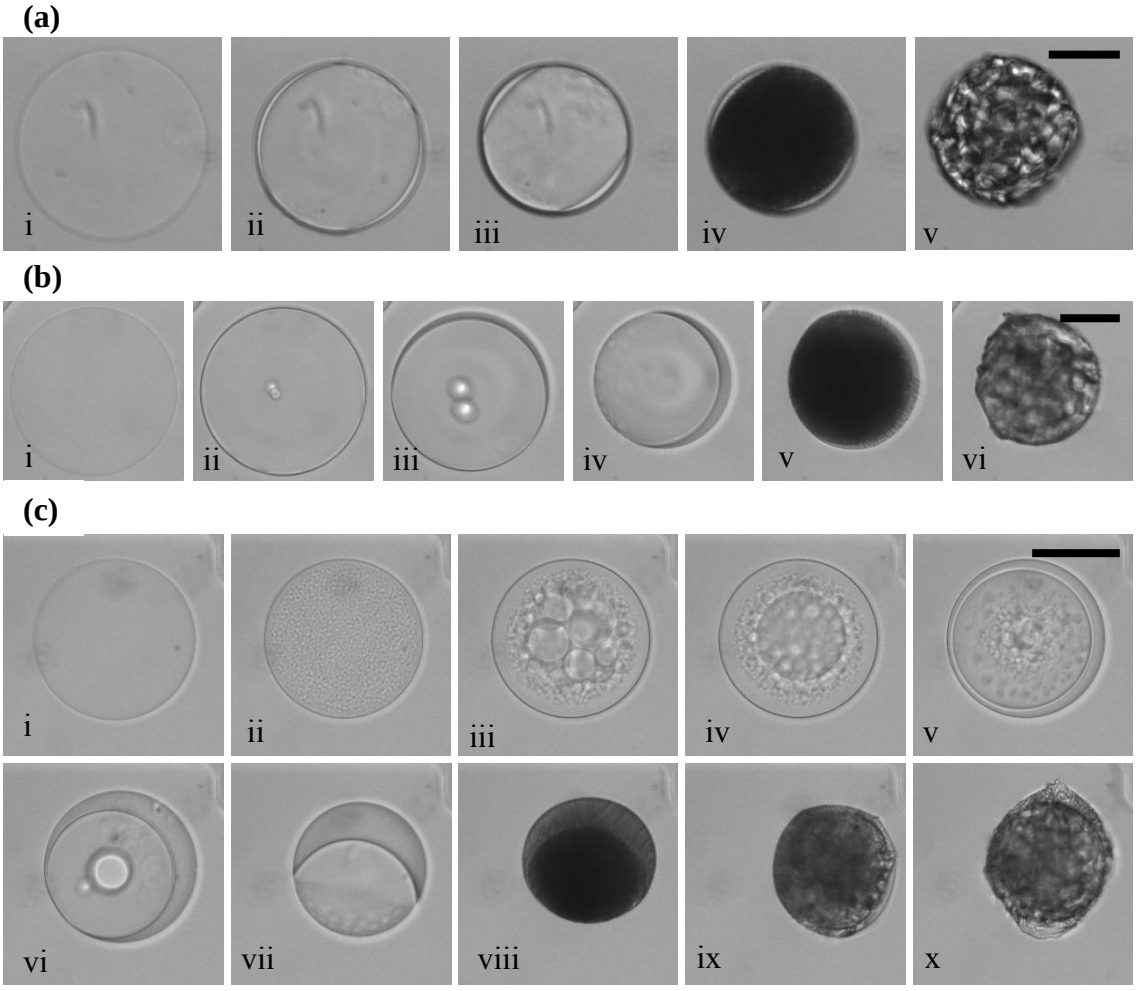

Figure 6. 7. Phase transitions observed in AS – 3MGA ternary aqueous solution with less acid than salt. Scale bar: 50 μm. (a) Brightfield images of solution droplet with OIR 1:10. LLPS time span (from ii to iii): ~25 minutes. (b) Brightfield images of solution droplet with OIR 1:5. LLPS time span (from ii to iv): ~25 minutes. (c) Brightfield images of solution droplet with OIR 1:2. LLPS time span (from ii to vii): ~45 minutes.

For OIR 1:1, again a different behavior is observed as same amount of acid as the salt is added to the solution, as shown in **Figure 6. 8**a. Tiny inclusions are seen to form in the solution droplet that eventually coalesce to form a core aqueous inorganic phase. The

inorganic phase stays right at the core and does not tend to share the outer surface with the organic phase shell, as was observed for the lower OIRs. Similarly, for OIR 2:1, a core-shell morphology is observed as seen in **Figure 6. 8**b. As can be seen in **Figure 6. 8**, as the amount of acid added increases with respect to the salt, the core becomes smaller. The appearance of the shell and core in some of the images are different because they differ in their concentrations, and hence refractive indices. The appearance of one concentric ring is due to liquid-liquid phase separation, with a core of one liquid inside of another liquid. Some images have what appears to be multiple concentric rings (e.g. **Figure 6. 6** (v)), and this is an artifact due to the lighting and shadow.

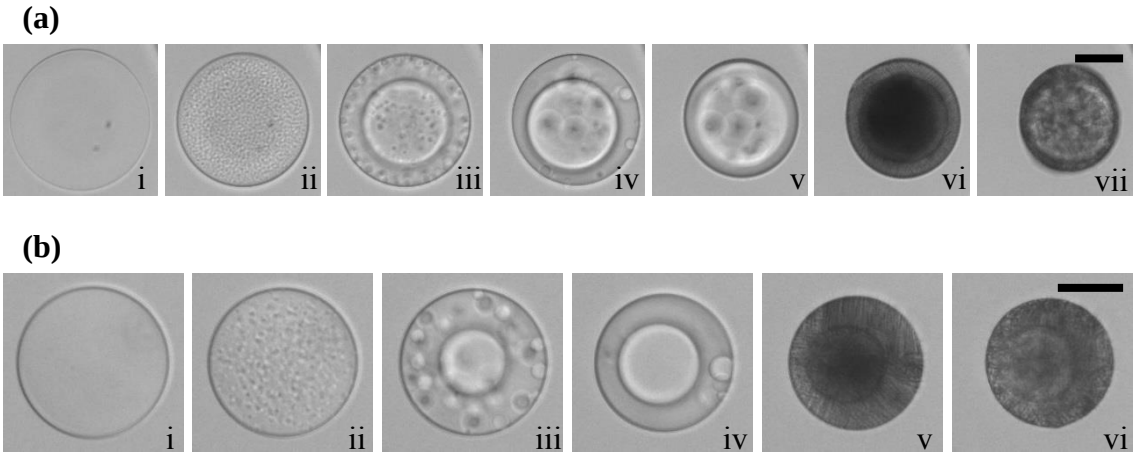

Figure 6. 8. Phase transitions observed in AS – 3MGA ternary aqueous solution with same or more acid than salt that show a core-shell morphology. Scale bar: 50 μm. (a) Brightfield images of solution droplet with OIR 1:1. LLPS time span (from ii to iv): ~10 minutes. (b) Brightfield images of solution droplet with OIR 2:1. LLPS time span (from ii to iv): ~15 minutes.

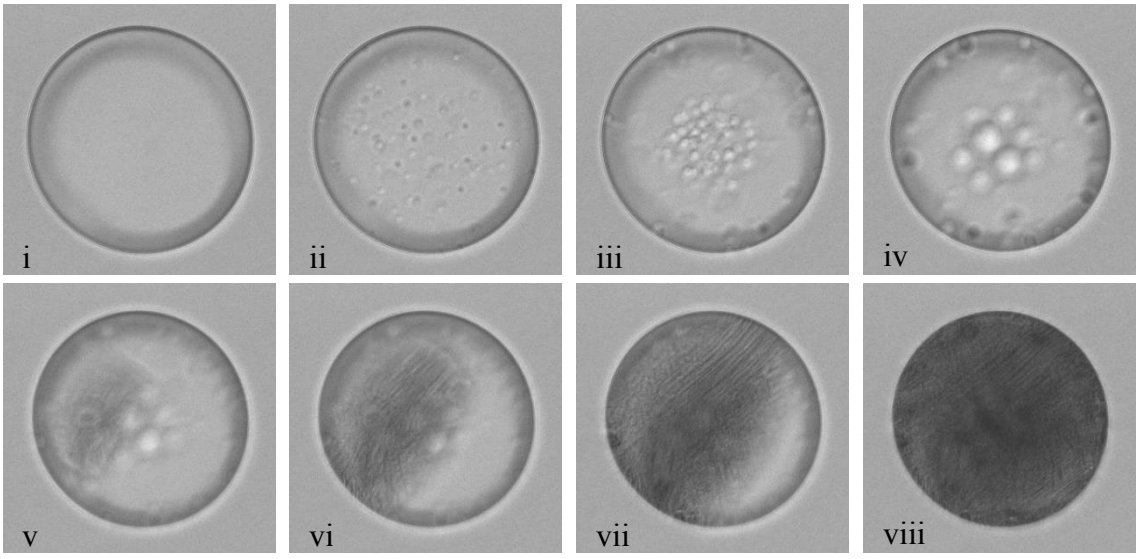

Figure 6. 9. Phase transitions observed in AS – 3MGA ternary aqueous solution; brightfield images of the solution droplet with OIR 3:1. LLPS time span (from ii to iv): ~10 minutes. Coating time span (from v to viii): ~6 seconds. Scale bar: 50 μm.

In **Figure 6. 9**, as more acid is added to make OIR 3:1, inclusions form and tend to move to the center, but they do not coalesce to form a core (**Figure 6. 9** (ii) – (iv)). However, a different behavior is seen during phase change from liquid to solid. The phase transition is not as spontaneous like the lower ratios or like just the binary salt solution. Crystallization starts at one point of the droplet surface and a solid coating is seen spreading throughout the surface of the droplet gradually, until it dehydrates completely (**Figure 6. 9** (v) – (viii)). In **Figure 6. 10**, no LLPS is observed when higher amount of the organic acid is added to the salt, i.e. OIR 5:1 and 10:1. Yet, the solid coating phase transition from a liquid droplet to a solid is seen in these experiments. The matched RI and final (efflorescence) concentrations of each solution experiment are reported in **Table 6. 2**. In addition, the concentrations when the phase separation starts and when the droplets form core-shell or partially engulfed structure are also reported in **Table 6. 2**. The time span of

the phase separation and coating behavior are reported in the figure captions. The initial droplet concentrations for the ternary solutions are approximately 0.89 molar, and a sensitivity analysis based on height yielded an error of ~1% in the final concentration reported.

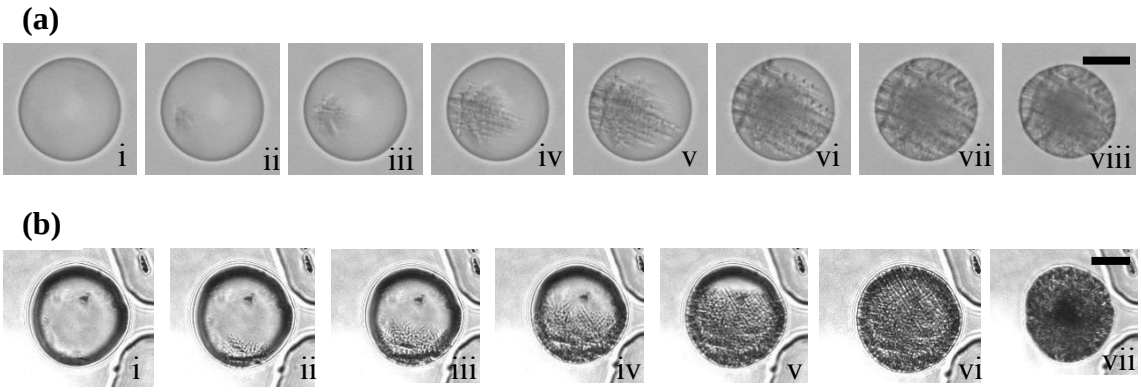

Figure 6. 10. Phase transitions observed in AS – 3MGA ternary aqueous solution with more acid than salt that show a solid coating during crystallization. Scale bar: 50 μm. (a) Brightfield images of solution droplet with OIR 5:1. Coating time span (from ii to vii): ~15 seconds. (b) Phase contrast images of solution droplet with OIR 10:1. Coating time span (from ii to vi): ~25 seconds.

OIR (by mass)	OIR (by moles)	initial concentration (M)	matched RI concentration (M)	final concentration (M)	LLPS start concentration (M)	complete core-shell concentra-tion (M)	partial engulfment concentrati-on (M)	coating start concen-tration (M)	complete coating concentra-tion (M)
0.1	0.090	0.825	4.59	8.02	4.41	-	6.16	-	-
0.2	0.181	0.894	4.44	7.96	4.45	-	5.72	-	-
0.5	0.452	1.100	4.62	7.32	5.11	5.19	7.06	-	-
1	0.904	0.721	4.20	8.41	4.93	4.98	-	-	-
2	1.808	1.063	3.82	7.85	4.33	5.46	-	-	-
3	2.713	0.937	4.42	7.24	5.86	-	-	6.56	6.63
5	4.521	0.836	5.53	7.75	-	-	-	7.05	7.21
10	9.042	0.760	4.05	8.71	-	-	-	6.97	7.09
-	-	0.684	4.06	10.72	-	-	-	-	-

Table 6. 2. Concentrations of aqueous ternary ammonium sulfate and 3-methyl glutaric acid solution. Channel height: 85 μm. OIR is organic-to-inorganic ratio by dry mass; final concentration is the concentration at which the solution droplet crystallizes; error in final

concentration is calculated by ±2 μm channel height sensitivity analysis, and found to be 1.03% average. Initial droplet volume range: 1.3 – 7.3 nl. The last row has data for binary organic acid solution.

3MAA + AS. Because 3-methyl adipic acid is not completely soluble in water, the highest concentration solution used for the experiments is 30 mg/mL. In **Figure 6. 11**, droplet images of the phase transitions can be seen for OIR 1:10, 1:5, and 1:2. For OIR 1:10, because the amount of acid is significantly low with respect to the amount of salt in the solution, the acid separates from the aqueous inorganic phase and tries to form a shell, but is unable to coat the entire aqueous core (**Figure 6. 12**). For OIR 1:5, partial engulfment can be seen, and on the other half where both phases share the surface, the organic phase again tries to coat the aqueous phase (**Figure 6. 11**). The same behavior can be seen for OIR 1:2 in **Figure 6. 11**c as well with subsequent efflorescence of the aqueous phase first. Phase transitions for solutions with OIR 1:1, 2:1 and 5:1 are shown in **Figure 6. 12**, where tiny inclusions coalesce to form a core aqueous inorganic phase. As the amount of acid increases, the core becomes smaller. However, in **Figure 6. 12**a, the core gradually moves toward the surface forming a partially engulfed-like structure. When even more acid is added (OIR 10:1), inclusions form and move toward the core, but do not coalesce to form a core, and eventually effloresce spontaneously (**Figure 6. 13**). The figures and image sequences are described in the figure captions. The concentrations of the matched RI droplet, the solidified droplet, concentrations when the phase separation starts and when the droplets form core-shell or partially engulfed structure are reported in **Table 6. 3**. The time spans of the phase separation are reported in the figure captions. The initial droplet concentrations for the ternary solutions are approximately 0.48 molar, and a sensitivity analysis yielded an error of ~1.7% in the final concentration reported in **Table 6. 3**. The error in 3MAA experiments is higher than the 3MGA experiments, because the solution droplets are dilute enough to shrink significantly losing the pancake shape. The reason for

using dilute solution concentrations in the 3MAA experiments, however, is the low solubility of 3MAA in water.

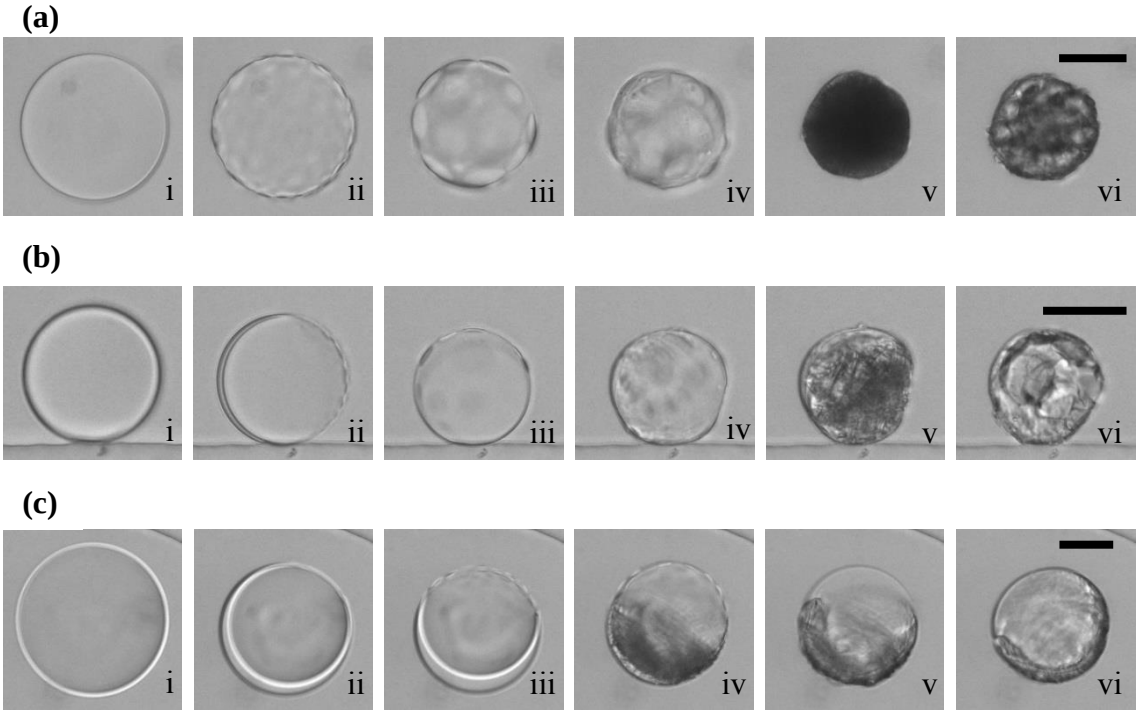

Figure 6. 11. Phase transitions observed in AS – 3MAA ternary aqueous solution with less acid than salt. Scale bar: 50 μm. (a). Brightfield images of solution droplet with OIR 1:10. LLPS time span (from ii to iv): ~10 minutes. (b). Brightfield images of solution droplet with OIR 1:5. LLPS time span (from ii to iii): ~5 minutes. (c). Brightfield images of solution droplet with OIR 1:2. LLPS time span (from ii to iv): ~60 minutes. In (a), LLPS (inclusions) is seen in (ii) – (iv), after which the droplet crystallizes, (v) and (vi). Similarly, LLPS (partial engulfment) is observed in (b),(c) in the sequences (ii) and (iii), after which the droplet crystallizes, (iv) – (vi).

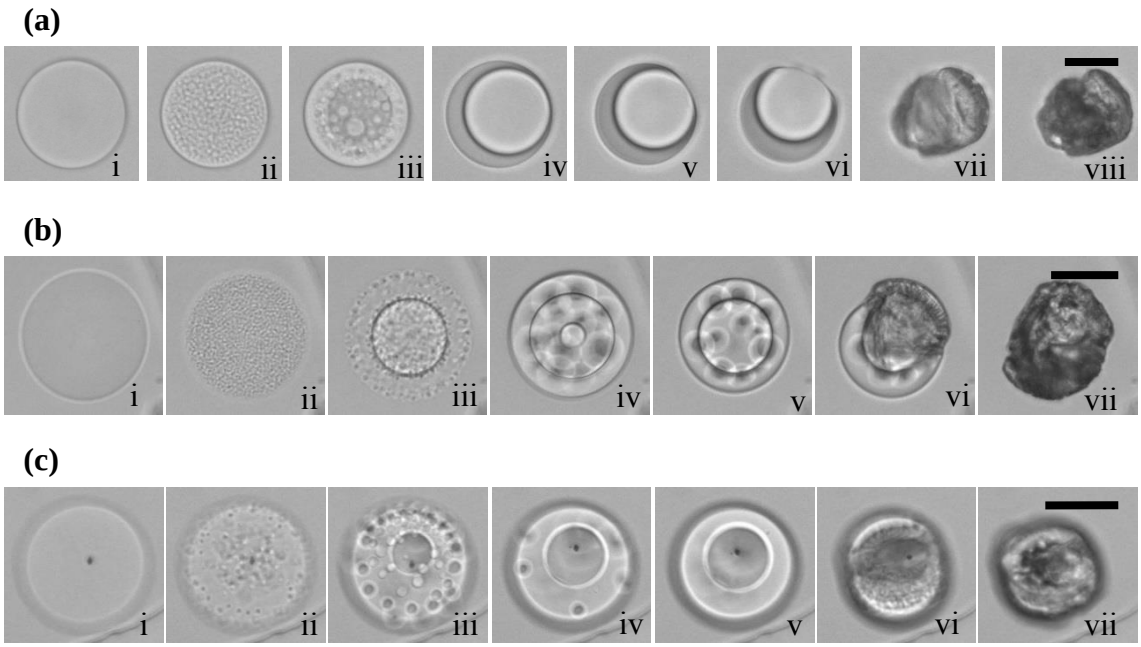

Figure 6. 12. Phase transitions observed in AS – 3MAA ternary aqueous solution with same or more acid than salt. Scale bar: 50 μm. (a). Brightfield images of solution droplet with OIR 1:1. LLPS time span (from ii to vi): ~25 minutes. (b). Brightfield images of solution droplet with OIR 2:1. LLPS time span (from ii to v): ~5 minutes. (c). Phase contrast images of solution droplet with OIR 5:1. LLPS time span (from ii to v): ~10 minutes. LLPS (tiny inclusions) is seen in the sequence (ii), after which the inclusions coalesce, and the phases separate to form a core-shell structure, (iii) - (v). The structure in (a)v, transforms into an engulfed morphology in sequence (vi), before it crystallizes.

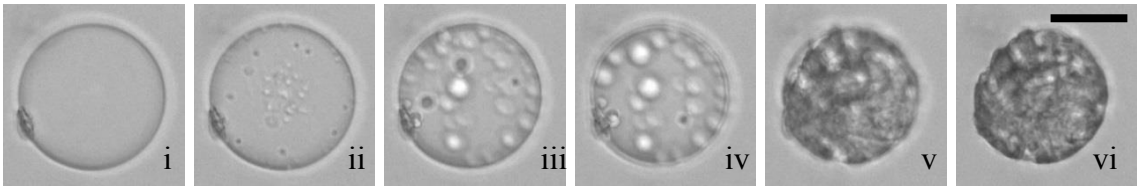

Figure 6. 13. Phase transitions observed in AS – 3MAA ternary aqueous solution - brightfield images of the solution droplet with OIR 10:1. LLPS time span (from ii to iv): 10~ minutes. Scale bar: 50 μm. LLPS (inclusions) is seen in (ii) – (iv), after which the droplet crystallizes, (v) and (vi). However, the inclusions here do not coalesce to form a core in a core-shell morphology.

OIR (by mass)	OIR (by moles)	initial concentration (M)	matched RI concentration (M)	final concentration (M)	LLPS start concentration (M)	complete core-shell concentration (M)	partial engulfment concentration (M)
0.1	0.083	0.819	-	7.63	3.02	-	-
0.2	0.165	0.882	-	5.98	3.74	-	-
0.5	0.413	0.535	-	6.14	3.60	-	5.25
1	0.825	0.345	-	5.86	2.92	3.36	4.25
2	1.650	0.301	-	5.15	3.73	4.71	-
5	4.125	0.233	4.09	5.70	4.65	5.22	-
10	8.250	0.210	3.13	4.30	3.24	-	-
-	-	0.187	-	4.06	-	-	-

Table 6. 3. Concentrations of aqueous ternary ammonium sulfate and 3-methyl adipic acid solution. Channel height: 95 μm. error in final concentration is calculated by ±2 μm channel height sensitivity analysis, and found to be 1.70% average. Initial droplet volume range: 1.9 – 5.8 nl. The last row has data for binary organic acid solution, which never crystallized and was still in a liquid state for which the volume remained constant last few hours.

The images for all the ternary solution experiments (**Figure 6. 6** – **Figure 6. 13**) are brightfield, except for the one in **Figure 6. 10**b. Because **Figure 6. 10** represents similar coating behavior, both brightfield and phase contrast microscopy techniques are used to verify the behavior. In addition, phase contrast microscopy is used for binary salt solution in **Figure 6. 3** to exemplify the droplet image at matched RI concentration (**Figure 6. 3**b (ii)). It is done because the optics of the phase contrast microscopy technique increases droplets' color contrast with the surrounding medium, making it possible to visualize certain images that are otherwise invisible.

The concentration of the solutions at which LLPS occurs is seen to be consistent for both the acid systems, and is slightly higher than the matched RI concentration. It implies that separation occurs typically at supersaturated concentrations. It is seen that the concentrations at which the ternary solution droplets effloresce (reported as the final concentration in the tables) have lower values than binary AS solution regardless of the amount of acid added (Tables 6.1 – 6.3). The final concentrations are plotted in **Figure 6. 14** with increasing OIR for both the organic acids. In **Figure 6. 14**, the black line is the average final concentration for binary ammonium sulfate solution. As the organic acid is added to the salt solution, the final concentrations decrease. With increasing OIR, the final concentrations have a decreasing trend, which means that the water activities will have an increasing trend with increasing amount of the organic acid added in the salt solution. Therefore, it can be concluded that the ERH increases with increasing addition of acid to the salt. However, in **Figure 6. 14**a (for 3MGA) two outliers are seen. With OIR 10:1, the outlier might be because there was no LLPS. Furthermore, the difference in the phase transition behavior of the two acids might be because of the difference in their solubilities

in water, i.e. elemental oxygen-to-carbon ratio (O/C). A brief study on the O/C dependence is in Appendix C.

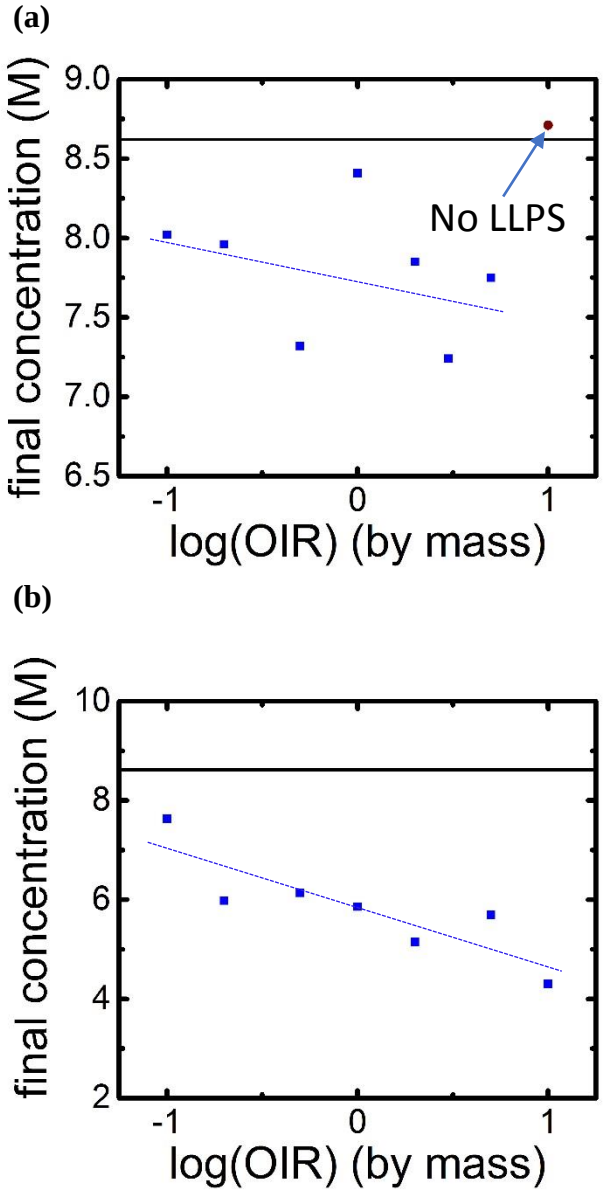

Figure 6. 14. Change in final concentration with OIR (logarithmic scale). (a) 3-methyl glutaric acid. (b) 3-methyl adipic acid. OIR is organic-to-inorganic ratio by dry mass. Symbols: blue square, final concentrations with LLPS; brown circle, final concentration with no LLPS. Lines: black solid, average final concentration of ammonium sulfate (averaged values from **Table 6. 1**). The dotted blue line is the trendline.

6.4 Conclusions and Atmospheric Implications

Microfluidic devices are developed for trapping of atmospheric aerosol chemical mimics that contain varied ratios of different organic acids and ammonium sulfate. Microfluidics is a cost-effective technique that has applications in lab-on-a-chip and medical studies, and here the method has a different use in atmospheric chemistry applications. The phase transition of the droplets with changing concentrations is observed by imaging techniques. The results report supersaturated concentrations with respect to their phase states, i.e. when the refractive index (RI) matches with that of the continuous phase oil, when the liquid phases separate in mixed organic/inorganic solutions, and lastly when the trapped droplet effloresces. The spontaneous uniform phase change observed in the microfluidic wells for both LLPS and crystallization in most systems is in contrast to the observed phase change upon dehydration for droplets on the glass slide directly exposed to air (referring to the series of images in Appendix C), in which the small inclusions start forming unevenly around the edges, near the solid-liquid-gas contact point. It suggests the difference in crystallization starting in the bulk and at the surface.[67,231]

The dicarboxylic acids studied here are known to be in abundance in the atmosphere and the mixing state of such aerosol particles are important to study that affects their physicochemical properties. The water content, phase state and internal heterogeneity of aerosol particles are investigated here, as they influence various atmospheric processes like gas-aerosol partitioning of organic compounds in the atmosphere and may have consequences on optical properties, heterogeneous chemistry and cloud condensation nuclei. In addition, the effect of adding increasing amount of organic species to ammonium sulfate solution on its efflorescence point is reported here. It is worth noting that while the

diameter of the droplets in our study is quite large, the characteristic length scale for the pervaporation process is actually the height, which is significantly smaller than the diameter for the bulk of the work shown here. It is because the droplets are confined between the top and bottom walls of the microfluidic well, as in a Hele-Shaw type geometry. However, the droplet size dependence on the crystallization of ternary solutions may be important, as previous studies of ERH of mixtures of ammonium sulfate and organic compounds have shown to be size-dependent for a particular mass fraction of the organic compound in the mixture.[76] In the current study, the droplets varied in size from 200 to 350 μm, over a wide range of mass fractions of the organic compound in the mixture. In future studies, the device height as well as the diameter of the well can be varied to further explore size-effects on the phase state. Further work is also required to accurately predict the efflorescence relative humidity of a ternary mixture that has atmospheric implications like radiative forcing, cloud activation and atmospheric chemical reactions. More complex atmospheric mixtures, like the secondary organic materials (SOM) can also be studied as they affect the efflorescence point of the sulfate component.[232–234]

Associated Content

Additional information is provided in Appendix C - Images of evaporation of 3-methyl adipic acid - ammonium sulfate ternary aqueous solution droplet with OIR 2:1 on a glass-slide; Description of calculations of the densities, molalities, and relative humidities; Study on O/C ratio.

Chapter 7

Using Microfluidic Wells with Collected Aerosol Samples

7.1 Motivation for Secondary Organic Aerosol and Sea Spray Aerosol Studies.

Secondary organic particles are formed when the oxidation products from the volatile organic compounds (VOCs) undergo gas-to-particle conversion process.[235] Isoprene-epoxydiol (IEPOX) - derived secondary organic aerosol (SOA) by multiphase chemistry has been found in the atmosphere in substantial amounts, leading to heterogeneous chemistry and absorbance of tropospheric ultraviolet and visible solar radiation.[236,237] The Southern Oxidant and Aerosol Study (SOAS) also suggests that particle-phase sulfate plays a major role in the formation of isoprene SOA.[236] Isoprene-derived epoxides on hydrolysis yield the products 2-methyl glyceric acid and 2-methyl tetrol (2MG and 2MT) that contribute to the ambient SOA.[238] Ozonolysis of isoprene in the presence of acidified sulfate seed aerosol yields organosulfates.[239] Measurements by a

filter inlet for gas and aerosol (FIGAERO) coupled to a mass spectrometer suggests that SOA comprises of low-volatility isoprene derived compounds and organosulfates (OS).[240] The partitioning of organic molecules between gas and particle phases can be affected by liquid-liquid phase separation (core-shell, core-shell with inclusions or partially engulfed).[40,65] Biogenic SOA produced from isoprene has been studied to understand its water uptake and phase state dependency on RH.[241] Phase miscibility studies suggest that the hygroscopic properties of mixed ammonium sulfate and SOA particles, and the phase transitions of ammonium sulfate are affected by the organic composition.[233] The study also concludes that liquid-liquid phase separation occurs for aqueous ammonium sulfate and terpene-derived SOA, and the partitioning for aqueous ammonium sulfate and isoprene-derived SOA occurs into a homogeneous phase. Studies with SOA produced by the ozonolysis of α-pinene free of inorganic salts reveal that liquid-liquid phase separation occurs at high RH that can potentially affect cloud condensation nuclei (CCN) activity of SOA particles.[242]

In addition to SOA, sea spray aerosol (SSA) are a major fraction of atmospheric aerosols,[24,243] with uncertainty in its abundance.[244] SSA is formed by bursting of generated bubbles by waves on the sea surface. The aqueous phase chemistry occurring in the bulk of deliquesced sea salt particles containing sodium chloride, magnesium chloride, sodium bromide, organic components, etc. may be understood by studying the water uptake and loss. Laboratory studies to investigate morphological changes have been done, that show that the sea salt particles undergo liquid-liquid phase separation (LLPS) at low RH.[245] Hygroscopic properties for sodium chloride-dicarboxylic acids have been measured using a hygroscopicity tandem differential mobility analyzer (HTDMA) system to study organic

matters in SSA, showing hygroscopic dependency on the type of organic acid.[155] The sea surface microlayer (SML) having physicochemical properties distinct from the bulk sea water[246] has also been known to significantly contribute to sea spray aerosol aqueous phase chemistry. Most of the organic matter present in the SSA is from the SML.[247]

Due to the chemically and physically complex nature of these aerosols, the phase behavior of SOA samples from Professor Jason D. Surratt's laboratory at the University of North Carolina, and SML samples from Professor Kimberly A. Prather's laboratory at the University of California, San Diego, are studied using microfluidic wells. The preliminary findings are presented here.

7.2 Preliminary Findings of SOA Samples.[5]

Dehydration experiments with 2-methyl glyceric acid (2MG) and 2-methyl tetrol (2MT), and their organosulfates (2MG OS and 2MT OS) added to ammonium sulfate were performed in microfluidic traps to study the phase transitions in these organic-salt solutions. The experiments were performed using silicone oil as the continuous phase; the dispersed phase aqueous solutions were the SOAs extracted and dissolved in methanol by the Surratt group. Solutions for the experiments were prepared by adding the SOAs to different concentrations of ammonium sulfate (AS, Avantor Performance Materials, CAS 7783−20−2) solutions prepared in HPLC-grade water (Sigma-Aldrich, CAS 7732−18−8). The experiments were performed under laboratory conditions (35-37% RH, 23^{o}C). Since the SOA standards are prepared in methanol, first only methanol and water (50% methanol

[5] SOA samples collected by Prof. Jason Surratt's group.

and 50% water by volume) solution is used for the trap experiment to observe the rate of evaporation. The volume reduced for approximately 9 hours after which the droplet volume remained constant. The final droplet of the solution remained is pure methanol, assuming all the water has evaporated. Secondly, AS solution prepared with 50% water and 50% methanol by volume was used. The elemental oxygen to carbon ratio (O:C) of methanol is 1, and very few inclusions were seen when a dilute AS solution of 0.01 molar was added to it. No LLPS was observed with a higher concentration of 1 molar AS solution. And lastly, SOA and AS solutions were prepared by dissolving in varied percentage volumes of water and methanol by volume for the microfluidic trap experiments.

Liquid-liquid phase separation was observed only in the dehydration experiment with ternary solution AS-2MT OS with a partially engulfed morphology (**Figure 7. 1**). The remaining solution droplets were homogeneous throughout and showed a spontaneous transition of the liquid to a solid phase; an example of 2MG OS experiment is shown in **Figure 7. 2**. The initial concentrations, OIRs and efflorescence concentrations of each solution experiment are reported in **Table 7. 1**. The O:C of 2MG is 1, 2MG OS is 1.75, 2MT is 0.8 and 2MT OS is 1.4. With such high O:C ratios, LLPS is not expected.[68] Methanol might be playing a role in LLPS in AS-2MT OS solution. In addition, the final concentrations for the ternary AS-SOA solutions with organic to inorganic ratio (OIR) (by dry mass) 1 are reported in **Table 7. 2**, and it is observed that for 2MT OS experiment, the final concentration is much lower than the other systems.

Figure 7. 1. Phase transitions observed in AS – 2MT OS ternary aqueous solution; phase contrast images of the solution droplet with OIR 1:4. LLPS time span (from ii to v): ~2 hours. Scale bar: 50 μm.

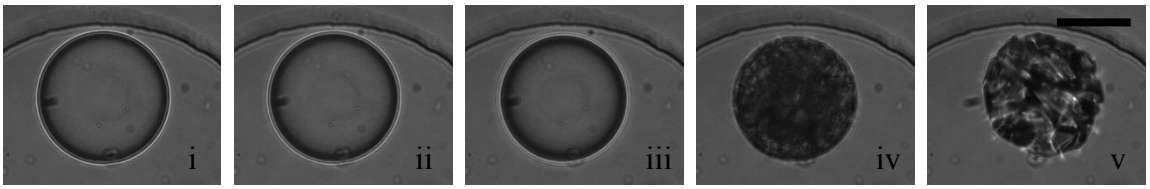

Figure 7. 2. Phase transitions observed in AS – 2MG OS ternary aqueous solution; phase contrast images of the solution droplet with OIR 1:4. Evaporation time span (from i to v): ~10 hours. Scale bar: 50 μm.

solution	OIR (by mass)	OIR (by moles)	initial concentration (M)	final concentration (M)	% MeOH
AS + MeOH	0	0	0.01	3.32	50
AS + MeOH	0	0	1.00	4.97	25
AS + 2MG	1	1.1011	0.40	3.11	50
AS + 2MG	0.2499	0.2752	0.14	4.18	33.33
AS + 2MT	1	0.9716	0.37	3.05	50
AS + 2MT	0.2499	0.2428	0.63	5.56	33.33
AS + 2MG OS	0.2525	0.1813	0.01	5.16	25
AS + 2MG OS	0.0244	0.0175	0.79	6.38	25
AS + 2MT OS	1	0.6117	0.03	1.80	50
AS + 2MT OS	0.25	0.1529	0.09	5.15	50

Table 7. 1. Concentrations of aqueous ternary ammonium sulfate and secondary organic aerosol standards. OIR is organic-to-inorganic ratio by dry mass; final concentration is the concentration at which the solution droplet crystallizes; M is moles/liter.

SOA+AS solution	component	final concentration (M)
OIR 0 and 0% MeOH	AS	8.6
OIR 0 and 50% MeOH	AS	3.32
OIR 1 and 50% MeOH	2MG:AS	3.11
OIR 1 and 50% MeOH	2MG OS:AS	3.16
OIR 1 and 50% MeOH	2MT:AS	3.05
OIR 1 and 50% MeOH	2MT OS:AS	1.8

Table 7. 2. Final concentrations of aqueous ternary ammonium sulfate and secondary organic aerosol standards with OIR 1 (by dry mass) and 50% methanol (by volume). MeOH is methanol.

7.3 Preliminary Findings of SSA Samples.[6]

Microfluidic trap evaporation experiments were done with binary sodium chloride (NaCl) solution, a major component of sea water, ternary NaCl and 3-methyl glutaric acid (3MGA) solution, synthetic sea water (SSW, Ricca Chemical company, R8363000, ASTM D 1141 Substitute Ocean Water without Heavy Metals) and SSW mixed with 3MGA solution. Finally, experiments with sea spray aerosol surface microlayer (SSA SML) sample from the Prather group, with and without 3MGA were performed in microfluidic traps[7] to study the phase transitions in these organic-inorganic solutions. The experiments were performed using silicone oil as the continuous phase, and the solutions as the dispersed phase. The experiments were performed under laboratory conditions (22-25% RH, 23^{o}C).

The efflorescence point of NaCl has previously been measured to be 44%.[248,249] For the binary NaCl experiments done here, the crystallized droplet is non-spherical (**Figure 7. 3**-xiv); hence it is difficult to calculate the volume using image analysis techniques used in previous chapter.[88] Therefore, the efflorescence relative humidity is not reported here, although the study has the potential to determine the concentrations and relative humidities at various phase states. The solid structure of the NaCl crystal is cubic in nature as seen in **Figure 7. 3**, and the crystallization starts at the surface of the droplet as seen in **Figure 7. 3**-ii.

[6] SSA samples collected by Prof. Kim Prather's group.

[7] Microfluidic trap devices sent by Prof. Siva Vanapalli's laboratory (Texas Tech University).

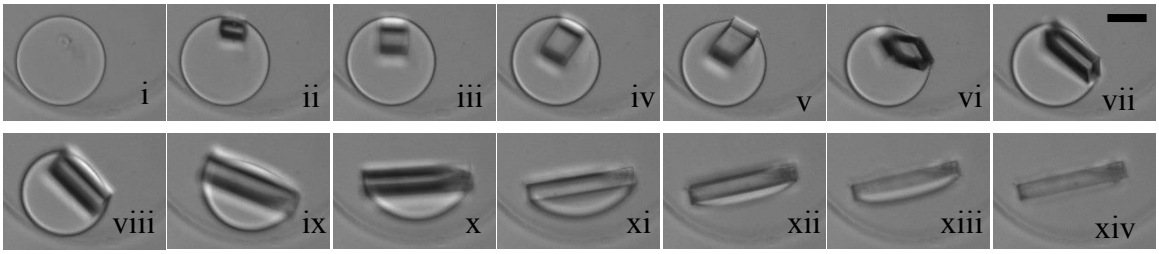

Figure 7. 3. Phase transitions observed in binary NaCl aqueous solution (50 mg/mL); brightfield images of the solution droplet. Crystallization time span (from ii to xiv): ~3 hours. Scale bar: 50 μm.

For the next experiment, an organic acid, 3MGA was added to study if there was liquid-liquid phase separation. No phase separation was observed as shown in **Figure 7. 4**, and a NaCl crystal was formed at the surface which gradually grew within a liquid coating, presumably organic acid, eventually evaporating completely.

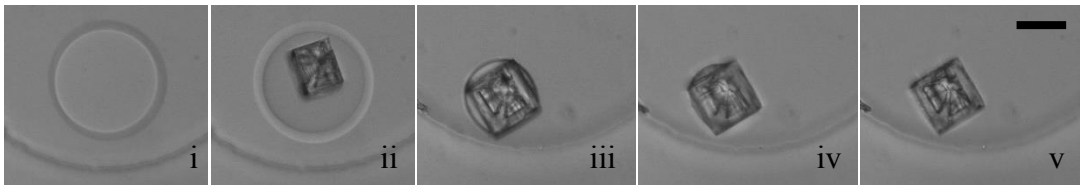

Figure 7. 4. Phase transitions observed in ternary NaCl – 3MGA aqueous solution (OIR 1; by dry mass); brightfield images of the solution droplet. Crystallization time span (from i to v): ~21 hours. Scale bar: 50 μm.

For the next set of experiments, the SSW was used as it is for one experiment (**Figure 7. 5**a), and then 3MGA was added for another experiment (**Figure 7. 5**b). The organic acid and sea water experiment showed an interesting behavior with LLPS occurring twice (**Figure 7. 5**c-ii,vi).

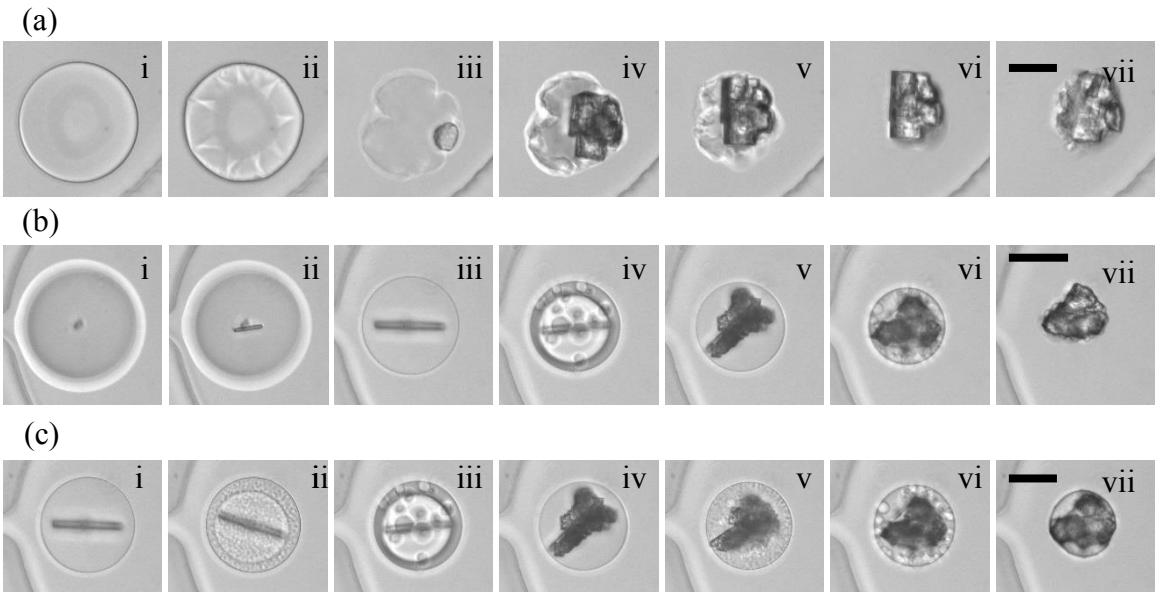

Figure 7. 5. Phase transitions observed in (a) SSW. Time span (from i to vii): ~6 hours. (b) SSW – 3MGA aqueous solution (50% by volume sea water and 50% by volume 50 mg/mL 3MGA). (c). LLPS in SSW – 3MGA aqueous solution (same experiment as in (b)); brightfield images of the solution droplet. LLPS time span (from ii to vi): ~5 hours. Scale bar: 50 μm.

Finally, the SSA SML sample from the Prather group was used for experiments to study phase behavior, as the surface microlayer is known to contain organic matter. For the last experiment, 3MGA was added to the SML, and behavior similar to SSW-3MGA was observed (**Figure 7. 6**).

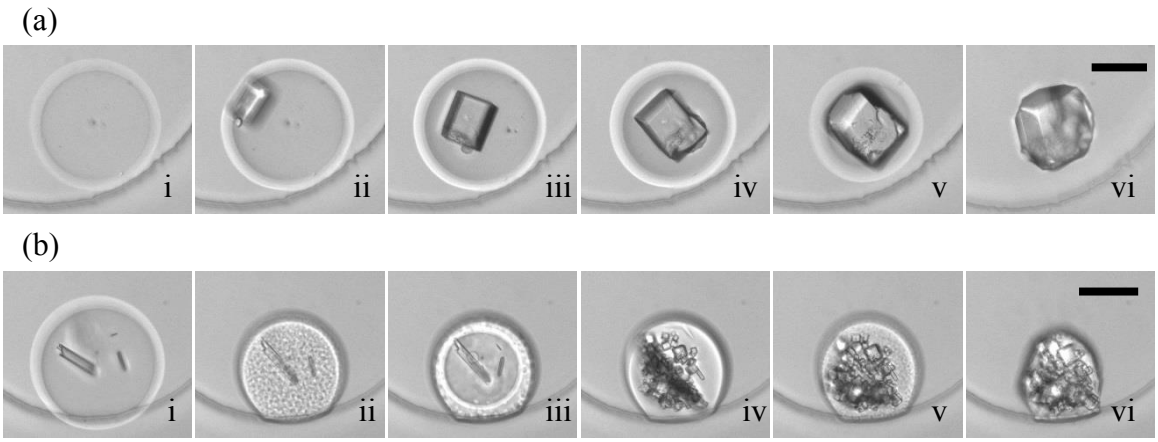

Figure 7. 6. Phase transitions observed in (a) SSA SML. Time span (from i to vi): ~100 minutes. (b) SSA SML – 3MGA aqueous solution (50% by volume SSA SML and 50% by volume 50 mg/mL 3MGA); brightfield images of the solution droplet. LLPS time span (from ii to vi): ~43 minutes. Scale bar: 50 μm.

7.4 Conclusions

Secondary organic aerosol and sea spray aerosol are found in abundance in the atmosphere, and studying the mixing state of such aerosol particles is vital for understanding the water uptake. The chapter provides preliminary results of different phase states of collected aerosol samples. To better understand the processes changing composition of aerosol in the atmosphere, microfluidic tools used here can be used to investigate systems of increasing complexity.

Chapter 8

Brief Remarks on Thesis Contributions and Future Research Directions

An adsorption isotherm model has been developed and parameterized in this dissertation to predict solute and solvent activities of both binary and ternary mixtures of organic-inorganic aqueous aerosol solutions over the entire concentration range. The aqueous solution property predictions are more accurate than existing thermodynamic models, especially at low relative humidities for a wide range of organic compounds that are both non-dissociating and partially dissociating, as well as totally dissociating inorganic compounds with arbitrary charged ions. The model is a faster, low cost computation method for better accuracy at supersaturated states. The predictions of thermodynamic

properties of aqueous aerosols is essential to better understand the relevance of organic-inorganic mixtures for atmospheric aerosols.

The key step in the model development is modification of the existing adsorption isotherm model to relate the model parameters to structure properties by a Coulombic model. The multilayer adsorption model is significant because it is accurate for highly concentrated aqueous solutions, both electrolyte solutions and organic solutions. Another important step is to significantly reduce the number of model parameters, even for ternary solutions with mixed charge type. Additionally, the partial dissociation of weak organic acids and the bisulfate ion in aqueous sulfuric acid is explicitly treated using the model.

The multilayer adsorption isotherm model is applied towards pH calculation of acidic particles in the atmosphere in a collaborative work with the Ault group. In addition, the model has been used to corroborate the findings from their pH paper-based measurements. The pH study is important as atmospheric multiphase chemical processes, such as formation of secondary organic aerosol and haze depend on the acidity of aerosol particles, and therefore improved pH predictions of thermodynamic models is required. The model is further used to interpret the hygroscopicity measurements of single particles performed by the Reid group. The hygroscopic properties have a direct impact on air quality and the radiative balance of the Earth's atmosphere through changing chemical composition by heterogeneous chemistry. Therefore, improved prediction of hygroscopicity is desired for better understanding of aerosol effect on the atmosphere as well as human health.

Moreover, the importance of temperature dependence on aerosol processes is discussed, and the temperature-dependent adsorption model may be used to predict solute and solvent activities in cold tropospheric conditions. Further, the goal of this dissertation to study and understand the role of organic compounds and their interactions with inorganic species is addressed. Microfluidic measurements provide a better understanding of aerosol phase states at atmospherically relevant relative humidity conditions, in addition to complementing the adsorption model predictions. Additionally, the water activity predictions at thermodynamically metastable states is a key outcome of the experiments and the model, that describes the hysteresis between deliquescence and efflorescence relative humidities in both binary and ternary aqueous solutions. The liquid-liquid phase separation studies provide a perspective to comprehend the influence on cloud formation.

Finally, the model and microfluidic measurement methods are applicable to various other research areas, such as determining thermodynamic properties of aqueous solutions in the fields of waste water treatment and industrial discharge, liquid-liquid phase separation in oil industry and pharmaceutical industry, and crystallization in the field of industrial process engineering.

Regarding next steps, the multilayer adsorption isotherm model in this dissertation is parameterized at room temperature at thermodynamic equilibrium; the temperature-dependent model developed in Chapter 5 may be further parameterized with additional thermodynamic data for complex mixture aqueous solutions with mixed charge. The model may also be extended to implement density predictions in complex mixtures for determining the efflorescence relative humidity. Besides, the model development and result predictions obtained in this dissertation have the potential to extend the study to

predict phases and phase separation in atmospheric aerosol particles that affect gas/particle partitioning.

Lastly, preliminary microfluidic experiments have been done to study phase behavior in secondary organic aerosols and sea spray aerosols, the motivation and preliminary results of which are presented in Chapter 7. The microfluidic platform provides a consistent tool for thermodynamic property measurements that complements the adsorption isotherm model to study phase states and morphology at atmospheric conditions. Further, the microfluidic platform has the potential to study the internal heterogeneity of aerosol particles.

Bibliography

(1) Intergovernmental Panel on Climate Change. *Climate Change 2014: Synthesis Report*; 2014.

(2) Bond, T. C.; Doherty, S. J.; Fahey, D. W.; Forster, P. M.; Berntsen, T.; Deangelo, B. J.; Flanner, M. G.; Ghan, S.; Kärcher, B.; Koch, D.; et al. Bounding the Role of Black Carbon in the Climate System: A Scientific Assessment. *J. Geophys. Res. Atmos.* **2013**, *118* (11), 5380–5552.

(3) Fiore, A. M.; Naik, V.; Leibensperger, E. M. Air Quality and Climate Connections. *J. Air Waste Manage. Assoc.* **2015**, *65* (6), 645–685.

(4) Hegg, D. A.; Baker, M. B. Nucleation in the Atmosphere. *Reports Prog. Phys.* **2009**, *72* (5).

(5) Weber, R. J.; Marti, J. J.; McMurry, P. H.; Eisele, F. L.; Tanner, D. J.; Jefferson, A. Measurements of New Particle Formation and Ultrafine Particle Growth Rates at a Clean Continental Site. *J. Geophys. Res. Atmos.* **1997**, *102*, 4375–4385.

(6) Marti, J. J.; Weber, R. J.; McMurry, P. H.; Eisele, F.; Tanner, D.; Jefferson, A. New Particle Formation at a Remote Continental Site: Assessing the Contributions of SO_2 and Organic Precursors. *J. Geophys. Res. Atmos.* **1997**, *102* (D5), 6331–6339.

(7) Kulmala, M.; Kerminen, V.-M.; Anttila, T.; Laaksonen, A.; O'Dowd, C. D. Organic Aerosol Formation via Sulphate Cluster Activation. *J. Geophys. Res. Atmos.* **2004**, *109* (D4), D04205-1-7.

(8) Mian Chin; Diehl, T.; Ginoux, P.; Malm, W. Intercontinental Transport of Pollution and Dust Aerosols: Implications for Regional Air Quality. *Atmos. Chem. Phys. Discuss.* **2007**, *7*, 9013–9051.

(9) Pöschl, U. Atmospheric Aerosols: Composition, Transformation, Climate and Health Effects. *Angew. Chemie - Int. Ed.* **2005**, *44* (46), 7520–7540.

(10) Flores, J. M.; Bar-Or, R. Z.; Bluvshtein, N.; Abo-Riziq, A.; Kostinski, A.; Borrmann, S.; Koren, I.; Koren, I.; Rudich, Y. Absorbing Aerosols at High Relative Humidity: Linking Hygroscopic Growth to Optical Properties. *Atmos. Chem. Phys.* **2012**, *12* (12), 5511–5521.

(11) Hyslop, N. P. Impaired Visibility: The Air Pollution People See. *Atmos. Environ.* **2009**, *43* (1), 182–195.

(12) Rosenfeld, D. Aerosols, Clouds, and Climate. *Science.* **2006**, *312*, 1323–1324.

(13) Kulmala, M.; Kerminen, V. M.; Anttila, T.; Laaksonen, A.; O'Dowd, C. D. Organic Aerosol Formation via Sulphate Cluster Activation. *J. Geophys. Res. Atmos.* **2004**,

109 (D4), D04205-1-7.

(14) Gilman, J. B.; Tervahattu, H.; Vaida, V. Interfacial Properties of Mixed Films of Long-Chain Organics at the Air-Water Interface. *Atmos. Environ.* **2006**, *40* (34), 6606–6614.

(15) Erdakos, G. B.; Pankow, J. F. Gas/particle Partitioning of Neutral and Ionizing Compounds to Single- and Multi-Phase Aerosol Particles. 2. Phase Separation in Liquid Particulate Matter Containing Both Polar and Low-Polarity Organic Compounds. *Atmos. Environ.* **2004**, *38* (7), 1005–1013.

(16) Chang, E. I.; Pankow, J. F. Prediction of Activity Coefficients in Liquid Aerosol Particles Containing Organic Compounds, Dissolved Inorganic Salts, and Water-Part 2: Consideration of Phase Separation Effects by an X-UNIFAC Model. *Atmos. Environ.* **2006**, *40* (33), 6422–6436.

(17) Ming, Y.; Russell, L. M. Thermodynamic Equilibrium of Organic-Electrolyte Mixtures in Aerosol Particles. *AIChE J.* **2002**, *48* (6), 1331–1348.

(18) McGraw, R.; Lewis, E. R. Deliquescence and Efflorescence of Small Particles. *J. Chem. Phys.* **2009**, *131* (19).

(19) Gao, Y.; Chen, S. B.; Yu, L. E. Efflorescence Relative Humidity for Ammonium Sulfate Particles. *J. Phys. Chem. A* **2006**, *110* (24), 7602–7608.

(20) Pant, A.; Parsons, M. T.; Bertram, A. K. Crystallization of Aqueous Ammonium Sulfate Particles Internally Mixed with Soot and Kaolinite: Crystallization Relative Humidities and Nucleation Rates. *J. Phys. Chem. A* **2006**, *110* (28), 8701–8709.

(21) Schlenker, J. C.; Malinowski, A.; Martin, S. T.; Hung, H. M.; Rudich, Y. Crystals Formed at 293 K by Aqueous Sulfate-Nitrate-Ammonium-Proton Aerosol Particles. *J. Phys. Chem. A* **2004**, *108* (43), 9375–9383.

(22) Marcolli, C.; Krieger, U. K. Phase Changes during Hygroscopic Cycles of Mixed Organic/inorganic Model Systems of Tropospheric Aerosols. *J. Phys. Chem. A* **2006**, *110* (5), 1881–1893.

(23) Song, M.; Liu, P.; Martin, S. T.; Bertram, A. K. Liquid-Liquid Phase Separation in Particles Containing Secondary Organic Material Free of Inorganic Salts. *Atmos. Chem. Phys.* **2017**, *17* (18), 11261–11271.

(24) Seinfeld, J. H.; Pandis, S. N. *Atmospheric Chemistry and Physics, from Air Pollution to Climate Change*; John Wiley, New York, 1998.

(25) Noble, C. A.; Prather, K. A. Real-Time Measurement of Correlated Size and Composition Profiles of Individual Atmospheric Aerosol Particles. *Environ. Sci. Technol.* **1996**, *30* (9), 2667–2680.

(26) Zhang, Q.; Jimenez, J. L.; Canagaratna, M. R.; Allan, J. D.; Coe, H.; Ulbrich, I.; Alfarra, M. R.; Takami, A.; Middlebrook, A. M.; Sun, Y. L.; et al. Ubiquity and

Dominance of Oxygenated Species in Organic Aerosols in Anthropogenically-Influenced Northern Hemisphere Midlatitudes. *Geophys. Res. Lett.* **2007**, *34* (13), 1–6.

(27) Saxena, P.; Hildemann, L. M. Water-Soluble Organics in Atmospheric Particles: A Critical Review of the Literature and Application of Thermodynamics to Identify Candidate Compounds. *J. Atmos. Chem.* **1996**, *24* (1), 57–109.

(28) Kawamura, K.; Ikushima, K. Seasonal Changes in the Distribution of Dicarboxylic Acids in the Urban Atmosphere. *Environ. Sci. Technol.* **1993**, *27* (10), 2227–2235.

(29) Richardson, C. B.; Spann, J. F. Measurement of the Water Cycle in a Levitated Ammonium Sulfate Particle. **1984**, *15* (5), 563–571.

(30) Song, M.; Marcolli, C.; Krieger, U. K.; Lienhard, D. M.; Peter, T. Morphologies of Mixed Organic/inorganic/aqueous Aerosol Droplets. *Faraday Discuss.* **2013**, *165*, 289.

(31) Brooks, S. D. Deliquescence Behavior of Organic/ammonium Sulfate Aerosol. *Geophys. Res. Lett.* **2002**, *29* (19), 2–5.

(32) Clegg, S. L.; Brimblecombe, P.; Wexler, A. S. Thermodynamic Model of the System H^+-NH_4^+-Na^+-SO_4^{2-}-NO_3^--Cl^--H_2O at 298.15 K. *J. Phys. Chem. A* **1998**, *102* (12), 2155–2171.

(33) Clegg, S. L.; Seinfeld, J. H. Thermodynamic Models of Aqueous Solutions Containing Inorganic Electrolytes and Dicarboxylic Acids at 298.15 K . 1 . The Acids as Nondissociating Components. *J. Phys. Chem. A* **2006**, *110*, 5692–5717.

(34) Clegg, S. L.; Seinfeld, J. H. Thermodynamic Models of Aqueous Solutions Containing Inorganic Electrolytes and Dicarboxylic Acids at 298.15 K . 2 . Systems Including Dissociation Equilibria. *J. Phys. Chem. A* **2006**, *110*, 5718–5734.

(35) Wexler, A. S.; Seinfeld, J. H. Second-Generation Inorganic Aerosol Model. *Atmos. Environ. Part A, Gen. Top.* **1991**, *25* (12), 2731–2748.

(36) Clegg, S. L.; Simonson, J. M. A BET Model of the Thermodynamics of Aqueous Multicomponent Solutions at Extreme Concentration. *J. Chem. Thermodyn.* **2001**, *33* (11), 1457–1472.

(37) Clegg, S. L.; Seinfeld, J. H.; Brimblecombe, P. Thermodynamic Modelling of Aqueous Aerosols Containing Electrolytes and Dissolved Organic Compounds. *J. Aerosol Sci.* **2001**, *32*, 713–738.

(38) Bertram, A. K.; Martin, S. T.; Hanna, S. J.; Smith, M. L.; Bodsworth, A.; Chen, Q.; Kuwata, M.; Liu, A.; You, Y.; Zorn, S. R. Predicting the Relative Humidities of Liquid-Liquid Phase Separation, Efflorescence, and Deliquescence of Mixed Particles of Ammonium Sulfate, Organic Material, and Water Using the Organic-to-Sulfate Mass Ratio of the Particle and the Oxygen-to-Carbon Ele. *Atmos. Chem. Phys.* **2011**, *11* (21), 10995–11006.

(39) O'Brien, R. E.; Wang, B.; Kelly, S. T.; Lundt, N.; You, Y.; Bertram, A. K.; Leone, S. R.; Laskin, A.; Gilles, M. K. Liquid–Liquid Phase Separation in Aerosol Particles: Imaging at the Nanometer Scale. *Environ. Sci. Technol.* **2015**, *49* (8), 4995–5002.

(40) You, Y.; Renbaum-Wolff, L.; Carreras-Sospedra, M.; Hanna, S. J.; Hiranuma, N.; Kamal, S.; Smith, M. L.; Zhang, X.; Weber, R. J.; Shilling, J. E.; et al. Images Reveal That Atmospheric Particles Can Undergo Liquid-Liquid Phase Separations. *Proc. Natl. Acad. Sci.* **2012**, *109* (33), 13188–13193.

(41) Zuend, A.; Marcolli, C.; Peter, T.; Seinfeld, J. H. Computation of Liquid-Liquid Equilibria and Phase Stabilities: Implications for RH-Dependent Gas/particle Partitioning of Organic-Inorganic Aerosols. *Atmos. Chem. Phys.* **2010**, *10* (16), 7795–7820.

(42) Cruz, C. N.; Pandis, S. N. A Study of the Ability of Pure Secondary Organic Aerosol to Act as Cloud Condensation Nuclei. *Atmos. Environ.* **1997**, *31* (15), 2205–2214.

(43) Rui, D.; Ariya, P. A. The Test Freezing Temperature of C_2-C_6 Dicarboxylic Acid: The Important Indicator for Ice Nucleation Processes. *Chinese Sci. Bull.* **2008**, *53* (17), 2685–2691.

(44) Yao, X.; Lau, A. P. S.; Fang, M.; Chan, C. K.; Hu, M. Size Distributions and Formation of Ionic Species in Atmospheric Particulate Pollutants in Beijing, China: 2 - Dicarboxylic Acids. *Atmos. Environ.* **2003**, *37* (21), 3001–3007.

(45) Kawamura, K.; Kasukabe, H.; Barrie, L. A. Source and Reaction Pathways of Dicarboxylic Acids, Ketoacids and Dicarbonyls in Arctic Aerosols: One Year of Observations. *Atmos. Environ.* **1996**, *30*, 1709–1722.

(46) Kawamura, K.; Richard, S.; Imai, Y. Water Soluble Dicarboxylic Acids and Related Compounds in Antarctic Aerosols. *J. Geophys. Res.* **1996**, *101*, 18721–18728.

(47) Loflund, M.; Kasper-Giebl, A.; Schuster, B.; Giebl, H.; Hitzenberger, R.; Puxbaum, H. Concentrations and Their Contribution to Organic Carbon in Cloud Water. *Atmos. Environ.* **2002**, *36*, 1553–1558.

(48) Soonsin, V.; Zardini, A. A.; Marcolli, C.; Zuend, A.; Krieger, U. K. The Vapor Pressures and Activities of Dicarboxylic Acids Reconsidered : The Impact of the Physical State of the Aerosol. *Atmos. Chem. Phys.* **2010**, *10*, 11753–11767.

(49) Peng, C.; Chan, M. N.; Chan, C. K. The Hygroscopic Properties of Dicarboxylic and Multifunctional Acids : Measurements and UNIFAC Predictions. *Environ. Sci. Technol.* **2001**, *35*, 4495–4501.

(50) Beyer, K. D.; Michael, R.; Reusch, B. Phase Diagrams and Water Activities of Aqueous Ammonium Salts of Malonic Acid. *J. Phys. Chem. A* **2011**, *115*, 3042–3049.

(51) Beyer, K. D.; Schroeder, J. R.; Pearson, C. S. Solid / Liquid Phase Diagram of the Ammonium Sulfate / Maleic Acid / Water System. *J. Phys. Chem. A* **2011**, *115*,

13842–13851.

(52) Beyer, K. D.; Pearson, C. S.; Henningfield, D. S. Solid/Liquid Phase Diagram of the Ammonium Sulfate/Glutaric Acid/ Water System. *J. Phys. Chem. A* **2013**, *117*, 3630–3641.

(53) Beyer, K. D.; Schroeder, J. R.; Kissinger, J. A. Temperature-Dependent Deliquescence Relative Humidities and Water Activities Using Humidity Controlled Thermogravimetric Analysis with Application to Malonic Acid. *J. Phys. Chem. A* **2014**, *118*, 2488–2497.

(54) Pearson, C. S.; Beyer, K. D. Solid/Liquid Phase Diagram of the Ammonium Sulfate/Succinic Acid/Water System. *J. Phys. Chem. A* **2015**, *119*, 4317–4328.

(55) Bilde, M.; Barsanti, K.; Booth, M.; Cappa, C. D.; Donahue, N. M.; Emanuelsson, E. U.; McFiggans, G.; Krieger, U. K.; Marcolli, C.; Topping, D.; et al. Saturation Vapor Pressures and Transition Enthalpies of Low-Volatility Organic Molecules of Atmospheric Relevance: From Dicarboxylic Acids to Complex Mixtures. *Chem. Rev.* **2015**, *115*, 4115–4156.

(56) Fredenslund, A.; Jones, R. L.; Prausnitz, J. M. Group-Contribution Estimation of Activity Coefficients in Nonideal Liquid Mixtures. *AIChE J.* **1975**, *21* (6), 1086.

(57) McGlashan, M. L. Deviations from Raoult's Law. *J. Chem. Educ.* **1963**, *40* (10), 516–518.

(58) Dutcher, C. S.; Ge, X.; Wexler, A. S.; Clegg, S. L. Statistical Mechanics of Multilayer Sorption: Extension of the Brunauer–Emmett–Teller (BET) and Guggenheim–Anderson–de Boer (GAB) Adsorption Isotherms. *J. Phys. Chem. C* **2011**, *115* (33), 16474–16487.

(59) Dutcher, C. S.; Ge, X.; Wexler, A. S.; Clegg, S. L. Statistical Mechanics of Multilayer Sorption: 2. Systems Containing Multiple Solutes. *J. Phys. Chem. C* **2012**, *116*, 1850–1864.

(60) Petrucci, S. *Ionic Interactions; from Dilute Solutions to Fused Salts*; Academic Press: New York and London, 1971.

(61) Clegg, S. L.; Pitzer, K. S. Thermodynamics of Multicomponent, Miscible, Ionic Solutions: Generalized Equations for Symmetrical Electrolytes. *J. Phys. Chem.* **1992**, *96* (8), 3513–3520.

(62) Clegg, S. L.; Pitzer, K. S.; Brimblecombe, P. Thermodynamics of Multicomponent, Miscible, Ionic Solutions. 2. Mixtures Including Unsymmetrical Electrolytes. *J. Phys. Chem.* **1992**, *96* (23), 9470–9479.

(63) Dutcher, C. S.; Ge, X.; Wexler, A. S.; Clegg, S. L. An Isotherm-Based Thermodynamic Model of Multicomponent Aqueous Solutions, Applicable over the Entire Concentration Range. *J. Phys. Chem. A* **2013**, *117*, 3198–3213.

(64) Ohm, P. B.; Asato, C.; Wexler, A. S.; Dutcher, C. S. Isotherm-Based Thermodynamic Model for Electrolyte and Nonelectrolyte Solutions Incorporating Long- and Short-Range Electrostatic Interactions. *J. Phys. Chem. A* **2015**, *119* (13), 3244–3252.

(65) You, Y.; Smith, M. L.; Song, M.; Martin, S. T.; Bertram, A. K. Liquid–liquid Phase Separation in Atmospherically Relevant Particles Consisting of Organic Species and Inorganic Salts. *Int. Rev. Phys. Chem.* **2014**, *33* (1), 43–77.

(66) Parsons, M. T.; Knopf, D. A.; Bertram, A. K. Deliquescence and Crystallization of Ammonium Sulfate Particles Internally Mixed with Water-Soluble Organic Compounds. *J. Phys. Chem. A* **2004**, *108* (52), 11600–11608.

(67) Pant, A.; Fok, A.; Parsons, M. T.; Mak, J.; Bertram, A. K. Deliquescence and Crystallization of Ammonium Sulfate-Glutaric Acid and Sodium Chloride-Glutaric Acid Particles. *Geophys. Res. Lett.* **2004**, *31* (12), 31–34.

(68) Song, M.; Marcolli, C.; Krieger, U. K.; Zuend, A.; Peter, T. Liquid-Liquid Phase Separation and Morphology of Internally Mixed Dicarboxylic Acids/ammonium Sulfate/water Particles. *Atmos. Chem. Phys.* **2012**, *12* (5), 2691–2712.

(69) Wills, J. B.; Knox, K. J.; Reid, J. P. Optical Control and Characterisation of Aerosol. *Chem. Phys. Lett.* **2009**, *481* (4–6), 153–165.

(70) Walker, J.; Wills, J.; Reid, J. Direct Comparison of the Thermodynamic Properties of Sodium Chloride and Ammonium Sulphate Aerosol at Relative Humidities Approaching Saturation. *Geophys. Res. Abstr.* **2011**, *13* (48), 12691–12691.

(71) Mitchem, L.; Reid, J. P. Optical Manipulation and Characterisation of Aerosol Particles Using a Single-Beam Gradient Force Optical Trap. *Chem. Soc. Rev.* **2008**, *37* (4), 756.

(72) Stewart, D. J.; Cai, C.; Nayler, J.; Preston, T. C.; Reid, J. P.; Krieger, U. K.; Marcolli, C.; Zhang, Y. H. Liquid–Liquid Phase Separation in Mixed Organic/Inorganic Single Aqueous Aerosol Droplets. *J. Phys. Chem. A* **2015**, *119* (18), 4177–4190.

(73) Peng, C.; Chow, A. H. L.; Chan, C. K. Hygroscopic Study of Glucose , Citric Acid , and Sorbitol Using an Electrodynamic Balance : Comparison with UNIFAC Predictions Hygroscopic Study of Glucose , Citric Acid , and Sorbitol Using an Electrodynamic Balance : Comparison with UNIFAC Predictions. *Aerosol Sci. Technol.* **2001**, *35*, 753–758.

(74) Marsh, A.; Miles, R. E. H.; Rovelli, G.; Cowling, A. G.; Nandy, L.; Dutcher, C. S.; Reid, J. P. Influence of Organic Compound Functionality on Aerosol Hygroscopicity: Dicarboxylic Acids, Alkyl-Substituents, Sugars and Amino Acids. *Atmos. Chem. Phys.* **2017**, *17* (9), 5583–5599.

(75) Krieger, U. K.; Marcolli, C.; Reid, J. P. Exploring the Complexity of Aerosol Particle Properties and Processes Using Single Particle Techniques. *Chem. Soc. Rev.*

2012, *41* (19), 6631–6662.

(76) Parsons, M. T.; Riffell, J. L.; Bertram, A. K. Crystallization of Aqueous Inorganic-Malonic Acid Particles: Nucleation Rates, Dependence on Size, and Dependence on the Ammonium-to-Sulfate Ratio. *J. Phys. Chem. A* **2006**, *110* (26), 8108–8115.

(77) Colberg, C. A.; Krieger, U. K.; Peter, T. Morphological Investigations of Single Levitated $H_2SO_4/NH_3/H_2O$ Aerosol Particles during Deliquescence/Efflorescence Experiments. *J. Phys. Chem. A* **2004**, *108* (14), 2700–2709.

(78) Kawamura, K.; Yasui, O. Diurnal Changes in the Distribution of Dicarboxylic Acids, Ketocarboxylic Acids and Dicarbonyls in the Urban Tokyo Atmosphere. *Atmos. Environ.* **2005**, *39* (10), 1945–1960.

(79) Kawamura, K.; Tachibana, E.; Okuzawa, K.; Aggarwal, S. G.; Kanaya, Y.; Wang, Z. F. High Abundances of Water-Soluble Dicarboxylic Acids, Ketocarboxylic Acids and α-Dicarbonyls in the Mountaintop Aerosols over the North China Plain during Wheat Burning Season. *Atmos. Chem. Phys.* **2013**, *13* (16), 8285–8302.

(80) Guenther, A.; Karl, T.; Harley, P.; Wiedinmyer, C.; Palmer, P. I.; Geron, C. Estimates of Global Terrestrial Isoprene Emissions Using MEGAN (Model of Emissions of Gases and Aerosols from Nature). *Atmos. Chem. Phys.* **2006**, *6* (11), 3181–3210.

(81) Lane, T. E.; Pandis, S. N. From the Oxidation of Isoprene in the Eastern United States Predicted Secondary Organic Aerosol Concentrations from the Oxidation of Isoprene in the Eastern United States. *Environ. Sci. Technol.* **2007**, *41* (11), 3984–3990.

(82) Ervens, B.; Carlton, A. G.; Turpin, B. J.; Altieri, K. E.; Kreidenweis, S. M.; Feingold, G. Secondary Organic Aerosol Yields from Cloud-Processing of Isoprene Oxidation Products. *Geophys. Res. Lett.* **2008**, *35* (2), 4–8.

(83) Lin, Y.-H. Y.; Zhang, H.; Pye, H. H. O. T.; Zhang, Z.; Marth, W. J.; Park, S.; Arashiro, M.; Cui, T.; Budisulistiorini, S. H.; Sexton, K. G.; et al. Epoxide as a Precursor to Secondary Organic Aerosol Formation from Isoprene Photooxidation in the Presence of Nitrogen Oxides. *Proc. Natl. Acad. Sci.* **2013**, *110* (17), 6718–6723.

(84) Zhang, Z.; Lin, Y. H.; Zhang, H.; Surratt, J. D.; Ball, L. M.; Gold, A. Technical Note: Synthesis of Isoprene Atmospheric Oxidation Products: Isomeric Epoxydiols and the Rearrangement Products Cis-and Trans-3-Methyl-3,4-Dihydroxytetrahydrofuran. *Atmos. Chem. Phys.* **2012**, *12* (18), 8529–8535.

(85) Lin, Y. H.; Zhang, Z.; Docherty, K. S.; Zhang, H.; Budisulistiorini, S. H.; Rubitschun, C. L.; Shaw, S. L.; Knipping, E. M.; Edgerton, E. S.; Kleindienst, T. E.; et al. Isoprene Epoxydiols as Precursors to Secondary Organic Aerosol Formation: Acid-Catalyzed Reactive Uptake Studies with Authentic Compounds. *Environ. Sci. Technol.* **2012**, *46* (1), 250–258.

(86) Nandy, L.; Ohm, P. B.; Dutcher, C. S. Isotherm-Based Thermodynamic Models for Solute Activities of Organic Acids with Consideration of Partial Dissociation. *J. Phys. Chem. A* **2016**, *120* (24), 4147–4154.

(87) Nandy, L.; Dutcher, C. S. Isotherm-Based Thermodynamic Model for Solute Activities of Asymmetric Electrolyte Aqueous Solutions. *J. Phys. Chem. A* **2017**, *121* (37), 6957–6965.

(88) Nandy, L.; Dutcher, C. S. Phase Behavior of Ammonium Sulfate with Organic Acid Solutions in Aqueous Aerosol Mimics Using Micro Fl Uidic Traps. *J. Phys. Chem. B* **2018**, *122*, 3480–3490.

(89) Rindelaub, J. D.; Craig, R. L.; Nandy, L.; Bondy, A. L.; Dutcher, C. S.; Shepson, P. B.; Ault, A. P. Direct Measurement of pH in Individual Particles via Raman Microspectroscopy and Variation in Acidity with Relative Humidity. *J. Phys. Chem. A* **2016**, *120* (6), 911–917.

(90) Craig, R. L.; Nandy, L.; Axson, J. L.; Dutcher, C. S.; Ault, A. P. Spectroscopic Determination of Aerosol pH from Acid-Base Equilibria in Inorganic, Organic, and Mixed Systems. *J. Phys. Chem. A* **2017**, *121* (30), 5690−5699.

(91) Dickerson, R. E.; Gray, H. B.; Haight, G. P. *Chemical Principles*; Benjamin/Cummings Publishing Company, Inc.: California, 1979.

(92) Zuend, A.; Marcolli, C.; Luo, B. P.; Peter, T. A Thermodynamic Model of Mixed Organic-Inorganic Aerosols to Predict Activity Coefficients. *Atmos. Chem. Phys. Discuss.* **2008**, *8* (2), 6069–6151.

(93) Zuend, A.; Marcolli, C.; Booth, A. M.; Lienhard, D. M.; Soonsin, V.; Krieger, U. K.; Topping, D. O.; McFiggans, G.; Peter, T.; Seinfeld, J. H. New and Extended Parameterization of the Thermodynamic Model AIOMFAC: Calculation of Activity Coefficients for Organic-Inorganic Mixtures Containing Carboxyl, Hydroxyl, Carbonyl, Ether, Ester, Alkenyl, Alkyl, and Aromatic Functional Groups. *Atmos. Chem. Phys.* **2011**, *11* (17), 9155–9206.

(94) Chen, C.-C.; Britt, H. I.; Boston, J. F.; Evans, L. B. Local Composition Model for Excess Gibbs Energy of Electrolyte Systems. Part 1: Single Solvent, Single Completely Dissociated Electrolyte Systems. *AIChE J.* **1982**, *28* (4), 588–596.

(95) Pitzer, K. S.; Simonson, J. M. Thermodynamics of Multicomponent, Miscible, Ionic Systems: Theory and Equations. *J. Phys. Chem.* **1986**, *90* (13), 3005–3009.

(96) Hansen, R. S.; Miller, F. A.; Christian, S. D. Activity Coefficients of Components in the Systems Water-Acetic Acid, Water-Propionic Acid and Water-N-Butyric Acid at 25°. *J. Phys. Chem.* **1955**, *59* (5), 391–395.

(97) Pirouzi, A.; Nosrati, M.; Haghtalab, A.; Vasheghani-Farahani, E. Experiment and Correlation of Osmotic Coefficient for Aqueous Solution of Carboxylic Acids Using NRTL Nonrandom Factor Model. *Fluid Phase Equilib.* **2012**, *327*, 38–44.

(98) Sebastiani, E.; Lacquaniti, L. Acetic Acid—water System Thermodynamical Correlation of Vapor—liquid Equilibrium Data. *Chem. Eng. Sci.* **1967**, *22* (9), 1155–1162.

(99) Davies, M.; Thomas, D. K. Isopiestic Studies of Aqueous Dicarboxylic Acid Solutions. *J. Phys. Chem.* **1956**, *60* (1), 41–44.

(100) Maffia, M. C.; Meirelles, A. J. A. Water Activity and pH in Aqueous Polycarboxylic Acid Systems. *J. Chem. Eng. Data* **2001**, *46* (3), 582–587.

(101) Marcolli, C.; Luo, B.; Peter, T. Mixing of the Organic Aerosol Fractions: Liquids as the Thermodynamically Stable Phases. *J. Phys. Chem. A* **2004**, *108* (12), 2216–2224.

(102) Robinson, R. A.; Smith, P. K.; Smith, E. R. B. The Osmotic Coefficients of Some Organic Compounds in Relation to Their Chemical Constitution. *Trans. Faraday Soc.* **1942**, *38*, 63–70.

(103) Reilly, P. J.; Wood, R. H. Prediction of the Properties of Mixed Electrolytes from Measurements on Common Ion Mixtures. *J. Phys. Chem.* **1969**, *73* (12), 4292–4297.

(104) Pilinis, C.; Seinfeld, J. H. Continued Development of a General Equilibrium Model for Inorganic Multicomponent Atmospheric Aerosols. *Atmos. Environ.* **1987**, *21* (11), 2453–2466.

(105) Hasseine, A.; Meniai, A. H.; Korichi, M. Salting-out Effect of Single Salts NaCl and KCl on the LLE of the Systems (Water + Toluene + Acetone), (Water + Cyclohexane + 2-Propanol) and (Water + Xylene + Methanol). *Desalination* **2009**, *242* (1–3), 264–276.

(106) Van der Bruggen, B.; Vandecasteele, C. Distillation vs. Membrane Filtration: Overview of Process Evolutions in Seawater Desalination. *Desalination* **2002**, *143* (3), 207–218.

(107) Khawaji, A. D.; Kutubkhanah, I. K.; Wie, J.-M. Advances in Seawater Desalination Technologies. *Desalination* **2008**, *221* (1–3), 47–69.

(108) Gupta, D.; Eom, H. J.; Cho, H. R.; Ro, C. U. Hygroscopic Behavior of NaCl-$MgCl_2$ Mixture Particles as Nascent Sea-Spray Aerosol Surrogates and Observation of Efflorescence during Humidification. *Atmos. Chem. Phys.* **2015**, *15* (19), 11273–11290.

(109) Loosli, F.; Le Coustumer, P.; Stoll, S. Effect of Electrolyte Valency, Alginate Concentration and pH on Engineered TiO2 Nanoparticle Stability in Aqueous Solution. *Sci. Total Environ.* **2015**, *535*, 28–34.

(110) Young, V. D. Improvement in Percolation of Water Thru Soils Having a High Clay Content and Restricted Drainage, 1925. (Thesis).

(111) Ansari, A. S.; Pandis, S. N. An Analysis of Four Models Predicting the Partitioning

of Semivolatile Inorganic Aerosol Components. *Aerosol Sci. Technol.* **1999**, *31* (2–3), 129–153.

(112) Kim, Y. P.; Seinfeld, J. H. Atmospheric Gas–Aerosol Equilibrium: III. Thermodynamics of Crustal Elements Ca^{2+} , K^{+} , and Mg^{2+}. *Aerosol Sci. Technol.* **1995**, *22* (1), 93–110.

(113) Meng, Z.; Seinfeld, J. H.; Saxena, P.; Kim, Y. P. Atmospheric Gas-Aerosol Equilibrium: IV. Thermodynamics of Carbonates. *Aerosol Sci. Technol.* **1995**, *23* (2), 131–154.

(114) Moya, M.; Pandis, S. N.; Jacobson, M. Z. Is the Size Distribution of Urban Aerosols Determined by Thermodynamic Equilibrium? An Application to Southern California. *Atmos. Environ.* **2002**, *36* (14), 2349–2365.

(115) Metzger, S.; Mihalopoulos, N.; Lelieveld, J. Importance of Mineral Cations and Organics in Gas-Aerosol Partitioning of Reactive Nitrogen Compounds: Case Study Based on MINOS Results. *Atmos. Chem. Phys. Discuss.* **2005**, *5* (6), 12857–12893.

(116) Fountoukis, C.; Nenes, A. ISORROPIA II: A Computationally Efficient Thermodynamic Equilibrium Model for K^{+}–Ca^{2+}–Mg^{2+}–NH_4^{+}–Na^{+}–SO_4^{2-}–NO_3^{-}–Cl^{-}–H_2O Aerosols. *Atmos. Chem. Phys. Atmos. Chem. Phys.* **2007**, *7*, 4639–4659.

(117) Cruz, J.; Renon, H. A New Thermodynamic Representation of Binary Electrolyte Solutions Nonideality in the Whole Range of Concentrations. *AIChE J.* **1978**, *24* (5), 817–830.

(118) Mock, B.; Evans, L. B.; Chen, C.-C. Thermodynamic Representation of Phase Equilibria of Mixed-Solvent Electrolyte Systems. *AIChE J.* **1986**, *32* (10), 1655–1664.

(119) Macías-Salinas, R.; Avendaño-Gómez, J. R.; García-Sánchez, F.; Díaz-Cruz, M. Thermodynamic Model for Aqueous Electrolyte Solutions with Partial Ionization. *Ind. Eng. Chem. Res.* **2013**, *52* (25), 8589–8601.

(120) Shannon, R. D. Revised Effective Ionic Radii and Systematic Studies of Interatomic Distances in Halides and Chalcogenides. *Acta Crystallogr. Sect. A* **1976**, *32* (5), 751–767.

(121) Jenkins, H. D. B.; Thakur, K. P. Reappraisal of Thermochemical Radii for Complex Ions. *J. Chem. Educ.* **1979**, *56* (9), 576.

(122) Masterton, W. L.; Bolocofsky, D.; Lee, T. P. Ionic Radii from Scaled Particle Theory of the Salt Effect. *J. Phys. Chem.* **1971**, *76* (18), 2809–2815.

(123) Goldberg, R. N.; Nuttall, R. L. Evaluated Activity and Osmotic Coefficients for Aqueous Solutions: The Alkaline Earth Metal Halides. *J. Phys. Chem. Ref. Data* **1978**, *7* (1), 263.

(124) Robinson, R. A.; Stokes, R. H. *Electrolyte Solutions Second Revised Edition*,

Second.; Dover Publications Inc., Mineola: New York, 2002.

(125) Goldberg, R. N.; Nuttall, R. L.; Staples, B. R. Evaluated Activity and Osmotic Coefficients for Aqueous Solutions: Iron Chloride and the Bi-Univalent Compounds of Nickel and Cobalt. *J. Phys. Chem. Ref. Data* **1979**, *8* (4), 923–1004.

(126) Goldberg, R. N. Evaluated Activity and Osmotic Coefficients for Aqueous Solutions: Bi-Univalent Compounds of Lead, Copper, Manganese, and Uranium. *J. Phys. Chem. Ref. Data* **1979**, *8* (4), 1005–1050.

(127) Staples, B. R. Activity and Osmotic Coefficients of Aqueous Sulfuric Acid at 298.15 K. *J. Phys. Chem. Ref. Data* **1981**, *10* (3), 779–798.

(128) Goldberg, R. N. Evaluated Activity and Osmotic Coefficients for Aqueous Solutions: Thirty Six Uni Bivalent Electrolytes. *J. Phys. Chem. Ref. Data* **1981**, *10* (3), 671–764.

(129) Robinson, R. A.; Wilson, J. M.; Stokes, R. H. The Activity Coefficients of Lithium, Sodium and Potassium Sulfate and Sodium Thiosulfate at 25° from Isopiestic Vapor Pressure Measurements. *J. Am. Chem. Soc.* **1941**, *63* (4), 1011–1013.

(130) Clegg, S. L.; Ho, S. S.; Chan, C. K.; Brimblecombe, P. Thermodynamic Properties of Aqueous (NH4)2SO4 to High Supersaturation as a Function of Temperature. *J. Chem. Eng. Data* **1995**, *40* (5), 1079–1090.

(131) Wishaw, B. F.; Stokes, R. H. Activities of Aqueous Ammonium Sulphate Solutions At 25. *Trans. Faraday Soc.* **1954**, *50*, 952–954.

(132) Tang, I. N.; Munkelwitz, H. R. Water Activities, Densities, and Refractive Indices of Aqueous Sulfates and Sodium Nitrate Droplets of Atmospheric Importance. *J. Geophys.* **1994**, *99*, 18801–18808.

(133) Clegg, S. L.; Milioto, S.; Palmer, D. A. Osmotic and Activity Coefficients of Aqueous $(NH_4)_2SO_4$ as a Function of Temperature , and Aqueous $(NH_4)_2SO_4$-H_2SO_4 Mixtures at 298.15 K and 323.15 K. *J. Chem. Eng. Data* **1996**, *41*, 455–467.

(134) Goldberg, R. N. Evaluated Activity and Osmotic Coefficients for Aqueous Solutions: Bi Univalent Compounds of Zinc, Cadmium, and Ethylene Bis(trimethylammonium) Chloride and Iodide. *J. Phys. Chem. Ref. Data* **1981**, *10* (1), 1–55.

(135) Platford, R. F. Thermodynamics of Aqueous Solutions of Orthophosphoric Acid from the Freezing Point to 298.15°K. *J. Solution Chem.* **1975**, *4* (7), 591–598.

(136) Scatchard, G.; Breckenridge, R. C. Isotonic Solutions. II. The Chemical Potential of Water in Aqueous Solutions of Potassium and Sodium Phosphates and Arsenates at 25°. *J. Phys. Chem.* **1954**, *58* (8), 596–602.

(137) Zafarani-Moattar, M. T.; Sarmad, S. Osmotic and Activity Coefficient of 1-Ethyl-3-Methylimidazolium Chloride in Aqueous Solutions of Tri-Potassium Phosphate,

Potassium Carbonate, and Potassium Chloride at T = 298.15 K. *J. Chem. Eng. Data* **2010**, *55*, 5182–5190.

(138) Hood, G. C.; Redlich, O.; Reilly, C. A. Ionization of Strong Electrolytes. III. Proton Magnetic Resonance in Nitric, Perchloric, and Hydrochloric Acids. *J. Chem. Phys.* **1954**, *22* (12), 2067–2071.

(139) Lide, D. R. *CRC Handbook of Chemistry and Physics: A Ready- Reference Book of Chemical and Physical Data*; CRC Press: Boca Raton, FL, 2009.

(140) Laliberté, M. A Model for Calculating the Heat Capacity of Aqueous Solutions, with Updated Density and Viscosity Data. *J. Chem. Eng. Data* **2009**, *54* (10), 1725–1760.

(141) Kielland, J. Individual Activity Coefficients of Ions in Aqueous Solutions. *J. Am. Chem. Soc.* **1937**, *59* (9), 1675–1678.

(142) Garrels, R., Christ, C. L. *Solutions, Minerals, and Equilibria.*; Harper & Row: New York, NY, 1965.

(143) Rovelli, G.; Miles, R. E. H.; Reid, J. P.; Clegg, S. L. Accurate Measurements of Aerosol Hygroscopic Growth over a Wide Range in Relative Humidity. *J. Phys. Chem. A* **2016**, *120* (25), 4376–4388.

(144) Davies, J. F.; Haddrell, A. E.; Rickards, A. M. J.; Reid, J. P. Simultaneous Analysis of the Equilibrium Hygroscopicity and Water Transport Kinetics of Liquid Aerosol. *Anal. Chem.* **2013**, *85* (12), 5819–5826.

(145) Barbaro, E.; Krol, M. C.; Vilà-Guerau de Arellano, J. Numerical Simulation of the Interaction between Ammonium Nitrate Aerosol and Convective Boundary-Layer Dynamics. *Atmos. Environ.* **2015**, *105*, 202–211.

(146) Matsumoto, K.; Uematsu, M. Free Amino Acids in Marine Aerosols over the Western North Pacific Ocean. *Atmos. Environ.* **2005**, *39* (11), 2163–2170.

(147) Duplissy, J.; De Carlo, P. F.; Dommen, J.; Alfarra, M. R.; Metzger, A.; Barmpadimos, I.; Prevot, A. S. H.; Weingartner, E.; Tritscher, T.; Gysel, M.; et al. Relating Hygroscopicity and Composition of Organic Aerosol Particulate Matter. *Atmos. Chem. Phys.* **2011**, *11* (3), 1155–1165.

(148) Massoli, P.; Lambe, A. T.; Ahern, A. T.; Williams, L. R.; Ehn, M.; Mikkilä, J.; Canagaratna, M. R.; Brune, W. H.; Onasch, T. B.; Jayne, J. T.; et al. Relationship between Aerosol Oxidation Level and Hygroscopic Properties of Laboratory Generated Secondary Organic Aerosol (SOA) Particles. *Geophys. Res. Lett.* **2010**, *37* (24), 1–5.

(149) Marshall, F. H.; Miles, R. E. H.; Song, Y.-C.; Ohm, P. B.; Power, R. M.; Reid, J. P.; Dutcher, C. S. Diffusion and Reactivity in Ultraviscous Aerosol and the Correlation with Particle Viscosity. *Chem. Sci.* **2016**, *7* (2), 1298–1308.

(150) Dennis-Smither, B. J.; Marshall, F. H.; Miles, R. E. H.; Preston, T. C.; Reid, J. P.

Volatility and Oxidative Aging of Aqueous Maleic Acid Aerosol Droplets and the Dependence on Relative Humidity. *J. Phys. Chem. A* **2014**, *118* (30), 5680–5691.

(151) Dennis-Smither, B. J.; Miles, R. E. H.; Reid, J. P. Oxidative Aging of Mixed Oleic Acid/sodium Chloride Aerosol Particles. *J. Geophys. Res. Atmos.* **2012**, *117* (20), 1–13.

(152) Power, R. M.; Simpson, S. H.; Reid, J. P.; Hudson, A. J. The Transition from Liquid to Solid-like Behaviour in Ultrahigh Viscosity Aerosol Particles. *Chem. Sci.* **2013**, *4* (6), 2597–2604.

(153) Song, Y. C.; Haddrell, A. E.; Bzdek, B. R.; Reid, J. P.; Bannan, T.; Topping, D. O.; Percival, C.; Cai, C. Measurements and Predictions of Binary Component Aerosol Particle Viscosity. *J. Phys. Chem. A* **2016**, *120* (41), 8123–8137.

(154) Hakala, J.; Mikkilä, J.; Hong, J.; Ehn, M.; Petäjä, T. VH-TDMA: A Description and Verification of an Instrument to Measure Aerosol Particle Hygroscopicity and Volatility. *Aerosol Sci. Technol.* **2017**, *51* (1), 97–107.

(155) Peng, C.; Jing, B.; Guo, Y. C.; Zhang, Y. H.; Ge, M. F. Hygroscopic Behavior of Multicomponent Aerosols Involving NaCl and Dicarboxylic Acids. *J. Phys. Chem. A* **2016**, *120* (7), 1029–1038.

(156) Zhang, R.; Wang, G.; Guo, S.; Zamora, M. L.; Ying, Q.; Lin, Y.; Wang, W.; Hu, M.; Wang, Y. Formation of Urban Fine Particulate Matter. *Chem. Rev.* **2015**, *115* (10), 3803–3855.

(157) Hennigan, C. J.; Izumi, J.; Sullivan, A. P.; Weber, R. J.; Nenes, A. A Critical Evaluation of Proxy Methods Used to Estimate the Acidity of Atmospheric Particles. *Atmos. Chem. Phys.* **2015**, *15*, 2775–2790.

(158) Hamill, P.; Turco, R. P.; Toon, O. B. On the Growth of Nitric and Sulfuric Acid Aerosol Particles Under Stratospheric Conditions. *J. Atmos. Chem.* **1988**, *7*, 287–315.

(159) Clegg, S. L.; Brimblecombe, P. Equilibrium Partial Pressures and Mean Activity and Osmotic Coefficients of 0-100% Nitric Acid as a Function of Temperature. *J. Phys. Chem.* **1990**, *94* (13), 5369–5380.

(160) Brimblecombe, P.; Clegg, L. Equilibrium Partial Pressures of Strong Acids over Concentrated Solutions - III. The Temperature Variation of HNO3 Solubility. *Atmos. Environ.* **1990**, *24A* (7), 1945–1955.

(161) Clarke, A. D.; Ahlquist, N. C.; Covert, D. S. The Pacific Marine Aerosol: Evidence for Natural Acid Sulfates. *J. Geophys. Res.* **1987**, *92* (D4), 4179–4190.

(162) Friese, E.; Ebel, A. Temperature Dependent Thermodynamic Model of the System H^+-NH_4^+-Na^+-SO_4^{2-}-NO_3^--Cl^--H_2O. *J. Phys. Chem. A* **2010**, *114* (3), 11595–11631.

(163) Galleguillos-Castro, H. R.; Hernández-Luis, F.; Fernandez-Merida, L.; Esteso, M.

A. Thermodynamic Study of the NaCl + Na_2SO_4 + H_2O System by Emf Measurements at Four Temperatures. *J. Solution Chem.* **1999**, *28* (6), 791–807.

(164) Bertram, A. K.; Sloan, J. J. Temperature-Dependent Nucleation Rate Constants and Freezing Behavior of Submicron Nitric Acid Dihydrate Aerosol Particles under Stratospheric Conditions. *J. Geophys. Res.* **1998**, *103* (D3), 3553–3561.

(165) Yue, G. K.; Deepak, A. Temperature Dependence of the Formation of Sulfate Aerosols in the Stratosphere. *J. Geophys. Res.* **1982**, *87* (C4), 3128–3134.

(166) Ganbavale, G.; Marcolli, C.; Krieger, U. K.; Zuend, A.; Stratmann, G.; Peter, T. Experimental Determination of the Temperature Dependence of Water Activities for a Selection of Aqueous Organic Solutions. *Atmos. Chem. Phys.* **2014**, *14* (18), 9993–10012.

(167) Weingartner, E.; Gysel, M.; Baltensperger, U. Hygroscopicity of Aerosol Particles at Low Temperatures. 1. New Low-Temperature H-TDMA Instrument: Setup and First Applications. *Environ. Sci. Technol.* **2002**, *36* (1), 55–62.

(168) Gysel, M.; Weingartner, E.; U, B. Hygroscopicity of Aerosol Particles at Low Temperatures. 2. Theoretical and Experimental Hygroscopic Properties of Laboratory Generated Aerosols. *Environ. Sci. Technol.* **2002**, *36* (1), 63–68.

(169) El Guendouzi, M.; Dinane, A. Determination of Water Activities, Osmotic and Activity Coefficients in Aqueous Solutions Using the Hygrometric Method. *J. Chem. Thermodyn.* **2000**, *32* (3), 297–310.

(170) Chelf, J. H.; Martin, S. T. Water Activity and Equilibrium Freezing Temperatures of Aqueous NH_4HSO_4 Solutions from -30 to 25°C. *Geophys. Res. Lett.* **1999**, *26* (15), 2391–2394.

(171) Chen, Y.; DeMott, P. J.; Kreidenweis, S. M.; Rogers, D. C.; Sherman, D. E. Ice Formation by Sulfate and Sulfuric Acid Aerosol Particles under Upper-Tropospheric Conditions. *J. Atmos. Sci.* **2000**, *57*, 3752–3766.

(172) Onasch, T. B.; McGraw, R.; Imre, D. Temperature-Dependent Heterogeneous Efflorescence of Mixed Ammonium Sulfate/Calcium Carbonate Particles. *J. Phys. Chem. A* **2000**, *104* (46), 10797–10806.

(173) Peckhaus, A.; Kiselev, A.; Wagner, R.; Duft, D.; Leisner, T. Temperature-Dependent Formation of NaCl Dihydrate in Levitated NaCl and Sea Salt Aerosol Particles. *J. Chem. Phys.* **2016**, *145* (24).

(174) Tang, I. N.; Munkelwitz, H. R. Composition and Temperature Dependence of the Deliquescence Properties of Hygroscopic Aerosols. *Atmos. Environ.* **1993**, *27A* (4), 467–473.

(175) Zobrist, B.; Marcolli, C.; Pedernera, D. A.; Koop, T. Do Atmospheric Aerosols Form Glasses? *Atmos. Chem. Phys.* **2008**, *8* (17), 5221–5244.

(176) Lienhard, D. M.; Huisman, A. J.; Krieger, U. K.; Rudich, Y.; Marcolli, C.; Luo, B. P.; Bones, D. L.; Reid, J. P.; Lambe, A. T.; Canagaratna, M. R.; et al. Viscous Organic Aerosol Particles in the Upper Troposphere: Diffusivity-Controlled Water Uptake and Ice Nucleation? *Atmos. Chem. Phys.* **2015**, *15* (23), 13599–13613.

(177) You, Y.; Bertram, A. K. Effects of Molecular Weight and Temperature on Liquid-Liquid Phase Separation in Particles Containing Organic Species and Inorganic Salts. *Atmos. Chem. Phys.* **2015**, *15* (3), 1351–1365.

(178) Vehkamäki, H.; Riipinen, I. Thermodynamics and Kinetics of Atmospheric Aerosol Particle Formation and Growth. *Chem. Soc. Rev.* **2012**, *41*, 5160.

(179) Yu, F.; Luo, G.; Nadykto, A. B.; Herb, J. Impact of Temperature Dependence on the Possible Contribution of Organics to New Particle Formation in the Atmosphere. *Atmos. Chem. Phys.* **2017**, *17* (8), 4997–5005.

(180) Shiraiwa, M.; Ammann, M.; Koop, T.; Poschl, U. Gas Uptake and Chemical Aging of Semisolid Organic Aerosol Particles. *Proc. Natl. Acad. Sci.* **2011**, *108* (27), 11003–11008.

(181) Swanson, B. D. How Well Does Water Activity Determine Homogeneous Ice Nucleation Temperature in Aqueous Sulfuric Acid and Ammonium Sulfate Droplets? *J. Atmos. Sci.* **2009**, *66* (3), 741–754.

(182) Starzak, M.; Mathlouthi, M. Temperature Dependence of Water Activity in Aqueous Solutions of Sucrose. *Food Chem.* **2006**, *96* (3), 346–370.

(183) Knopf, D. A.; Luo, B. P.; Krieger, U. K.; Koop, T. Thermodynamic Dissociation Constant of the Bisulfate Ion from Raman and Ion Interaction Modeling Studies of Aqueous Sulfuric Acid at Low Temperatures. *J. Phys. Chem. A* **2003**, *107*, 4322–4332.

(184) Knopf, D. A.; Luo, B. P.; Krieger, U. K.; Koop, T. Reply to "Comment on the 'Thermodynamic Dissociation Constant of the Bisulfate Ion from Raman and Ion Interaction Modeling Studies of Aqueous Sulfuric Acid at Low Temperatures.'" *J. Phys. Chem. A* **2005**, *109*, 2707–2709.

(185) Carslaw, K. S.; Clegg, S. L.; Brimblecombe, P. A Thermodynamic Model of the System HCl-HNO3-H2SO4-H2O, Including Solubilities of HBr, from <200 to 328 K. *J. Phys. Chem.* **1995**, *99* (29), 11557–11574.

(186) Massucci, M.; Clegg, S. L.; Brimblecombe, P. Equilibrium Partial Pressures, Thermodynamic Properties of Aqueous and Solid Phases, and Cl 2 Production from Aqueous HCl and HNO_3 and Their Mixtures. *J. Phys. Chem. A* **1999**, *103* (21), 4209–4226.

(187) Clegg, S. L.; Brimblecombe, P. Comment on The "thermodynamic Dissociation Constant of the Bisulfate Ion from Raman and Ion Interaction Modeling Studies of Aqueous Sulfuric Acid at Low Temperatures." *J. Phys. Chem. A* **2005**, *109*, 2703–

2706.

(188) Knopf, D. A.; Forrester, S. M. Freezing of Water and Aqueous NaCl Droplets Coated by Organic Monolayers as a Function of Surfactant Properties and Water Activity. *J. Phys. Chem. A* **2011**, *115* (22), 5579–5591.

(189) Berkemeier, T.; Shiraiwa, M.; Pöschl, U.; Koop, T. Competition between Water Uptake and Ice Nucleation by Glassy Organic Aerosol Particles. *Atmos. Chem. Phys.* **2014**, *14* (22), 12513–12531.

(190) Koop, T.; Luo, B.; Tsias, A.; Peter, T. Water Activity as the Determinant for Homogeneous Ice Nucleation in Aqueous Solutions. *Nature* **2000**, *406* (1), 611–614.

(191) Zuberi, B.; Bertram, A. K.; Cassa, C. A.; Molina, L. T.; Molina, M. J. Heterogeneous Nucleation of Ice in $(NH_4)_2SO_4$-H_2O Particles with Mineral Dust Immersions. *Geophys. Res. Lett.* **2002**, *29* (10), 142-1-142–144.

(192) Knopf, D. A.; Alpert, P. A. A Water Activity Based Model of Heterogeneous Ice Nucleation Kinetics for Freezing of Water and Aqueous Solution Droplets. *Faraday Discuss.* **2013**, *165*, 513.

(193) Cheng, Y.; Su, H.; Koop, T.; Mikhailov, E.; Pöschl, U. Size Dependence of Phase Transitions in Aerosol Nanoparticles. *Nat. Commun.* **2015**, *6*, 1–7.

(194) Marcolli, C.; Luo, B.; Peter, T. Mixing of the Organic Aerosol Fractions : Liquids as the Thermodynamically Stable Phases. *J. Phys. Chem. A* **2004**, *108*, 2216–2224.

(195) Debenedetti, P. G.; Stillinger, F. H. Supercooled Liquids and the Glass Transition. *Nature* **2001**, *410* (6825), 259–267.

(196) Schill, G. P.; Tolbert, M. A. Heterogeneous Ice Nucleation on Phase-Separated Organic-Sulfate Particles: Effect of Liquid vs. Glassy Coatings. *Atmos. Chem. Phys.* **2013**, *13* (9), 4681–4695.

(197) Swanepoel, R. M.; Schwarz, C. E. Influence of Temperature on the Liquid-Liquid Phase Equilibria of Ternary (Water + Alcohol + Entrainer) Systems. *J. Chem. Eng. Data* **2017**, *62* (9), 2740–2754.

(198) Xu, Y.; Yu, W.; Zhou, C. Liquid–liquid Phase Separation and Its Effect on the Crystallization in Polylactic Acid/poly(ethylene Glycol) Blends. *RSC Adv.* **2014**, *4* (98), 55435–55444.

(199) Yu, F.; Luo, G.; Turco, R. P.; Ogren, J. A.; Yantosca, R. M. Decreasing Particle Number Concentrations in a Warming Atmosphere and Implications. *Atmos. Chem. Phys.* **2012**, *12* (5), 2399–2408.

(200) King, S. M.; Rosenoern, T.; Shilling, J. E.; Chen, Q.; Wang, Z.; Biskos, G.; McKinney, K. A.; Pöschl, U.; Martin, S. T. Cloud Droplet Activation of Mixed Organic-Sulfate Particles Produced by the Photooxidation of Isoprene. *Atmos.*

Chem. Phys. **2010**, *10* (8), 3953–3964.

(201) Christensen, S. I.; Petters, M. D. The Role of Temperature in Cloud Droplet Activation. *J. Phys. Chem. A* **2012**, *116* (39), 9706–9717.

(202) Brewster, M. Q.; Wang, K.-T.; Wu, W.-H.; Khan, M. G. Temperature Effect on Phase-Transition Radiation of Water. *J. Heat Transfer* **2014**, *136* (6), 62704.

(203) Wexler, A. S.; Clegg, S. L. Atmospheric Aerosol Models for Systems Including the Ions H^+, NH_4^+, Na^+, SO_4^{2-}, NO_3^-, Cl^-, Br^-, and H_2O. *J. Geophys. Res.* **2002**, *107* (D14), 4207.

(204) Parsons, M. T.; Mak, J.; Lipetz, S. R.; Bertram, A. K. Deliquescence of Malonic, Succinic, Glutaric, and Adipic Acid Particles. *J. Geophys. Res. Atmos.* **2004**, *109* (D6), 1–8.

(205) Song, M.; Marcolli, C.; Krieger, U. K.; Zuend, A.; Peter, T. Liquid-Liquid Phase Separation in Aerosol Particles: Dependence on O:C, Organic Functionalities, and Compositional Complexity. *Geophys. Res. Lett.* **2012**, *39* (19), 1–5.

(206) Losey, D. J.; Parker, R. G.; Freedman, M. A. pH Dependence of Liquid–Liquid Phase Separation in Organic Aerosol. *J. Phys. Chem. Lett.* **2016**, *7* (19), 3861–3865.

(207) Streets, D. G.; Wu, Y.; Chin, M. Two-Decadal Aerosol Trends as a Likely Explanation of the Global Dimming/brightening Transition. *Geophys. Res. Lett.* **2006**, *33* (15), 2–5.

(208) Bodenschatz, E.; Malinowski, S. P.; Shaw, R. A.; Stratmann, F. Can We Understand Clouds Without Turbulence? *Atmos. Sci.* **2010**, *327* (5968), 970–971.

(209) Bithi, S. S.; Vanapalli, S. a. Behavior of a Train of Droplets in a Fluidic Network with Hydrodynamic Traps. *Biomicrofluidics* **2010**, *4* (4), 44110.

(210) Boukellal, H.; Selimović, Š.; Jia, Y.; Cristobal, G.; Fraden, S. Simple, Robust Storage of Drops and Fluids in a Microfluidic Device. *Lab Chip* **2009**, *9* (2), 331–338.

(211) Christopher, G. F.; Noharuddin, N. N.; Taylor, J. a.; Anna, S. L. Experimental Observations of the Squeezing-to-Dripping Transition in T-Shaped Microfluidic Junctions. *Phys. Rev. E - Stat. Nonlinear, Soft Matter Phys.* **2008**, *78* (3), 1–12.

(212) Qin, D.; Xia, Y.; Whitesides, G. M. Soft Lithography for Micro- and Nanoscale Patterning. *Nat. Protoc.* **2010**, *5* (3), 491–502.

(213) McDonald, J. C.; Duffy, D. C.; Anderson, J. R.; Chiu, D. T.; Wu, H.; Schueller, O. J.; Whitesides, G. M. Fabrication of Microfluidic Systems in Poly(dimethylsiloxane). *Electrophoresis* **2000**, *21* (1), 27–40.

(214) Metcalf, A. R.; Boyer, H. C.; Dutcher, C. S. Interfacial Tensions of Aged Organic Aerosol Particle Mimics Using a Biphasic Microfluidic Platform. *Environ. Sci.*

Technol. **2016**, *50* (3), 1251–1259.

(215) Thorsen, T.; Roberts, R. W.; Arnold, F. H.; Quake, S. R. Dynamic Pattern Formation in a Vesicle-Generating Microfluidic Device. *Phys. Rev. Lett.* **2001**, *86* (18), 4163–4166.

(216) Zheng, B.; Tice, J. D.; Ismagilov, R. F. Forming Droplets in Microfluidic Channels with Alternating Composition and Application to Indexing Concentrations in Droplet-Based Assays. *Anal. Chem.* **2004**, *76* (17), 4977–4982.

(217) Garstecki, P.; Stone, H. A.; Whitesides, G. M. Mechanism for Flow-Rate Controlled Breakup in Confined Geometries: A Route to Monodisperse Emulsions. *Phys. Rev. Lett.* **2005**, *94* (16), 1–4.

(218) Seemann, R.; Brinkmann, M.; Pfohl, T.; Herminghaus, S. Droplet Based Microfluidics. *Rep. Prog. Phys.* **2012**, *75*, 1–41.

(219) Ziemecka, I.; Haut, B.; Scheid, B. Continuous Separation, with Microfluidics, of the Components of a Ternary Mixture: From Vacuum to Purge Gas Pervaporation. *Microfluid. Nanofluidics* **2017**, *21* (5), 1–13.

(220) Laval, C.; Bouchaudy, A.; Salmon, J.-B. Fabrication of Microscale Materials with Programmable Composition Gradients. *Lab Chip* **2016**, *16*, 1234–1242.

(221) Ziane, N.; Salmon, J. B. Solidification of a Charged Colloidal Dispersion Investigated Using Microfluidic Pervaporation. *Langmuir* **2015**, *31* (29), 7943–7952.

(222) Bleier, B. J.; Anna, S. L.; Walker, L. M. Microfluidic Droplet-Based Tool To Determine Phase Behavior of a Fluid System with High Composition Resolution. *J. Phys. Chem. B* **2018**, acs.jpcb.8b01013.

(223) Schindelin, J.; Arganda-Carreras, I.; Frise, E.; Kaynig, V.; Longair, M.; Pietzsch, T.; Preibisch, S.; Rueden, C.; Saalfeld, S.; Schmid, B.; et al. Fiji: An Open-Source Platform for Biological-Image Analysis. *Nat. Methods* **2012**, *9* (7), 676–682.

(224) Vuong, S. M.; Anna, S. L. Tuning Bubbly Structures in Microchannels. *Biomicrofluidics* **2012**, *6* (2), 1–18.

(225) Vuong, S. M. A Microfluidic Platform for the Control and Analysis of Phase Transitions in Concentrating Droplets, 2014.

(226) Laliberte, M.; Cooper, W. E. Model for Calculating the Density of Aqueous Electrolyte Solutions. *J. Chem. Eng. Data* **2004**, *49* (5), 1141–1151.

(227) Cai, C.; Marsh, A.; Zhang, Y.-H.; Reid, J. P. A Group Contribution Approach to Predict the Refractive Index of Pure Organic Components in Ambient Organic Aerosol. *Environ. Sci. Technol.* **2017**, *51* (17), 9683–9690.

(228) Stelson, A. W.; Seinfeld, J. H. Thermodynamic Prediction of the Water Activity,

NH_4NO_3 Dissociation-Constant, Density And Refractive-Index For The NH_4NO_3-$(NH_4)_2SO_4$-H_2O System At 25-Degrees-C. *Atmos. Environ.* **1982**, *16* (10), 2507–2514.

(229) Tang, I. N.; Wong, W. T.; Munkelwitz, H. R. The Relative Importance of Atmospheric Sulfates and Nitrates in Visibility Reduction. *Atmos. Environ.* **1981**, *15* (12), 2463–2471.

(230) Gelest. Silicone Fluids Property Profile Guide. 2012, pp 1–31.

(231) Ciobanu, V. G.; Marcolli, C.; Krieger, U. K.; Zuend, A.; Peter, T. Evidence for Surface Nucleation : Efflorescence of Ammonium Sulfate and Coated Ammonium Sulfate Aerosol Particles. *J. Phys. Chem. A* **2010**, *12*, 10978.

(232) Smith, M. L.; Kuwata, M.; Martin, S. T. Secondary Organic Material Produced by the Dark Ozonolysis of α-Pinene Minimally Affects the Deliquescence and Efflorescence of Ammonium Sulfate. *Aerosol Sci. Technol.* **2011**, *45* (2), 244–261.

(233) Smith, M. L.; Bertram, A. K.; Martin, S. T. Deliquescence, Efflorescence, and Phase Miscibility of Mixed Particles of Ammonium Sulfate and Isoprene-Derived Secondary Organic Material. *Atmos. Chem. Phys.* **2012**, *12* (20), 9613–9628.

(234) Smith, M. L.; You, Y.; Kuwata, M.; Bertram, A. K.; Martin, S. T. Phase Transitions and Phase Miscibility of Mixed Particles of Ammonium Sulfate, Toluene-Derived Secondary Organic Material, and Water. *J. Phys. Chem. A* **2013**, *117* (36), 8895–8906.

(235) Hallquist, M.; Wenger, J. C.; Baltensperger, U.; Rudich, Y.; Simpson, D.; Claeys, M.; Dommen, J.; Donahue, N. M.; George, C.; Goldstein, a. H.; et al. The Formation, Properties and Impact of Secondary Organic Aerosol: Current and Emerging Issues. *Atmos. Chem. Phys.* **2009**, *9* (14), 5155–5236.

(236) Budisulistiorini, S. H.; Li, X.; Bairai, S. T.; Renfro, J.; Liu, Y.; Liu, Y. J.; McKinney, K. A.; Martin, S. T.; McNeill, V. F.; Pye, H. O. T.; et al. Examining the Effects of Anthropogenic Emissions on Isoprene-Derived Secondary Organic Aerosol Formation during the 2013 Southern Oxidant and Aerosol Study (SOAS) at the Look Rock, Tennessee Ground Site. *Atmos. Chem. Phys.* **2015**, *15* (15), 8871–8888.

(237) Lin, Y. H.; Budisulistiorini, S. H.; Chu, K.; Siejack, R. A.; Zhang, H.; Riva, M.; Zhang, Z.; Gold, A.; Kautzman, K. E.; Surratt, J. D. Light-Absorbing Oligomer Formation in Secondary Organic Aerosol from Reactive Uptake of Isoprene Epoxydiols. *Environ. Sci. Technol.* **2014**, *48* (20), 12012–12021.

(238) Kramer, A. J.; Rattanavaraha, W.; Zhang, Z.; Gold, A.; Surratt, J. D.; Lin, Y. H. Assessing the Oxidative Potential of Isoprene-Derived Epoxides and Secondary Organic Aerosol. *Atmos. Environ.* **2016**, *130*, 211–218.

(239) Riva, M.; Budisulistiorini, S. H.; Zhang, Z.; Gold, A.; Surratt, J. D. Chemical Characterization of Secondary Organic Aerosol Constituents from Isoprene

Ozonolysis in the Presence of Acidic Aerosol. *Atmos. Environ.* **2016**, *130*, 5–13.

(240) Lopez-Hilfiker, F. D.; Mohr, C.; D'Ambro, E. L.; Lutz, A.; Riedel, T. P.; Gaston, C. J.; Iyer, S.; Zhang, Z.; Gold, A.; Surratt, J. D.; et al. Molecular Composition and Volatility of Organic Aerosol in the Southeastern U.S.: Implications for IEPOX Derived SOA. *Environ. Sci. Technol.* **2016**, *50* (5), 2200–2209.

(241) Rastak, N.; Pajunoja, A.; Acosta Navarro, J. C.; Ma, J.; Song, M.; Partridge, D. G.; Kirkevåg, A.; Leong, Y.; Hu, W. W.; Taylor, N. F.; et al. Microphysical Explanation of the RH-Dependent Water Affinity of Biogenic Organic Aerosol and Its Importance for Climate. *Geophys. Res. Lett.* **2017**, *44* (10), 5167–5177.

(242) Renbaum-Wolff, L.; Song, M.; Marcolli, C.; Zhang, Y.; Liu, P. F.; Grayson, J. W.; Geiger, F. M.; Martin, S. T.; Bertram, A. K. Observations and Implications of Liquid-Liquid Phase Separation at High Relative Humidities in Secondary Organic Material Produced by α-Pinene Ozonolysis without Inorganic Salts. *Atmos. Chem. Phys.* **2016**, *16* (12), 7969–7979.

(243) Finlayson-Pitts, B. J. The Tropospheric Chemistry of Sea Salt: A Molecular-Level View of the Chemistry of NaCl and NaBr. *Chem. Rev.* **2003**, *103* (12), 4801–4822.

(244) Grythe, H.; Ström, J.; Krejci, R.; Quinn, P.; Stohl, A. A Review of Sea-Spray Aerosol Source Functions Using a Large Global Set of Sea Salt Aerosol Concentration Measurements. *Atmos. Chem. Phys.* **2014**, *14* (3), 1277–1297.

(245) Patterson, J. P.; Collins, D. B.; Michaud, J. M.; Axson, J. L.; Sultana, C. M.; Moser, T.; Dommer, A. C.; Conner, J.; Grassian, V. H.; Stokes, M. D.; et al. Sea Spray Aerosol Structure and Composition Using Cryogenic Transmission Electron Microscopy. *ACS Cent. Sci.* **2016**, *2* (1), 40–47.

(246) Zhang, Z.; Liu, L.; Liu, C.; Cai, W. Studies on the Sea Surface Microlayer: II. The Layer of Sudden Change of Physical and Chemical Properties. *J. Colloid Interface Sci.* **2003**, *264* (1), 148–159.

(247) de Leeuw, G.; Andreas, E. .; Anguelova, M. .; Fairall, C. W.; Ernie, R.; O'Dowd, C.; Schulz, M.; Schwartz, S. E. Production Flux of Sea-Spray Aerosol. *Rev. Geophys.* **2011**, *49* (2010), 1–39.

(248) Koop, T.; Kapilashrami, A.; Molina, L. T.; Molina, M. J. Phase Transitions of Sea-Salt/water Mixtures at Low Temperatures: Implications for Ozone Chemistry in the Polar Marine Boundary Layer. *J. Geophys. Res.* **2000**, *105* (D21), 26393–26402.

(249) Tang, I. N. Chemical and Size Effects of Hygroscopic Aerosols on Light Scattering Coefficients. *J. Geophys. Res. Atmos.* **1996**, *101* (D14), 19245–19250.

(250) You, Y.; Renbaum-Wolff, L.; Bertram, A. K. Liquid-Liquid Phase Separation in Particles Containing Organics Mixed with Ammonium Sulfate, Ammonium Bisulfate, Ammonium Nitrate or Sodium Chloride. *Atmos. Chem. Phys.* **2013**, *13* (23), 11723–11734.

(251) Maffia, M. C.; Meirelles, A. J. A. Water Activity and pH in Aqueous Polycarboxylic Acid Systems. *J. Chem. Eng. Data* **2001**, *46*, 582–587.

(252) AIOMFAC, Aerosol Inorganic-Organic Mixtures Functional groups Activity Coefficients, Website URL: http://www.aiomfac.caltech.edu

(253) E-AIM, Extended AIM Aerosol Thermodynamics Model, Website URL: http://www.aim.env.uea.ac.uk/aim/aim.php

Appendix A

Additional Information for Chapter 2

A1. Figures

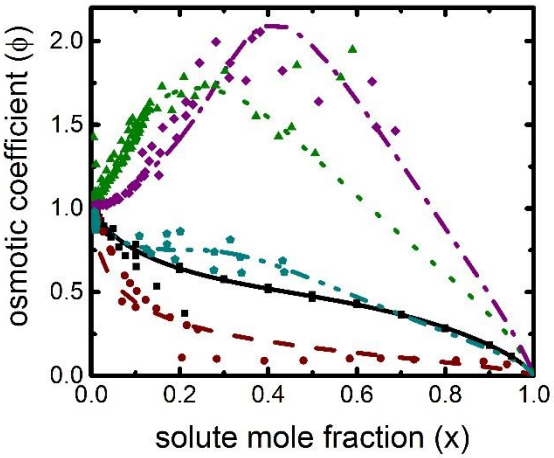

Figure A1. Osmotic coefficient (φ = -ln $(a_w)/M_w \sum_j v_j m_j$), plotted against the solute mole fraction (x = $\sum_j v_j m_j/(\sum_j v_j m_j + 1/M_w)$) at 298.15 K. All energy "$C_{j,i}$" parameters are as adjustable fit parameters. Lines: black solid, Acetic acid; brown dash, Butyric acid; green dot, Citric acid; purple dash-dot, Malic acid; cyan dash-dot-dot, Succinic acid. Symbols: black square, Acetic acid data; brown circle, Butyric acid data; green triangle, Citric acid data; purple diamond, Malic acid data; cyan pentagon, Succinic acid data, where references for the data given in **Table 2. 1**.

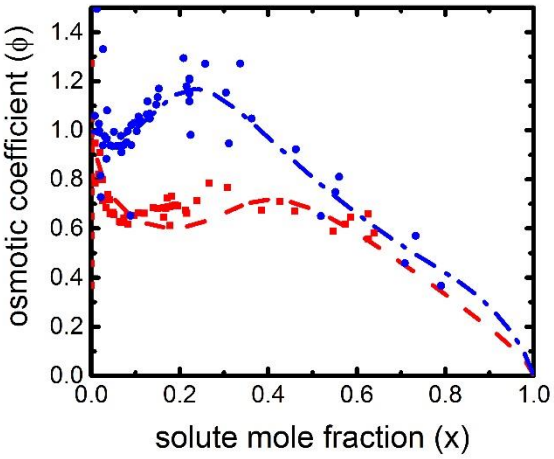

Figure A2. Osmotic coefficient plotted against the solute mole at 298.15 K (see caption from Figure A1). All energy "$C_{j,i}$" parameters are as adjustable fit parameters. Lines: red dash, Glutaric acid; blue dash-dot, Malonic acid. Symbols: red square, Glutaric acid data; blue circle, Malonic acid data, where references for the data given in **Table 2. 1**.

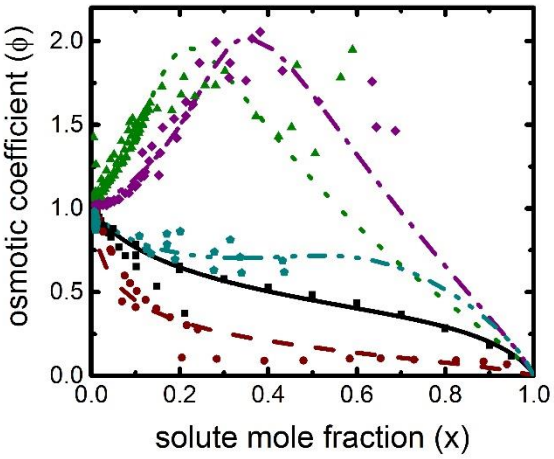

Figure A3. Osmotic coefficient plotted against the solute mole fraction at 298.15 K (see caption from Figure A1). The model fits the first $C_{j,i}$ parameter, $C_{j,1}$, and calculates the rest of the $C_{j,i}$ parameters using a power law relationship $C_{j,i} = (i/n)^P$. Lines: (see caption from Figure A1). Symbols: (see caption from Figure A1).

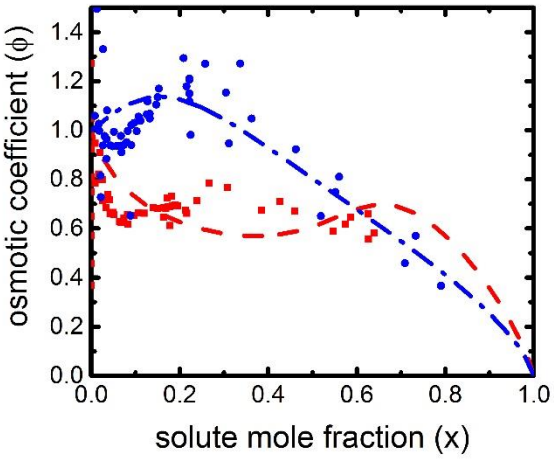

Figure A4. Osmotic coefficient plotted against the solute mole at 298.15 K (see caption from Figure A1). The model fits the first $C_{j,i}$ parameter, $C_{j,1}$, and calculates the rest of the $C_{j,i}$ parameters using a power law relationship $C_{j,i} = (i/n)^P$. Lines: (see caption from Figure A2). Symbols: (see caption from Figure A2).

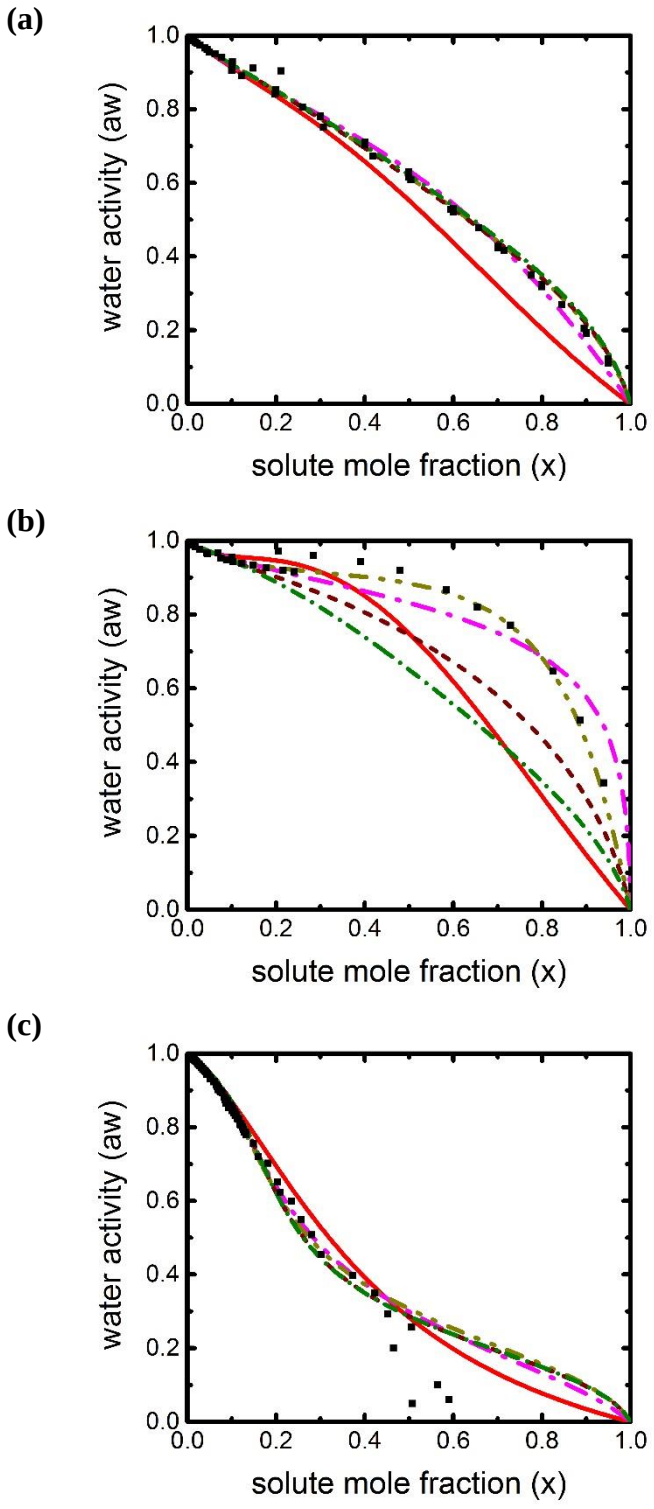

Figure A5. Water activity plotted against the solute mole fraction (x = $\sum_j v_j m_j/(\sum_j v_j m_j + 1/M_w)$) at 298.15 K, comparing different models for (a). Acetic acid. (b). Butyric acid.

(c). Citric acid. Lines: red solid, UNIFAC (AIOMFAC);[92,93,40] magenta dash-dot, Equation 2.3; gold dash-dot-dot, Equation 2.10 (3-fit); maroon short-dash, Equation 2.10 (2-fit); cyan dash-dot-dash, Equation 2.10 (1-fit); black squares, experimental data, where references for the experimental data given in **Table 2. 1**.

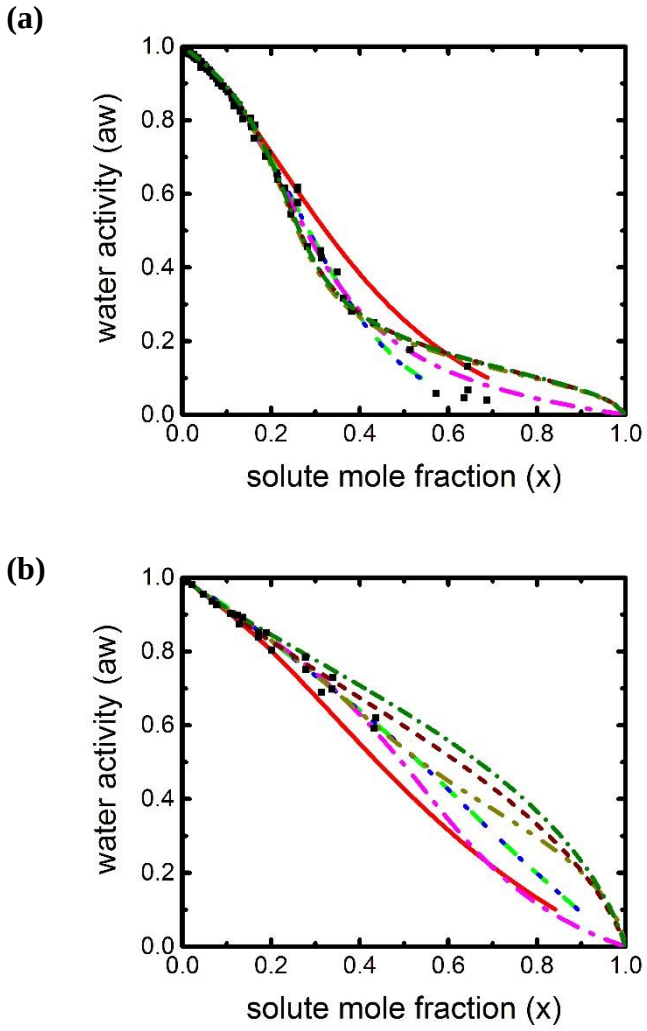

Figure A6. Water activity plotted against the solute mole fraction (see caption from Figure A5) at 298.15 K, comparing different models for (a). Malic acid. (b). Succinic acid. Lines: red solid, UNIFAC (Peng et al.);[49,41] green dash, E-AIM (RK)[33,41] No dissociation; blue dotted, E-AIM (RK)[34,41] Dissociation; magenta dash-dot, Equation 2.3; gold dash-dot-dot, Equation 2.10 (3-fit); maroon short-dash, Equation 2.10 (2-fit); cyan dash-dot-dash,

Equation 2.10 (1-fit); black squares, experimental data, where references for the experimental data given in **Table 2. 1**.

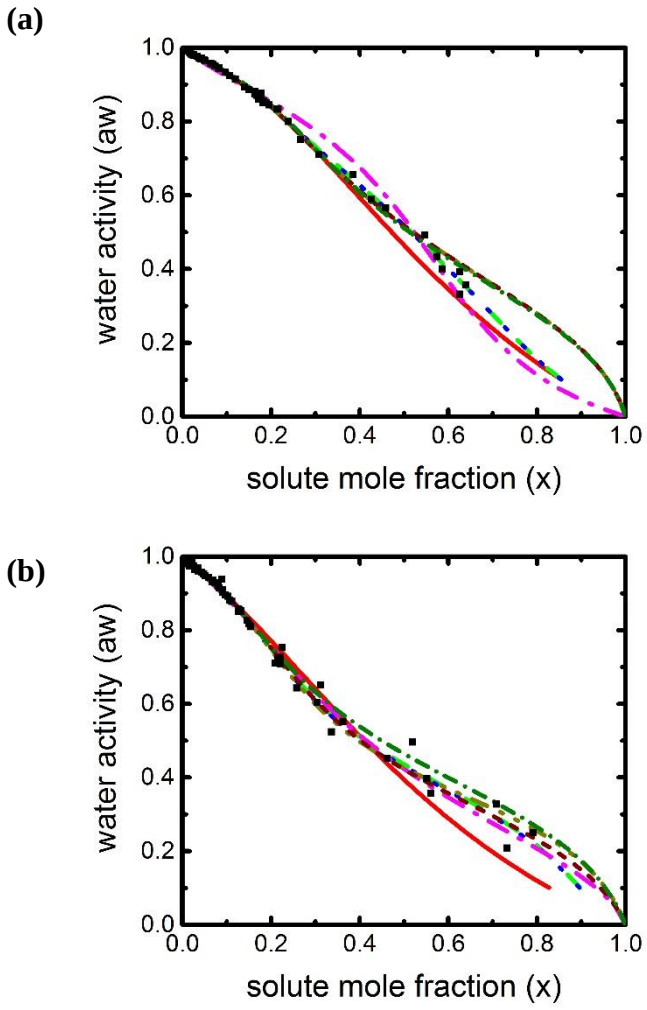

Figure A7. Water activity plotted against the solute mole (see caption from Figure A5) at 298.15 K, comparing different models for (a). Glutaric acid. (b). Malonic acid. Lines: (see caption from Figure A6); black squares, experimental data, where references for the experimental data given in **Table 2. 1**.

A2. Tables

Models	n	$C_{j,i}$	$C_{j,1}$	P	MSE[a]
All $C_{j,i}$'s fit	4	{0.2728, 2.9509, 0.3679}	-	-	0.0061
Power law	4	-	0.6058	0.6589	0.0085

Table A1. Fitted Parameters at 298.15 K for Acetic acid. Experimental data from references given in **Table 2. 1**. Values for n, ρ, $C_{j,i}$, $C_{j,1}$ and P were fit. [a]MSE is a normalized mean-square error, equal to $\left(\frac{1}{n_p}\right)\sum_{i=1}^{n_p}((m_{model,i} - m_{data,i})/(m_{model,i}))^2$, where n_p is the number of data points.

Models	n	$C_{j,i}$	$C_{j,1}$	P	MSE[a]
All $C_{j,i}$'s fit	5	{0.0376, 0.0003, 0.5093, 6277.3}	-	-	0.1141
Power law	5	-	2.07E-10[b]	-11.512	0. 1332

Table A2. Fitted Parameters at 298.15 K for Butyric acid. (See caption from Table A1). [b]Unrealistic value.

Models	n	$C_{j,i}$	$C_{j,1}$	P	MSE[a]
All $C_{j,i}$'s fit	7	{3.1965, 0.0052, 1355.52, 0.2372, 0.0076, 469.941}	-	-	0.0255
Power law	6	-	0.402	-1.4413	0. 0501

Table A3. Fitted Parameters at 298.15 K for Citric acid. (See caption from Table A1).

Models	n	$C_{j,i}$	$C_{j,1}$	P	MSE[a]
All $C_{j,i}$'s fit	3	{8.5918, 4.4192}	-	-	0.0051
Power law	3	-	0.9576	-7.372	0.0123

Table A4. Fitted Parameters at 298.15 K for Malic acid. (See caption from Table A1).

Models	n	$C_{j,i}$	$C_{j,1}$	P	MSE[a]
All $C_{j,i}$'s fit	6	{0.3491, 0.0014, 0.9599, 5382.21, 0.1457}	-	-	0.0044
Power law	7	-	2.1051	0.2944	0.0055

Table A5. Fitted Parameters at 298.15 K for Succinic acid. (See caption from Table A1).

Models	n	$C_{j,i}$	$C_{j,1}$	P	MSE[a]
All $C_{j,i}$'s fit	5	{0.3896, 0.0003, 27452.3, 0.0921}	-	-	0.0087
Power law	4	-	3.0049	1.6034	0.0202

Table A6. Fitted Parameters at 298.15 K for Glutaric acid. (See caption from Table A1).

Models	n	$C_{j,i}$	$C_{j,1}$	P	MSE[a]
All $C_{j,i}$'s fit	7	{1.5325, 0.0124, 70.5216, 0.3208, 18.7443, 0.2156}	-	-	0.039
Power law	8	-	0.909	-0.1992	0. 0402

Table A7. Fitted Parameters at 298.15 K for Malonic acid. (See caption from Table A1).

Appendix B

Additional Information for Chapter 3

B1. Figures

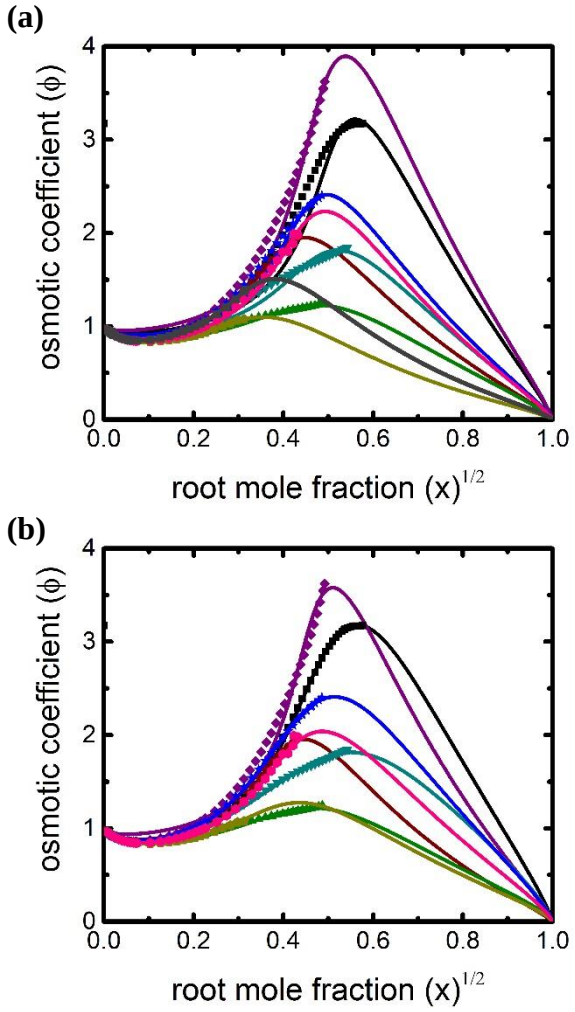

Figure B1. Family of chlorides with divalent cations. (a) Two-parameter fitting. (b) Three-parameter fitting. Osmotic coefficient (φ = -ln $(a_w)/M_w \sum_j v_j m_j$), plotted against the square root of the solute mole fraction (x = $\sum_j v_j m_j/(\sum_j v_j m_j + 1/M_w)$) of chlorides at

298.15 K. Lines (predictions): black solid, $CaCl_2$; brown solid, $CoBr_2$; green solid, $CuCl_2$; purple solid, $MgCl_2$; cyan solid, $MnCl_2$; blue solid, $NiCl_2$; dark yellow solid, $BaCl_2$; magenta solid, $SrCl_2$; dark gray solid, $FeCl_2$. Symbols: black square, $CaCl_2$ experimental data; brown circle, $CoCl_2$ experimental data; green triangle, $CuCl_2$ experimental data; purple diamond, $MgCl_2$ experimental data; cyan inverted triangle, $MnCl_2$ experimental data; blue star, $NiCl_2$ experimental data; dark yellow pentagon, $BaCl_2$ experimental data; magenta hexagon, $SrCl_2$ experimental data; dark gray square, $FeCl_2$ experimental data, where references for the experimental data are given in **Table 3. 1** for two-parameter model, and in **Table 3. 2** for three-parameter model.

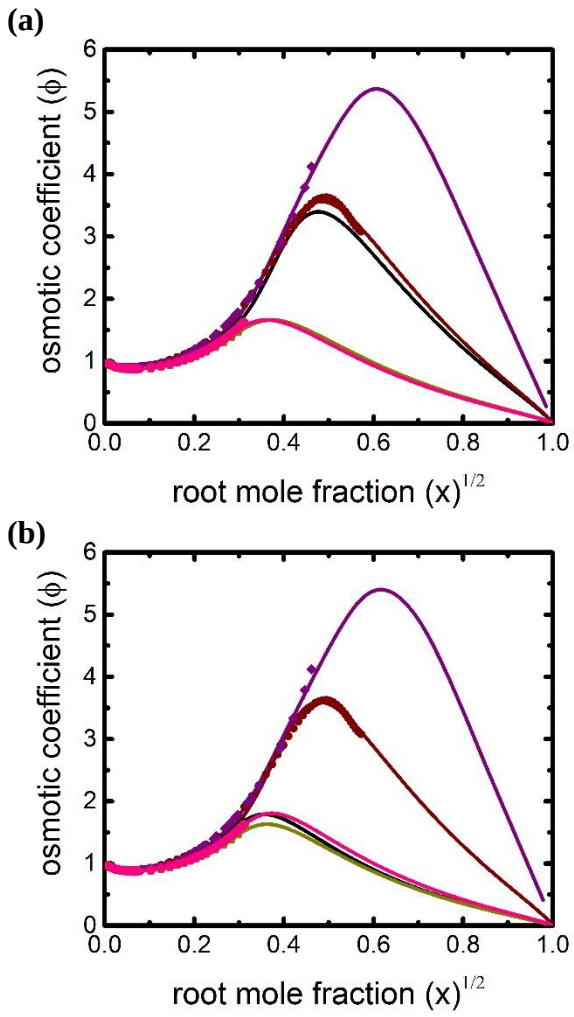

Figure B2. Family of iodides with divalent cations. (a) Two-parameter fitting. (b) Three-parameter fitting. Osmotic coefficient plotted against the square root of the solute mole fraction of iodides at 298.15 K (see caption from Figure B1). Lines (predictions): black solid, CaI_2; brown solid, CoI_2; purple solid, MgI_2; dark yellow solid, BaI_2; magenta solid, SrI_2. Symbols: black square, CaI_2 experimental data; brown circle, CoI_2 experimental data; purple diamond, MgI_2 experimental data; dark yellow pentagon, BaI_2 experimental data; magenta hexagon, SrI_2 experimental data, where references for the experimental data given in **Table 3. 1** for two-parameter model, and in **Table 3. 2** for three-parameter model.

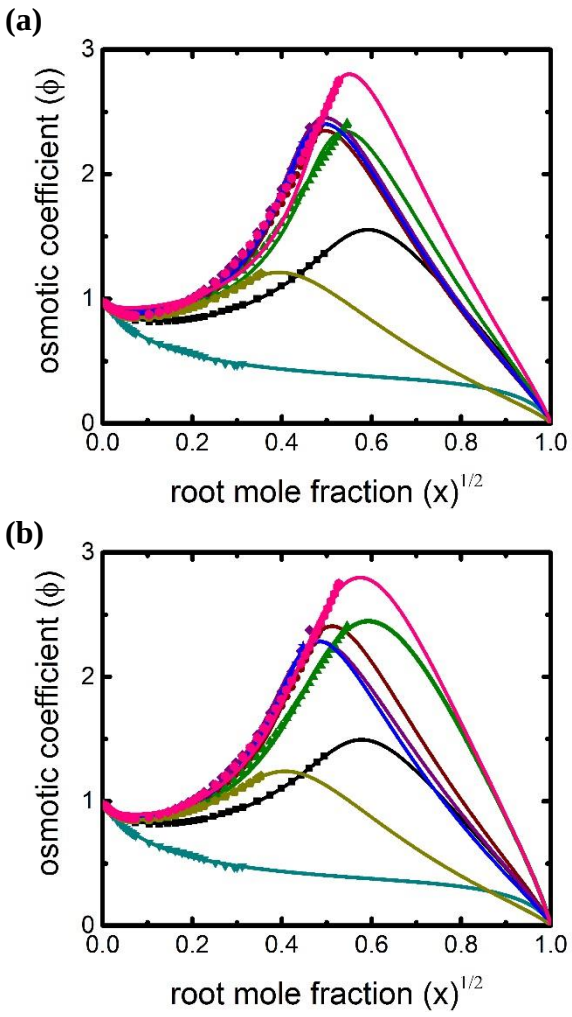

Figure B3. Family of nitrates with divalent cations. (a) Two-parameter fitting. (b) Three-parameter fitting. Osmotic coefficient plotted against the square root of the solute mole fraction of nitrates at 298.15 K (see caption from Figure B1). Lines (predictions): black solid, $Ca(NO_3)_2$; brown solid, $Co(NO_3)_2$; green solid, $Cu(NO_3)_2$; purple solid, $Mg(NO_3)_2$; cyan solid, $Pb(NO_3)_2$; blue solid, $Ni(NO_3)_2$; dark yellow solid, $Cd(NO_3)_2$; magenta solid, $Zn(NO_3)_2$. Symbols: black square, $Ca(NO_3)_2$ experimental data; brown circle, $Co(NO_3)_2$ experimental data; green triangle, $Cu(NO_3)_2$ experimental data; purple diamond, $Mg(NO_3)_2$ experimental data; cyan inverted triangle, $Pb(NO_3)_2$ experimental data; blue star, $Ni(NO_3)_2$ experimental data; dark yellow pentagon, $Cd(NO_3)_2$ experimental data; magenta hexagon, $Zn(NO_3)_2$ experimental data, where references for the experimental data are given in **Table 3. 1** for two-parameter model, and in **Table 3. 2** for three-parameter model.

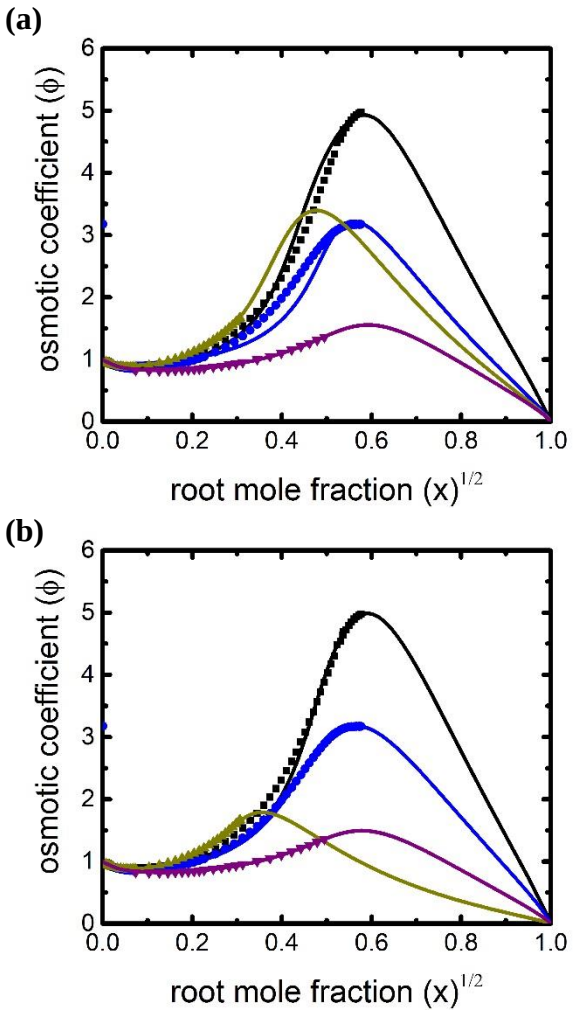

Figure B4. Family of calcium with univalent anions. (a) Two-parameter fitting. (b) Three-parameter fitting. Osmotic coefficient plotted against the square root of the solute mole fraction of calcium at 298.15 K (see caption from Figure B1). Lines (predictions): black solid, $CaBr_2$; blue solid, $CaCl_2$; dark yellow solid, CaI_2; purple solid, $Ca(NO_3)_2$. Symbols: black square, $CaBr_2$ experimental data; blue circle, $CaCl_2$ experimental data; dark yellow triangle, CaI_2 experimental data; purple inverted triangle, $Ca(NO_3)_2$ experimental data, where references for the experimental data given in **Table 3. 1** for two-parameter model, and in **Table 3. 2** for three-parameter model.

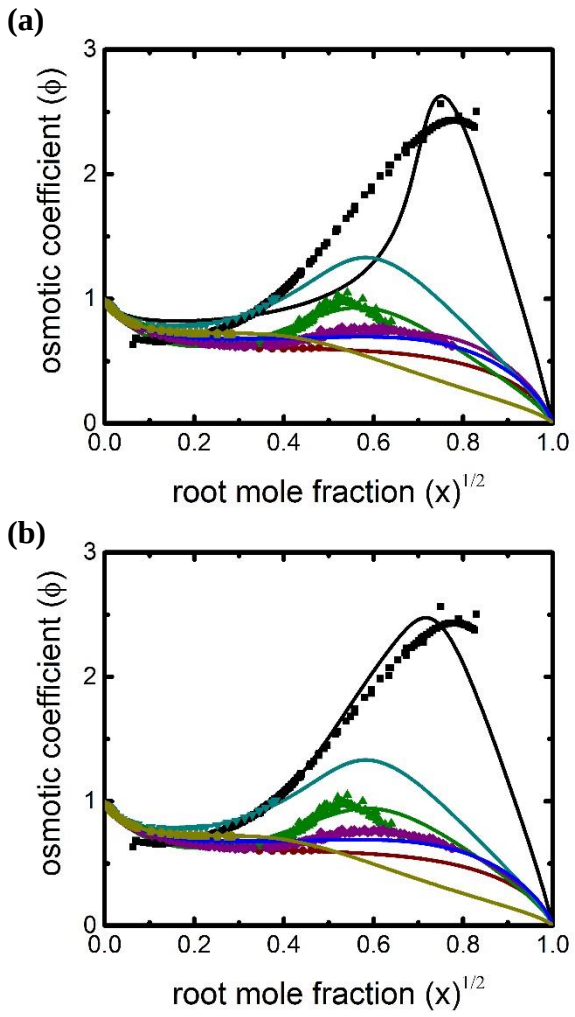

Figure B5. Family of sulfates with univalent cations. (a) Two-parameter fitting. (b) Three-parameter fitting. Osmotic coefficient plotted against the square root of the solute mole fraction of sulfates at 298.15 K (see caption from Figure B1). Lines (predictions): black solid, $H_2SO_4^*$; brown solid, K_2SO_4; green solid, Na_2SO_4; purple solid, $(NH_4)_2SO_4$; cyan solid, Li_2SO_4; blue solid, Rb_2SO_4; dark yellow solid, Cs_2SO_4. Symbols: black square, H_2SO_4 experimental data; brown circle, K_2SO_4 experimental data; green triangle, Na_2SO_4 experimental data; purple diamond, $(NH_4)_2SO_4$ experimental data; cyan inverted triangle, Li_2SO_4 experimental data; blue star, Rb_2SO_4 experimental data; dark yellow pentagon, Cs_2SO_4 experimental data, where references for the experimental data given in **Table 3. 1** for two-parameter model, and in **Table 3. 2** for three-parameter model. $^*H_2SO_4$ is treated separately in section 3.4 by consideration of partial dissociation of the bisulfate ion.

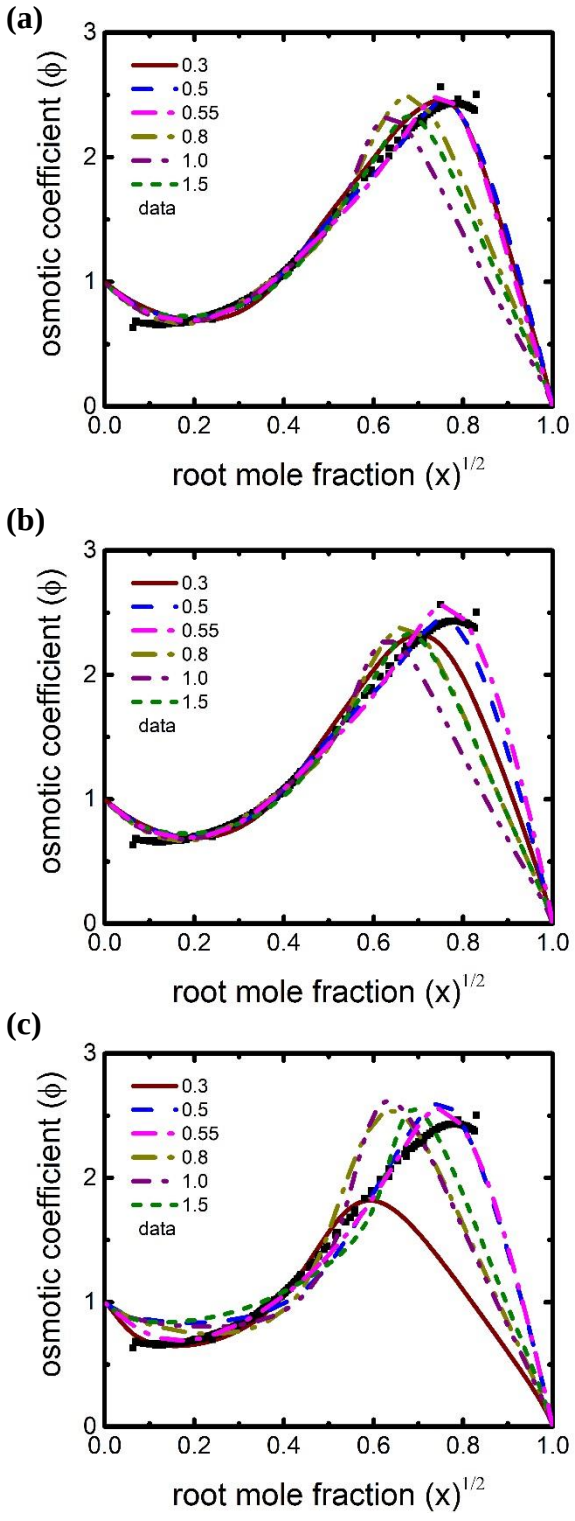

Figure B6. Sulfuric acid - Osmotic coefficient plotted against the square root of the solute mole fraction of sulfuric acid at 298.15 K (see caption from Figure B1). (a) Fitting four

parameters - $r_{jj,BS}$, $r_{jj,S}$, ρ_{BS}, ρ_S (b) Fitting three parameters - $r_{jj,BS}$, $r_{jj,S}$, ρ (c) Fitting two parameters - $r_{jj,BS}$, $r_{jj,S}$. Lines (predictions): brown solid, β = 0.3; blue dash, β = 0.5; magenta dash-dot, β = 0.55; dark yellow dash-dot, β = 0.8; purple dash-dot-dot, β = 1.0; green short dash, β = 1.5. Symbols: black square, experimental data, where references for the experimental data and parameter values given in **Table 3. 5**.

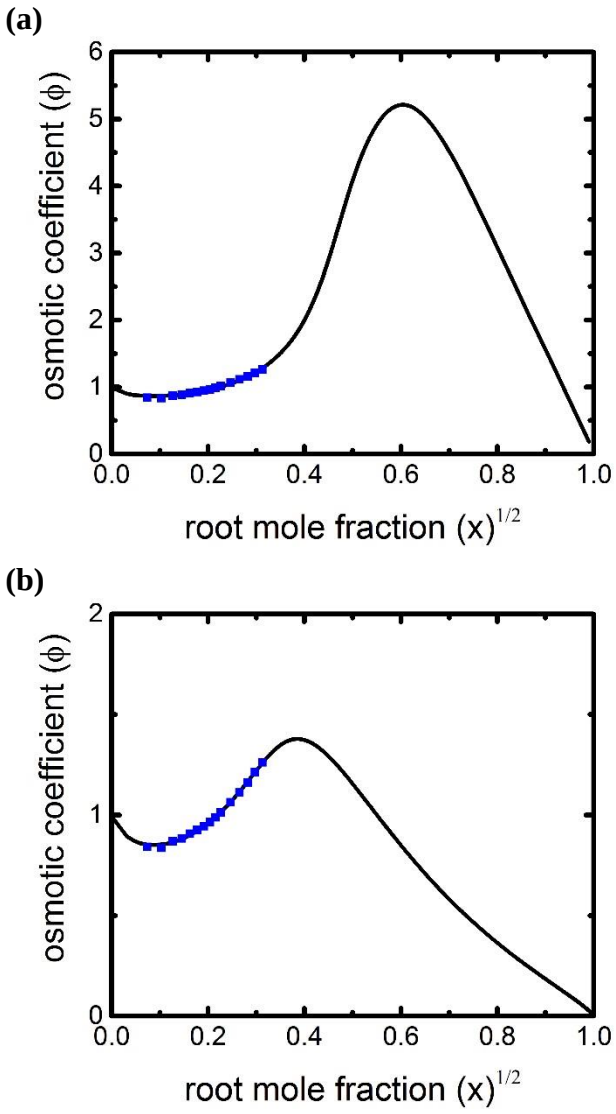

Figure B7. Barium bromide. (a) Two-parameter fitting. (b) Three-parameter fitting. Osmotic coefficient plotted against the square root of the solute mole fraction at 298.15 K (see caption from Figure B1). Lines (model calculations): black solid. Symbols: blue square, experimental data, where references for the experimental data and parameter values given in **Table 3. 1** for two-parameter model, and in **Table 3. 2** for three-parameter model.

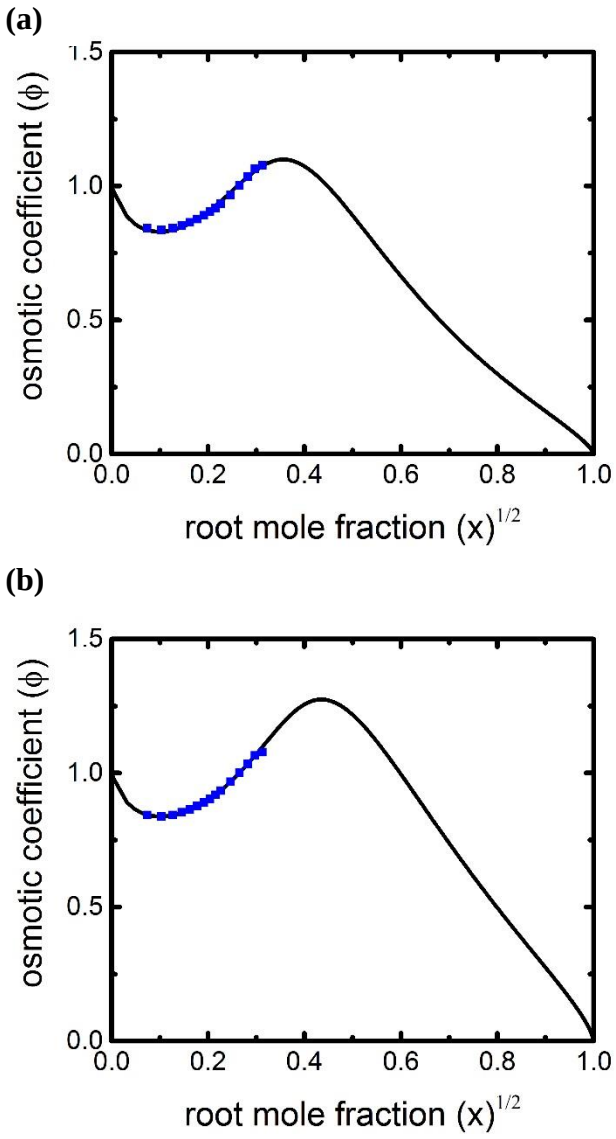

Figure B8. Barium chloride. (a) Two-parameter fitting. (b) Three-parameter fitting. Osmotic coefficient plotted against the square root of the solute mole fraction at 298.15 K (see caption from Figure B1). Lines (model calculations): black solid. Symbols: blue square, experimental data, where references for the experimental data and parameter values given in **Table 3. 1** for two-parameter model, and in **Table 3. 2** for three-parameter model.

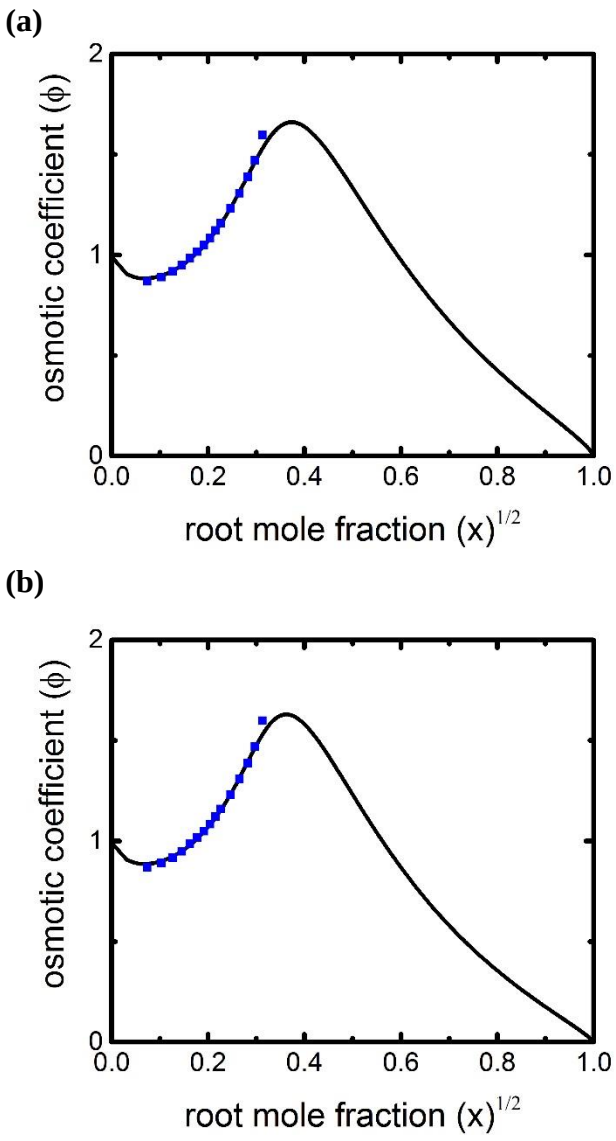

Figure B9. Barium iodide. (a) Two-parameter fitting. (b) Three-parameter fitting. Osmotic coefficient plotted against the square root of the solute mole fraction at 298.15 K (see caption from Figure B1). Lines (model calculations): black solid. Symbols: blue square, experimental data, where references for the experimental data and parameter values given in **Table 3. 1** for two-parameter model, and in **Table 3. 2** for three-parameter model.

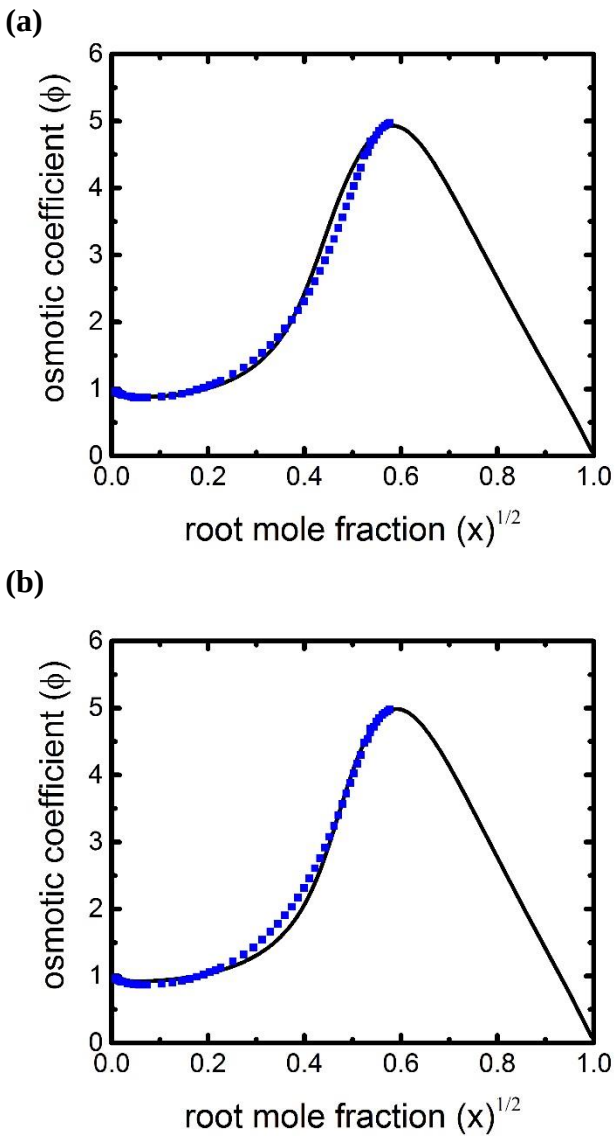

Figure B10. Calcium bromide. (a) Two-parameter fitting. (b) Three-parameter fitting. Osmotic coefficient plotted against the square root of the solute mole fraction at 298.15 K (see caption from Figure B1). Lines (model calculations): black solid. Symbols: blue square, experimental data, where references for the experimental data and parameter values given in **Table 3. 1** for two-parameter model, and in **Table 3. 2** for three-parameter model.

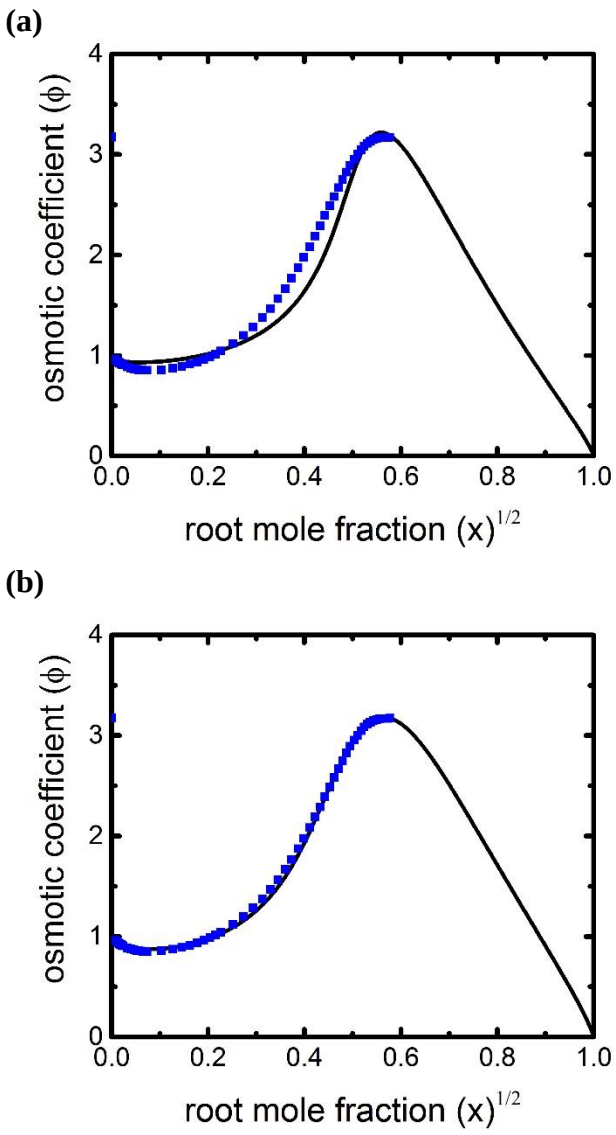

Figure B11. Calcium chloride. (a) Two-parameter fitting. (b) Three-parameter fitting. Osmotic coefficient plotted against the square root of the solute mole fraction at 298.15 K (see caption from Figure B1). Lines (model calculations): black solid. Symbols: blue square, experimental data, where references for the experimental data and parameter values given in **Table 3. 1** for two-parameter model, and in **Table 3. 2** for three-parameter model.

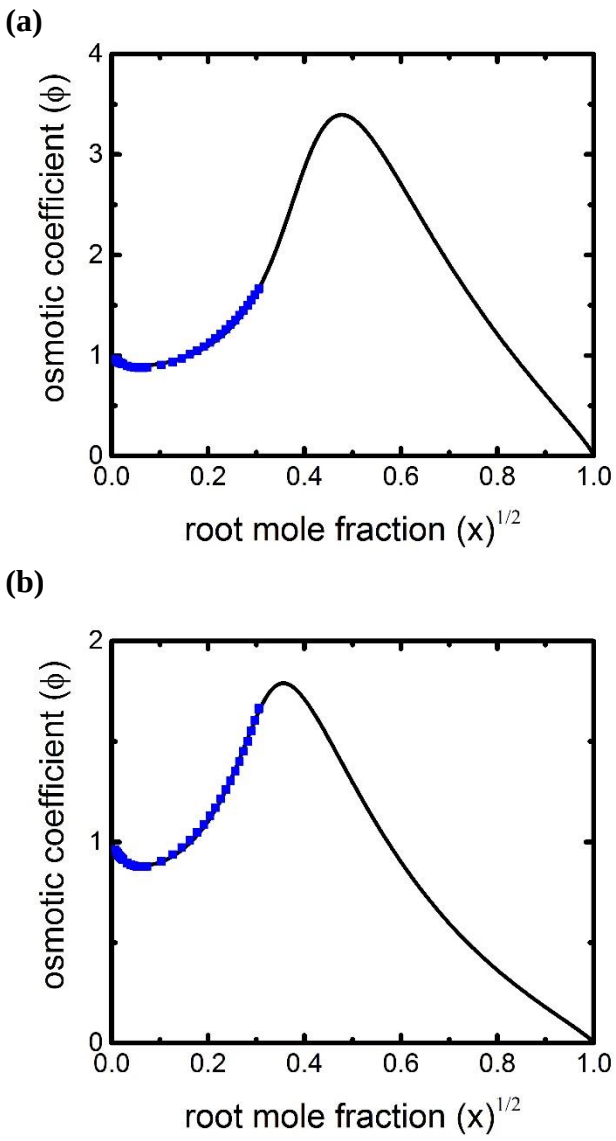

Figure B12. Calcium iodide. (a) Two-parameter fitting. (b) Three-parameter fitting. Osmotic coefficient plotted against the square root of the solute mole fraction at 298.15 K (see caption from Figure B1). Lines (model calculations): black solid. Symbols: blue square, experimental data, where references for the experimental data and parameter values given in **Table 3. 1** for two-parameter model, and in **Table 3. 2** for three-parameter model.

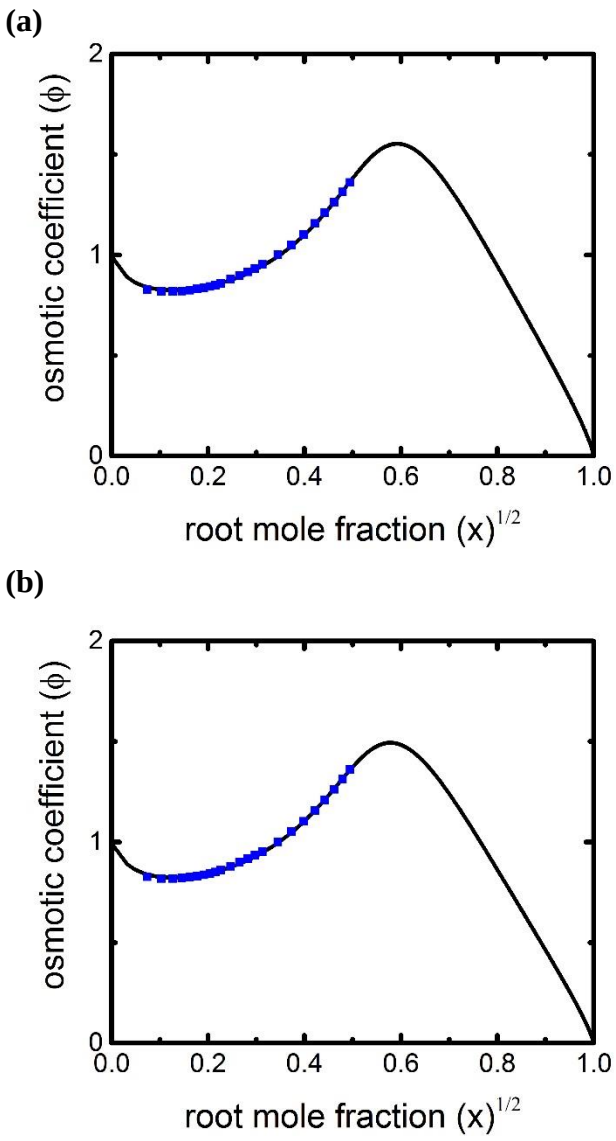

Figure B13. Calcium nitrate. (a) Two-parameter fitting. (b) Three-parameter fitting. Osmotic coefficient plotted against the square root of the solute mole fraction at 298.15 K (see caption from Figure B1). Lines (model calculations): black solid. Symbols: blue square, experimental data, where references for the experimental data and parameter values given in **Table 3. 1** for two-parameter model, and in **Table 3. 2** for three-parameter model.

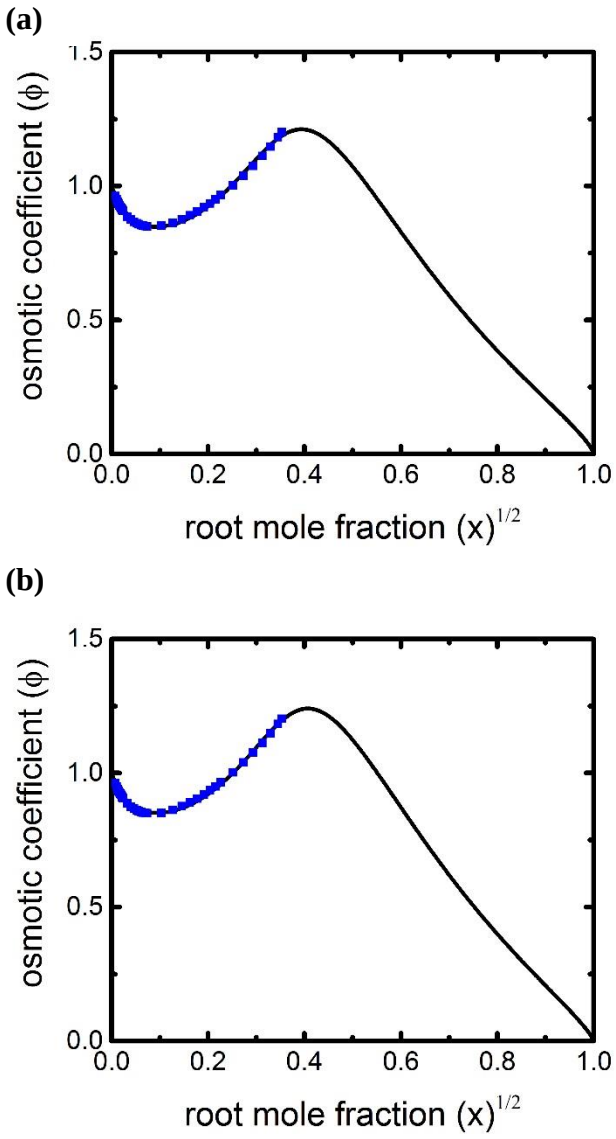

Figure B14. Cadmium nitrate. (a) Two-parameter fitting. (b) Three-parameter fitting. Osmotic coefficient plotted against the square root of the solute mole fraction at 298.15 K (see caption from Figure B1). Lines (model calculations): black solid. Symbols: blue square, experimental data, where references for the experimental data and parameter values given in **Table 3. 1** for two-parameter model, and in **Table 3. 2** for three-parameter model.

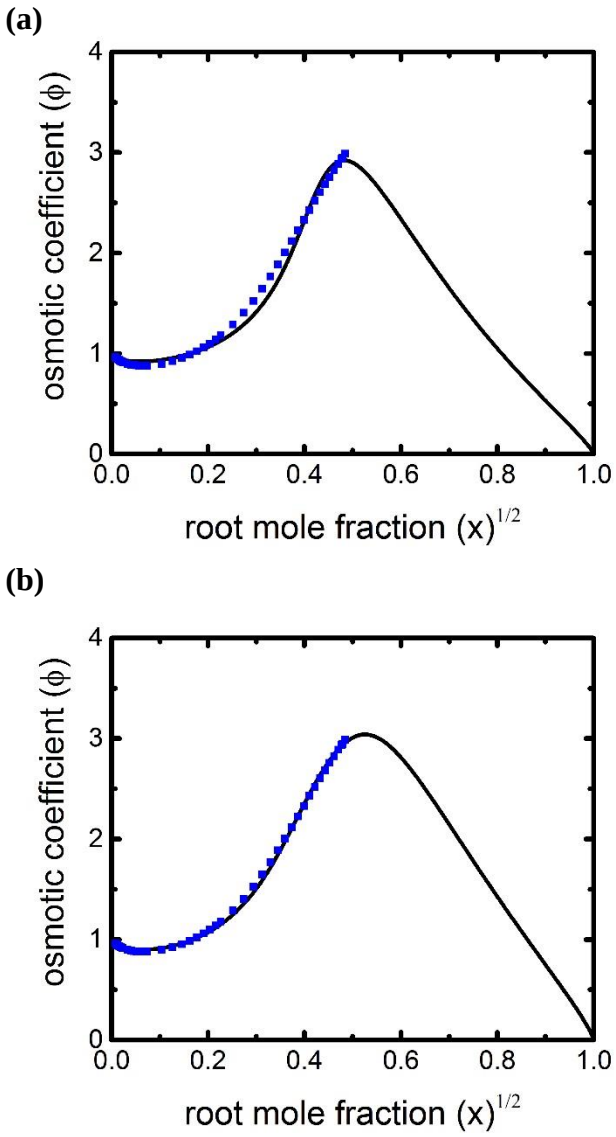

Figure B15. Cobalt bromide. (a) Two-parameter fitting. (b) Three-parameter fitting. Osmotic coefficient plotted against the square root of the solute mole fraction at 298.15 K (see caption from Figure B1). Lines (model calculations): black solid. Symbols: blue square, experimental data, where references for the experimental data and parameter values given in **Table 3. 1** for two-parameter model, and in **Table 3. 2** for three-parameter model.

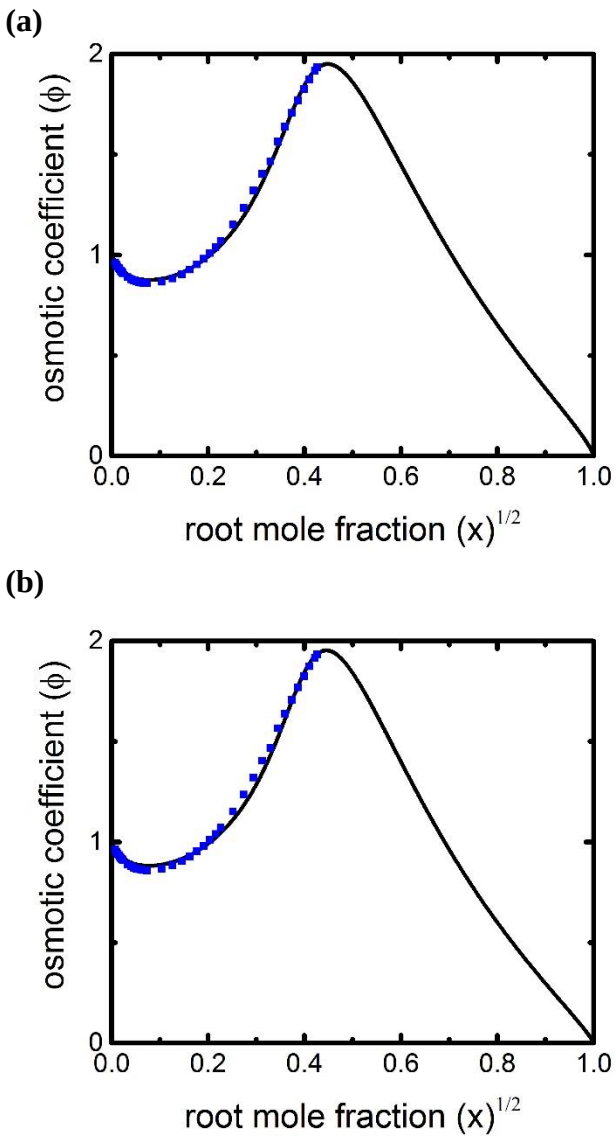

Figure B16. Cobalt chloride. (a) Two-parameter fitting. (b) Three-parameter fitting. Osmotic coefficient plotted against the square root of the solute mole fraction at 298.15 K (see caption from Figure B1). Lines (model calculations): black solid. Symbols: blue square, experimental data, where references for the experimental data and parameter values given in **Table 3. 1** for two-parameter model, and in **Table 3. 2** for three-parameter model.

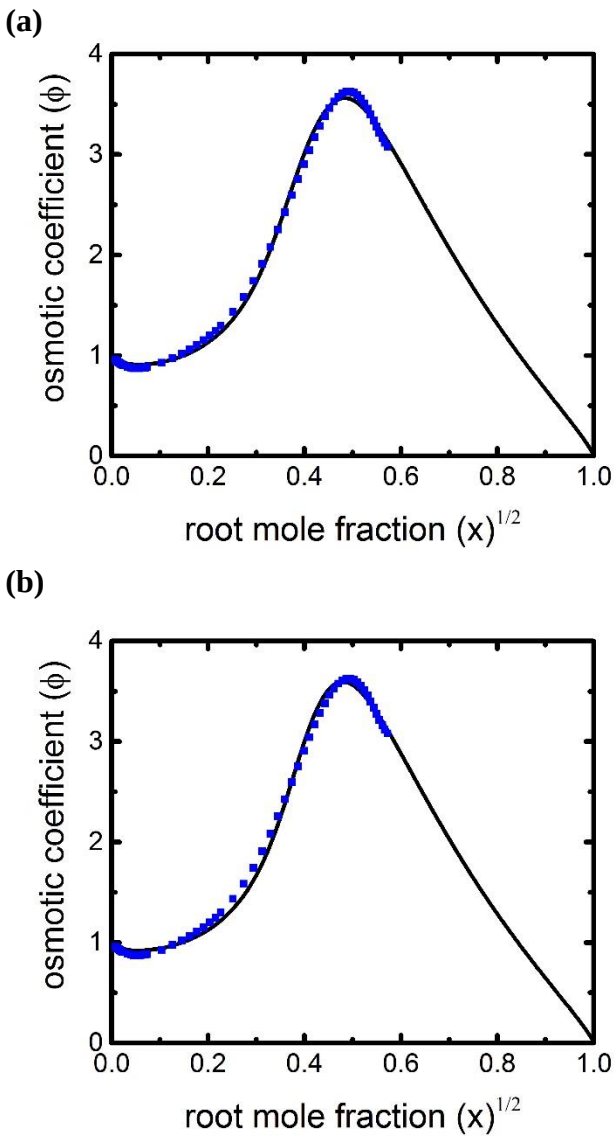

Figure B17. Cobalt iodide. (a) Two-parameter fitting. (b) Three-parameter fitting. Osmotic coefficient plotted against the square root of the solute mole fraction at 298.15 K (see caption from Figure B1). Lines (model calculations): black solid. Symbols: blue square, experimental data, where references for the experimental data and parameter values given in **Table 3. 1** for two-parameter model, and in **Table 3. 2** for three-parameter model.

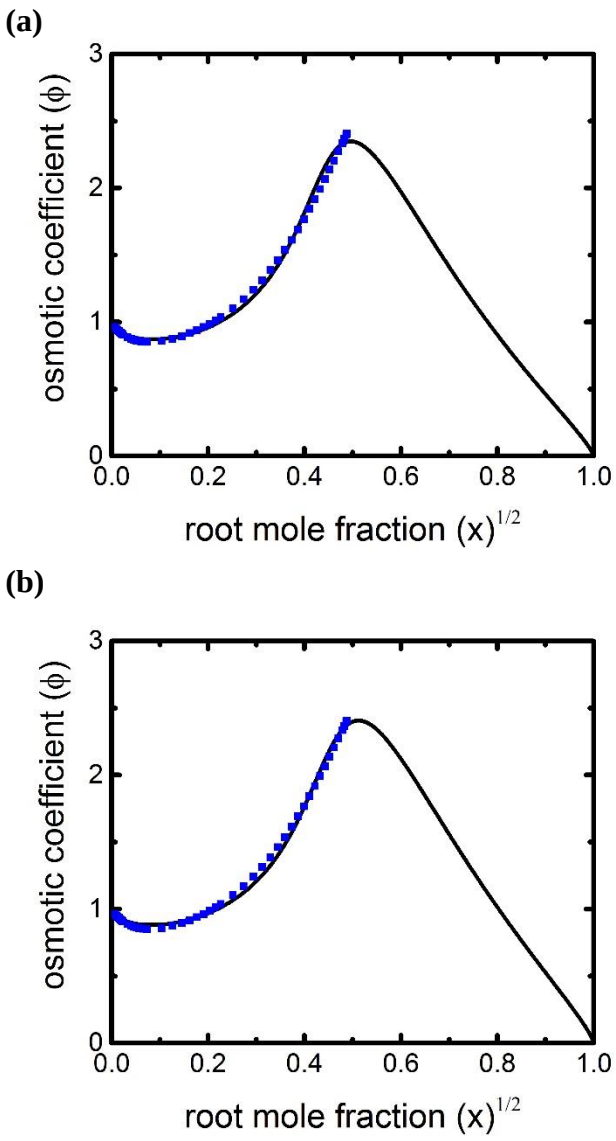

Figure B18. Cobalt nitrate. (a) Two-parameter fitting. (b) Three-parameter fitting. Osmotic coefficient plotted against the square root of the solute mole fraction at 298.15 K (see caption from Figure B1). Lines (model calculations): black solid. Symbols: blue square, experimental data, where references for the experimental data and parameter values given in **Table 3. 1** for two-parameter model, and in **Table 3. 2** for three-parameter model.

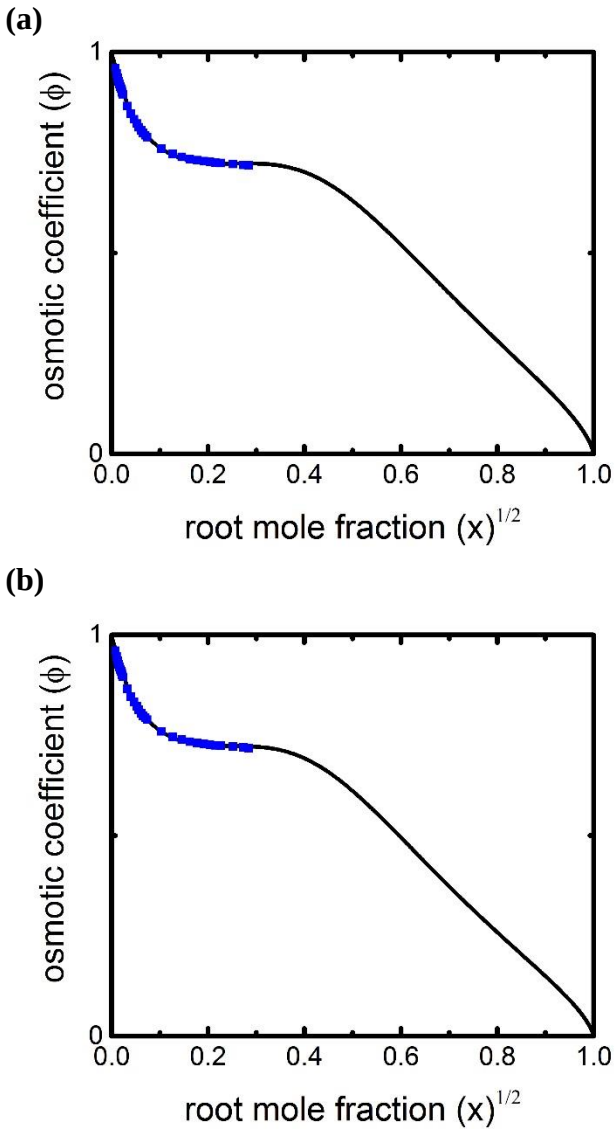

Figure B19. Cesium sulfate. (a) Two-parameter fitting. (b) Three-parameter fitting. Osmotic coefficient plotted against the square root of the solute mole fraction at 298.15 K (see caption from Figure B1). Lines (model calculations): black solid. Symbols: blue square, experimental data, where references for the experimental data and parameter values given in **Table 3. 1** for two-parameter model, and in **Table 3. 2** for three-parameter model.

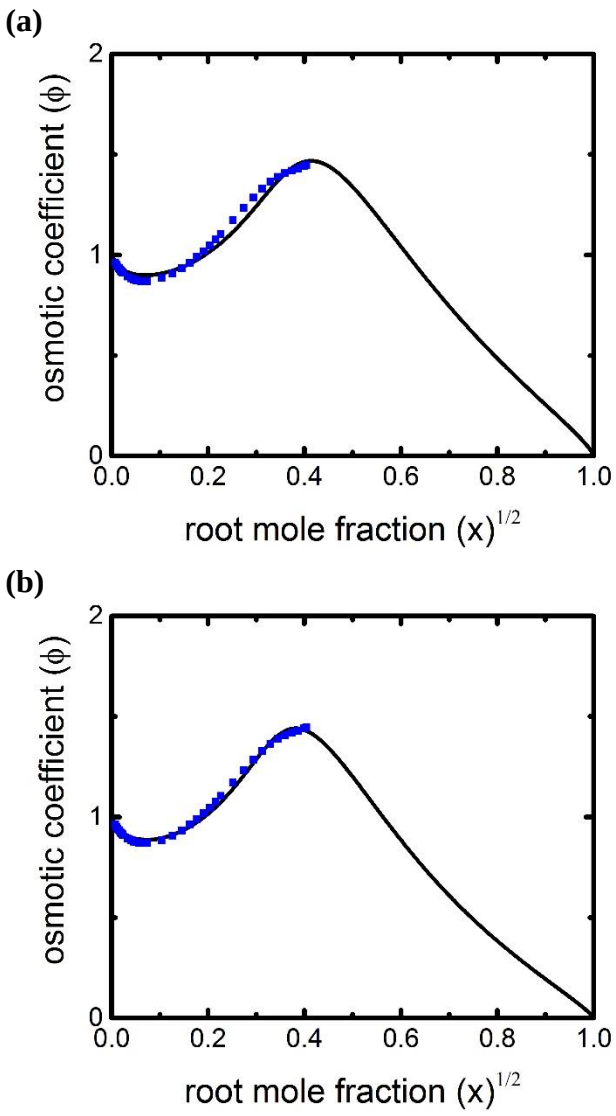

Figure B20. Copper bromide. (a) Two-parameter fitting. (b) Three-parameter fitting. Osmotic coefficient plotted against the square root of the solute mole fraction at 298.15 K (see caption from Figure B1). Lines (model calculations): black solid. Symbols: blue square, experimental data, where references for the experimental data and parameter values given in **Table 3. 1** for two-parameter model, and in **Table 3. 2** for three-parameter model.

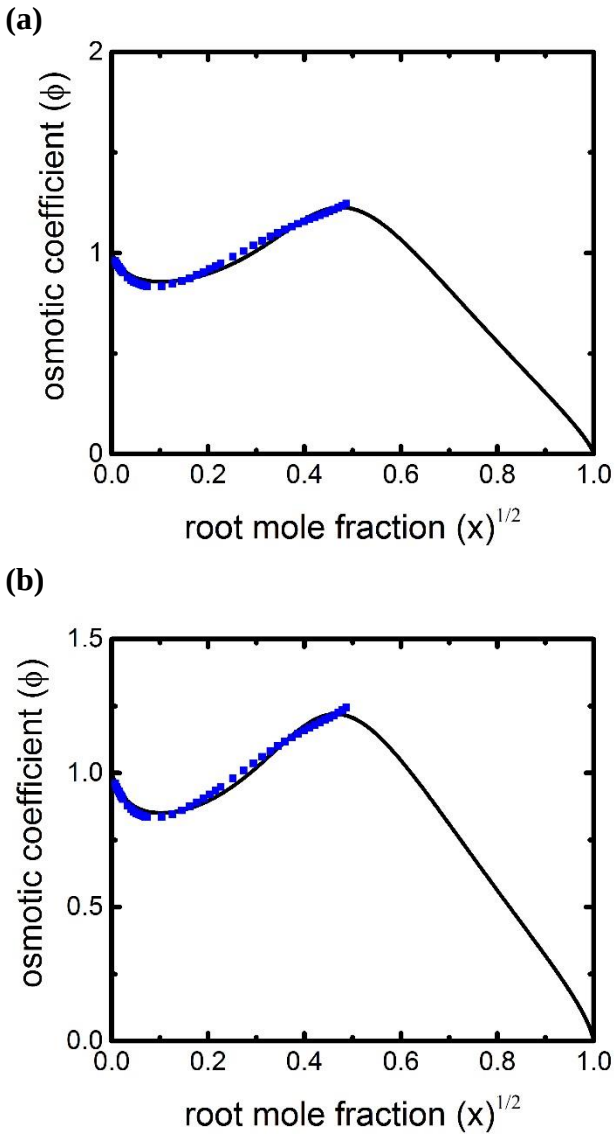

Figure B21. Copper chloride. (a) Two-parameter fitting. (b) Three-parameter fitting. Osmotic coefficient plotted against the square root of the solute mole fraction at 298.15 K (see caption from Figure B1). Lines (model calculations): black solid. Symbols: blue square, experimental data, where references for the experimental data and parameter values given in **Table 3. 1** for two-parameter model, and in **Table 3. 2** for three-parameter model.

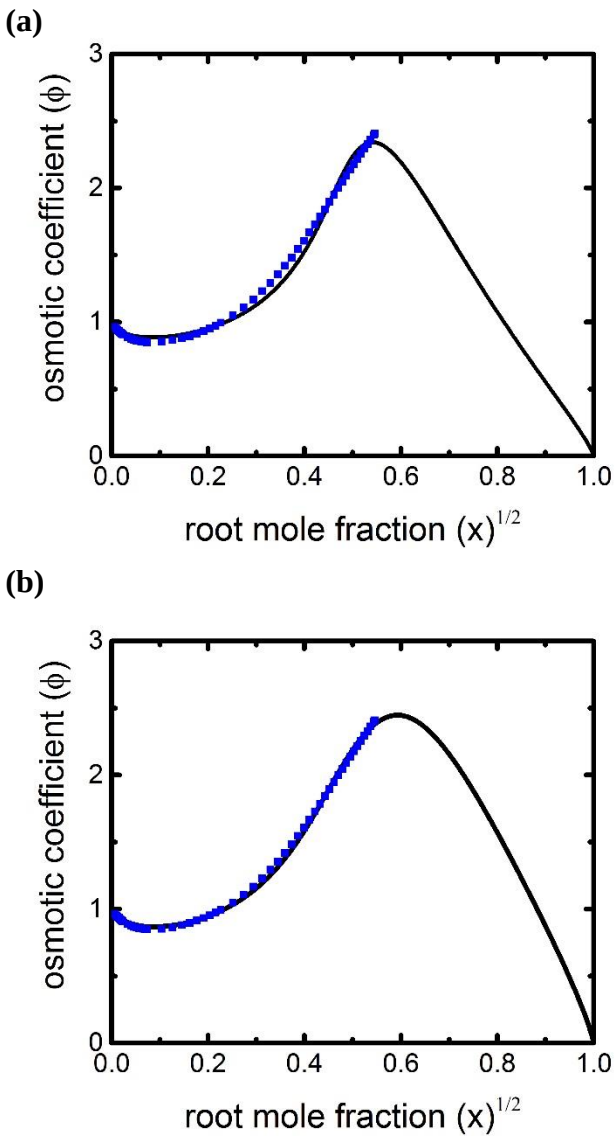

Figure B22. Copper nitrate. (a) Two-parameter fitting. (b) Three-parameter fitting. Osmotic coefficient plotted against the square root of the solute mole fraction at 298.15 K (see caption from Figure B1). Lines (model calculations): black solid. Symbols: blue square, experimental data, where references for the experimental data and parameter values given in **Table 3. 1** for two-parameter model, and in **Table 3. 2** for three-parameter model.

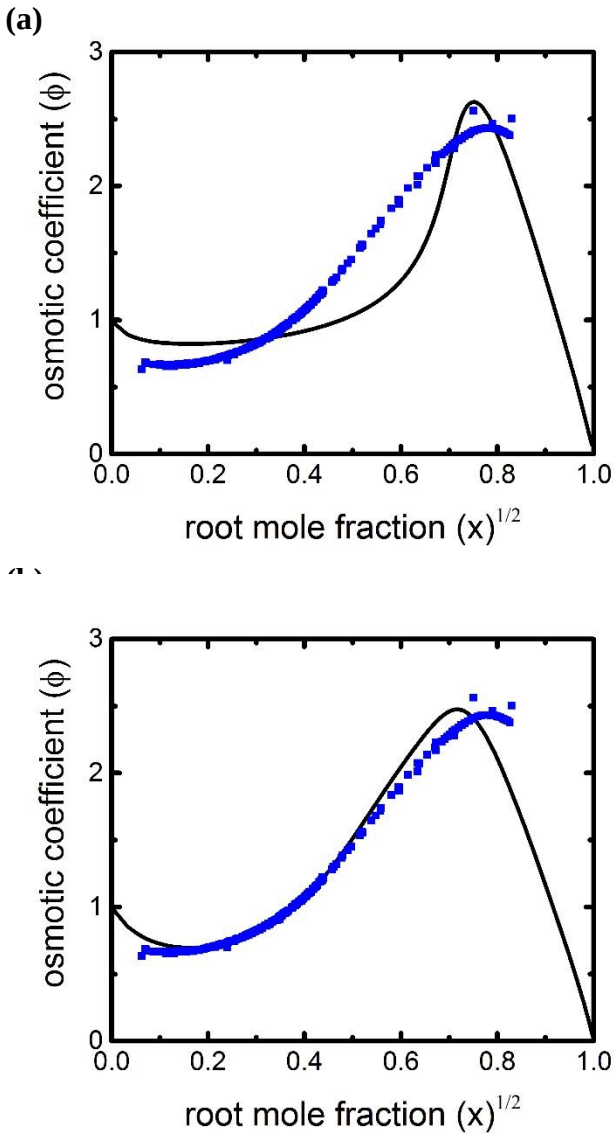

Figure B23. Sulfuric acid. (a) Two-parameter fitting. (b) Three-parameter fitting. Osmotic coefficient plotted against the square root of the solute mole fraction at 298.15 K (see caption from Figure B1). Lines (model calculations): black solid. Symbols: blue square, experimental data, where references for the experimental data and parameter values given in **Table 3. 1** for two-parameter model, and in **Table 3. 2** for three-parameter model. H_2SO_4 is treated separately in section 3.4 by consideration of partial dissociation of the bisulfate ion.

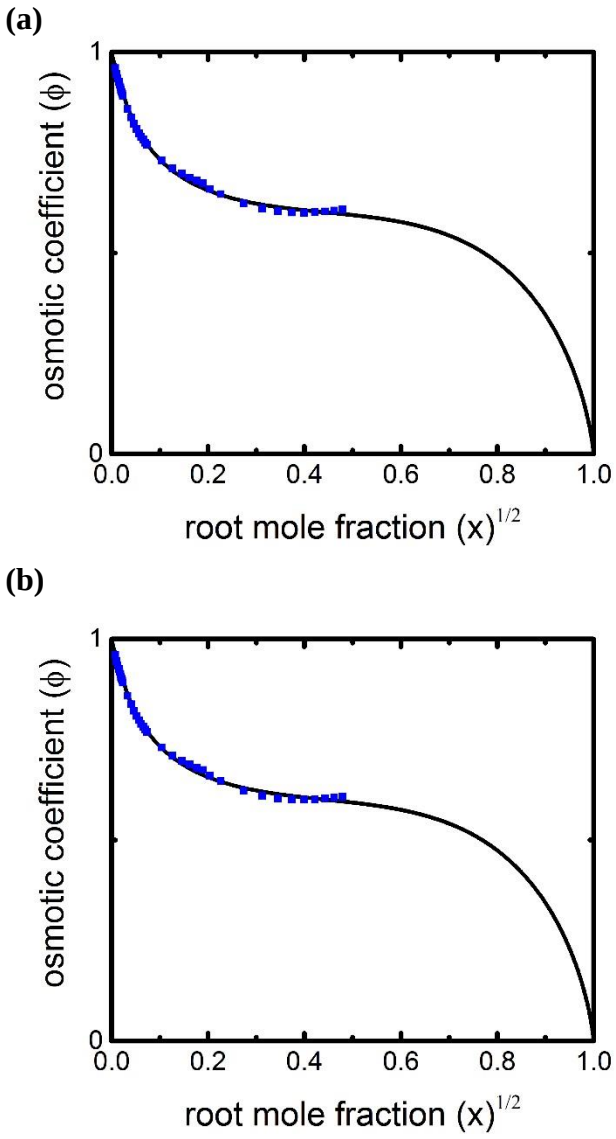

Figure B24. Potassium sulfate. (a) Two-parameter fitting. (b) Three-parameter fitting. Osmotic coefficient plotted against the square root of the solute mole fraction at 298.15 K (see caption from Figure B1). Lines (model calculations): black solid. Symbols: blue square, experimental data, where references for the experimental data and parameter values given in **Table 3. 1** for two-parameter model, and in **Table 3. 2** for three-parameter model.

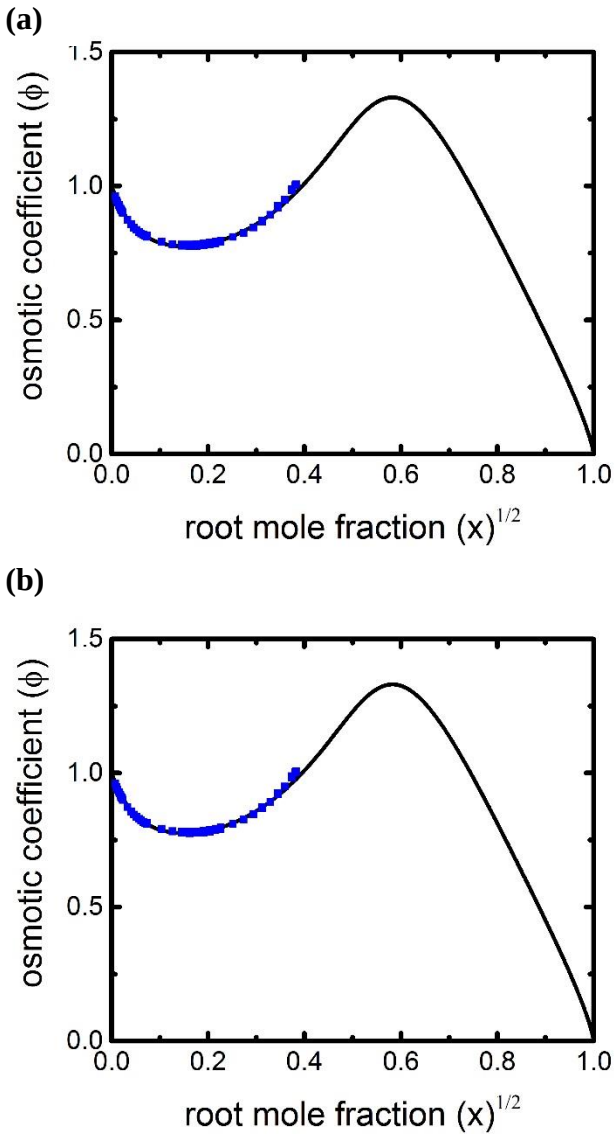

Figure B25. Lithium sulfate. (a) Two-parameter fitting. (b) Three-parameter fitting. Osmotic coefficient plotted against the square root of the solute mole fraction at 298.15 K (see caption from Figure B1). Lines (model calculations): black solid. Symbols: blue square, experimental data, where references for the experimental data and parameter values given in **Table 3. 1** for two-parameter model, and in **Table 3. 2** for three-parameter model.

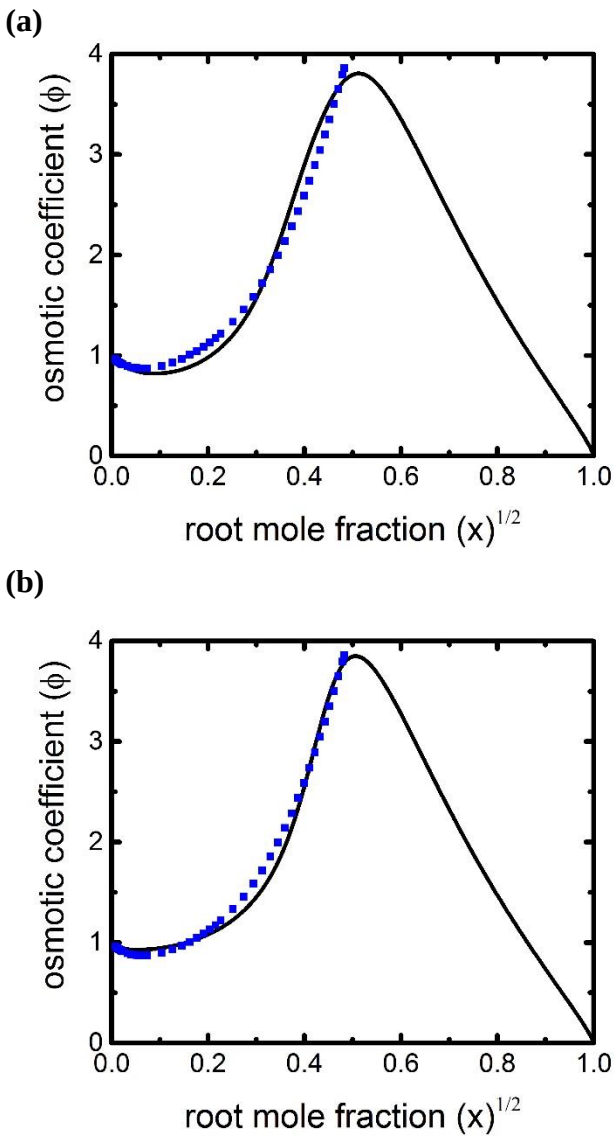

Figure B26. Magnesium bromide. (a) Two-parameter fitting. (b) Three-parameter fitting. Osmotic coefficient plotted against the square root of the solute mole fraction at 298.15 K (see caption from Figure B1). Lines (model calculations): black solid. Symbols: blue square, experimental data, where references for the experimental data and parameter values given in **Table 3. 1** for two-parameter model, and in **Table 3. 2** for three-parameter model.

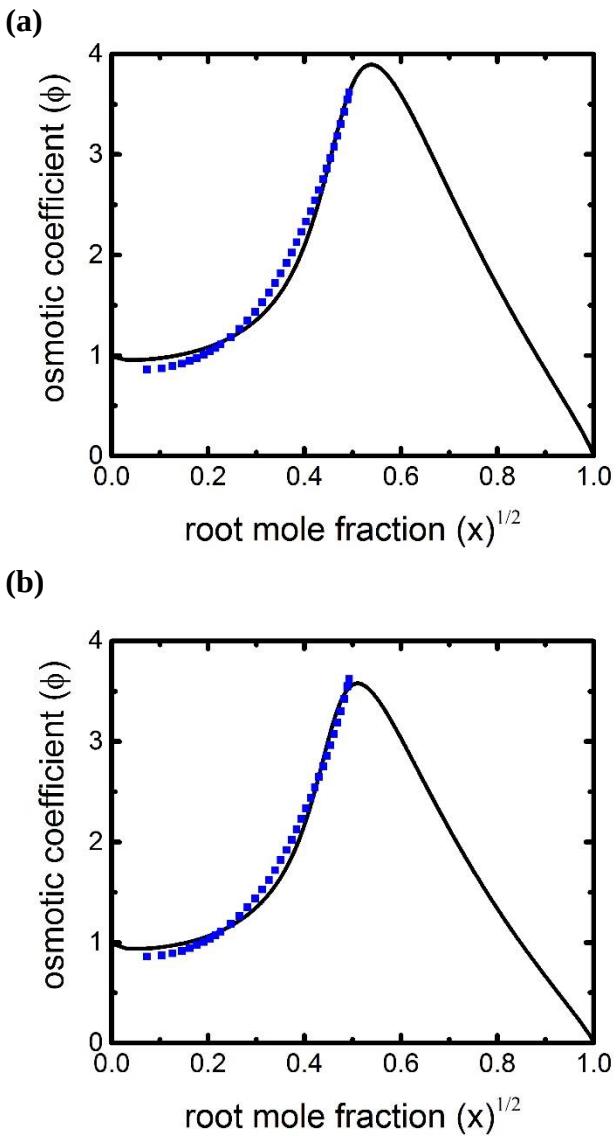

Figure B27. Magnesium chloride. (a) Two-parameter fitting. (b) Three-parameter fitting. Osmotic coefficient plotted against the square root of the solute mole fraction at 298.15 K (see caption from Figure B1). Lines (model calculations): black solid. Symbols: blue square, experimental data, where references for the experimental data and parameter values given in **Table 3. 1** for two-parameter model, and in **Table 3. 2** for three-parameter model.

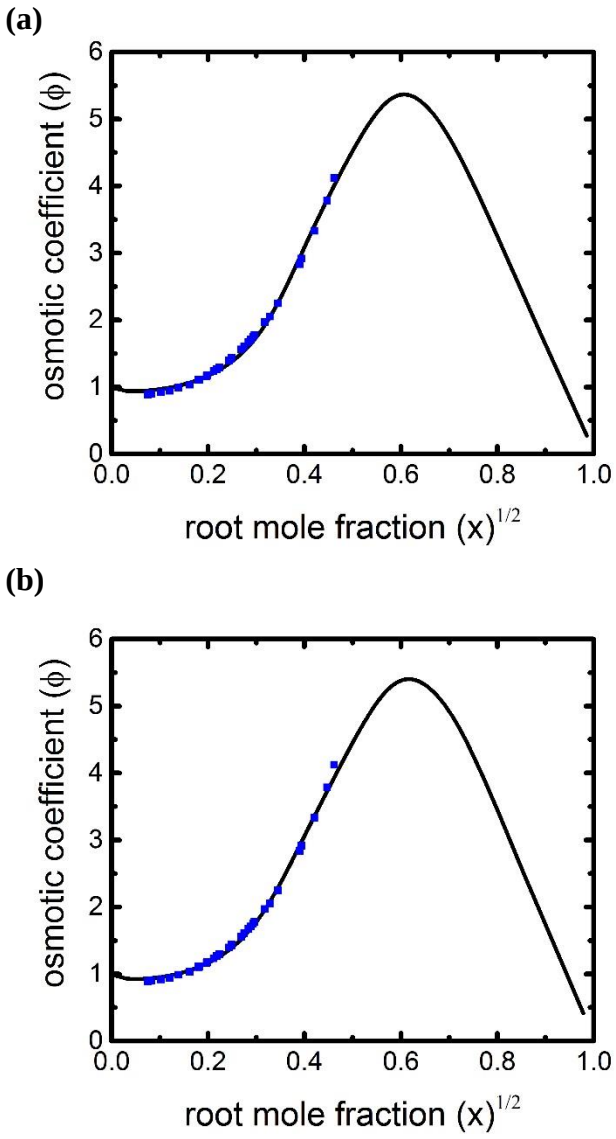

Figure B28. Magnesium iodide. (a) Two-parameter fitting. (b) Three-parameter fitting. Osmotic coefficient plotted against the square root of the solute mole fraction at 298.15 K (see caption from Figure B1). Lines (model calculations): black solid. Symbols: blue square, experimental data, where references for the experimental data and parameter values given in **Table 3. 1** for two-parameter model, and in **Table 3. 2** for three-parameter model.

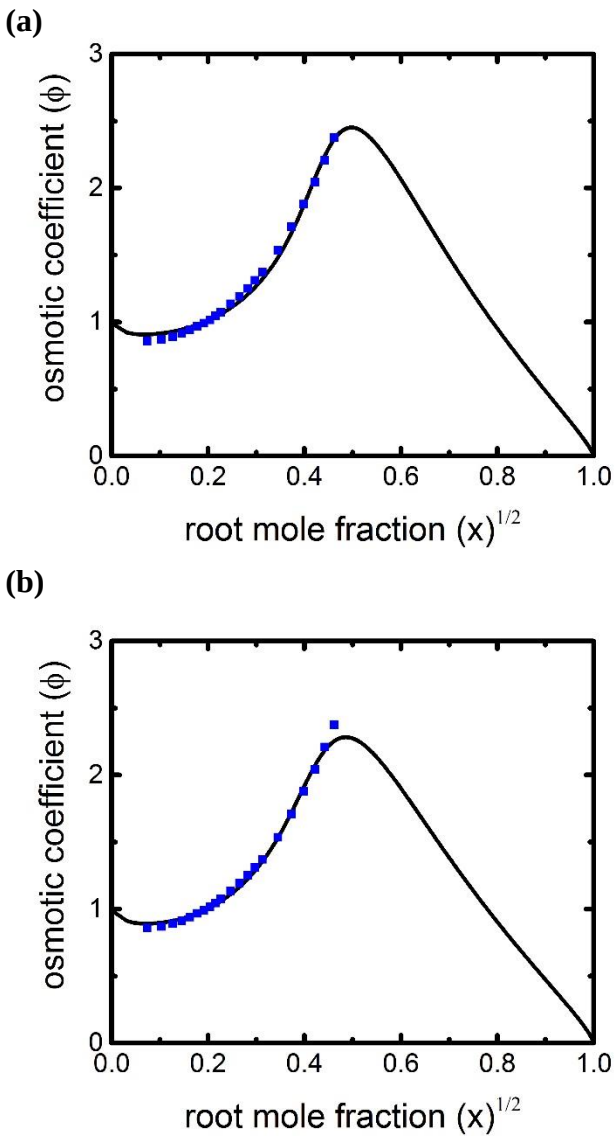

Figure B29. Magnesium nitrate. (a) Two-parameter fitting. (b) Three-parameter fitting. Osmotic coefficient plotted against the square root of the solute mole fraction at 298.15 K (see caption from Figure B1). Lines (model calculations): black solid. Symbols: blue square, experimental data, where references for the experimental data and parameter values given in **Table 3. 1** for two-parameter model, and in **Table 3. 2** for three-parameter model.

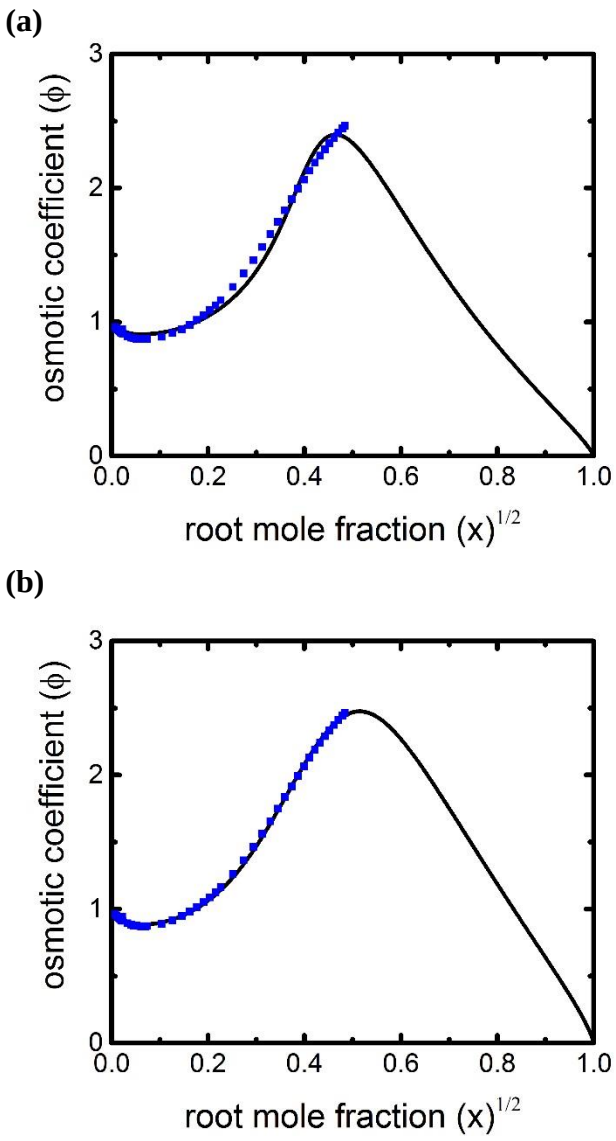

Figure B30. Manganese bromide. (a) Two-parameter fitting. (b) Three-parameter fitting. Osmotic coefficient plotted against the square root of the solute mole fraction at 298.15 K (see caption from Figure B1). Lines (model calculations): black solid. Symbols: blue square, experimental data, where references for the experimental data and parameter values given in **Table 3. 1** for two-parameter model, and in **Table 3. 2** for three-parameter model.

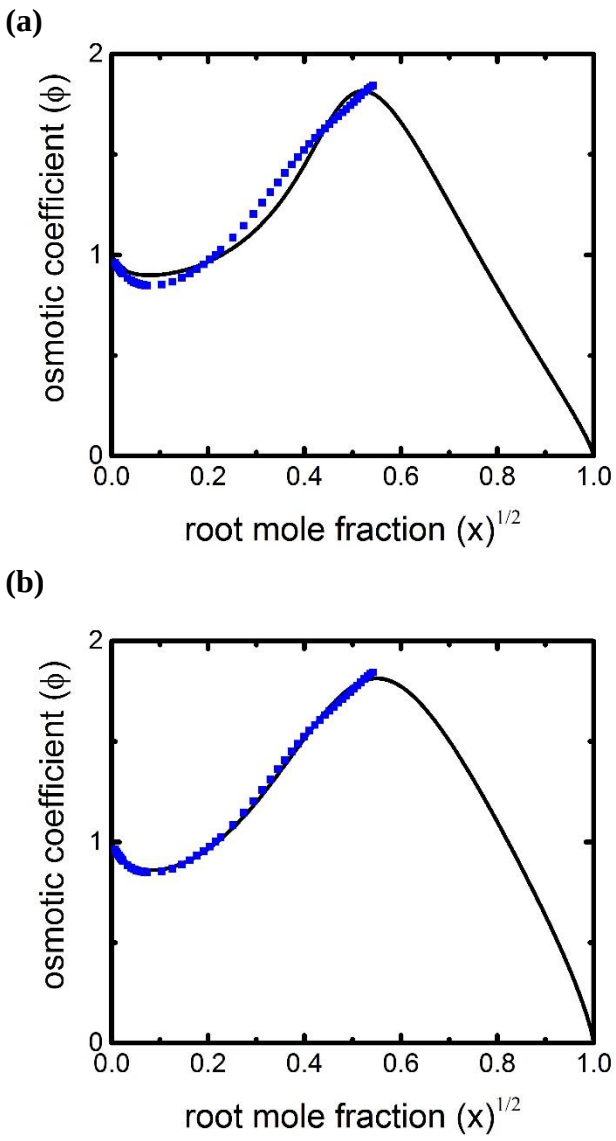

Figure B31. Manganese chloride. (a) Two-parameter fitting. (b) Three-parameter fitting. Osmotic coefficient plotted against the square root of the solute mole fraction at 298.15 K (see caption from Figure B1). Lines (model calculations): black solid. Symbols: blue square, experimental data, where references for the experimental data and parameter values given in **Table 3. 1** for two-parameter model, and in **Table 3. 2** for three-parameter model.

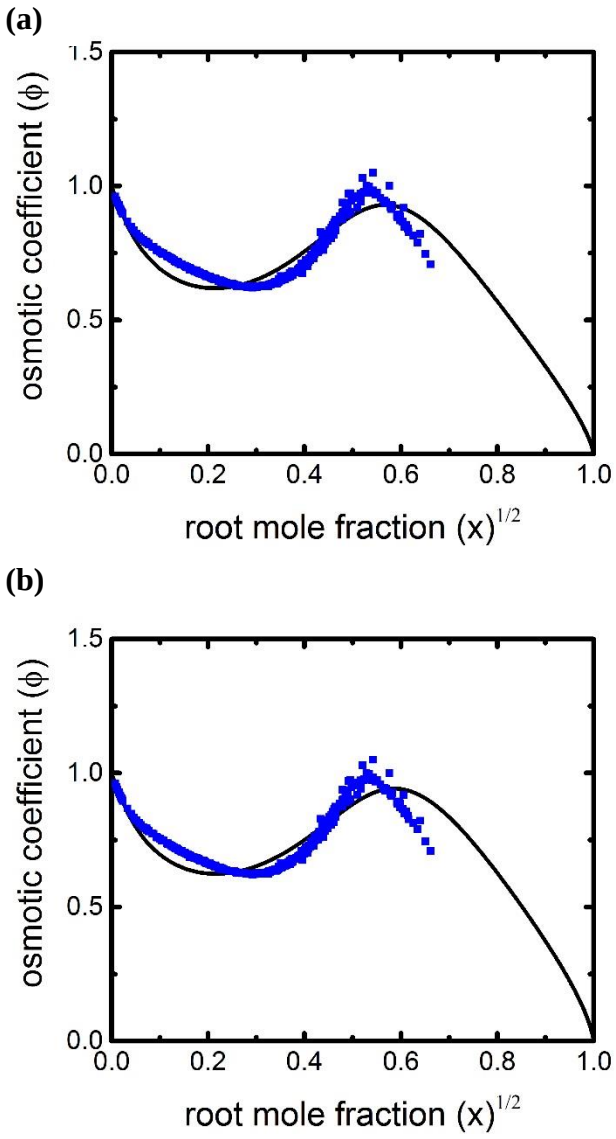

Figure B32. Sodium sulfate. (a) Two-parameter fitting. (b) Three-parameter fitting. Osmotic coefficient plotted against the square root of the solute mole fraction at 298.15 K (see caption from Figure B1). Lines (model calculations): black solid. Symbols: blue square, experimental data, where references for the experimental data and parameter values given in **Table 3. 1** for two-parameter model, and in **Table 3. 2** for three-parameter model.

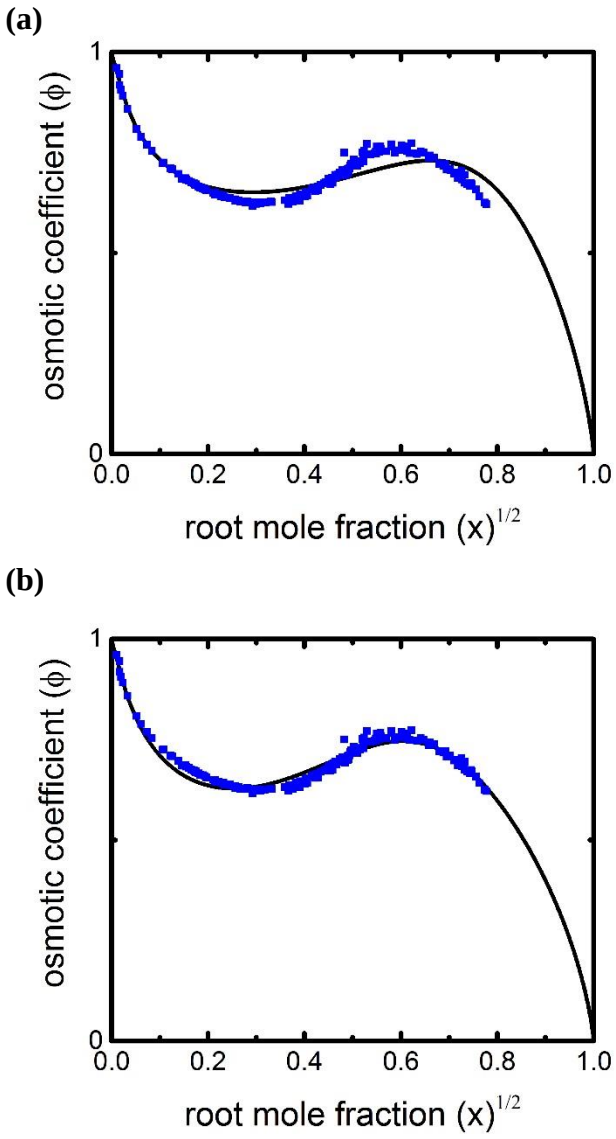

Figure B33. Ammonium sulfate. (a) Two-parameter fitting. (b) Three-parameter fitting. Osmotic coefficient plotted against the square root of the solute mole fraction at 298.15 K (see caption from Figure B1). Lines (model calculations): black solid. Symbols: blue square, experimental data, where references for the experimental data and parameter values given in **Table 3. 1** for two-parameter model, and in **Table 3. 2** for three-parameter model.

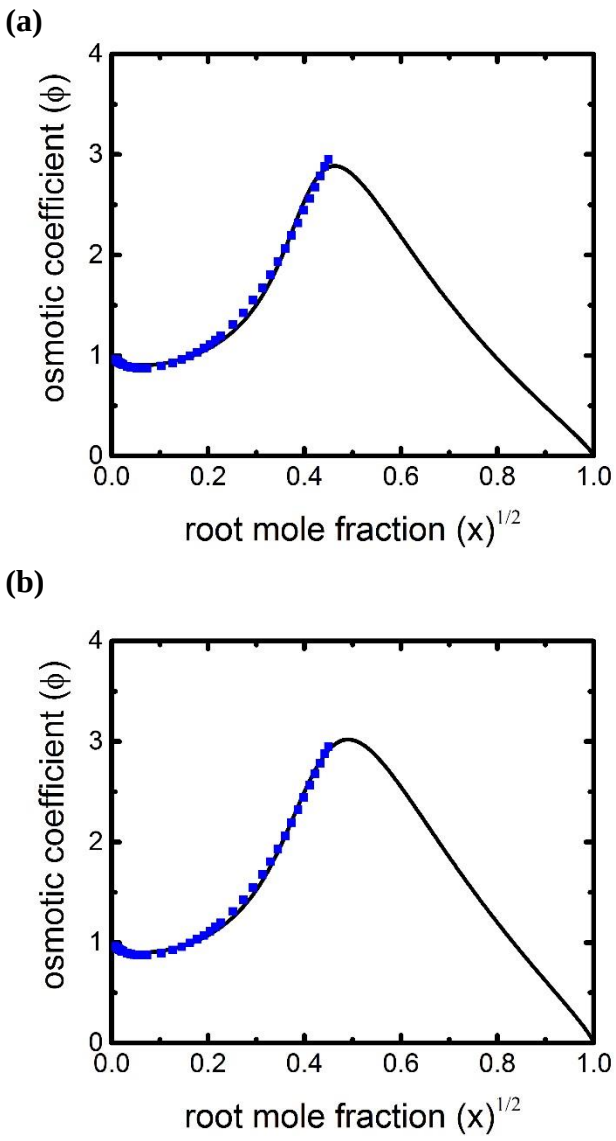

Figure B34. Nickel bromide. (a) Two-parameter fitting. (b) Three-parameter fitting. Osmotic coefficient plotted against the square root of the solute mole fraction at 298.15 K (see caption from Figure B1). Lines (model calculations): black solid. Symbols: blue square, experimental data, where references for the experimental data and parameter values given in **Table 3. 1** for two-parameter model, and in **Table 3. 2** for three-parameter model.

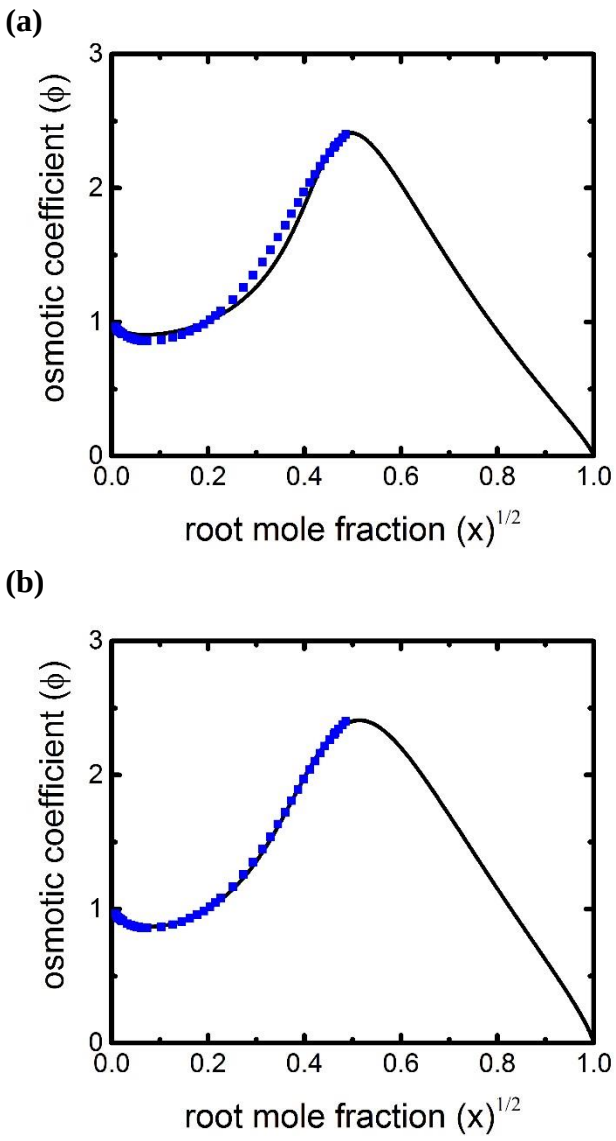

Figure B35. Nickel chloride. (a) Two-parameter fitting. (b) Three-parameter fitting. Osmotic coefficient plotted against the square root of the solute mole fraction at 298.15 K (see caption from Figure B1). Lines (model calculations): black solid. Symbols: blue square, experimental data, where references for the experimental data and parameter values given in **Table 3. 1** for two-parameter model, and in **Table 3. 2** for three-parameter model.

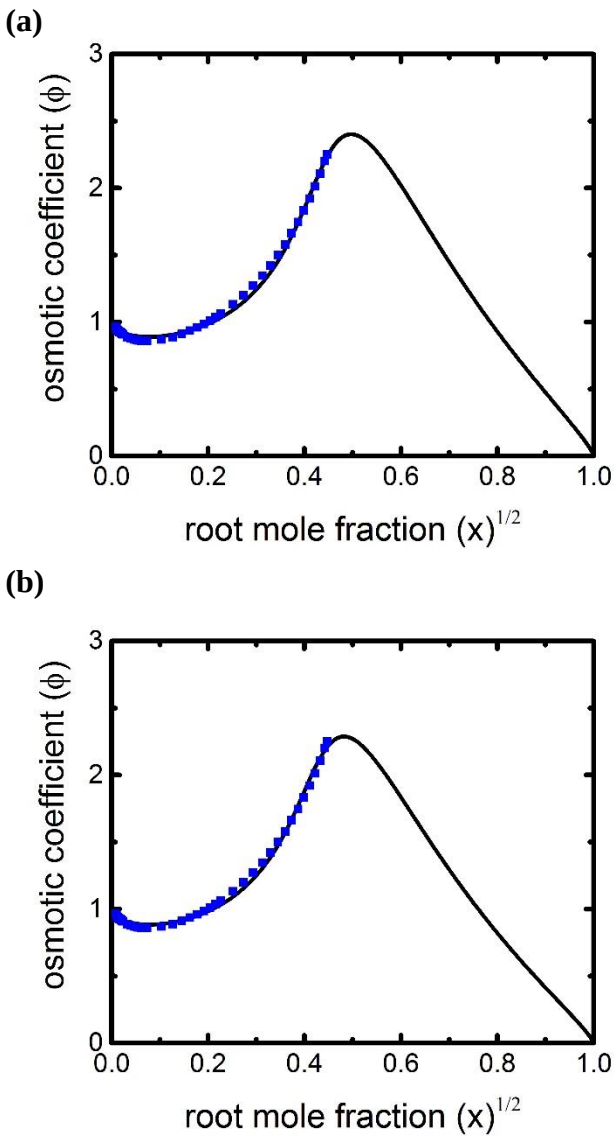

Figure B36. Nickel nitrate. (a) Two-parameter fitting. (b) Three-parameter fitting. Osmotic coefficient plotted against the square root of the solute mole fraction at 298.15 K (see caption from Figure B1). Lines (model calculations): black solid. Symbols: blue square, experimental data, where references for the experimental data and parameter values given in **Table 3. 1** for two-parameter model, and in **Table 3. 2** for three-parameter model.

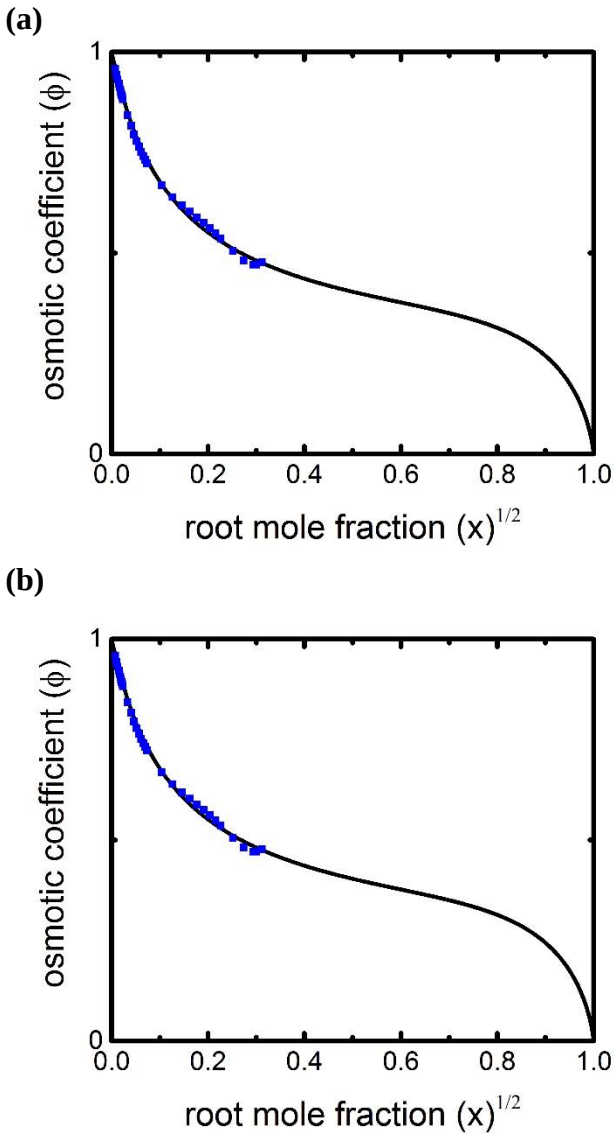

Figure B37. Lead nitrate. (a) Two-parameter fitting. (b) Three-parameter fitting. Osmotic coefficient plotted against the square root of the solute mole fraction at 298.15 K (see caption from Figure B1). Lines (model calculations): black solid. Symbols: blue square, experimental data, where references for the experimental data and parameter values given in **Table 3. 1** for two-parameter model, and in **Table 3. 2** for three-parameter model.

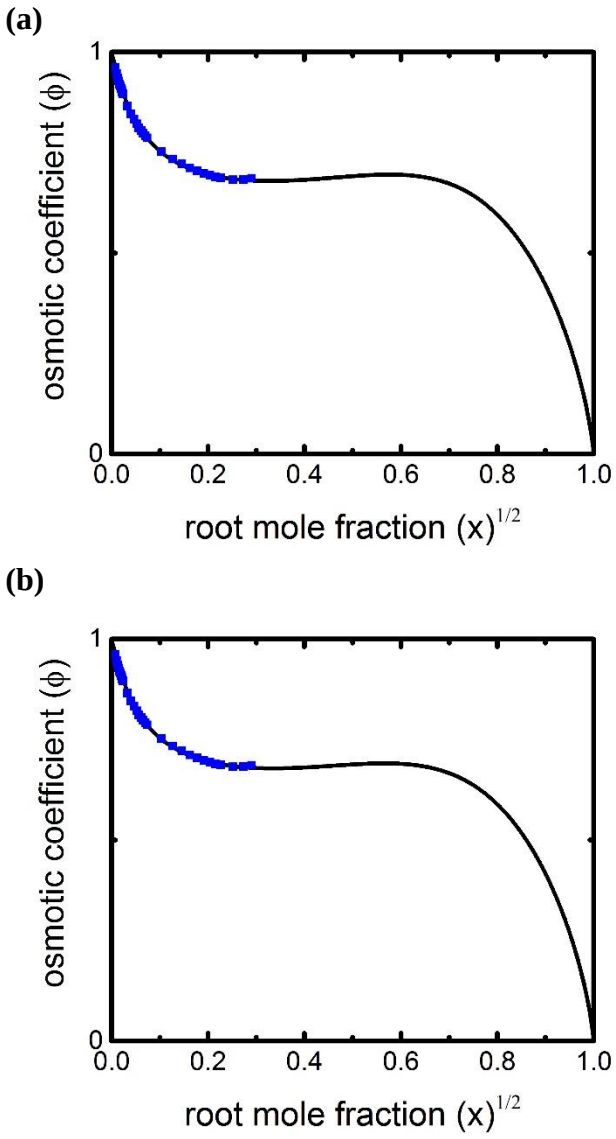

Figure B38. Rubidium sulfate. (a) Two-parameter fitting. (b) Three-parameter fitting. Osmotic coefficient plotted against the square root of the solute mole fraction at 298.15 K (see caption from Figure B1). Lines (model calculations): black solid. Symbols: blue square, experimental data, where references for the experimental data and parameter values given in **Table 3. 1** for two-parameter model, and in **Table 3. 2** for three-parameter model.

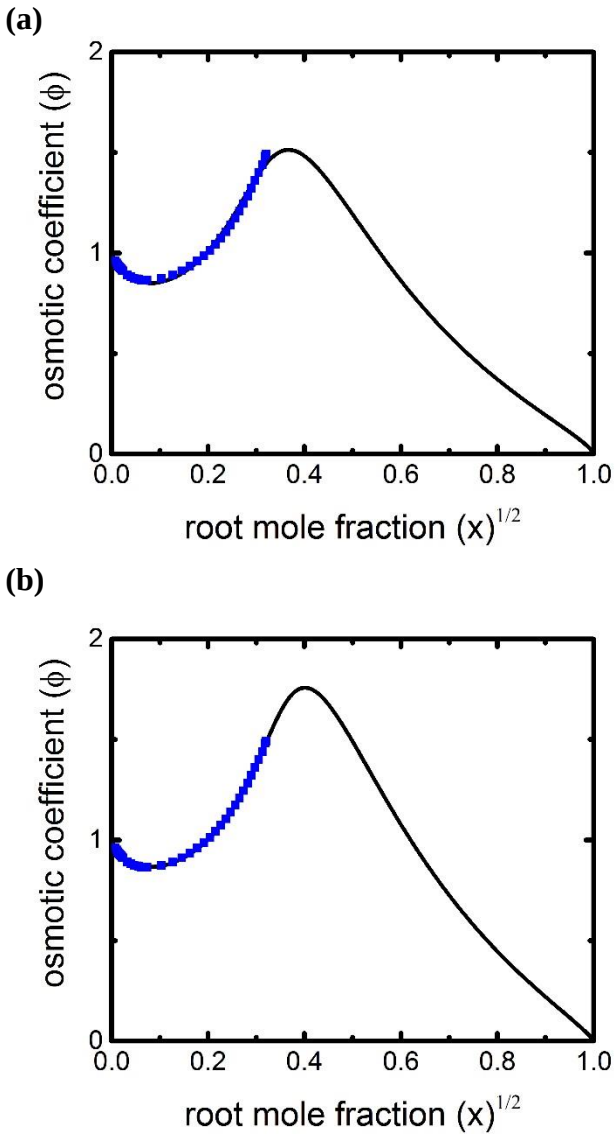

Figure B39. Strontium bromide. (a) Two-parameter fitting. (b) Three-parameter fitting. Osmotic coefficient plotted against the square root of the solute mole fraction at 298.15 K (see caption from Figure B1). Lines (model calculations): black solid. Symbols: blue square, experimental data, where references for the experimental data and parameter values given in **Table 3. 1** for two-parameter model, and in **Table 3. 2** for three-parameter model.

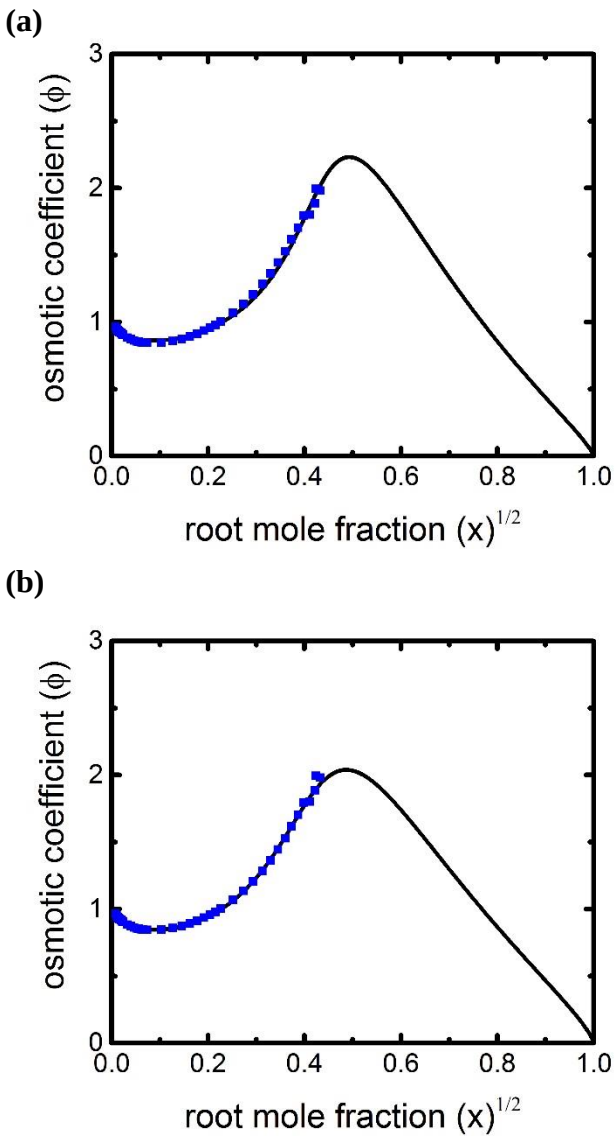

Figure B40. Strontium chloride. (a) Two-parameter fitting. (b) Three-parameter fitting. Osmotic coefficient plotted against the square root of the solute mole fraction at 298.15 K (see caption from Figure B1). Lines (model calculations): black solid. Symbols: blue square, experimental data, where references for the experimental data and parameter values given in **Table 3. 1** for two-parameter model, and in **Table 3. 2** for three-parameter model.

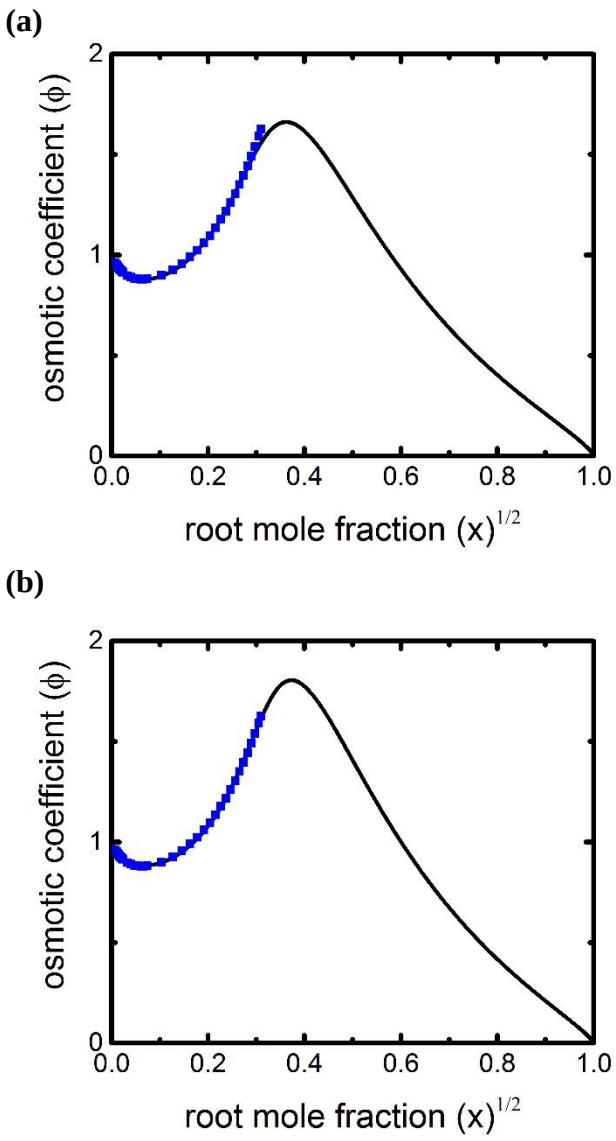

Figure B41. Strontium iodide. (a) Two-parameter fitting. (b) Three-parameter fitting. Osmotic coefficient plotted against the square root of the solute mole fraction at 298.15 K (see caption from Figure B1). Lines (model calculations): black solid. Symbols: blue square, experimental data, where references for the experimental data and parameter values given in **Table 3. 1** for two-parameter model, and in **Table 3. 2** for three-parameter model.

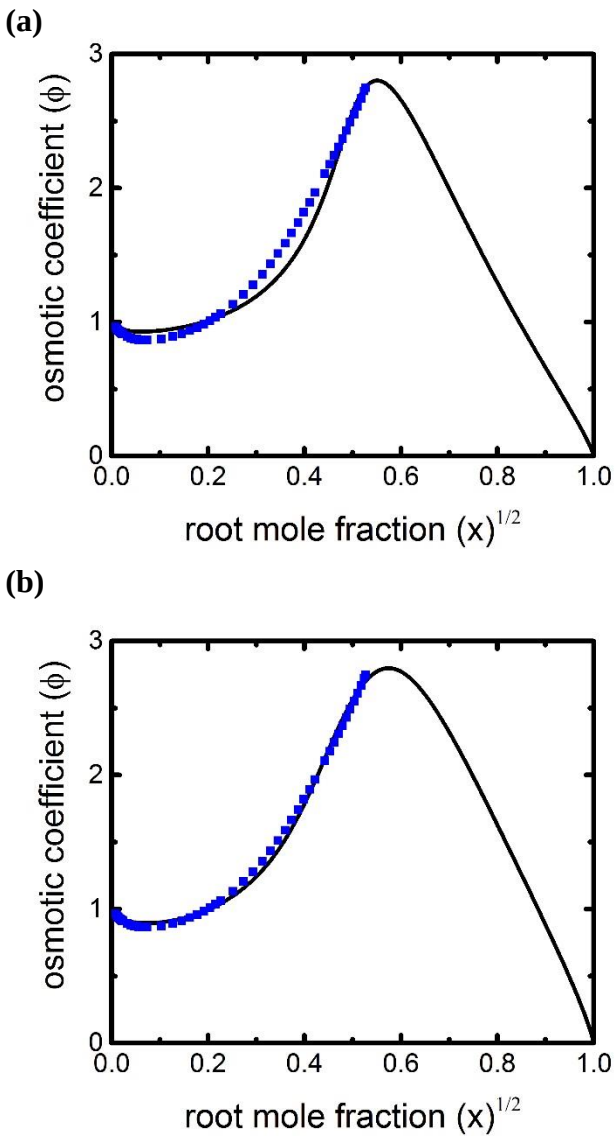

Figure B42. Zinc nitrate. (a) Two-parameter fitting. (b) Three-parameter fitting. Osmotic coefficient plotted against the square root of the solute mole fraction at 298.15 K (see caption from Figure B1). Lines (model calculations): black solid. Symbols: blue square, experimental data, where references for the experimental data and parameter values given in **Table 3. 1** for two-parameter model, and in **Table 3. 2** for three-parameter model.

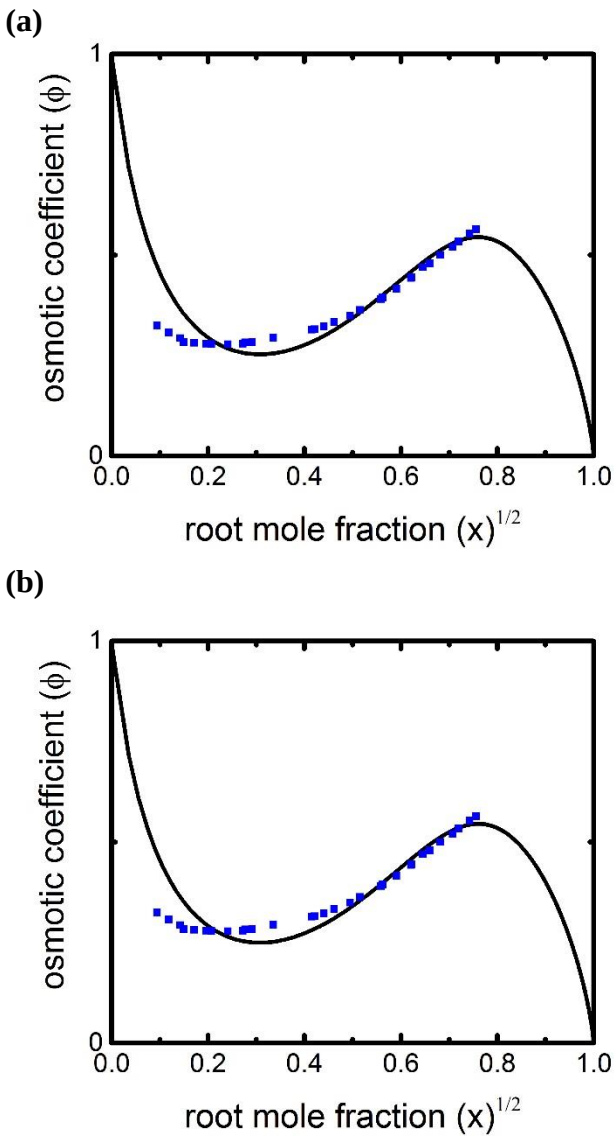

Figure B43. Phosphoric acid. (a) Two-parameter fitting. (b) Three-parameter fitting. Osmotic coefficient plotted against the square root of the solute mole fraction at 298.15 K (see caption from Figure B1). Lines (model calculations): black solid. Symbols: blue square, experimental data, where references for the experimental data and parameter values given in **Table 3. 3** for two-parameter model, and in **Table 3. 4** for three-parameter model.

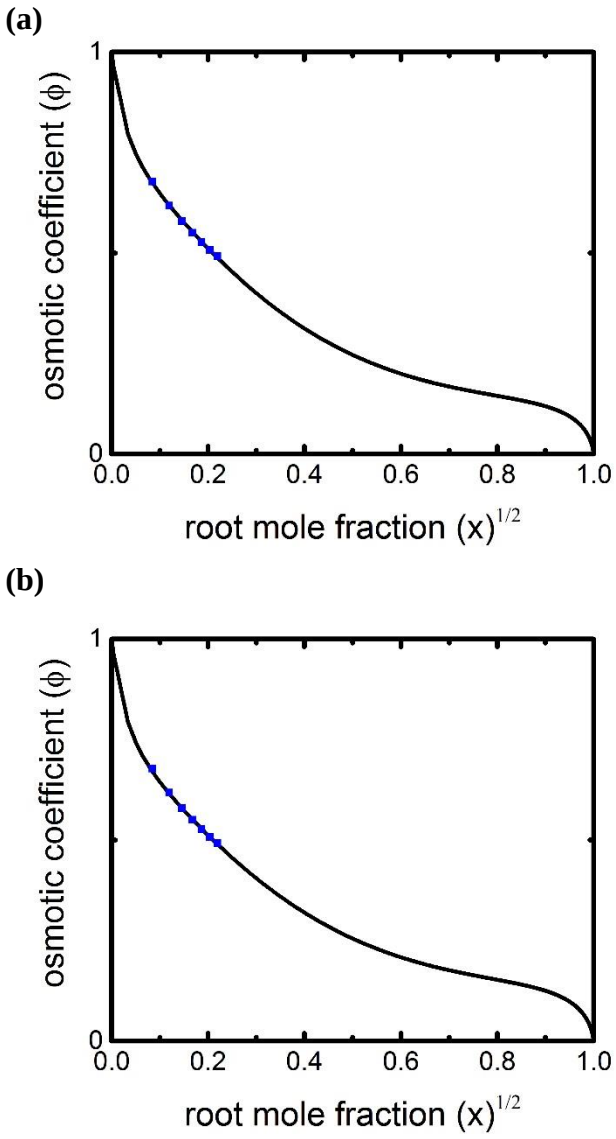

Figure B44. Sodium phosphate. (a) Two-parameter fitting. (b) Three-parameter fitting. Osmotic coefficient plotted against the square root of the solute mole fraction at 298.15 K (see caption from Figure B1). Lines (model calculations): black solid. Symbols: blue square, experimental data, where references for the experimental data and parameter values given in **Table 3. 3** for two-parameter model, and in **Table 3. 4** for three-parameter model.

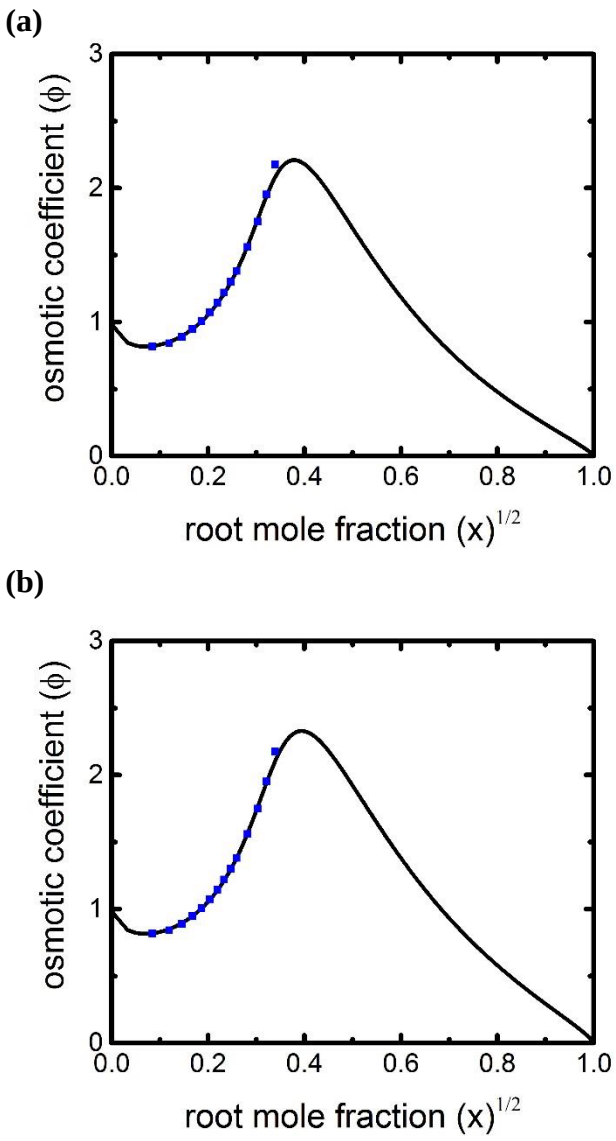

Figure B45. Aluminium chloride. (a) Two-parameter fitting. (b) Three-parameter fitting. Osmotic coefficient plotted against the square root of the solute mole fraction at 298.15 K (see caption from Figure B1). Lines (model calculations): black solid. Symbols: blue square, experimental data, where references for the experimental data and parameter values given in **Table 3. 3** for two-parameter model, and in **Table 3. 4** for three-parameter model.

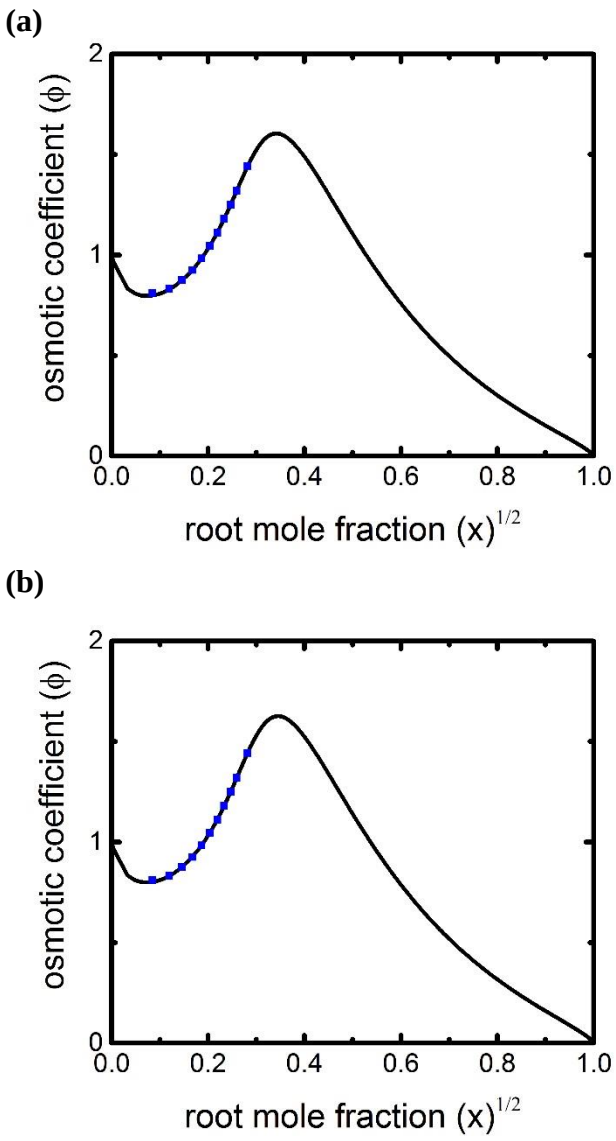

Figure B46. Chromium chloride. (a) Two-parameter fitting. (b) Three-parameter fitting. Osmotic coefficient plotted against the square root of the solute mole fraction at 298.15 K (see caption from Figure B1). Lines (model calculations): black solid. Symbols: blue square, experimental data, where references for the experimental data and parameter values given in **Table 3. 3** for two-parameter model, and in **Table 3. 4** for three-parameter model.

Appendix C

Additional Information for Chapter 6

C1. Representative images of a droplet on a glass slide exposed to air.

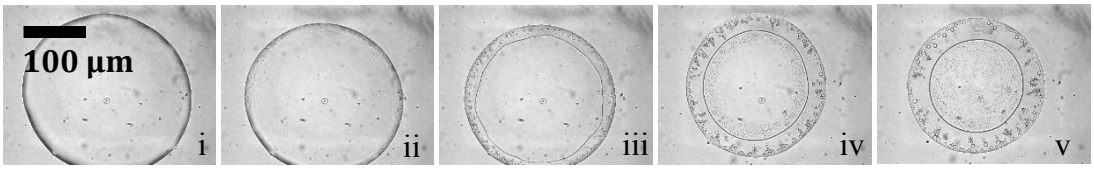

Figure C1. Images of evaporation of 3-methyl adipic acid - ammonium sulfate ternary aqueous solution droplet with OIR 2:1 on a glass-slide.

The images represent liquid-liquid phase separation of a ternary solution droplet on a glass-slide directly exposed to air over a time span of ~7 seconds in which droplet liquid-liquid phase separation occurs.

However, the images in **Figure 6. 6** represent liquid-liquid phase separation of a ternary solution droplet in a microfluidic well over a time span of 15 minutes, in which the organic phase separates to form a shell surrounding the aqueous inorganic phase in the core. The droplet is in silicone oil, that plays a significant role in slowing the phase change. It is because the water diffuses through the extremely thin layer of oil (lubrication layer) wetting the drop-PDMS contact.

C2. Step-by-step description of calculations of the densities, molalities, and relative humidities.

The densities of aqueous solutions of electrolytes, here ammonium sulfate, are calculated using the model by Laliberte and Cooper.[226] The mathematical model calculates the apparent density, $\rho_{app,i}$ (kg/m^3) of the solute *i* in aqueous solution as a function of the solute mass fraction by using dimensionless empirical constants, c_0 to c_4 from their experimental data.

$$\rho_{app,i} = \frac{(c_0.w_i + c_1).e^{(10^{-6}(t+c_4)^2)}}{w_i + c_2 + c_3.t} \quad \text{(C1)}$$

where, w_i is the weight fraction of the solute *i*, and *t* is the temperature in ^{o}C. The values of the constants[226] are c_0 = -123.22 kg/m^3; c_1 = 452.59 kg/m^3; c_2 = 3.2898 (dimensionless); c_3 = 0.016292 ^{o}C^{-1}; c_4 = 1692.4 ^{o}C.

The solution mixture density, ρ_m (kg/m^3) is then calculated using the apparent density and the solute mass fraction by using the equation below.

$$\rho_m = \frac{1}{\sum \frac{w_i}{\rho_{app,i}} + \frac{w_w}{\rho_w}} \quad \text{(C2)}$$

where, w_w is the mass fraction of water and is equal to $(1 - \sum w_i)$, and ρ_w is the density of water in kg/m^3. Therefore, densities are calculated over a wide range of the solute mass fraction, and the molality concentrations, m (moles of solute/kg of water) are then be calculated for each value of the solute mass fraction by using the following equation.

$$m = \frac{w_i}{(1 - w_i).M_s} \quad \text{(C3)}$$

where, M_s is the molar mass of the solute in kg/mole.

The molarity concentrations, M (moles of solute/liter of solution) are then calculated for each value of molality by using the solution density in the following equation.

$$M = \frac{m.\rho_m}{1+m.M_s} \text{ (moles/m}^3\text{) x } 10^{-3} \text{ (m}^3\text{/liter)} = \frac{10^{-3}.m.\rho_m}{1+m.M_s} \quad \text{(C4)}$$

This way, the corresponding molality for each value of molarity measured from the experiments is available.

Finally, the adsorption isotherm model[63,64,86,87] is used to predict the water activity for each value of molality. The equation used to calculate the molality as a function of water activity from the isotherm model is as follows.

$$\bar{m}_j^o = \frac{\left(\frac{1-\bar{a}_w}{M_w v_j \bar{a}_w}\right)\left(1 - \sum_{i=1}^{n_j-1}\left((\bar{a}_w)^i\left(1 - C_{j,i}\right)\prod_{k=1}^{i-1} C_{j,k}\right)\right)}{(1-\bar{a}_w)^2 \sum_{p=1}^{n_j-2}\left(p(\bar{a}_w)^{p-1}\prod_{k=1}^{p} C_{j,k}\right) + \left(\left(n_j-1\right) - \left(n_j-2\right)\bar{a}_w\right)(\bar{a}_w)^{n_j-2}\prod_{k=1}^{n_j-1} C_{j,k}} \quad \text{(C5)}$$

where, $\bar{m}_j^o$ is the molality of solute *j* in a pure aqueous solution, $\bar{a}_w$ is the water activity of the mixture normalized by long-range Debye-Hückel term, M_w (kg mol^{-1}) is the molecular weight of the solvent, and v_j is the stoichiometric coefficient (number of moles of ions) of fully dissociated solute *j*. The Debye-Hückel term has a parameter, ρ_j, that serves as a fitting parameter, and can be related to the hard-core collision diameter of the solute. The adsorption energy parameter, $C_{j,i}$, that is related to the change in energy, $\Delta\varepsilon_{j,i}$, of the free solvent in the bulk from the bound solvent to the respective monolayer, *i*, of the solute, *j*, is expressed by the following equation.[64]

$$C_{j,i} = \exp\left(\frac{\Delta\varepsilon_{j,i}}{kT}\right) \quad \text{(C6)}$$

The most recent approach to calculate the energy parameters is to determine the dipole-dipole interaction energy that depends on the solute and solvent molecules' size by the following relationship.[64]

$$\Delta\varepsilon_{j,i} = \frac{\mu_j \mu_w D^2}{4\pi\varepsilon_0\left(r_{jw} + (i-1)r_{ww}\right)^3} - \frac{\mu_w \mu_w D^2}{4\pi\varepsilon_0 (i \cdot r_{ww})^3} \quad \text{(C7)}$$

where, μ_j is the dipole moment of solute *j*, μ_w = 2.9, $4\pi\varepsilon_o = 1.113 \times 10^{-10}$ $C^2N^{-1}m^{-2}$, ε_o is the permittivity of space, r_{jw} is the intermolecular distance between solute *j* and solvent *w*, $r_{ww} = 2.82 \times 10^{-10}\ m$, and *D* is a unit of conversion (Debye), $D = 3.33564 \times 10^{-30}$ Cm.

The density, molality and molarity calculations for a few values of the solute mass fraction have been demonstrated in Table C1.

solute mass fraction	solute apparent density (kg/m^3)	solution density (kg/m^3)	molality (mol/kg)	molarity (mol/lt)
0.05	2275	1029	0.40	0.39
0.10	2214	1058	0.84	0.80
0.15	2155	1087	1.34	1.23
0.20	2097	1117	1.89	1.69
0.25	2041	1146	2.52	2.17
0.30	1986	1175	3.24	2.67
0.35	1932	1203	4.08	3.19
0.40	1880	1230	5.05	3.72
0.45	1829	1256	6.19	4.28
0.50	1779	1280	7.57	4.84
0.55	1730	1302	9.25	5.42
0.60	1683	1322	11.35	6.00
0.65	1636	1338	14.05	6.58
0.70	1591	1351	17.66	7.16
0.75	1547	1361	22.70	7.72

0.80	1503	1366	30.27	8.27
0.85	1461	1366	42.89	8.79
0.90	1419	1362	68.11	9.28
0.95	1379	1353	143.79	9.73

Table C1. Densities and concentrations corresponding to the solute mass fractions.

Consider an example of a final concentration from the binary salt solution experiment, e.g. molarity = 8.27. The value approximately corresponds to a solute mass fraction of 0.8 (therefore, water mass fraction = 0.2), and a molality of 30.27. Now, from Figure C2 (black dash line), the molality of 30.27 corresponds to a water activity of 0.3651 (36.51% relative humidity).

C3. Study on O:C ratio.

Experiments with OIR 1:1 were performed for other organic acids such as glutaric acid, malic acid and maleic acid having higher O:C ratios (elemental oxygen-to-carbon ratio) to compare the concentrations at which they solidified. As seen in Figure C2, assuming a fixed concentration, it may be inferred that, as the O:C ratio decreases, ERH will increase. The figure has experimental literature data and isotherm model predictions for ammonium sulfate, glutaric acid, malic acid and maleic acid; data for 3MGA and 3MAA are not available in the literature. The final concentrations along with O:C ratios are reported in Table C2 that have a decreasing trend as the O:C ratio decreases as seen in the subplot of Figure C2. Therefore, it may imply that the ERH increases with decreasing O:C ratios. No LLPS was observed with the systems with O:C ratios greater than or equal to 0.8, consistent with literature.[38,68,205,250] The 3MGA and 3MAA systems with visible LLPS have O:C ratios 0.67 and 0.57 respectively. However, LLPS did not occur at extremely low (< 0.1) or high (> 10) OIRs. In addition, LLPS was observed for OIR 10:1 in 3MAA and not in 3MGA solution because 3MAA has a lower solubility in water than 3MGA.

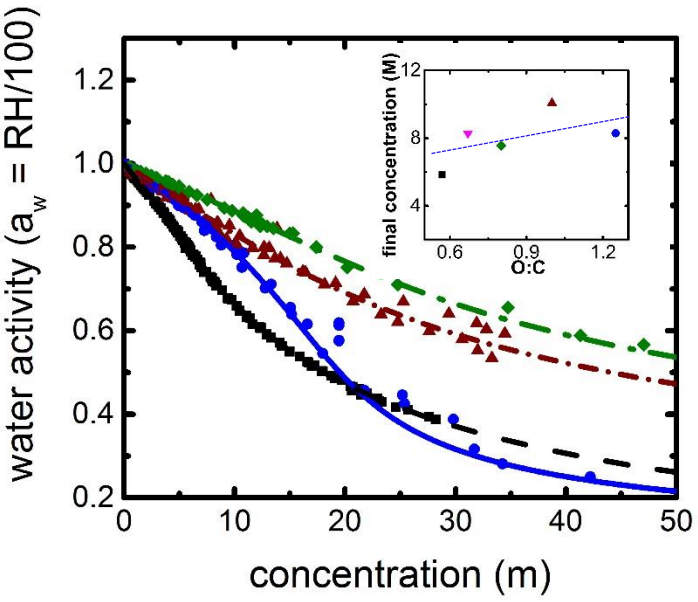

Figure C2. Water activity data versus molality concentration for aqueous binary solutions – isotherm model predictions. Symbols: black square – ammonium sulfate experimental literature data,[130–133] blue circle - malic acid experimental literature data,[49,99,101,251] brown triangle – maleic acid experimental literature data,[49,99,101,251] green diamond – glutaric acid experimental literature data.[49,99,101] Lines: black dash – ammonium sulfate model prediction using the adsorption isotherm Coulombic model,[87] blue solid – malic acid model prediction,[86] brown short-dash-dot – maleic acid model prediction,[86] green dash-dot – glutaric acid model prediction.[86] Subplot: O:C versus final molarity concentration of OIR 1 systems in aqueous ternary solutions from the experiments. Symbols: blue circle – malic acid, brown triangle – maleic acid, green diamond – glutaric acid, magenta inverted triangle – 3-methyl glutaric acid, black square – 3-methyl adipic acid. The dotted blue line is the trendline. O:C – oxygen-to-carbon elemental ratio.

solution	O:C	OIR (by moles)	initial total conc (M)	matched RI conc (M)	final total conc (M)	error (%)
AS + malic acid	1.25	0.986	1.503	4.55	8.29	0.36
AS + maleic acid	1	1.138	1.618	4.83	10.08	0.34
AS + glutaric acid	0.8	1.000	2.225	4.06	7.56	0.26
AS + 3MGA	0.67	0.904	0.721	4.20	8.41	0.47
AS + 3MAA	0.57	0.825	0.345	-	5.86	1.62

Table C2. Concentrations of aqueous ternary ammonium sulfate (AS) and organic acids solution with OIR 1 by mass. O:C is oxygen-to-carbon elemental ratio; OIR is organic-to-inorganic ratio; M is moles/liter; error is calculated by ±2 μm channel height sensitivity analysis for final concentration; 3MGA is 3-methyl glutaric acid; 3MAA is 3-methyl adipic acid. Initial droplet volume ~ 2 nl.

Appendix D

MATLAB Codes

D1. One-Parameter Fitting Routine for Solute Molality and Activity of Partially-Dissociating Aqueous Organic Acids by Coulombic Model.

```
clear
typeoffit = 'Acid dissociation'; % Name of fit type
robustoptn = 'on'; % Turn robust fitting 'on' or 'off'

Mw = 0.0180152; % Molecular weight of water

Solute = 'OrganicAcid_data';

nOrg = 3; % nondisassociating component
nAcid = 8; % disassociating component
n = [nOrg,nAcid];

zzOrg = 0; % nondisassociating is organic, no charge
zzAcid = 1; % disassociating is treated as 1:1 electrolyte
zz = [zzOrg,zzAcid];

vOrg = 1;
vAcid = 2;
v = [vOrg,vAcid];

% Location of .m file
dataloc = 'D:\Dicarboxylic Acids\DissociationModel\Data\';
datafile = strcat(dataloc,Solute,'.m');
run(datafile)

 m_data = x; % Q = Osmotic coefficient
osm_data = Q; % x = molality
aw_data = exp(-Q.*1.*Mw.*x);
x_data = x./(x+1/Mw);

soluteratio = [1,0.5];

%% Model Fit
[ rhoAcid, rjwAcid, rjwOrg, mujAcid, mujOrg, CjkA, CjkO, mse, P0 ] =
Fit_Coul_Dissoc_One_parameter(aw_data,osm_data,nAcid,nOrg,robustoptn,so
luteratio,m_data);
```

```
% rho for nondisassociating is zero, rho for disassociating from fit
rho = [0,rhoAcid];
% Store C parameters as a cell array.
CJK = {CjkO,CjkA};

%% Model Prediction

aw = [0.001:0.001:0.999,0.9999,0.99999,0.9999999999]; % Water activity
as input array

% Molality

m = zeros(size(aw)); % Reference Molality
mtot = zeros(size(aw)); % Total molality

m = Molality(rho,CJK,v,n,zz,aw,soluteratio,length(n),1);

for jj = 1:length(n)
    mtot = mtot + m.*soluteratio(jj).*v(jj);
end

x1 = mtot./(mtot+1/Mw);
osm = -log(aw)./(mtot.*Mw);

for k=1:length(n),
    m_array(k,:)=soluteratio(k)*m;
end

% Activity and Activity coefficient

for j = 1:length(n)
    [a(j,:),f_Inf(j,:),K(j,:),Ix(j,:),Kw(j,:),awbar(j,:),abar0(j,:)] =
Activity( aw,m_array,v,zz,rho,CJK{j},n(j),j,length(n) );
    if zz(j) == 1
        f_FS(j,:) =
(mtot+(1./Mw)).*((a(j,:))./((m_array(j,:)).*(m_array(j,:)))).^(1./v(j))
;  % Fused salt reference state; Mole fraction basis
    else
        f_FS(j,:) = (mtot+(1./Mw)).*(a(j,:)./m_array(j,:)); % Fused
salt reference state; Mole fraction basis
    end
end

osm = osm';
a = a';
f_FS = f_FS';
f_Inf = f_Inf';
aw=aw';
x1=x1';
m_array=m_array';
mtot=mtot';
```

```
% msecalc =
mseCalc_dicarb(osm_data,m_data,v,zz,n,CJK{1},CJK{2},rho,soluteratio);

%% Plot
fig = figure;
set(fig,'Position',[400 100 1200 800]);

subplot(1,3,1);%%%%%%%%%%%%%%%%%%%%%%%  Left Plot
plt = plot(x1,osm,x_data,osm_data,'.');
set(plt(1),'LineWidth', 2);
set(plt(2),'MarkerSize',10);
axis([0 max(x_data) (min(osm_data)-0.1) (max(osm_data)+0.1)])
title(sprintf(strcat(Solute,sprintf(', nO=%d, nA=%d',nOrg,nAcid))))
xlabel('molefraction')
ylabel('osmotic coeff \phi')

subplot(1,3,2);%%%%%%%%%%%%%%%%%%%%%%   Mid Plot
plt = plot(x1,osm,x_data,osm_data,'.');
set(plt(1),'LineWidth', 2)
title(sprintf(strcat(Solute,sprintf(', nO=%d, nA=%d',nOrg,nAcid))))
xlabel('molefraction')
ylabel('osmotic coeff \phi')

subplot(1,3,3);%%%%%%%%%%%%%%%%%%%%%    Right Plot
title(sprintf(strcat(typeoffit,', Robust:',robustoptn)));
txstr(1) = {sprintf('Ratio Org:Acid   %g:%g',soluteratio)};
txstr(2) = {sprintf('nOrg = %d'     ,nOrg)};
txstr(3) = {sprintf('mujOrg = %g'   ,mujOrg)};
txstr(4) = {sprintf('rjwOrg = %g'   ,rjwOrg)};
txstr(5) = {sprintf('nAcid = %d'    ,nAcid)};
txstr(6) = {sprintf('mujAcid = %g'  ,mujAcid)};
txstr(7) = {sprintf('rjwAcid = %g'  ,rjwAcid)};
txstr(8) = {sprintf('rhoAcid = %g'  ,rhoAcid)};
% txstr(9) = {sprintf('P0 = [%g, %g, %g]',P0(1),P0(2),P0(3))};
% txstr(10) = {sprintf('msenorm = %g',msecalc)};
txstr(11) = {sprintf('msematlab = %g',mse)};

text(0.05,0.5,txstr);

%Save Figure Results
dirname = strcat('./Results/',Solute);
nid = sprintf('_nO%d_nA%d',nOrg,nAcid);
if isequal(exist(strcat('./Results/',Solute),'dir'),7)
    fprintf(strcat('./Results/',Solute,'\n'))
else
    mkdir(strcat('.\Results\',Solute))
    fprintf(strcat('./Results/',Solute,'\n'))
end
figname = strcat(dirname,'/',Solute,nid,'.fig');
saveas(fig,figname)
figname = strcat(dirname,'/',Solute,nid,'.jpg');
set(fig,'PaperPositionMode','auto')
print(fig,'-djpeg',figname)%saveas(fig,figname)
```

One-Parameter Fitting Sub-Routine

```
function [ rhoAcid,rjwAcid,rjwOrg,mujAcid,mujOrg,CjkA,CjkO,mse,P0 ] =
Fit_Coul_Dissoc_One_parameter(aw_data,osm_data,nAcid,nOrg,robustoptn,so
luteratio,m_data )

% Parameter fitting for dissociating species
tic

PrjwA = 1;

kb = 1.38*10^-23;    % Boltzmann constant
T = 298.15;          % Temperature
pieps4 = 1.113*10^-10; %=4*pi*eps0
Mw = 0.0180152;      % Water molar mass
D = 3.33564*10^-30; %
muw = 2.9;           % Water dipole moment
echarge = 1.60218*10^-19; % electron charge
rww = 2.1711 * 10^-10 + 0.6489 * 10 ^-10; % water-water distance
NA = 6.023*10^23; % Avogadro's number
density = 1000; % Water density

vA = 2;
vO = 1;
zzA = 1;
zzO = 0;

    function [OUT] = CalCO(rjw,n)
        % Calculate energy C parameters for nondisassociating species
        rjw = abs(rjw);
        muj = 0.1208*(rjw*10^10)^3;
        C = zeros(1,n-1);
        for i = 1:(n-1)
            C(1,i) = exp( (muj*muw*D^2/(pieps4*(rjw + (i-1)*rww).^3) -
(muw*muw*D^2)/(pieps4*(i*rww)^3))/ (kb*T) );
        end
        OUT = C;
    end

    function [OUT] = CalCA(rjw,n)
        % Calculate energy C parameters for disassociating species
        rjw = abs(rjw);
        muj = echarge*(rjw)/D;
        C = zeros(1,n-1);
        for i = 1:(n-1)
            C(1,i) = exp( (muj*muw*D^2/(pieps4*(rjw + (i-1)*rww).^3) -
(muw*muw*D^2)/(pieps4*(i*rww)^3))/ (kb*T) );
        end
        OUT = C;
    end

    function [OUT] = CBETm(P,aw)
        CA = CalCA(P(PrjwA),nAcid);
        CO = CalCO(P(PrjwA)/2,nOrg);
```

```
        rhoA =
abs(P(PrjwA)/2).*sqrt((2*echarge^2*NA*density*4*pi)./(Mw*pieps4*D*kb*T)
);

        mref = Molality([0,rhoA], {CO,CA}, [vO,vA], [nOrg,nAcid],
[zzO,zzA], aw, soluteratio, 2,m_data);
        OUT = [mref.*soluteratio(1),mref.*soluteratio(2)];
    end

    function [OUT] = CBETosm(P,aw)
        m = CBETm(P,aw);
        OUT = -log(aw)./(Mw*( vO*m(:,1) + vA*m(:,2)));
    end

% Initial parameter guess P0 = [rhoAcid,rjwAcid,rjwOrg]
% P0 = [10,6*10^-10,4*10^-10];

% Initial parameter guess P0 = [rhoAcid,rjwAcid]
% P0 = [10,15*10^-10];

% Initial parameter guess P0 = [rjwAcid]
P0 = 8*10^-10;

options = statset('MaxIter',1000,'Robust',robustoptn,'TolFun',1e-
30,'TolX',1e-30,'FunValCheck','off','Display','iter');
[Pfit,r,J,cov,mse] = nlinfit(aw_data,osm_data,@CBETosm,P0,options);

rjwAcid = abs(Pfit(PrjwA));
rjwOrg  = abs(Pfit(PrjwA)/2);
CjkA = CalCA(rjwAcid,nAcid);
CjkO = CalCO(rjwOrg,nOrg);

rhoAcid =
rjwOrg.*sqrt((2*echarge^2*NA*density*4*pi)./(Mw*pieps4*78.2*kb*T));

mujAcid = echarge*(rjwAcid)/D;
mujOrg  = 0.1208*(rjwOrg*10^10)^3;

toc

end
```

Molality Sub-Routine

```
function [OUT] = Molality(rho,C_JK,v,n,zz,aw,RO,N,m_data)

    function [DEN]=molality_function(m)
        DEN = 0;
        for j=1:N,

DEN=DEN+RO(j)./CalcMjbar(rho,C_JK{j},v,n(j),zz,aw,m,RO,N,j);
        end
        DEN = 1./(DEN);
    end

f = @(x) x - molality_function(x);
dx = 0.0000001;
df = @(x) (f(x+dx)-f(x-dx))./(2*dx);
xold = m_data;
for i = 1:20
    xnew = xold - f(xold)./df(xold);
    xold = abs(xnew);
end
OUT = xold;

end

function [OUT]=CalcMjbar(rho,C_jk,v,nj,zz,aw,m,RO,N,j)

Mw=0.0180152; % Molecular weight water (kg/mol)
Ax=2.917; % Debye-Huckel coeff. mol frac @ 298.15K

% Calculate Ionic strength
IxTop = 0; IxBottom = 0;
for ii = 1:N
    IxTop = IxTop + RO(ii).*zz(ii).*v(ii);
    IxBottom = IxBottom + RO(ii).*v(ii);
end
Ix = (1/2)* (m.*IxTop)./(m.*IxBottom+1/Mw);

% Calculate the Kw debye-huckel contribution
KwTop = 0;
for ii = 1:N
    KwTop = KwTop + RO(ii).*zz(ii).*v(ii)./(1+rho(ii)*Ix.^0.5);
end
Kw = exp(Ax.*(Ix.^0.5).*(m.*KwTop)./(m.*IxBottom+1/Mw));

awbar=aw./(Kw);

% Calculate molality Using EQN.27 from Dutcher et al. 2013
NumorSum=0;
for i=1:(nj-1),
    NumorSum=NumorSum+(awbar.^i).*(1-C_jk(i)).*prod(C_jk(1:i-1));
end
DenomSum=0;
for i=1:(nj-2),
```

```
    DenomSum=DenomSum+i*(awbar.^(i-1)).*prod(C_jk(1:i));
end
Denom=(1-awbar).^2.*(DenomSum)+...
    (nj-1-(nj-2).*awbar).*awbar.^(nj-2).*prod(C_jk(1:nj-1));

OUT=((1-awbar)./(Mw.*v(j).*awbar)).*(1-NumorSum)./Denom;

end
```

Activity Sub-Routine

```
function [a,f_Inf,K,Ix,Kw,awbar,abar0] = Activity(
aw,m,v,zz,rho,Cj,nj,j,N )
global a
Mw = 0.0180152; % Molecular weight of water (kg/mol)
Ax = 2.917; % Debye-Huckel coeff. mol frac. @298.15K

% Calculate Ionic strength
IxTop=0;
for k=1:N,
    IxTop=IxTop+m(k,:)*zz(k).*v(k);
end
IxBottom=0;
for k=1:N,
    IxBottom=IxBottom+m(k,:).*v(k);
end
Ix = (1/2)* (IxTop)./(IxBottom+1/Mw);

% Ixref = (1/2)* zz(k);
% IxFS = (1/2)* zz(k);
Ixref = (1/2)* (IxTop)./(IxBottom);
IxFS = (1/2)* (IxTop)./(IxBottom);

% Calculate awbar
KwTop=0;
for k=1:N,
    KwTop=KwTop+(m(k,:)*zz(k).*v(k))./(1+rho(k)*Ix.^0.5);
end
Kw = exp((Ax.*(Ix.^0.5).*(KwTop))./(IxBottom+1/Mw));
awbar = aw./Kw;

%Calculate a0
DenSum=0;
for k=1:(nj-1),
    DenSum=DenSum+(awbar.^k).*(1-Cj(k)).*prod(Cj(1:k-1));
end
abar0 = ((1-awbar)./(1-DenSum)).^v(j);

%%Debye Huckel Contribution j
if zz(j) == 0,
    K=exp((-Ax.*(IxFS-Ix).*KwTop)./((IxBottom+1./Mw).*Ix.^0.5));
else
    SumKjTerm=0;
```

```
    for k=1:N,

SumKjTerm=SumKjTerm+(m(k,:).*zz(k).*v(k))./(2.*Ix.^0.5.*(1+rho(k).*Ix.^
0.5));
    end
    K = exp(-
zz(j).*Ax.*(2./rho(j).*log((1+rho(j).*Ix.^0.5)./(1+rho(j).*Ixref.^0.5))
+((1-Ix./IxFS)./(IxBottom+1./Mw)).*SumKjTerm)).^v(j);
end

% Reference state --> Fused Salt or Pure liquid solute
a = abar0.*K.*(m(j,:)./(m(1,:)+m(2,:)));

% Reference state --> Infinite dilution
Ixref = 0;

for k=1:(nj-1),
    Cprod=prod(Cj(1:k));
end

if zz(j) == 0,
    K_Inf=exp((-Ax.*(IxFS-Ix).*KwTop)./((IxBottom+1./Mw).*Ix.^0.5));
    f_Inf = ((IxBottom+(1./Mw))./IxBottom).*abar0.*Cprod.*K_Inf; %
Infinite dilution reference state; Mole fraction basis Activity
Coefficient for Non-dissociating species
else
    K_Inf = (exp(-
zz(j).*Ax.*(2./rho(j).*log((1+rho(j).*Ix.^0.5)./(1+rho(j).*Ixref.^0.5))
+((1-Ix./IxFS)./(IxBottom+1./Mw)).*SumKjTerm))).^v(j);
    f_Inf =
((IxBottom+(1./Mw))./IxBottom).*(abar0.^(1./v(j))).*Cprod.*K_Inf;  %
Infinite dilution reference state; Mole fraction basis Activity
Coefficient for Dissociating species
end

end
```

D2. Fitting Routine for Solute Molality and Activity of Aqueous Electrolytes by Coulombic Model.

```
clear   %%% 1-2 asymmetric electrolytes: two-parameter model

Mw = 0.01802;  % Mol wt of H2O (kg/mol)

prompt = 'Enter solute of aqueous solution   ';
Solute = input(prompt,'s');

if isequal(Solute,'CaBr2')
    n = 6; zpos = 2; zneg = 1; v = 3; r_pos = 1e-10; r_neg = 1.88e-10;
elseif isequal(Solute,'CaCl2')
    n = 4; zpos = 2; zneg = 1; v = 3; r_pos = 1e-10; r_neg = 1.72e-10;
elseif isequal(Solute,'CaI2')
    n = 8; zpos = 2; zneg = 1; v = 3; r_pos = 1e-10; r_neg = 2.1e-10;
elseif isequal(Solute,'CaNO32')
    n = 3; zpos = 2; zneg = 1; v = 3; r_pos = 1e-10; r_neg = 1.79e-10;
elseif isequal(Solute,'CoBr2')
    n = 6; zpos = 2; zneg = 1; v = 3; r_pos = 1.25e-10; r_neg = 1.88e-
10;
elseif isequal(Solute,'CoCl2')
    n = 6; zpos = 2; zneg = 1; v = 3; r_pos = 1.25e-10; r_neg = 1.72e-
10;
elseif isequal(Solute,'CoI2')
    n = 9; zpos = 2; zneg = 1; v = 3; r_pos = 1.25e-10; r_neg = 2.1e-
10;
elseif isequal(Solute,'CoNO32')
    n = 5; zpos = 2; zneg = 1; v = 3; r_pos = 1.25e-10; r_neg = 1.79e-
10;
elseif isequal(Solute,'CuBr2')
    n = 6; zpos = 2; zneg = 1; v = 3; r_pos = 0.73e-10; r_neg = 1.88e-
10;
elseif isequal(Solute,'CuCl2')
    n = 4; zpos = 2; zneg = 1; v = 3; r_pos = 0.73e-10; r_neg = 1.72e-
10;
elseif isequal(Solute,'CuNO32')
    n = 4; zpos = 2; zneg = 1; v = 3; r_pos = 0.73e-10; r_neg = 1.79e-
10;
elseif isequal(Solute,'FeCl2')
    n = 8; zpos = 2; zneg = 1; v = 3; r_pos = 0.7e-10; r_neg = 1.72e-
10;
elseif isequal(Solute,'MgBr2')
    n = 9; zpos = 2; zneg = 1; v = 3; r_pos = 0.72e-10; r_neg = 1.88e-
10;
elseif isequal(Solute,'MgCl2')
    n = 5; zpos = 2; zneg = 1; v = 3; r_pos = 0.72e-10; r_neg = 1.72e-
10;
elseif isequal(Solute,'MgI2')
    n = 9; zpos = 2; zneg = 1; v = 3; r_pos = 0.72e-10; r_neg = 2.1e-
10;
elseif isequal(Solute,'MgNO32')
```

```
    n = 5; zpos = 2; zneg = 1; v = 3; r_pos = 0.72e-10; r_neg = 1.79e-
10;
elseif isequal(Solute,'MnBr2')
    n = 6; zpos = 2; zneg = 1; v = 3; r_pos = 0.7e-10; r_neg = 1.88e-
10;
elseif isequal(Solute,'MnCl2')
    n = 4; zpos = 2; zneg = 1; v = 3; r_pos = 0.7e-10; r_neg = 1.72e-
10;
elseif isequal(Solute,'NiBr2')
    n = 7; zpos = 2; zneg = 1; v = 3; r_pos = 0.7e-10; r_neg = 1.88e-
10;
elseif isequal(Solute,'NiCl2')
    n = 5; zpos = 2; zneg = 1; v = 3; r_pos = 0.7e-10; r_neg = 1.72e-
10;
elseif isequal(Solute,'NiNO32')
    n = 5; zpos = 2; zneg = 1; v = 3; r_pos = 0.7e-10; r_neg = 1.79e-
10;
elseif isequal(Solute,'H2SO4')
    n = 2; zpos = 1; zneg = 2; v = 3; r_pos = 0.21e-10; r_neg = 2.58e-
10;
elseif isequal(Solute,'K2SO4')
    n = 2; zpos = 1; zneg = 2; v = 3; r_pos = 1.38e-10; r_neg = 2.58e-
10;
elseif isequal(Solute,'Na2SO4')
    n = 3; zpos = 1; zneg = 2; v = 3; r_pos = 1.02e-10; r_neg = 2.58e-
10;
elseif isequal(Solute,'NH42SO4')
    n = 2; zpos = 1; zneg = 2; v = 3; r_pos = 1.37e-10; r_neg = 2.58e-
10;
elseif isequal(Solute,'Li2SO4')
    n = 3; zpos = 1; zneg = 2; v = 3; r_pos = 0.76e-10; r_neg = 2.58e-
10;
elseif isequal(Solute,'Rb2SO4')
    n = 2; zpos = 1; zneg = 2; v = 3; r_pos = 1.52e-10; r_neg = 2.58e-
10;
elseif isequal(Solute,'Cs2SO4')
    n = 4; zpos = 1; zneg = 2; v = 3; r_pos = 1.67e-10; r_neg = 2.58e-
10;
elseif isequal(Solute,'BaBr2')
    n = 5; zpos = 2; zneg = 1; v = 3; r_pos = 1.33e-10; r_neg = 1.88e-
10;
elseif isequal(Solute,'BaCl2')
    n = 7; zpos = 2; zneg = 1; v = 3; r_pos = 1.33e-10; r_neg = 1.72e-
10;
elseif isequal(Solute,'BaI2')
    n = 9; zpos = 2; zneg = 1; v = 3; r_pos = 1.33e-10; r_neg = 2.10e-
10;
elseif isequal(Solute,'PbNO32')
    n = 2; zpos = 2; zneg = 1; v = 3; r_pos = 1.19e-10; r_neg = 1.79e-
10;
elseif isequal(Solute,'SrBr2')
    n = 9; zpos = 2; zneg = 1; v = 3; r_pos = 1.18e-10; r_neg = 1.88e-
10;
elseif isequal(Solute,'SrCl2')
    n = 5; zpos = 2; zneg = 1; v = 3; r_pos = 1.18e-10; r_neg = 1.72e-
10;
elseif isequal(Solute,'SrI2')
```

```
    n = 10; zpos = 2; zneg = 1; v = 3; r_pos = 1.18e-10; r_neg = 2.10e-
10;
elseif isequal(Solute,'CdNO32')
    n = 6; zpos = 2; zneg = 1; v = 3; r_pos = 0.95e-10; r_neg = 1.79e-
10;
elseif isequal(Solute,'ZnNO32')
    n = 4; zpos = 2; zneg = 1; v = 3; r_pos = 0.74e-10; r_neg = 1.79e-
10;
elseif isequal(Solute,'Na2CO3')
    n = 2; zpos = 1; zneg = 2; v = 3; r_pos = 1.02e-10; r_neg = 1.78e-
10;
% elseif isequal(Solute,'PbCl2')
%     n = 5; zpos = 2; zneg = 1; v = 3; r_pos = 1.19e-10; r_neg =
1.72e-10;
% elseif isequal(Solute,'ZnF2')
%     n = 5; zpos = 2; zneg = 1; v = 3; r_pos = 0.74e-10; r_neg =
1.26e-10;
% elseif isequal(Solute,'ZnI2')
%     n = 2; zpos = 2; zneg = 1; v = 3; r_pos = 0.74e-10; r_neg =
2.10e-10;
% elseif isequal(Solute,'ZnCl2')
%     n = 3; zpos = 2; zneg = 1; v = 3; r_pos = 0.74e-10; r_neg =
1.72e-10;
%     elseif isequal(Solute,'ZnBr2')
%     n = 3; zpos = 2; zneg = 1; v = 3; r_pos = 0.74e-10; r_neg =
1.88e-10;
% % elseif isequal(Solute,'K2HPO4')
    % %     n = 4; zpos = 2; zneg = 1; v = 3; r_pos = 1e-10; r_neg =
1.72e-10;
    % % elseif isequal(Solute,'MnClO42')
    % %     n = 4; zpos = 2; zneg = 1; v = 3; r_pos = 1e-10; r_neg =
1.72e-10;
    % % elseif isequal(Solute,'Na2S2O3')
    % %     n = 4; zpos = 2; zneg = 1; v = 3; r_pos = 1e-10; r_neg =
1.72e-10;
    % % elseif isequal(Solute,'NiClO42')
    % %     n = 4; zpos = 2; zneg = 1; v = 3; r_pos = 1e-10; r_neg =
1.72e-10;
    % % elseif isequal(Solute,'CoClO42')
    % %     n = 4; zpos = 2; zneg = 1; v = 3; r_pos = 1e-10; r_neg =
1.72e-10;
    % % elseif isequal(Solute,'CuClO42')
    % %     n = 4; zpos = 2; zneg = 1; v = 3; r_pos = 1e-10; r_neg =
1.72e-10;
end

dataloc = 'D:\Work\DataLit\Data_Single_Salts\';
datafile = strcat(dataloc,Solute,'.m');
run(datafile)

m_data = x;     % x = molality
o_data = Q;     % Q = Osmotic coefficient

aw_data = exp(-o_data.*v.*Mw.*m_data);
x_data = v.*m_data./(v.*m_data+1/Mw); % Mole fraction
root_x_data = sqrt(x_data);
```

```
[rho,mse,r_jj,r_jw,mu_j,C,P0]=FitElec(aw_data,o_data,zpos,zneg,v,n,m_da
ta,r_pos,r_neg);

[aw_modelinput,m_model,o_model,x_model] =
modelElec(n,C,rho,v,zpos,zneg);

root_x_model = sqrt(x_model);

[normMSE,m_model_new,o_model_new,x_model_new] =
mseElec(o_data,m_data,aw_data,n,C,rho,v,zpos,zneg);

% Activity and Activity coefficient

zz = zpos*zneg;
    [a,f_Inf,gamma_Inf,K,Ix,Kw,awbar,abar0] = Activity(
aw_modelinput,m_model,v,zz,rho,C,n,length(n)); % Fused salt reference
state; Mole fraction basis Activity array
%     if zz(j) == 1
        f_FS =
(m_model.*v+(1./Mw)).*((a)./(((zneg.*m_model).^zneg).*((zpos.*m_model).
^zpos))).^(1./v);  % Fused salt reference state; Mole fraction basis
Activity Coefficient for electrolyte
%     else
%         f_FS(j,:) = (mtot+(1./Mw)).*(a(j,:)./m_array(j,:)); % Fused
salt reference state; Mole fraction basis Activity Coefficient for
organic
%     end

aw_modelinput=aw_modelinput';
x_model=x_model';
o_model=o_model';

root_x_model=root_x_model';
f_Inf=f_Inf';
gamma_Inf=gamma_Inf';

dataloc = 'D:\Work\DataLit\Act coeffs\';
datafile = strcat(dataloc,Solute,'.m');
run(datafile)

gamma_data = y;     % Q = Osmotic coefficient

fig = figure;
set(fig,'Position',[400 50 1200 400]);

subplot(2,2,1);
plt = plot(root_x_model,o_model,root_x_data,o_data,'.');
hold
% plot(root_x_data2,o_data,'.');
set(plt(1),'LineWidth', 2);
set(plt(2),'MarkerSize',10);
%axis([0 max(m_data) (min(o_data)-0.1) (max(o_data))+0.1])
title(sprintf(strcat(Solute,sprintf(', fitting rho and rjj'))))
```

```
xlabel('root mole fraction')
ylabel('osmotic coeff')

grid on

subplot(2,2,2);
plt = plot(root_x_model,o_model,root_x_data,o_data,'.');
set(plt(1),'LineWidth', 2);
set(plt(2),'MarkerSize',10);
axis([0 max(root_x_data) (min(o_data)-0.1) (max(o_data))+0.1])
title(sprintf(strcat(Solute,sprintf(', n=%d,rho = %g,r_jj = %g,r_jw =
%g,mu_j = %g, Normalized-MSE=%g,C =
%g,\n',n,rho,r_jj,r_jw,mu_j,normMSE,C))))
xlabel('root mole fraction')
ylabel('osmotic coeff')

grid on

subplot(2,2,3);
plt = plot(root_x_model,gamma_Inf,root_x_data,gamma_data,'.');
hold
set(plt(1),'LineWidth', 2);
set(plt(2),'MarkerSize',10);
axis([0 max(root_x_data) (min(gamma_data)-0.1) (max(gamma_data))+0.1])
title(sprintf(strcat(Solute,sprintf(', molality based infinite dilution
ref state'))))
xlabel('root mole fraction')
ylabel('activity coeff - gamma')

subplot(2,2,4);
plt = plot(root_x_model,gamma_Inf,root_x_data,gamma_data,'.');
hold
set(plt(1),'LineWidth', 2);
set(plt(2),'MarkerSize',10);
axis([0 0.4 (min(gamma_data)-0.1) 2])
title(sprintf(strcat(Solute,sprintf(', molality based infinite dilution
ref state'))))
xlabel('root mole fraction')
ylabel('activity coeff - gamma')

% % txstr(1) = {sprintf('n = %g',n)};
% % txstr(3) = {sprintf('rho = %g',rho)};
% % txstr(4) = {sprintf('r_jj = %g',r_jj)};
% % txstr(5) = {sprintf('r_jw = %g',r_jw)};
% % txstr(6) = {sprintf('mu_j = %g',mu_j)};
% % txstr(8) = {sprintf('C = %g,\n',C)};
% % txstr(10) = {sprintf('Normalized-MSE = %g',normMSE)};
% % text(0.01,0.5,txstr);
% % grid on

dirname = strcat('./Fitting-Results/',Solute);
nid = sprintf('_n%d',n);
if isequal(exist(strcat('./Fitting-Results/',Solute),'dir'),7)
    fprintf(strcat('./Fitting-Results/',Solute,'\n'))
else
```

```
    mkdir(strcat('.\Fitting-Results\',Solute))
    fprintf(strcat('./Fitting-Results/',Solute,'\n'))
end
figname = strcat(dirname,'/',Solute,nid,'.fig');
saveas(fig,figname)
figname = strcat(dirname,'/',Solute,nid,'.jpg');
set(fig,'PaperPositionMode','auto')
print(fig,'-djpeg',figname)

matfile = strcat(dirname,'/',Solute,nid,'.mat');
save(matfile,'m_model_new','o_model_new');
```

Two-Parameter Fitting Sub-Routine

```
function [rho,mse,r_jj,r_jw,mu_j,C,P0] =
FitElec(aw_data,o_data,zpos,zneg,v,n,m_data,r_pos,r_neg)

% function [rho,C,P0,P] =
FitElec(aw_data,o_data,m_data,zpos,zneg,v,n,type)

%   The fit parameters are rho and r_jj.

    k = 1.38e-23;
    T = 298.15;
    Mw = 0.01802;  % Mol wt of H2O (kg/mol)
    q = 2;
    e = 1.60218e-19;
    mu_w = 2.9;
    r_ww = 2.82e-10;
    D = 3.33564e-30;

     function [OUT] = f(P,aw)
       OUT = OsmFuncElec(P,aw,zpos,zneg,v,n,m_data,r_pos,r_neg);
    end

    prompt = 'Enter initial guess of [rho, r_jj]   ';
    P0 = input(prompt);

    options = statset('MaxIter',400,'Robust','on');
    options.RobustWgtFun = 'huber';
    [Pfit,r,J,cov,mse] = nlinfit(aw_data,o_data,@f,P0,options);

    rho = Pfit(1);
    r_jj = Pfit(2) ;
    mu_j = (0.866*q*e*((r_pos+r_neg) + r_jj))/D;
    r_jw = 0.866*(r_jj + (r_pos+r_neg)) + r_ww/2;
    for layer=1:(n-1)
        deltaE(layer) = ((mu_j*mu_w*D^2)/((1.113e-10)*(r_jw+(layer-
1)*r_ww)^3))-((mu_w^2*D^2)/((1.113e-10)*(layer*r_ww)^3));
        C(layer) = exp(deltaE(layer)/(k*T)); % Energy parameter
    end
    end
```

Objective Function Sub-Routine

```
function [OUT] = OsmFuncElec(P,aw,zpos,zneg,v,n,m_data,r_pos,r_neg)


    k = 1.38e-23;
    T = 298.15;
    Mw = 0.01802;  % Mol wt of H2O (kg/mol)
    q = 2;
    e = 1.60218e-19;
    mu_w = 2.9;
    r_ww = 2.82e-10;
    D = 3.33564e-30;

    Ax = 2.917; % Debye-Huckel coeff

    Ix = 0.5.*m_data.*zpos.*zneg.*v./(v.*m_data+1/Mw);

    rho = P(1);
    r_jj = P(2);
    mu_j = (0.866.*q.*e.*((r_pos+r_neg) + r_jj))./D;
    r_jw = 0.866.*(r_jj + (r_pos+r_neg)) + r_ww./2;
    deltaE = @(layer) ((mu_j.*mu_w.*D.^2)./((1.113e-10).*(r_jw+(layer-
1).*r_ww).^3))-((mu_w.^2.*D.^2)./((1.113e-10).*(layer.*r_ww).^3));
    C = @(layer) exp(deltaE(layer)./(k.*T)); % Energy parameter

    Kw = exp((2.*Ax.*Ix.^1.5)./(1+rho.*Ix.^(0.5)));

    awbar = aw./Kw;

    NumorSum=0;
    for k=1:(n-1),
        NumorSum=NumorSum+(awbar.^k).*(1-C(k)).*prod(C(1:k-1));
    end
    DenomSum=0;
    for k=1:(n-2),
        DenomSum=DenomSum+k.*(awbar.^(k-1)).*prod(C(1:k));
    end
    Denom=(1-awbar).^2.*(DenomSum)+(n-1-(n-2).*awbar).*awbar.^(n-
2).*prod(C(1:n-1));

    molality = ((1-awbar)./(Mw.*v.*awbar)).*(1-NumorSum)./Denom;

    OUT = -(log(aw))./(Mw.*v.*molality);

 end
```

Molality Calculation Sub-Routine

```
function [aw_modelinput,m_model,o_model,x_model] =
modelElec(n,C,rho,v,zpos,zneg)
```

```
Mw=0.0180152; % Molecular weight water (kg/mol)

aw_modelinput =
[0.00001,0.0001:0.001:0.9999,0.99999,0.999999,0.9999999,0.99999999];

t = length(aw_modelinput);
m = zeros(size(aw_modelinput));

for i = 1:t

    m_model(i) = NR(rho,v,n,zpos,zneg,C,aw_modelinput(i));
    o_model(i) = -(log(aw_modelinput(i)))/(Mw.*v.*m_model(i));
    x_model(i) = v.*m_model(i)./(v.*m_model(i)+1/Mw); % Mole fraction

end

end

function [mout] = NR(rho,v,n,zpos,zneg,C,aw_modelinput)

dm = 0.00001; % step size for derivative of function f
m1 = 1; % Give an initial starting molality guess.

% Newton raphson method
f = @(m) molalCalc(rho,v,n,zpos,zneg,C,m,aw_modelinput) - m;
df = @(m)(f(m+dm)-f(m))/dm;
for ii = 1:10
    m2 = abs(m1 - f(m1)/df(m1));
    m1 = m2;
end

mout = m1;

end

function [OUT] = molalCalc(rho,v,n,zpos,zneg,C,m,aw_modelinput)

Mw=0.0180152; % Molecular weight water (kg/mol)
Ax=2.917; % Debye-Huckel coeff. mol frac @ 298.15K

% Calculate molality Using EQN.27

    IxTop = zpos.*zneg.*v;
    IxBottom = v;
    Ix = (1/2).* (m.*IxTop)./(m.*IxBottom+1/Mw);
    KwTop = zpos.*zneg.*v./(1+rho.*Ix.^0.5);
    Kw = exp(Ax.*(Ix.^0.5).*(m.*KwTop)./(m.*IxBottom+1/Mw));

    awbar=aw_modelinput./(Kw);

    NumorSum=0;
    for k=1:(n-1),
```

```
        NumorSum=NumorSum+(awbar.^k).*(1-C(k)).*prod(C(1:k-1));
    end
    DenomSum=0;
    for k=1:(n-2),
        DenomSum=DenomSum+k.*(awbar.^(k-1)).*prod(C(1:k));
    end
    Denom=(1-awbar).^2.*(DenomSum)+(n-1-(n-2).*awbar).*awbar.^(n-
2).*prod(C(1:n-1));

    OUT = ((1-awbar)./(Mw.*v.*awbar)).*(1-NumorSum)./Denom;

end
```

Mean Square Error Calculation Sub-Routine

```
function [normMSE,m_model_new,o_model_new,x_model_new] =
mseElec(o_data,m_data,aw_data,n,C,rho,v,zpos,zneg)

Mw=0.0180152; % Molecular weight water (kg/mol)

t = length(aw_data);
m = zeros(size(aw_data));

for i = 1:t

    m_model_new(i) = NR(rho,v,n,zpos,zneg,C,aw_data(i));
    o_model_new(i) = -(log(aw_data(i)))/(Mw.*v.*m_model_new(i));
    x_model_new(i) = v.*m_model_new(i)./(v.*m_model_new(i)+1/Mw); %
Mole fraction

end

m_model_new = m_model_new';
o_model_new = o_model_new';

% assignin('base', 'molality', m_model_new);
% assignin('base', 'osm', o_model_new);

% Normalized mean square error
normMSE = sum(((m_model_new - m_data)./m_model_new).^2)/t;
% normMSE = sum(((o_model_new - o_data)./o_model_new).^2)/t;

end

function [mout] = NR(rho,v,n,zpos,zneg,C,aw_data)

dm = 0.00001; % step size for derivative of function f
m1 = 1; % Give an initial starting molality guess.

% Newton raphson method
f = @(m) molalCalc(rho,v,n,zpos,zneg,C,m,aw_data) - m;
df = @(m)(f(m+dm)-f(m))/dm;
```

```
for ii = 1:10
    m2 = abs(m1 - f(m1)/df(m1));
    m1 = m2;
end

mout = m1;

end

function [OUT] = molalCalc(rho,v,n,zpos,zneg,C,m,aw_data)

Mw=0.0180152; % Molecular weight water (kg/mol)
Ax=2.917; % Debye-Huckel coeff. mol frac @ 298.15K

% Calculate molality Using EQN.27

    IxTop = zpos.*zneg.*v;
    IxBottom = v;
    Ix = (1/2).* (m.*IxTop)./(m.*IxBottom+1/Mw);
    KwTop = zpos.*zneg.*v./(1+rho.*Ix.^0.5);
    Kw = exp(Ax.*(Ix.^0.5).*(m.*KwTop)./(m.*IxBottom+1/Mw));

    awbar=aw_data./(Kw);

    NumorSum=0;
    for k=1:(n-1),
        NumorSum=NumorSum+(awbar.^k).*(1-C(k)).*prod(C(1:k-1));
    end
    DenomSum=0;
    for k=1:(n-2),
        DenomSum=DenomSum+k.*(awbar.^(k-1)).*prod(C(1:k));
    end
    Denom=(1-awbar).^2.*(DenomSum)+(n-1-(n-2).*awbar).*awbar.^(n-
2).*prod(C(1:n-1));

    OUT = ((1-awbar)./(Mw.*v.*awbar)).*(1-NumorSum)./Denom;

end
```

Activity Calculation Sub-Routine

```
function [a,f_Inf,gamma_Inf,K,Ix,Kw,awbar,abar0] = Activity(
aw,m,v,zz,rho,Cj,nj,N )
global a
Mw = 0.0180152; % Molecular weight of water (kg/mol)
Ax = 2.917; % Debye-Huckel coeff. mol frac. @298.15K

% Calculate Ionic strength
IxTop=0;
for k=1:N,
    IxTop=IxTop+m(k,:)*zz(k).*v(k);
end
IxBottom=0;
```

```
for k=1:N,
    IxBottom=IxBottom+m(k,:).*v(k);
end
Ix = (1/2)* (IxTop)./(IxBottom+1/Mw);

% Ixref = (1/2)* zz(k);
% IxFS = (1/2)* zz(k);
Ixref = (1/2)* (IxTop)./(IxBottom);
IxFS = (1/2)* (IxTop)./(IxBottom);

% Calculate awbar
KwTop=0;
for k=1:N,
    KwTop=KwTop+(m(k,:)*zz(k).*v(k))./(1+rho(k)*Ix.^0.5);
end
Kw = exp((Ax.*(Ix.^0.5).*(KwTop))./(IxBottom+1/Mw));
awbar = aw./Kw;

%Calculate a0
DenSum=0;
for k=1:(nj-1),
    DenSum=DenSum+(awbar.^k).*(1-Cj(k)).*prod(Cj(1:k-1));
end
abar0 = ((1-awbar)./(1-DenSum)).^v;

%%Debye Huckel Contribution j
% if zz(j) == 0,
%     K=exp((-Ax.*(IxFS-Ix).*KwTop)./((IxBottom+1./Mw).*Ix.^0.5));
% else
    SumKjTerm=0;
    for k=1:N,

SumKjTerm=SumKjTerm+(m(k,:).*zz(k).*v(k))./(2.*Ix.^0.5.*(1+rho(k).*Ix.^
0.5));
    end
    K = exp(-
zz.*Ax.*(2./rho.*log((1+rho.*Ix.^0.5)./(1+rho.*Ixref.^0.5))+((1-
Ix./IxFS)./(IxBottom+1./Mw)).*SumKjTerm)).^v;
% end

% Reference state --> Fused Salt or Pure liquid solute
a = abar0.*K;

% Reference state --> Infinite dilution
Ixref = 0;

for k=1:(nj-1),
    Cprod=prod(Cj(1:k));
end

% if zz(j) == 0,
%     K_Inf=exp((-Ax.*(IxFS-Ix).*KwTop)./((IxBottom+1./Mw).*Ix.^0.5));
%     f_Inf = ((IxBottom+(1./Mw))./IxBottom).*abar0.*Cprod.*K_Inf; %
Infinite dilution reference state; Mole fraction basis Activity
Coefficient for organic
```

```
% else
    K_Inf = (exp(-
zz.*Ax.*(2./rho.*log((1+rho.*Ix.^0.5)./(1+rho.*Ixref.^0.5))+((1-
Ix./IxFS)./(IxBottom+1./Mw)).*SumKjTerm))).^v;
    f_Inf =
((IxBottom+(1./Mw))./IxBottom).*(abar0.^(1./v)).*Cprod.*K_Inf;  %
Infinite dilution reference state; Mole fraction basis Activity
Coefficient for electrolyte
% end

% Molality basis Inf dilution reference state Activity coefficient (eq.
30)
gamma_Inf = (Cprod./(Mw.*IxBottom)).*((abar0.*K_Inf).^(1./v));

end
```

D3. One-Parameter Fitting Routine for Solute Molality and Activity of Aqueous Neutral Organics by Coulombic Model.

```
clear

Mw = 0.0180152; % Mol wt of water kg/mol
Ax = 2.917; % Debye-Huckel coeff

prompt = 'Enter solute of aqueous solution';
Solute = input(prompt,'s');

v = 1;

if isequal(Solute,'glycerol')
    n = 3;
elseif isequal(Solute,'sucrose')
    n = 7;
elseif isequal(Solute,'AceticAcid_data')
    n = 6;
elseif isequal(Solute,'ButyricAcid_data')
    n = 3;
elseif isequal(Solute,'CitricAcid')
    n = 9;
elseif isequal(Solute,'MalicAcid_data')
    n = 4;
elseif isequal(Solute,'SuccinicAcid_data')
    n = 10;
elseif isequal(Solute,'GlutaricAcid_data')
    n = 7;
elseif isequal(Solute,'MalonicAcid_data')
    n = 3;
elseif isequal(Solute,'ethanol')
    n = 3;
elseif isequal(Solute,'Methanol')
    n = 3;
elseif isequal(Solute,'Pentanediol_1_2')
    n = 10;
elseif isequal(Solute,'Pentanediol_1_4')
    n = 8;
elseif isequal(Solute,'Pentanediol_1_5')
    n = 10;
elseif isequal(Solute,'Pentanediol_2_4')
    n = 12;
elseif isequal(Solute,'Propanediol_1_2')
    n = 3;
elseif isequal(Solute,'Propanediol_1_3')
    n = 3;
elseif isequal(Solute,'sorbitol_fulldata')
    n = 12;
elseif isequal(Solute,'Urea')
    n = 3;
elseif isequal(Solute,'TartaricAcid_data')
    n = 4;
end
```

```
% Location of .m datafile
dataloc = 'D:\Work\DataLit\Data_Organics\';
datafile = strcat(dataloc,Solute,'.m');
run(datafile)

m_data = x;      % x = molality
o_data = Q;      % Q = Osmotic coefficient

aw_data = exp(-o_data.*v.*Mw.*m_data);
x_data = m_data./(m_data+1/Mw); % Mole fraction

[mse,C,P0,r_jw,mu_j]=FitOrg(aw_data,o_data,v,n);

[aw_modelinput,m_model,o_model,x_model] = modelOrg(n,C,v);

[normMSE,m_model_new,o_model_new] =
mseOrg(o_data,m_data,aw_data,v,n,C);

fig = figure;
set(fig,'Position',[400 50 1200 400]);

subplot(1,2,1);
plt = plot(x_model,o_model,x_data,o_data,'.');
set(plt(1),'LineWidth', 2);
set(plt(2),'MarkerSize',10);
%axis([0 max(m_data) (min(o_data)-0.1) (max(o_data))+0.1])
% title(sprintf(strcat(Solute,sprintf(', n=%d, Normalized-
MSE=%g',n,normMSE))))
xlabel('mole fraction')
ylabel('osmotic coeff')

x_model=x_model';
o_model=o_model';

subplot(1,2,2);
txstr(1) = {sprintf('r_jw = %g',r_jw)};
txstr(3) = {sprintf('mu_j = %g',mu_j)};
txstr(5) = {sprintf('n = %g',n)};
txstr(7) = {sprintf('C = %g,\n',C)};
txstr(9) = {sprintf('Normalized-MSE = %g',normMSE)};
text(0.01,0.5,txstr);

dirname = strcat('./Fitting-Results/',Solute);
nid = sprintf('_n%d',n);
if isequal(exist(strcat('./Fitting-Results/',Solute),'dir'),7)
    fprintf(strcat('./Fitting-Results/',Solute,'\n'))
else
    mkdir(strcat('.\Fitting-Results\',Solute))
    fprintf(strcat('./Fitting-Results/',Solute,'\n'))
end
figname = strcat(dirname,'/',Solute,nid,'.fig');
saveas(fig,figname)
figname = strcat(dirname,'/',Solute,nid,'.jpg');
set(fig,'PaperPositionMode','auto')
```

```
print(fig,'-djpeg',figname)

matfile = strcat(dirname,'/',Solute,nid,'.mat');
save(matfile,'m_model_new','o_model_new');
```

One-Parameter Fitting Sub-Routine

```
function [mse,C,P0,r_jw,mu_j] = FitOrg(aw_data,o_data,v,n)

% function [C,P0,r_jw] = FitOrg(aw_data,o_data,v,n)

%   The fit parameter is r_jw.

    k = 1.38e-23;
    T = 298.15;
    Mw = 0.01802;  % Mol wt of H2O (kg/mol)
    q = 1;
    e = 1.60218e-19;
    mu_w = 2.9;
    r_ww = 2.82e-10;
    D = 3.33564e-30;

    prompt = 'Enter initial guess of r_jw    ';
    P0 = input(prompt);

% P0 = 5e-10;  %Initial guess r_jw

% P0 = [5e-10 15];  %Initial guess [r_jw mu_j]

    function [OUT] = f(P,aw)
       OUT = OsmFuncOrg(P,aw,v,n);
    end


options = statset('MaxIter',400,'Robust','on');
[Pfit,r,J,cov,mse] = nlinfit(aw_data,o_data,@f,P0,options);

r_jw = Pfit
mu_j = (r_jw/2.023e-10).^3

% r_jw = 5.02e-10; % glycerol from Paper 4 - Single-parameter fit
% mu_j =(r_jw/2.023e-10).^3;

% r_jw = 6.05e-10; % sucrose from Paper 4 - Single-parameter fit
% mu_j = (r_jw/2.023e-10).^3

% r_jw = Pfit(1)
% mu_j = Pfit(2)

% r_jw = 3.04e-10; % glycerol from Paper 4 - Two-parameter fit
% mu_j = 3.804; % glycerol from Paper 4
```

```
for layer=1:(n-1)
    deltaE(layer) = ((mu_j*mu_w*D^2)/((1.113e-10)*(r_jw+(layer-
1)*r_ww)^3))-((mu_w^2*D^2)/((1.113e-10)*(layer*r_ww)^3));
    C(layer) = exp(deltaE(layer)/(k*T)); % Energy parameter
end

% Pmodel = fitnlm(aw_data,o_data,@f,P0);
% Pfit = Pmodel.Coefficients.Estimate
%
% r_jw = Pfit;
% % r_jw = 5.02e-10;
% mu_j = (r_jw/2.023e-10).^3
% for layer=1:(n-1)
%     deltaE(layer) = ((mu_j*mu_w*D^2)/((1.113e-10)*(r_jw+(layer-
1)*r_ww)^3))-((mu_w^2*D^2)/((1.113e-10)*(layer*r_ww)^3));
%     C(layer) = exp(deltaE(layer)/(k*T)); % Energy parameter
% end

end
```

Objective Function Sub-Routine

```
    function [OUT] = OsmFuncOrg(P,aw,v,n)

    k = 1.38e-23;
    T = 298.15;
    Mw = 0.01802;  % Mol wt of H2O (kg/mol)
    q = 1;
    e = 1.60218e-19;
    mu_w = 2.9;
    r_ww = 2.82e-10;
    D = 3.33564e-30;

    r_jw = P;
    mu_j = (r_jw/2.023e-10).^3;

%     r_jw = P(1)
%     mu_j = P(2)

    deltaE = @(layer) ((mu_j.*mu_w.*D.^2)./((1.113e-10).*(r_jw+(layer-
1).*r_ww).^3))-((mu_w.^2.*D.^2)./((1.113e-10).*(layer.*r_ww).^3));
    C = @(layer) exp(deltaE(layer)./(k.*T)); % Energy parameter

    Kw = 1;
    awbar = aw./Kw;

    NumorSum=0;
    for k=1:(n-1),
        NumorSum=NumorSum+(awbar.^k).*(1-C(k)).*prod(C(1:k-1));
    end
    DenomSum=0;
    for k=1:(n-2),
```

```
        DenomSum=DenomSum+k*(awbar.^(k-1)).*prod(C(1:k));
    end
    Denom=(1-awbar).^2.*(DenomSum)+(n-1-(n-2).*awbar).*awbar.^(n-
2).*prod(C(1:n-1));

    molality = ((1-awbar)./(Mw.*v.*awbar)).*(1-NumorSum)./Denom;

    OUT = (-log(aw)./(Mw*v*molality));

    end
```

Molality Calculation Sub-Routine

```
function [aw_modelinput,m_model,o_model,x_model] = modelOrg(n,C,v)

Mw=0.0180152; % Molecular weight water (kg/mol)

aw_modelinput =
[0.0001:0.001:0.9999,0.99999,0.999999,0.9999999,0.99999999];

t = length(aw_modelinput);
m = zeros(size(aw_modelinput));

for i = 1:t

m_model(i) = molalCalc(v,n,C,aw_modelinput(i));
o_model(i) = -(log(aw_modelinput(i)))/(Mw*v*m_model(i));
x_model(i) = m_model(i)./(m_model(i)+1/Mw); % Mole fraction

end

function [OUT] = molalCalc(v,n,C,aw_modelinput)

Mw=0.0180152; % Molecular weight water (kg/mol)


% Calculate molality Using EQN.27

    Kw = 1;

    awbar=aw_modelinput./(Kw);

    NumorSum=0;
    for k=1:(n-1),
        NumorSum=NumorSum+(awbar.^k).*(1-C(k)).*prod(C(1:k-1));
    end
    DenomSum=0;
    for k=1:(n-2),
        DenomSum=DenomSum+k*(awbar.^(k-1)).*prod(C(1:k));
    end
    Denom=(1-awbar).^2.*(DenomSum)+(n-1-(n-2).*awbar).*awbar.^(n-
2).*prod(C(1:n-1));
```

```
    OUT = ((1-awbar)./(Mw.*v.*awbar)).*(1-NumorSum)./Denom;

end

end
```

Mean Square Error Calculation Sub-Routine

```
function [ normMSE,m_model_new,o_model_new ] =
mseOrg(o_data,m_data,aw_data,v,n,C)

Mw=0.0180152; % Molecular weight water (kg/mol)

t = length(aw_data);
m = zeros(size(aw_data));

for i = 1:t

m_model_new(i) = molalCalc(v,n,C,aw_data(i));
o_model_new(i) = -(log(aw_data(i)))/(Mw*v*m_model_new(i));
x_model_new(i) = m_model_new(i)./(m_model_new(i)+1/Mw); % Mole fraction

end

m_model_new = m_model_new';
o_model_new = o_model_new';

% assignin('base', 'molality', m_model_new);
% assignin('base', 'osm', o_model_new);

% Normalized mean square error
normMSE = sum(((m_model_new - m_data)./m_model_new).^2)/t;
% normMSE = sum(((o_model_new - o_data)./o_model_new).^2)/t;

end
function [OUT] = molalCalc(v,n,C,aw_data)

Mw=0.0180152; % Molecular weight water (kg/mol)

% Calculate molality Using EQN.27

    Kw = 1;

    awbar=aw_data./(Kw);

    NumorSum=0;
    for k=1:(n-1),
        NumorSum=NumorSum+(awbar.^k).*(1-C(k)).*prod(C(1:k-1));
    end
    DenomSum=0;
    for k=1:(n-2),
        DenomSum=DenomSum+k*(awbar.^(k-1)).*prod(C(1:k));
```

```
    end
    Denom=(1-awbar).^2.*(DenomSum)+(n-1-(n-2).*awbar).*awbar.^(n-
2).*prod(C(1:n-1));

    OUT = ((1-awbar)./(Mw.*v.*awbar)).*(1-NumorSum)./Denom;

end
```

D4. Routine for Solute Molality and Activity of Multicomponent Aqueous Mixtures by Coulombic Model.

```
function [ m ] = Paper4Mixture(j,C)

aw =
[0.0000001,0.000001,0.00001,0.0001,0.001:0.001:0.999,0.9999,0.99999,0.9
99999];

% aw = [0.56    0.56    0.59    0.57    0.58    0.59    0.59    0.59
0.59    0.6 0.6 0.6 0.59    0.62    0.63    0.62    0.59    0.63
0.61    0.62    0.62    0.63    0.62    0.64    0.66];

N = 2; % number of solutes

k = 1.38e-23;
T = 298.15;
Mw = 0.01802;  % Mol wt of H2O (kg/mol)
q1 = 1;
q2 = 2;
e = 1.60218e-19;
mu_w = 2.9;
r_ww = 2.82e-10;
D = 3.33564e-30;

for kk = 1:N

    prompt = 'Enter solute of aqueous solution     ';
    Solute = input(prompt,'s');

    if isequal(Solute,'GlutaricAcid')
        j(kk) = 1; zpos(kk) = 0; zneg(kk) = 0; v(kk) = 1; rho(kk) = 0;
n(kk) = 7; mu_j(kk) = 0.159749; r_jw(kk) = 1.04E-10; r_jj(kk) = 0;
r_pos(kk) = 0; r_neg(kk) = 0;
        %         if isequal(Solute,'MalicAcid')
        %         j(kk) = 1; zpos(kk) = 0; zneg(kk) = 0; v(kk) = 1;
rho(kk) = 0; n(kk) = 4; mu_j(kk) = 7.67324; r_jw(kk) = 3.57E-10;
r_jj(kk) = 0; r_pos(kk) = 0; r_neg(kk) = 0;
        %         if isequal(Solute,'ButyricAcid')
        %         j(kk) = 1; zpos(kk) = 0; zneg(kk) = 0; v(kk) = 1;
rho(kk) = 0; n(kk) = 3; mu_j(kk) = 157.781; r_jw(kk) = 13.5E-10;
r_jj(kk) = 0; r_pos(kk) = 0; r_neg(kk) = 0;
        %         if isequal(Solute,'AceticAcid')
        %         j(kk) = 1; zpos(kk) = 0; zneg(kk) = 0; v(kk) = 1;
rho(kk) = 0; n(kk) = 6; mu_j(kk) = 1.43626; r_jw(kk) = 2.28E-10;
r_jj(kk) = 0; r_pos(kk) = 0; r_neg(kk) = 0;
    elseif isequal(Solute,'SuccinicAcid')
        j(kk) = 2; zpos(kk) = 0; zneg(kk) = 0; v(kk) = 1; rho(kk) = 0;
n(kk) = 10; mu_j(kk) = 2.70024; r_jw(kk) = 2.81706E-10; r_jj(kk) = 0;
r_pos(kk) = 0; r_neg(kk) = 0;
        % elseif isequal(Solute,'TartaricAcid')
```

```
        %                       j(kk) = 2; zpos(kk) = 0; zneg(kk) = 0;
v(kk) = 1; rho(kk) = 0; n(kk) = 4; mu_j(kk) = 77.68; r_jw(kk) = 8.63E-
10; r_jj(kk) = 0; r_pos(kk) = 0; r_neg(kk) = 0;
        %     elseif isequal(Solute,'glycerol')
        %         j(kk) = 2; zpos(kk) = 0; zneg(kk) = 0; v(kk) = 1;
rho(kk) = 0; n(kk) = 12; mu_j(kk) = 3.804; r_jw(kk) = 3.04E-10;
r_jj(kk) = 0; r_pos(kk) = 0; r_neg(kk) = 0;
    elseif isequal(Solute,'CitricAcid')
        j(kk) = 3; zpos(kk) = 0; zneg(kk) = 0; v(kk) = 1; rho(kk) = 0;
n(kk) = 9; mu_j(kk) = 16.1368; r_jw(kk) = 5E-10; r_jj(kk) = 0;
r_pos(kk) = 0; r_neg(kk) = 0;
    elseif isequal(Solute,'sucrose')
        j(kk) = 4; zpos(kk) = 0; zneg(kk) = 0; v(kk) = 1; rho(kk) = 0;
n(kk) = 20; mu_j(kk) = 13.923; r_jw(kk) = 4.55659E-10; r_jj(kk) = 0;
r_pos(kk) = 0; r_neg(kk) = 0;
    elseif isequal(Solute,'MaleicAcid')
        j(kk) = 5; zpos(kk) = 0; zneg(kk) = 0; v(kk) = 1; rho(kk) = 0;
n(kk) = 3; mu_j(kk) = 4.3206; r_jw(kk) = 3.17995E-10; r_jj(kk) = 0;
r_pos(kk) = 0; r_neg(kk) = 0;
%     elseif isequal(Solute,'MalonicAcid')
%         j(kk) = 5; zpos(kk) = 0; zneg(kk) = 0; v(kk) = 1; rho(kk) =
0; n(kk) = 3; mu_j(kk) = 40.2079; r_jw(kk) = 7.09E-10; r_jj(kk) = 0;
r_pos(kk) = 0; r_neg(kk) = 0;
    elseif isequal(Solute,'HNO3')
        j(kk) = 6; zpos(kk) = 1; zneg(kk) = 1; v(kk) = 2; rho(kk) =
37.287; n(kk) = 3; mu_j(kk) = 0; r_jw(kk) = 0; r_jj(kk) = 2.27E-10;
r_pos(kk) = 2.1E-11; r_neg(kk) = 1.65E-10;
    elseif isequal(Solute,'NaNO3')
        j(kk) = 7;  zpos(kk) = 1; zneg(kk) = 1; v(kk) = 2; rho(kk) =
9.7517; n(kk) = 2; mu_j(kk) = 0; r_jw(kk) = 0; r_jj(kk) = 2.26E-10;
r_pos(kk) = 1.01E-10; r_neg(kk) = 1.65E-10;
        %     elseif isequal(Solute,'LiCl')
        %         j(kk) = 7; zpos(kk) = 1; zneg(kk) = 1; v(kk) = 2;
rho(kk) = 27.275; n(kk) = 6; mu_j(kk) = 0; r_jw(kk) = 0; r_jj(kk) =
1.25E-10; r_pos(kk) = 7.6E-11; r_neg(kk) = 1.81E-10;
    elseif isequal(Solute,'NaOH')
        j(kk) = 8; zpos(kk) = 1; zneg(kk) = 1; v(kk) = 2; rho(kk) =
11.706; n(kk) = 4; mu_j(kk) = 0; r_jw(kk) = 0; r_jj(kk) = 1.5E-10;
r_pos(kk) = 1.01E-10; r_neg(kk) = 1.53E-10;
    elseif isequal(Solute,'NaCl')
        j(kk) = 9; zpos(kk) = 1; zneg(kk) = 1; v(kk) = 2; rho(kk) =
8.5709; n(kk) = 4; mu_j(kk) = 0; r_jw(kk) = 0; r_jj(kk) = 2.24E-10;
r_pos(kk) = 1.01E-10; r_neg(kk) = 1.81E-10;
    elseif isequal(Solute,'NH4NO3')
        j(kk) = 10;  zpos(kk) = 1; zneg(kk) = 1; v(kk) = 2; rho(kk) =
8.0672; n(kk) = 2; mu_j(kk) = 0; r_jw(kk) = 0; r_jj(kk) = 2.16E-10;
r_pos(kk) = 1.78E-10; r_neg(kk) = 1.65E-10;
    elseif isequal(Solute,'NH4Cl')
        j(kk) = 11;  zpos(kk) = 1; zneg(kk) = 1; v(kk) = 2; rho(kk) =
14.586; n(kk) = 3; mu_j(kk) = 0; r_jw(kk) = 0; r_jj(kk) = 2.23E-10;
r_pos(kk) = 1.78E-10; r_neg(kk) = 1.81E-10 ;
    elseif isequal(Solute,'HCl')
        j(kk) = 12;  zpos(kk) = 1; zneg(kk) = 1; v(kk) = 2; rho(kk) =
28.172; n(kk) = 7; mu_j(kk) = 0; r_jw(kk) = 0; r_jj(kk) = 1.47E-10;
r_pos(kk) = 0.21E-10; r_neg(kk) = 1.81E-10 ;
    elseif isequal(Solute,'NaHCO3')
```

```
        j(kk) = 13;  zpos(kk) = 1; zneg(kk) = 1; v(kk) = 2; rho(kk) =
13.00; n(kk) = 2; mu_j(kk) = 0; r_jw(kk) = 0; r_jj(kk) = 4.02E-10;
r_pos(kk) = 1.02E-10; r_neg(kk) = 1.56E-10 ;
%     elseif isequal(Solute,'Na2CO3')
%         j(kk) = 14;  zpos(kk) = 1; zneg(kk) = 2; v(kk) = 3; rho(kk) =
13.60; n(kk) = 2; mu_j(kk) = 0; r_jw(kk) = 0; r_jj(kk) = 4.02E-10;
r_pos(kk) = 1.02E-10; r_neg(kk) = 1.79E-10 ;
    elseif isequal(Solute,'NH42SO4')
        j(kk) = 14;  zpos(kk) = 1; zneg(kk) = 2; v(kk) = 3; rho(kk) =
9.6; n(kk) = 3; mu_j(kk) = 5.44; r_jw(kk) = 3.41E-10; r_jj(kk) = 0;
r_pos(kk) = 1.02E-10; r_neg(kk) = 1.79E-10 ;
    elseif isequal(Solute,'H2CO3')
        j(kk) = 15;  zpos(kk) = 1; zneg(kk) = 2; v(kk) = 3; rho(kk) =
13.00; n(kk) = 2; mu_j(kk) = 0; r_jw(kk) = 0; r_jj(kk) = 4.02E-10;
r_pos(kk) = 0.21E-10; r_neg(kk) = 1.79E-10 ;
%     elseif isequal(Solute,'NH4HC2O4')
%         j(kk) = 13;  zpos(kk) = 1; zneg(kk) = 1; v(kk) = 2; rho(kk) =
13.00; n(kk) = 2; mu_j(kk) = 0; r_jw(kk) = 0; r_jj(kk) = 4.02E-10;
r_pos(kk) = 1.78E-10; r_neg(kk) = 1.56E-10 ;
%     elseif isequal(Solute,'(NH4)2C2O4')
%         j(kk) = 14;  zpos(kk) = 1; zneg(kk) = 2; v(kk) = 3; rho(kk) =
13.00; n(kk) = 2; mu_j(kk) = 0; r_jw(kk) = 0; r_jj(kk) = 4.02E-10;
r_pos(kk) = 1.78E-10; r_neg(kk) = 1.79E-10 ;
%     elseif isequal(Solute,'H2C2O4')
%         j(kk) = 15;  zpos(kk) = 1; zneg(kk) = 2; v(kk) = 3; rho(kk) =
13.00; n(kk) = 2; mu_j(kk) = 0; r_jw(kk) = 0; r_jj(kk) = 4.02E-10;
r_pos(kk) = 0.21E-10; r_neg(kk) = 1.79E-10 ;
    end

    if j(kk) >= 6 && j(kk) <= 13
        mu_j(kk) = q1*e*((r_pos(kk)+r_neg(kk))/2 + r_jj(kk))/D;
        r_jw(kk) = r_jj(kk) + (r_pos(kk)+r_neg(kk))/2 + r_ww/2;
    end

%     if j(kk) >= 14
%         mu_j(kk) = 0.866*q2*e*((r_pos(kk)+r_neg(kk)) + r_jj(kk))/D;
%         r_jw(kk) = 0.866*(r_jj(kk) + (r_pos(kk)+r_neg(kk))) + r_ww/2;
%     end

    for ii = 1:n(kk)-1
        deltaE(kk,ii) = ((mu_j(kk)*mu_w*D^2)/((1.113e-
10)*(r_jw(kk)+(ii-1)*r_ww)^3))-((mu_w^2*D^2)/((1.113e-
10)*(ii*r_ww)^3));
        C(kk,ii) = exp(deltaE(kk,ii)/(k*T)); % Energy parameter
        % C(kk,ii) = 1;
    end

end

for kk = 1:N-1
    prompt = 'Enter ratio of current solute to last solute in the form
"number" as in (number:1)';
    soluteratio(kk) = input(prompt);
end

assignin('base', 'soluteratio', soluteratio);
```

```
t = length(aw);

for i = 1:t
    m(N,i) = NR(i,j,rho,v,n,zpos,zneg,C,aw(i),N,soluteratio(N-1,:));
    for kk = 1:N-1
        m(kk,i) = m(N,i).*soluteratio(N-1,kk);
    end

    m_total(i) = 0;
    for k = 1:N
        m_total(i) = m_total(i) + m(k,i)*v(k);
    end
    o(i) = -log(aw(i))./(Mw*m_total(i));
    root_m(i) = power(m_total(i),0.5);
    x (i) = m_total(i)./(m_total(i)+1/Mw); % Mole fraction of solute
    root_x(i) = sqrt(x(i));
    m_dry_total(i) = sum(m(:,i));
    for kkk = 1:N
        xstar(kkk) = m(kkk,i)./m_dry_total(i);
    end
    for p =1:N

[a(p,i),f_Inf(p,i),gamma_Inf(p,i),K(p,i),Ix(p,i),Kw(p,i),awbar(p,i),aba
r0(p,i),K_Inf(p,i)] =
SoluteActivity(N,i,j(p),rho,v,n(p),zpos,zneg,C(p,:),m,aw(i),p,xstar(p))
;
        xpos(p,i) = m(p,i)./m_total(i);
        xneg(p,i) = m(p,i)./m_total(i);
        if j(p) >= 6 && j(p) <= 15
            f_FS(p,i) =
(m_total(i)+(1./Mw)).*((a(p,i))./((m(p,i).^zpos(p)).*(m(p,i).^zneg(p)))
).^(1./v(p));  % Fused salt reference state; Mole fraction basis
        else
            f_FS(p,i) = (m_total(i)+(1./Mw)).*(a(p,i)./m(p,i)); % Fused
salt reference state; Mole fraction basis
        end
    end
end

aw=aw';
assignin('base', 'WaterActivity', aw);
m=m';

    x2(:,2) = 1./(1+soluteratio+(1./(m(:,2).*Mw)));
    mf2(:,2) =
(0.116072./(0.116072+(1./m(:,2))+(soluteratio.*0.3422965))); % mass
fraction of maleic acid in sucrose mixture

assignin('base', 'SoluteMolality', m);
assignin('base', 'molefraction2', x2);
assignin('base', 'massfraction2', mf2);
m_total=m_total';
o=o';
abar0=abar0';
a=a';
```

```
x=x';
f_FS=f_FS';
f_Inf=f_Inf';
gamma_Inf=gamma_Inf';
K=K';
Ix=Ix';
Kw=Kw';
awbar=awbar';
K_Inf=K_Inf';

assignin('base', 'MixtureMolality', m_total);
assignin('base', 'OsmoticCoeff', o);
assignin('base', 'SoluteActivity', a);
assignin('base', 'MoleFraction', x);
assignin('base', 'ActCoeff_f_FS', f_FS);
assignin('base', 'ActCoeff_f_Inf', f_Inf);
assignin('base', 'ActCoeff_f_Inf_Molality', gamma_Inf);
assignin('base', 'K', K);
assignin('base', 'Ix', Ix);
assignin('base', 'abar0', abar0);
assignin('base', 'Kw', Kw);
assignin('base', 'awbar', awbar);
assignin('base', 'C', C);
assignin('base', 'xstar', xstar);
assignin('base', 'K_Inf', K_Inf);

plot(root_x,o);
xlabel ('Root-MoleFraction')
ylabel ('OsmoticCoeff')

figure;
plot(aw,f_FS(:,2));
xlabel ('WaterActivity')
ylabel ('ActivityCoeffMA')
figure;
plot(aw,mf2);
xlabel ('WaterActivity')
ylabel ('MassFractionMA')
figure;
plot(aw,x2);
xlabel ('WaterActivity')
ylabel ('MoleFractionMA')

grid on

end

function [mout] = NR(i,j,rho,v,n,zpos,zneg,C,aw,N,soluteratio)

dm = 0.0000000001; % step size for derivative of function f
m1 = 1; % Give an initial starting molality guess.

% Newton raphson method

f = @(m) molalCalc(i,j,rho,v,n,zpos,zneg,C,m,aw,N,soluteratio) - m;
```

```
df = @(m)(f(m+dm)-f(m))/dm;
for i = 1:10
    m2 = abs(m1 - f(m1)/df(m1));
    m1 = m2;
end

mout = m1;

end

function [OUT] = molalCalc(i,j,rho,v,n,zpos,zneg,C,m,aw,N,soluteratio)

Mw=0.0180152; % Molecular weight water (kg/mol)
Ax=2.917; % Debye-Huckel coeff. mol frac @ 298.15K

% disp(aw); fprintf('\b'); disp(m); fprintf('\b'); disp(soluteratio);

IxTop = zpos(N)*zneg(N).*v(N);
for kk = 1:N-1
    IxTop = (IxTop + soluteratio(kk)*zpos(kk)*zneg(kk).*v(kk));
    IxTop = m*IxTop;
end

IxBottom = v(N);
for kk = 1:N-1
    IxBottom = (IxBottom + soluteratio(kk).*v(kk));
    IxBottom = m*IxBottom;
end

Ix = (1/2)* (IxTop)./(IxBottom+1/Mw);

KwTop = (zpos(N)*zneg(N)*v(N))./(1+rho(N)*Ix.^0.5);
for kk = 1:N-1
    KwTop = (KwTop +
(zpos(kk)*zneg(kk).*v(kk)*soluteratio(kk))./(1+rho(kk)*Ix.^0.5));
    KwTop = m*KwTop;
end
Kw = exp((Ax.*(Ix.^0.5).*(KwTop))./(IxBottom+1/Mw));
awbar=aw./(Kw);

% disp(Ix); fprintf('\b'); disp(Kw); fprintf('\b'); disp(awbar);

% Calculate molality Using EQN.27
for p =1:N

    if j(p) >= 1 && j(p) <= 5
        NumorSum(p)=0;
        for k=1:(n(p)-1),
            NumorSum(p)=NumorSum(p)+(awbar.^k).*(1-
C(p,k)).*prod(C(p,1:k-1));
        end
        DenomSum(p)=0;
        for k=1:(n(p)-2),
            DenomSum(p)=DenomSum(p)+k*(awbar.^(k-1)).*prod(C(p,1:k));
```

```
        end
        Denom(p)=(1-awbar).^2.*(DenomSum(p))+(n(p)-1-(n(p)-
2).*awbar).*awbar.^(n(p)-2).*prod(C(p,1:n(p)-1));
        m0(p)=((1-awbar)/(Mw*v(p)*awbar))*(1-NumorSum(p))/Denom(p);
    else
        NumorSum(p)=0;
        for k=1:(n(p)-1),
            NumorSum(p)=NumorSum(p)+(awbar.^k).*(1-
C(p,k)).*prod(C(p,1:k-1));
        end
        DenomSum(p)=0;
        for k=1:(n(p)-2),
            DenomSum(p)=DenomSum(p)+k*(awbar.^(k-1)).*prod(C(p,1:k));
        end
        Denom(p)=(1-awbar).^2.*(DenomSum(p))+(n(p)-1-(n(p)-
2).*awbar).*awbar.^(n(p)-2).*prod(C(p,1:n(p)-1));
        m0(p)=((1-awbar)/(Mw*v(p)*awbar))*(1-NumorSum(p))/Denom(p);
    end

end

mixturemodel=1./m0(N);
for k=1:N-1,
    mixturemodel=mixturemodel+soluteratio(kk)/m0(kk);
end

OUT = 1./mixturemodel;

end

function [a,f_Inf,gamma_Inf,K,Ix,Kw,awbar,abar0,K_Inf] =
SoluteActivity(N,i,j,rho,v,n,zpos,zneg,C,m,aw,p,xstar)

Mw=0.0180152; % Molecular weight water (kg/mol)
Ax=2.917; % Debye-Huckel coeff. mol frac @ 298.15K

IxTop=0;
for k=1:N,
    IxTop=IxTop+m(k,i)*zpos(k)*zneg(k).*v(k);
end

IxBottom=0;
for k=1:N,
    IxBottom=IxBottom+m(k,i).*v(k);
end

Ix = (1/2)* (IxTop)./(IxBottom+1/Mw);

% Ixref = (1/2)* zpos(p).*zneg(p);
% IxFS = (1/2)* zpos(p).*zneg(p);
Ixref = (1/2)* (IxTop)./(IxBottom);
IxFS = (1/2)* (IxTop)./(IxBottom);

KwTop=0;
for k=1:N,
```

```
    KwTop=KwTop+(m(k,i)*zpos(k)*zneg(k).*v(k))./(1+rho(k)*Ix.^0.5);
end

Kw = exp((Ax.*(Ix.^0.5).*(KwTop))./(IxBottom+1/Mw));
awbar=aw./(Kw);

%
% IxTop = m(1,i)*zpos(1)*zneg(1).*v(1) + m(2,i)*zpos(2)*zneg(2).*v(2);
% IxBottom = m(1,i)*v(1) + m(2,i)*v(2);
% KwTop = (m(1,i)*zpos(1)*zneg(1).*v(1))./(1+rho(1)*Ix.^0.5) +
(m(2,i)*zpos(2)*zneg(2)*v(2))./(1+rho(2)*Ix.^0.5);

% disp(Ix); fprintf('\b'); disp(Kw); fprintf('\b'); disp(awbar);

DenSum=0;
for k=1:(n-1),
    DenSum=DenSum+(awbar.^k).*(1-C(k)).*prod(C(1:k-1));
end

abar0 = ((1-awbar)./(1-DenSum)).^v(p);

if j >= 1 && j <= 5

    K = exp((Ax*Ix^0.5*KwTop)/(IxBottom+1/Mw)); % mixture with only
neutral species
%     K=exp((-Ax.*(IxFS-Ix).*KwTop)./((IxBottom+1./Mw).*Ix.^0.5)); %
mixture with atleast one eletrolyte

else
    SumKjTerm=0;
    for k=1:N,

SumKjTerm=SumKjTerm+(m(k,i)*zpos(k)*zneg(k).*v(k))./(2.*Ix.^0.5.*(1+rho
(k)*Ix.^0.5));
    end
    K = (exp(-
zpos(p).*zneg(p)*Ax*(2/rho(p)*log((1+rho(p)*Ix^0.5)/(1+rho(p)*Ixref^0.5
))+((1-Ix./IxFS)/(IxBottom+1/Mw))*SumKjTerm)))^v(p);
end

a = xstar.*K.*abar0;

% Reference state --> Infinite dilution
Ixref = 0;

for k=1:(n-1),
    Cprod=prod(C(1:k));
end

if j >= 1 && j <= 5

    K_Inf = exp((Ax*Ix^0.5*KwTop)/(IxBottom+1/Mw)); % mixture with only
neutral species
```

```
%     K_Inf=exp((-Ax.*(IxFS-Ix).*KwTop)./((IxBottom+1./Mw).*Ix.^0.5));
% mixture with atleast one eletrolyte

    f_Inf = ((IxBottom+(1./Mw))./IxBottom).*abar0.*Cprod.*K_Inf; %
Infinite dilution reference state; Mole fraction basis Activity
Coefficient for Non-dissociating species
else
    K_Inf = (exp(-
zpos(p).*zneg(p)*Ax*(2/rho(p)*log((1+rho(p)*Ix^0.5)/(1+rho(p)*Ixref^0.5
))+((1-Ix./IxFS)/(IxBottom+1/Mw))*SumKjTerm)))^v(p);
    f_Inf =
((IxBottom+(1./Mw))./IxBottom).*(abar0.^(1./v(p))).*Cprod.*K_Inf;  %
Infinite dilution reference state; Mole fraction basis Activity
Coefficient for Dissociating species
end

% Molality basis Inf dilution reference state Activity coefficient (eq.
30)
gamma_Inf = (Cprod./(Mw.*IxBottom)).*((abar0.*K_Inf).^(1./v(p)));

end
```

D5. Fitting Routine for Solute Molality and Activity of Aqueous Electrolytes by Power Law Model.

```
clear

Mw = 0.0180152; % Mol wt of water kg/mol
Ax = 2.917; % Debye-Huckel coeff

prompt = 'Enter solute of aqueous solution';
Solute = input(prompt,'s');

% if isequal(Solute,'NaCl')
%     n = 4; zpos = 1; zneg = 1; v = 2; type = 1;
if isequal(Solute,'HCl')
    n = 5; zpos = 1; zneg = 1; v = 2; type = 1;
elseif isequal(Solute,'AceticAcid_data')
    n = 2; zpos = 1; zneg = 1; v = 2; type = 1;
% if isequal(Solute,'MgSO4')
%     n = 9; zpos = 2; zneg = 2; v = 2; type = 2;
elseif isequal(Solute,'NH4NO3')
    n = 5; zpos = 1; zneg = 1; v = 2; type = 2;
% elseif isequal(Solute,'NaOH')
%     n = 4; zpos = 1; zneg = 1; v = 2; type = 1;
elseif isequal(Solute,'H2SO4')
    n = 5; zpos = 1; zneg = 2; v = 3; type = 1;
elseif isequal(Solute,'NaNO3')
    n = 11; zpos = 1; zneg = 1; v = 2; type = 1;
elseif isequal(Solute,'NH42SO4')
    n = 9; zpos = 1; zneg = 2; v = 3; type = 3;
% elseif isequal(Solute,'Na2SO4')
%     n = 4; zpos = 1; zneg = 2; v = 3; type = 1;
elseif isequal(Solute,'Na2CO3')
    n = 6; zpos = 1; zneg = 2; v = 3; type = 1;
elseif isequal(Solute,'NH4Cl')
    n = 4; zpos = 1; zneg = 1; v = 2; type = 1;
elseif isequal(Solute,'TMACl')
    n = 7; zpos = 1; zneg = 1; v = 2; type = 1;

end

% type = 1 is Power law from layer 2 to n-1
% type = 2 is Power law from layer 1 to n-1
% type = 3 is Power law from layer 2 to n-1
% type = 4 is All-C fit

dataloc = 'D:\Work\DataLit\Data_Single_Salts\';
datafile = strcat(dataloc,Solute,'.m');
run(datafile)

m_data = x;     % x = molality
o_data = Q;     % Q = Osmotic coefficient

aw_data = exp(-o_data.*v.*Mw.*m_data);
```

```
% % m_data = x;      % x = molality
% % aw_data = Q;      % Q = water activity
% % o_data = zeros(size(aw_data));
% % o_data = -(log(aw_data))./(Mw.*2.*m_data);    % osmotic coeff

x_data = v.*m_data./(v.*m_data+1/Mw); % Mole fraction
root_x_data = sqrt(x_data);

[rho,C,mse,P]=FitElec(aw_data,o_data,zpos,zneg,v,n,type,m_data);

[aw_modelinput,m_model,o_model,x_model] =
modelElec(n,C,rho,v,zpos,zneg);

[normMSE,m_model_new,o_model_new] =
mseElec(o_data,m_data,aw_data,n,C,rho,v,zpos,zneg);

root_x_model = sqrt(x_model);

aw_modelinput=aw_modelinput';
x_model=x_model';
m_model=m_model';

fig = figure;
set(fig,'Position',[400 50 1200 400]);

subplot(1,2,1);
% plt = plot(x_model,o_model,x_data,o_data,'.');
plt = plot(root_x_model,o_model,root_x_data,o_data,'.');
set(plt(1),'LineWidth', 2);
set(plt(2),'MarkerSize',10);
%axis([0 max(m_data) (min(o_data)-0.1) (max(o_data))+0.1])
% title(sprintf(strcat(Solute,sprintf(', n=%d, Normalized-
MSE=%g',n,normMSE))))
xlabel('root mole fraction')
ylabel('osmotic coeff')

subplot(1,2,2);
txstr(1) = {sprintf('n = %g',n)};
txstr(3) = {sprintf('rho = %g',rho)};
txstr(5) = {sprintf('P = %g',P)};
txstr(7) = {sprintf('C = %g,\n',C)};
txstr(9) = {sprintf('Normalized-MSE = %g',normMSE)};
text(0.01,0.5,txstr);

dirname = strcat('./Fitting-Results/',Solute);
nid = sprintf('_n%d',n);
if isequal(exist(strcat('./Fitting-Results/',Solute),'dir'),7)
    fprintf(strcat('./Fitting-Results/',Solute,'\n'))
else
    mkdir(strcat('.\Fitting-Results\',Solute))
    fprintf(strcat('./Fitting-Results/',Solute,'\n'))
end
figname = strcat(dirname,'/',Solute,nid,'.fig');
saveas(fig,figname)
```

```
figname = strcat(dirname,'/',Solute,nid,'.jpg');
set(fig,'PaperPositionMode','auto')
print(fig,'-djpeg',figname)

matfile = strcat(dirname,'/',Solute,nid,'.mat');
save(matfile,'m_model_new','o_model_new','rho','P','C');
```

Fitting Sub-Routine

```
function [rho,C,mse,P] =
FitElec(aw_data,o_data,zpos,zneg,v,n,type,m_data)

% function [rho,C,P0,P] =
FitElec(aw_data,o_data,m_data,zpos,zneg,v,n,type)

    function [OUT] = f(P,aw)
       OUT = OsmFuncElec(P,aw,zpos,zneg,v,n,type,m_data);
    end

if type == 1

    prompt = 'Enter initial guess of [rho, C1, P]    ';
    P0 = input(prompt);

%     P0 = [13 1 -1];  %Initial guess [rho, C1, P] for NaCl

%     P0 = [15 45 -1];  %Initial guess [rho, C1, P] for NaOH

    options = statset('MaxIter',400,'Robust','on');
    [Pfit,r,J,cov,mse] = nlinfit(aw_data,o_data,@f,P0,options);

    rho = abs(Pfit(1));
    C(1) = abs(Pfit(2));
    P = Pfit(3)
    for layer=2:(n-1)
        C(layer) = (layer./n).^P;
    end

elseif type == 2

    prompt = 'Enter initial guess of [rho, P]    ';
    P0 = input(prompt);

%     P0 = [13 0.1];  %Initial guess [rho, P] for NH4NO3

    options = statset('MaxIter',400,'Robust','on');
    [Pfit,r,J,cov,mse] = nlinfit(aw_data,o_data,@f,P0,options);

    rho = abs(Pfit(1));
    P = Pfit(2)
    for layer=1:(n-1)
        C(layer) = n.^-P.*layer.^P;
    end
```

```
elseif type == 3

    prompt = 'Enter initial guess of [rho, C1, P]    ';
    P0 = input(prompt);

%     P0 = [13 1 -0.5];  %Initial guess [rho, C1, P] for NH42SO4

    options = statset('MaxIter',400,'Robust','on');
    [Pfit,r,J,cov,mse] = nlinfit(aw_data,o_data,@f,P0,options);

    rho = abs(Pfit(1));
    C(1) = abs(Pfit(2));
    P = Pfit(3)
    for layer=2:(n-1)
        C(layer) = C(1).*layer.^P;
    end

elseif type == 4

%     prompt = 'Enter initial guess of [rho C1]    ';
%         prompt = 'Enter initial guess of [rho C1 C2]    ';
%             prompt = 'Enter initial guess of [rho C1 C2 C3]    ';
                prompt = 'Enter initial guess of [rho C1 C2 C3 C4]    ';
%                     prompt = 'Enter initial guess of [rho C1 C2 C3 C4
C5]   ';
%                                 prompt = 'Enter initial guess of [rho C1
C2 C3 C4 C5 C6]   ';
%                                     prompt = 'Enter initial guess of [rho
C1 C2 C3 C4 C5 C6 C7]   ';
%                                     prompt = 'Enter initial guess of [rho
C1 C2 C3 C4 C5 C6 C7 C8]   ';
%                                     prompt = 'Enter initial guess of [rho
C1 C2 C3 C4 C5 C6 C7 C8 C9]   ';
%                                     prompt = 'Enter initial guess of [rho
C1 C2 C3 C4 C5 C6 C7 C8 C9 C10]   ';
%                                     prompt = 'Enter initial guess of [rho
C1 C2 C3 C4 C5 C6 C7 C8 C9 C11]   ';

    P0 = input(prompt);

    options = statset('MaxIter',400,'Robust','on');
    [Pfit,r,J,cov,mse] = nlinfit(aw_data,o_data,@f,P0,options);

    rho = abs(Pfit(1));
    C(1) = Pfit(2);
    C(2) = Pfit(3);
     C(3) = Pfit(4);
      C(4) = Pfit(5);
%        C(5) = Pfit(6);
%         C(6) = Pfit(7);
%          C(7) = Pfit(8);
%          C(8) = Pfit(9);
%                   C(9) = Pfit(10);
%                   C(10) = Pfit(11);
%           C(11) = Pfit(12);
```

```
    P=1;

% Pmodel = fitnlm(aw_data,o_data,@f,P0);
% Pfit = Pmodel.Coefficients.Estimate;
%
% rho = abs(Pfit(1));
% C(1) = abs(Pfit(2));
% P = Pfit(3);
% for layer=2:(n-1)
%     C(layer) = C(1).*layer.^P;
% end

end

end
```

Objective Function Sub-Routine

```
function [OUT] = OsmFuncElec(P,aw,zpos,zneg,v,n,type,m_data)

    Mw = 0.0180152; % Mol wt of water kg/mol

    Ax = 2.917; % Debye-Huckel coeff

    Ix = 0.5.*m_data.*zpos.*zneg.*v./(v.*m_data+1/Mw);

if type == 1

    rho = P(1);
    C1 = P(2);
    C = @(layer) n.^-P(3).*layer.^P(3);

    Kw = exp((2.*Ax.*Ix.^1.5)./(1+rho.*Ix.^(0.5)));

    awbar = aw./Kw;

    NumorSum=(awbar).*(1-C1);
    for k=2:(n-1),
        NumorSum=NumorSum+(awbar.^k).*(1-C(k)).*C1*prod(C(2:k-1));
    end
    DenomSum=0;
    for k=1:(n-2),
        DenomSum=DenomSum+k.*(awbar.^(k-1)).*C1*prod(C(2:k));
    end
    Denom=(1-awbar).^2.*(DenomSum)+(n-1-(n-2).*awbar).*awbar.^(n-
2).*C1*prod(C(2:n-1));

    molality = ((1-awbar)./(Mw.*v.*awbar)).*(1-NumorSum)./Denom;

    OUT = -(log(aw))./(Mw.*v.*molality);
```

```
elseif type == 2

    rho = P(1);
    C = @(layer) n.^-P(2).*layer.^P(2);
    Kw = exp((2.*Ax.*Ix.^1.5)./(1+rho.*Ix.^(0.5)));

    awbar = aw./Kw;

    NumorSum=0;
    for k=1:(n-1),
        NumorSum=NumorSum+(awbar.^k).*(1-C(k)).*prod(C(1:k-1));
    end
    DenomSum=0;
    for k=1:(n-2),
        DenomSum=DenomSum+k.*(awbar.^(k-1)).*prod(C(1:k));
    end
    Denom=(1-awbar).^2.*(DenomSum)+(n-1-(n-2).*awbar).*awbar.^(n-
2).*prod(C(1:n-1));

    molality = ((1-awbar)./(Mw.*v.*awbar)).*(1-NumorSum)./Denom;

    OUT = -(log(aw))./(Mw.*v.*molality);

elseif type == 3

    rho = P(1);
    C1 = P(2);
    C = @(layer) C1.*layer.^P(3);
    Kw = exp((2.*Ax.*Ix.^1.5)./(1+rho.*Ix.^(0.5)));

    awbar = aw./Kw;

    NumorSum=(awbar).*(1-C1);
    for k=2:(n-1),
        NumorSum=NumorSum+(awbar.^k).*(1-C(k)).*C1*prod(C(2:k-1));
    end
    DenomSum=0;
    for k=1:(n-2),
        DenomSum=DenomSum+k.*(awbar.^(k-1)).*C1*prod(C(2:k));
    end
    Denom=(1-awbar).^2.*(DenomSum)+(n-1-(n-2).*awbar).*awbar.^(n-
2).*C1*prod(C(2:n-1));

    molality = ((1-awbar)./(Mw.*v.*awbar)).*(1-NumorSum)./Denom;

    OUT = -(log(aw))./(Mw.*v.*molality);

elseif type == 4

    rho = P(1);
    C(1) = P(2);
     C(2) = P(3);
     C(3) = P(4);
      C(4) = P(5);
```

```
%         C(5) = P(6);
%          C(6) = P(7);
%           C(7) = P(8);
%                    C(8) = P(9);
%                    C(9) = P(10);
%                                      C(10) = P(11);
%                                               C(11) = P(12);
%

    P=1;
    Kw = exp((2.*Ax.*Ix.^1.5)./(1+rho.*Ix.^(0.5)));

    awbar = aw./Kw;

    NumorSum=0;
    for k=1:(n-1),
        NumorSum=NumorSum+(awbar.^k).*(1-C(k)).*prod(C(1:k-1));
    end
    DenomSum=0;
    for k=1:(n-2),
        DenomSum=DenomSum+k.*(awbar.^(k-1)).*prod(C(1:k));
    end
    Denom=(1-awbar).^2.*(DenomSum)+(n-1-(n-2).*awbar).*awbar.^(n-
2).*prod(C(1:n-1));

    molality = ((1-awbar)./(Mw.*v.*awbar)).*(1-NumorSum)./Denom;

    OUT = -(log(aw))./(Mw.*v.*molality);

end

end
```

Molality Calculation Sub-Routine

```
function [aw_modelinput,m_model,o_model,x_model] =
modelElec(n,C,rho,v,zpos,zneg)

Mw=0.0180152; % Molecular weight water (kg/mol)
aw_modelinput =
[0.0001:0.001:0.9999,0.99999,0.999999,0.9999999,0.99999999];

t = length(aw_modelinput);
m = zeros(size(aw_modelinput));

for i = 1:t

    m_model(i) = NR(rho,v,n,zpos,zneg,C,aw_modelinput(i));
    o_model(i) = -(log(aw_modelinput(i)))/(Mw.*v.*m_model(i));
    x_model(i) = v.*m_model(i)./(v.*m_model(i)+1/Mw); % Mole fraction
end
end
```

```
function [mout] = NR(rho,v,n,zpos,zneg,C,aw_modelinput)

dm = 0.00001; % step size for derivative of function f
m1 = 1; % Give an initial starting molality guess.

% Newton raphson method
f = @(m) molalCalc(rho,v,n,zpos,zneg,C,m,aw_modelinput) - m;
df = @(m)(f(m+dm)-f(m))/dm;
for ii = 1:10
    m2 = abs(m1 - f(m1)/df(m1));
    m1 = m2;
end

mout = m1;

end

function [OUT] = molalCalc(rho,v,n,zpos,zneg,C,m,aw_modelinput)

Mw=0.0180152; % Molecular weight water (kg/mol)
Ax=2.917; % Debye-Huckel coeff. mol frac @ 298.15K

% Calculate molality Using EQN.27

    IxTop = zpos.*zneg.*v;
    IxBottom = v;
    Ix = (1/2).* (m.*IxTop)./(m.*IxBottom+1/Mw);
    KwTop = zpos.*zneg.*v./(1+rho.*Ix.^0.5);
    Kw = exp(Ax.*(Ix.^0.5).*(m.*KwTop)./(m.*IxBottom+1/Mw));

    awbar=aw_modelinput./(Kw);

    NumorSum=0;
    for k=1:(n-1),
        NumorSum=NumorSum+(awbar.^k).*(1-C(k)).*prod(C(1:k-1));
    end
    DenomSum=0;
    for k=1:(n-2),
        DenomSum=DenomSum+k.*(awbar.^(k-1)).*prod(C(1:k));
    end
    Denom=(1-awbar).^2.*(DenomSum)+(n-1-(n-2).*awbar).*awbar.^(n-
2).*prod(C(1:n-1));

    OUT = ((1-awbar)./(Mw.*v.*awbar)).*(1-NumorSum)./Denom;

end
```

Mean Square Error Calculation Sub-Routine

```
function [normMSE,m_model_new,o_model_new] =
mseElec(o_data,m_data,aw_data,n,C,rho,v,zpos,zneg)
```

```
Mw=0.0180152; % Molecular weight water (kg/mol)
t = length(aw_data);
m = zeros(size(aw_data));

for i = 1:t

m_model_new(i) = NR(rho,v,n,zpos,zneg,C,aw_data(i));
o_model_new(i) = -(log(aw_data(i)))/(Mw.*v.*m_model_new(i));

end

m_model_new = m_model_new';
o_model_new = o_model_new';

% assignin('base', 'molality', m_model_new);
% assignin('base', 'osm', o_model_new);

% Normalized mean square error
normMSE = sum(((m_model_new - m_data)./m_model_new).^2)/t;
% normMSE = sum(((o_model_new - o_data)./o_model_new).^2)/t;

end

function [mout] = NR(rho,v,n,zpos,zneg,C,aw_data)

dm = 0.00001; % step size for derivative of function f
m1 = 1; % Give an initial starting molality guess.

% Newton raphson method
f = @(m) molalCalc(rho,v,n,zpos,zneg,C,m,aw_data) - m;
df = @(m)(f(m+dm)-f(m))/dm;
for ii = 1:10
    m2 = abs(m1 - f(m1)/df(m1));
    m1 = m2;
end

mout = m1;

end

function [OUT] = molalCalc(rho,v,n,zpos,zneg,C,m,aw_data)

Mw=0.0180152; % Molecular weight water (kg/mol)
Ax=2.917; % Debye-Huckel coeff. mol frac @ 298.15K

% Calculate molality Using EQN.27

    IxTop = zpos.*zneg.*v;
    IxBottom = v;
    Ix = (1/2).* (m.*IxTop)./(m.*IxBottom+1/Mw);
    KwTop = zpos.*zneg.*v./(1+rho.*Ix.^0.5);
    Kw = exp(Ax.*(Ix.^0.5).*(m.*KwTop)./(m.*IxBottom+1/Mw));
```

```
    awbar=aw_data./(Kw);

    NumorSum=0;
    for k=1:(n-1),
        NumorSum=NumorSum+(awbar.^k).*(1-C(k)).*prod(C(1:k-1));
    end
    DenomSum=0;
    for k=1:(n-2),
        DenomSum=DenomSum+k.*(awbar.^(k-1)).*prod(C(1:k));
    end
    Denom=(1-awbar).^2.*(DenomSum)+(n-1-(n-2).*awbar).*awbar.^(n-
2).*prod(C(1:n-1));

    OUT = ((1-awbar)./(Mw.*v.*awbar)).*(1-NumorSum)./Denom;
end
```

D6. Fitting Routine for Solute Molality and Activity of Aqueous Neutral Organics by Power Law Model.

```
clear

Mw = 0.0180152; % Mol wt of water kg/mol

prompt = 'Enter solute of aqueous solution    ';
Solute = input(prompt,'s');

if isequal(Solute,'dimethylGA')
    n = 35; v = 1;
% elseif isequal(Solute,'Propanol')
%     n = 5; zpos = 1; zneg = 1; v = 2; type = 2;
% elseif isequal(Solute,'Sucrose')
%     n = 4; zpos = 1; zneg = 1; v = 2; type = 1;
% elseif isequal(Solute,'HNO3')
%     n = 8; zpos = 1; zneg = 1; v = 2;
% elseif isequal(Solute,'NH42SO4')
%     n = 9; zpos = 1; zneg = 2; v = 3; type = 3;
% elseif isequal(Solute,'CaCl2')
%     n = 6; zpos = 2; zneg = 1; v = 2;
end

dataloc = 'D:\Work\DataLit\';
datafile = strcat(dataloc,Solute,'.m');
run(datafile)

m_data = x;     % x = molality
o_data = Q;     % Q = Osmotic coefficient

aw_data = exp(-o_data.*v.*Mw.*m_data);
x_data = m_data./(m_data+1/Mw); % Mole fraction

[C,P0,P]=FitOrg(aw_data,o_data,v,n);

[aw_modelinput,o_model,x_model,m_model] = modelOrg(n,C,v);

[normMSE,m_model_new,o_model_new] =
mseOrg(o_data,m_data,aw_data,v,n,C);

fig = figure;
set(fig,'Position',[400 50 1200 400]);

subplot(1,2,1);
plt = plot(x_model,o_model,x_data,o_data,'.');
set(plt(1),'LineWidth', 2);
set(plt(2),'MarkerSize',10);
%axis([0 max(m_data) (min(o_data)-0.1) (max(o_data))+0.1])
% title(sprintf(strcat(Solute,sprintf(', n=%d, Normalized-
MSE=%g',n,normMSE))))
xlabel('mole fraction')
ylabel('osmotic coeff')
```

```
subplot(1,2,2);
txstr(1) = {sprintf('n = %g',n)};
txstr(3) = {sprintf('P = %g,\n',P)};
txstr(5) = {sprintf('C = %g,\n',C)};
txstr(9) = {sprintf('Normalized-MSE = %g',normMSE)};
text(0.01,0.5,txstr);

dirname = strcat('./Fitting-Results/',Solute);
nid = sprintf('_n%d',n);
if isequal(exist(strcat('./Fitting-Results/',Solute),'dir'),7)
    fprintf(strcat('./Fitting-Results/',Solute,'\n'))
else
    mkdir(strcat('.\Fitting-Results\',Solute))
    fprintf(strcat('./Fitting-Results/',Solute,'\n'))
end
figname = strcat(dirname,'/',Solute,nid,'.fig');
saveas(fig,figname)
figname = strcat(dirname,'/',Solute,nid,'.jpg');
set(fig,'PaperPositionMode','auto')
print(fig,'-djpeg',figname)

matfile = strcat(dirname,'/',Solute,nid,'.mat');
save(matfile,'m_model_new','o_model_new');

aw_modelinput=aw_modelinput';
m_model=m_model';
```

Fitting Sub-Routine

```
% function [mse,C,P0,P] = FitOrg(aw_data,o_data,v,n)

function [C,P0,P] = FitOrg(aw_data,o_data,v,n)

    prompt = 'Enter initial guess of [C1 P]    ';
%     prompt = 'Enter initial guess of P    ';

    P0 = input(prompt);

% P0 = -1;  %Initial guess [P]

    function [OUT] = f(P,aw)
       OUT = OsmFuncOrg(P,aw,v,n);
    end

options = statset('MaxIter',400,'Robust','on');
[Pfit,r,J,cov,mse] = nlinfit(aw_data,o_data,@f,P0,options);

C(1) = abs(Pfit(1));
P = Pfit(2);
for layer=2:(n-1)
    C(layer) = n.^-P.*layer.^P;
end
```

```
% Pmodel = fitnlm(aw_data,o_data,@f,P0);
% Pfit = Pmodel.Coefficients.Estimate;

% % C(1) = abs(Pfit(1));
% % P = Pfit(2);
% %
% % % P = Pfit;
% %
% % for layer=2:(n-1)
% %     C(layer) = n.^-P.*layer.^P;
% % end

% for layer=1:(n-1)
%     C(layer) = n.^-P.*layer.^P;
% end

end
```

Objective Function Sub-Routine

```
    function [OUT] = OsmFuncOrg(P,aw,v,n)

    Mw = 0.0180152; % Mol wt of water kg/mol

    C1 = P(1);
    C = @(layer)n.^-P(2).*layer.^P(2);

% C = @(layer)n.^-P(1).*layer.^P(1);

    Kw = 1;
    awbar = aw./Kw;

        NumorSum=(awbar).*(1-C1);
    for k=2:(n-1),
        NumorSum=NumorSum+(awbar.^k).*(1-C(k)).*C1*prod(C(2:k-1));
    end
    DenomSum=0;
    for k=1:(n-2),
        DenomSum=DenomSum+k.*(awbar.^(k-1)).*C1*prod(C(2:k));
    end
    Denom=(1-awbar).^2.*(DenomSum)+(n-1-(n-2).*awbar).*awbar.^(n-
2).*C1*prod(C(2:n-1));

    molality = ((1-awbar)./(Mw.*v.*awbar)).*(1-NumorSum)./Denom;

    OUT = -(log(aw))./(Mw.*v.*molality);

%     NumorSum=0;
%     for k=1:(n-1),
%         NumorSum=NumorSum+(awbar.^k).*(1-C(k)).*prod(C(1:k-1));
%     end
%     DenomSum=0;
%     for k=1:(n-2),
```

```
%          DenomSum=DenomSum+k.*(awbar.^(k-1)).*prod(C(1:k));
%      end
%      Denom=(1-awbar).^2.*(DenomSum)+(n-1-(n-2).*awbar).*awbar.^(n-
2).*prod(C(1:n-1));
%
%      molality = ((1-awbar)./(Mw.*v.*awbar)).*(1-NumorSum)./Denom;
%
%      OUT = -(log(aw))./(Mw.*v.*molality);

    end
```

Molality Calculation Sub-Routine

```
function [aw_modelinput,o_model,x_model,m_model] = modelOrg(n,C,v)

Mw=0.0180152; % Molecular weight water (kg/mol)

aw_modelinput =
[0.0001:0.001:0.9999,0.99999,0.999999,0.9999999,0.99999999];

t = length(aw_modelinput);
m_model = zeros(size(aw_modelinput));

for i = 1:t

m_model(i) = molalCalc(v,n,C,aw_modelinput(i));
o_model(i) = -(log(aw_modelinput(i)))/(Mw*v*m_model(i));
x_model(i) = m_model(i)./(m_model(i)+1/Mw); % Mole fraction

end

% function [mout] = NR(v,n,C,aw_modelinput)
%
% dm = 0.00001; % step size for derivative of function f
% m1 = 1; % Give an initial starting molality guess.
%
% % Newton raphson method
% f = @(m) molalCalc(v,n,C,m,aw_modelinput) - m;
% df = @(m)(f(m+dm)-f(m))/dm;
% for ii = 1:10
%     m2 = abs(m1 - f(m1)/df(m1));
%     m1 = m2;
% end
%
% mout = m1;
%
% end

function [OUT] = molalCalc(v,n,C,aw_modelinput)

Mw=0.0180152; % Molecular weight water (kg/mol)

% Calculate molality Using EQN.27
```

```
    Kw = 1;

    awbar=aw_modelinput./(Kw);

    NumorSum=0;
    for k=1:(n-1),
        NumorSum=NumorSum+(awbar.^k).*(1-C(k)).*prod(C(1:k-1));
    end
    DenomSum=0;
    for k=1:(n-2),
        DenomSum=DenomSum+k*(awbar.^(k-1)).*prod(C(1:k));
    end
    Denom=(1-awbar).^2.*(DenomSum)+(n-1-(n-2).*awbar).*awbar.^(n-
2).*prod(C(1:n-1));

    OUT = ((1-awbar)./(Mw.*v.*awbar)).*(1-NumorSum)./Denom;

end

end
```

Mean Square Error Calculation Sub-Routine

```
function [normMSE,m_model_new,o_model_new] =
mseOrg(o_data,m_data,aw_data,v,n,C)

Mw=0.0180152; % Molecular weight water (kg/mol)

t = length(aw_data);
m = zeros(size(aw_data));

for i = 1:t

m_model_new(i) = molalCalc(v,n,C,aw_data(i));
o_model_new(i) = -(log(aw_data(i)))/(Mw.*v.*m_model_new(i));

end

m_model_new = m_model_new';
o_model_new = o_model_new';

% Normalized mean square error
normMSE = sum(((m_model_new - m_data)./m_model_new).^2)/t;
% normMSE = sum(((o_model_new - o_data)./o_model_new).^2)/t;

end

function [OUT] = molalCalc(v,n,C,aw_data)

Mw=0.0180152; % Molecular weight water (kg/mol)
```

```
Kw = 1;

awbar=aw_data./(Kw);

NumorSum=0;
for k=1:(n-1),
    NumorSum=NumorSum+(awbar.^k).*(1-C(k)).*prod(C(1:k-1));
end
DenomSum=0;
for k=1:(n-2),
    DenomSum=DenomSum+k.*(awbar.^(k-1)).*prod(C(1:k));
end
Denom=(1-awbar).^2.*(DenomSum)+(n-1-(n-2).*awbar).*awbar.^(n-
2).*prod(C(1:n-1));

OUT = ((1-awbar)./(Mw.*v.*awbar)).*(1-NumorSum)./Denom;

end
```

D7. Routine for Solute Molality and Activity of Multicomponent Aqueous Mixtures by Power Law Model.

```
function [ m ] = Paper3Mixture(j,C)

aw =
[0.000001,0.00001,0.0001:0.0001:0.9999,0.99999,0.999999,0.9999999,0.999
99999];
% aw = [0.960286708 0.944079883 0.961204336 0.960989047 0.950973435
0.987008522 0.990369509 0.989201244 0.986506292 0.98161219  0.916740315
0.837320024 0.930269489 0.897306905 0.85426791  0.909578937 0.932249019
0.950273019 0.961937746 0.944902935 0.963103276 0.967793187 0.955040868
0.976854496                ];

Mw = 0.0180152; % Molecular weight water (kg/mol)

N = 3; % number of solutes

for k = 1:N

    prompt = 'Enter solute of aqueous solution     ';
    Solute1 = input(prompt,'s');

        if isequal(Solute1,'NaCl')
                    j(k) = 1; zpos(k) = 1; zneg(k) = 1; v(k) = 2;
rho(k) = 13.9086; n(k) = 4; P(k) = -1.6332; C1(k) = 2.5452; cation(k) =
1; anion(k) = 1;
```

```
%             j(k) = 1; zpos(k) = 1; zneg(k) = 1; v(k) = 3; rho(k) =
9.7912; n(k) = 5; P(k) = -0.90625; C1(k) = 70.5109; cation(k) = 2;
anion(k) = 1;
%     if isequal(Solute1,'HNO3')
%         j(k) = 1; zpos(k) = 1; zneg(k) = 1; v(k) = 2; rho(k) =
15.341; n(k) = 8; P(k) = -0.2520; C1(k) = 8.5978;
%     if isequal(Solute1,'NH4Cl')
%         j(k) = 1; zpos(k) = 1; zneg(k) = 1; v(k) = 2; rho(k) =
14.3129; n(k) = 4; P(k) = -0.7632; C1(k) = 1.08578;
    elseif isequal(Solute1,'AceticAcid_data')
        j(k) = 2; zpos(k) = 1; zneg(k) = 1; v(k) = 2; rho(k) = 9.3566;
n(k) = 2; P(k) = -1; cation(k) = 1; anion(k) = 1;
%     elseif isequal(Solute1,'NH4NO3')
%         j(k) = 2; zpos(k) = 1; zneg(k) = 1; v(k) = 2; rho(k) =
13.4745; n(k) = 5; P(k) = 0.1304; cation(k) = 1; anion(k) = 1;
%     elseif isequal(Solute1,'(NH4)2C2O4')
%         j(k) = 2; zpos(k) = 1; zneg(k) = 2; v(k) = 3; rho(k) = 13.00;
n(k) = 2; P(k) = -0.1; cation(k) = 2; anion(k) = 1;
        %     elseif isequal(Solute1,'NaOH')
        %         j(k) = 3;
        %     elseif isequal(Solute1,'HNO3')
        %         j(k) = 4;
%     elseif isequal(Solute1,'H2SO4')
%         j(k) = 3; zpos(k) = 1; zneg(k) = 2; v(k) = 3; rho(k) =
9.7912; n(k) = 5; P(k) = -0.90625; C1(k) = 70.5109; cation(k) = 2;
anion(k) = 1;
    elseif isequal(Solute1,'HCl')
        j(k) = 3; zpos(k) = 1; zneg(k) = 1; v(k) = 2; rho(k) = 58.89;
n(k) = 5; P(k) = -1.55372; C1(k) = 442.981; cation(k) = 1; anion(k) =
1;
%     elseif isequal(Solute1,'MgSO4')
%         j(k) = 4; zpos(k) = 2; zneg(k) = 2; v(k) = 2; rho(k) =
13.7029; n(k) = 7; P(k) = -1.26831; cation(k) = 1; anion(k) = 1;
%     elseif isequal(Solute1,'NH4HC2O4')
%         j(k) = 4; zpos(k) = 1; zneg(k) = 1; v(k) = 2; rho(k) = 13.00;
n(k) = 2; P(k) = -0.1; cation(k) = 1; anion(k) = 1;
%     elseif isequal(Solute1,'NaCH3COO')
%         j(k) = 4; zpos(k) = 1; zneg(k) = 1; v(k) = 2; rho(k) = 13.00;
n(k) = 2; P(k) = -0.1; cation(k) = 1; anion(k) = 1;
    elseif isequal(Solute1,'NH4HSO4')
        j(k) = 4; zpos(k) = 1; zneg(k) = 1; v(k) = 2; rho(k) = 13.00;
n(k) = 2; P(k) = -0.1; C1(k) = 1; cation(k) = 1; anion(k) = 1;
    elseif isequal(Solute1,'(NH4)2SO4')
        j(k) = 5; zpos(k) = 1; zneg(k) = 2; v(k) = 3; rho(k) = 13.516;
n(k) = 9; P(k) = -0.2778; C1(k) = 1.5413; cation(k) = 2; anion(k) = 1;
%     elseif isequal(Solute1,'CaCl2')
%         j(k) = 6;
    elseif isequal(Solute1,'CaCl2')
        j(k) = 6;
%     elseif isequal(Solute1,'Glycerol')
%         j(k) = 7;
    elseif isequal(Solute1,'H2SO4')
        j(k) = 7; zpos(k) = 1; zneg(k) = 2; v(k) = 3; rho(k) = 9.82174;
n(k) = 5; P(k) = -0.897278; C1(k) = 114.082; cation(k) = 2; anion(k) =
1;
    elseif isequal(Solute1,'NaNO3')
```

```
        j(k) = 8; zpos(k) = 1; zneg(k) = 1; v(k) = 2; rho(k) = 18.3287;
n(k) = 11; P(k) = -0.0435372; C1(k) = 1.81043;
            elseif isequal(Solute1,'GlutaricAcid')
                        j(k) = 9; zpos(k) = 1; zneg(k) = 1; v(k) = 2;
rho(k) = 0; n(k) = 4; P(k) = 1.6034; C1(k) = 3.0049; cation(k) = 1;
anion(k) = 1;

%     elseif isequal(Solute1,'PEG200')
%         j(k) = 9; zpos(k) = 1; zneg(k) = 1; v(k) = 2; rho(k) = 0;
n(k) = 4; P(k) = -0.2053; C1(k) = 1.719; cation(k) = 1; anion(k) = 1;
    end

    for i = 2:n(k)-1
        C(k,i) = power((i/n(k)),P(k)) % Energy parameter
        % C(k,i) = 1; C1(k)=1;
        if (j(k) == 5)
            C(k,i) = C1(k)*power(i,P(k));
        end
    end


    if(j(k) == 2 || j(k) == 9)
        C(k,1) = power((1/n(k)),P(k))
    else
        C(k,1) = C1(k);
    end

end

% % % % dataloc = 'D:\Work\DataLit\Data_Single_Salts\';
% % % % datafile = strcat(dataloc,Solute1,'.m');
% % % % run(datafile)
% % % %
% % % % m_data(1,:) = x;      % x = molality
% % % % o_data(1,:) = Q;     % Q = Osmotic coefficient
% % % %
% % % % aw_data(1,:) = exp(-o_data(1,:).*v(1).*Mw.*m_data(1,:));
% % % %
% % % % x_data(1,:) = v(1).*m_data(1,:)./(v(1).*m_data(1,:)+1/Mw); %
Mole fraction
% % % % root_x_data(1,:) = sqrt(x_data(1,:));


t = length(aw);
prompt = 'Enter Ratio of first solute to second solute in the form
"number" as in (number:1)';
soluteratio = input(prompt);

assignin('base', 'soluteratio', soluteratio);

    m = zeros(size(aw));
    num = zeros(size(aw));
    den = zeros(size(aw));

for i = 1:t
```

```
    m(N,i) = NR(i,j,rho,v,n,zpos,zneg,C,aw(i),N,soluteratio(i,:));
% %     m(N,i) = NR(i,j,rho,v,n,zpos,zneg,C,aw(i),N,soluteratio);

    for kk = 1:N-1
        m(kk,i) = m(N,i)*soluteratio(i,kk);
% %         m(kk,i) = m(N,i)*soluteratio;
% %  m(kk,i) = m(N,i)*soluteratio(kk);

    end

    m_total(i) = 0;
    for k = 1:N
        m_total(i) = m_total(i) + m(k,i)*v(k);
    end
    o(i) = -log(aw(i))./(Mw*m_total(i));
    root_m(i) = power(m_total(i),0.5);
    x (i) = m_total(i)./(m_total(i)+1/Mw); % Mole fraction of solute
    %     x (1,i) = m(1,i)./(m(1,i)+1/Mw);
    %     x (2,i) = m(2,i)./(m(2,i)+1/Mw);
    root_x(i) = sqrt(x(i));
    m_dry_total(i) = sum(m(:,i));
    for kkk = 1:N
        xstar(kkk) = m(kkk,i)./m_dry_total(i);
    end
    for p =1:N

[a(p,i),f_Inf(p,i),gamma_Inf(p,i),K(p,i),Ix(p,i),Kw(p,i),awbar(p,i),aba
r0(p,i),K_Inf(p,i)] =
SoluteActivity(N,i,j(p),rho,v,n(p),zpos,zneg,C(p,:),m,aw(i),p,xstar(p))
;
        xpos(p,i) = m(p,i)./m_total(i);
        xneg(p,i) = m(p,i)./m_total(i);
        %         if j(p) >= 6 && j(p) <= 12
        f_FS(p,i) =
(m_total(i)+(1./Mw)).*((abar0(p,i)*xstar(p))./(((cation(p)*m(p,i)).^cat
ion(p)).*((anion(p)*m(p,i)).^anion(p)))).^(1./v(p));  % Fused salt
reference state; Mole fraction basis; eqn A2
        %         else
        %             f_FS(p,i) =
(m_total(i)+(1./Mw)).*(a(p,i)./m(p,i)); %
        %             Fused salt reference state; Mole fraction basis
        %         end
    end
end

aw=aw';
assignin('base', 'WaterActivity', aw);
m=m';
assignin('base', 'SoluteMolality', m);
m_total=m_total';
o=o';
abar0=abar0';
a=a';
x=x';
f_FS=f_FS';
f_Inf=f_Inf';
```

```
gamma_Inf=gamma_Inf';
K=K';
Ix=Ix';
Kw=Kw';
awbar=awbar';
K_Inf=K_Inf';

assignin('base', 'MixtureMolality', m_total);
assignin('base', 'OsmoticCoeff', o);
assignin('base', 'SoluteActivity', a);
assignin('base', 'MoleFraction', x);
assignin('base', 'ActCoeff_f_FS', f_FS);
assignin('base', 'ActCoeff_f_Inf', f_Inf);
assignin('base', 'ActCoeff_f_Inf_Molality', gamma_Inf);
assignin('base', 'K', K);
assignin('base', 'Ix', Ix);
assignin('base', 'abar0', abar0);
assignin('base', 'Kw', Kw);
assignin('base', 'awbar', awbar);
assignin('base', 'C', C);
assignin('base', 'xstar', xstar);
assignin('base', 'K_Inf', K_Inf);

plot(x,o,'.');

plot(root_x,o,'-',root_x_data,o_data,'.');
xlabel ('Root-MoleFraction')
ylabel ('OsmoticCoeff')

grid on

end

function [mout] = NR(i,j,rho,v,n,zpos,zneg,C,aw,N,soluteratio)

dm = 0.0000000001; % step size for derivative of function f
m1 = 1; % Give an initial starting molality guess.

% Newton raphson method

f = @(m) molalCalc(i,j,rho,v,n,zpos,zneg,C,m,aw,N,soluteratio) - m;
df = @(m)(f(m+dm)-f(m))/dm;
for i = 1:10
    m2 = abs(m1 - f(m1)/df(m1));
    m1 = m2;
end

mout = m1;

end

function [OUT] = molalCalc(i,j,rho,v,n,zpos,zneg,C,m,aw,N,soluteratio)

Mw=0.0180152; % Molecular weight water (kg/mol)
```

```
Ax=2.917; % Debye-Huckel coeff. mol frac @ 298.15K

% disp(aw); fprintf('\b'); disp(m); fprintf('\b'); disp(soluteratio);

IxTop = zpos(N)*zneg(N).*v(N);
for kk = 1:N-1
    IxTop = (IxTop + soluteratio(kk)*zpos(kk)*zneg(kk).*v(kk));
    IxTop = m*IxTop;
end

IxBottom = v(N);
for kk = 1:N-1
    IxBottom = (IxBottom + soluteratio(kk).*v(kk));
    IxBottom = m*IxBottom;
end

Ix = (1/2)* (IxTop)./(IxBottom+1/Mw);

KwTop = (zpos(N)*zneg(N)*v(N))./(1+rho(N)*Ix.^0.5);
for kk = 1:N-1
    KwTop = (KwTop +
(zpos(kk)*zneg(kk).*v(kk)*soluteratio(kk))./(1+rho(kk)*Ix.^0.5));
    KwTop = m*KwTop;
end
Kw = exp((Ax.*(Ix.^0.5).*(KwTop))./(IxBottom+1/Mw));
awbar=aw./(Kw);

% Calculate molality Using EQN.27
for p =1:N

% % % %     if j(p) >= 1 && j(p) <= 5
% % % %         NumorSum(p)=0;
% % % %         for k=1:(n(p)-1),
% % % %             NumorSum(p)=NumorSum(p)+(awbar.^k).*(1-
C(p,k)).*prod(C(p,1:k-1));
% % % %         end
% % % %         DenomSum(p)=0;
% % % %         for k=1:(n(p)-2),
% % % %             DenomSum(p)=DenomSum(p)+k*(awbar.^(k-
1)).*prod(C(p,1:k));
% % % %         end
% % % %         Denom(p)=(1-awbar).^2.*(DenomSum(p))+(n(p)-1-(n(p)-
2).*awbar).*awbar.^(n(p)-2).*prod(C(p,1:n(p)-1));
% % % %         m0(p)=((1-awbar)/(Mw*v(p)*awbar))*(1-
NumorSum(p))/Denom(p);
% % % %     else
        NumorSum(p)=0;
        for k=1:(n(p)-1),
            NumorSum(p)=NumorSum(p)+(awbar.^k).*(1-
C(p,k)).*prod(C(p,1:k-1));
        end
        DenomSum(p)=0;
        for k=1:(n(p)-2),
            DenomSum(p)=DenomSum(p)+k*(awbar.^(k-1)).*prod(C(p,1:k));
        end
```

```
        Denom(p)=(1-awbar).^2.*(DenomSum(p))+(n(p)-1-(n(p)-
2).*awbar).*awbar.^(n(p)-2).*prod(C(p,1:n(p)-1));
        m0(p)=((1-awbar)/(Mw*v(p)*awbar))*(1-NumorSum(p))/Denom(p);
% % % %     end

end

mixturemodel=1./m0(N);
for k=1:N-1,
    mixturemodel=mixturemodel+soluteratio(kk)/m0(kk);
end

OUT = 1./mixturemodel;

end

function [a,f_Inf,gamma_Inf,K,Ix,Kw,awbar,abar0,K_Inf] =
SoluteActivity(N,i,j,rho,v,n,zpos,zneg,C,m,aw,p,xstar)

Mw=0.0180152; % Molecular weight water (kg/mol)
Ax=2.917; % Debye-Huckel coeff. mol frac @ 298.15K

IxTop=0;
for k=1:N,
    IxTop=IxTop+m(k,i)*zpos(k)*zneg(k).*v(k);
end

IxBottom=0;
for k=1:N,
    IxBottom=IxBottom+m(k,i).*v(k);
end

Ix = (1/2)* (IxTop)./(IxBottom+1/Mw);

% Ixref = (1/2)* zpos(p).*zneg(p);
% IxFS = (1/2)* zpos(p).*zneg(p);
Ixref = (1/2)* (IxTop)./(IxBottom);
IxFS = (1/2)* (IxTop)./(IxBottom);

KwTop=0;
for k=1:N,
    KwTop=KwTop+(m(k,i)*zpos(k)*zneg(k).*v(k))./(1+rho(k)*Ix.^0.5);
end

Kw = exp((Ax.*(Ix.^0.5).*(KwTop))./(IxBottom+1/Mw));
awbar=aw./(Kw);

%
% IxTop = m(1,i)*zpos(1)*zneg(1).*v(1) + m(2,i)*zpos(2)*zneg(2).*v(2);
% IxBottom = m(1,i)*v(1) + m(2,i)*v(2);
% KwTop = (m(1,i)*zpos(1)*zneg(1).*v(1))./(1+rho(1)*Ix.^0.5) +
(m(2,i)*zpos(2)*zneg(2)*v(2))./(1+rho(2)*Ix.^0.5);

% disp(Ix); fprintf('\b'); disp(Kw); fprintf('\b'); disp(awbar);
```

```
DenSum=0;
for k=1:(n-1),
    DenSum=DenSum+(awbar.^k).*(1-C(k)).*prod(C(1:k-1));
end

abar0 = ((1-awbar)./(1-DenSum)).^v(p);
for k=1:N,
    zz(k) = zpos(k)*zneg(k);
end
if zz(p) == 0
    %     K = exp((Ax*Ix^0.5*KwTop)/(IxBottom+1/Mw));
    K=exp((-Ax.*(IxFS-Ix).*KwTop)./((IxBottom+1./Mw).*Ix.^0.5));
else
    SumKjTerm=0;
    for k=1:N,

SumKjTerm=SumKjTerm+(m(k,i)*zpos(k)*zneg(k).*v(k))./(2.*Ix.^0.5.*(1+rho
(k)*Ix.^0.5));
    end
    K = (exp(-
zpos(p).*zneg(p)*Ax*(2/rho(p)*log((1+rho(p)*Ix^0.5)/(1+rho(p)*Ixref^0.5
))+((1-Ix./IxFS)/(IxBottom+1/Mw))*SumKjTerm)))^v(p);
end

a = xstar.*K.*abar0;

% Reference state --> Infinite dilution
Ixref = 0;

for k=1:(n-1),
    Cprod=prod(C(1:k));
end

if zz(p) == 0
    K_Inf=exp((-Ax.*(IxFS-Ix).*KwTop)./((IxBottom+1./Mw).*Ix.^0.5));
    f_Inf = ((IxBottom+(1./Mw))./IxBottom).*abar0.*Cprod.*K_Inf; %
Infinite dilution reference state; Mole fraction basis Activity
Coefficient for Non-dissociating species
else
    K_Inf = (exp(-
zpos(p).*zneg(p)*Ax*(2/rho(p)*log((1+rho(p)*Ix^0.5)/(1+rho(p)*Ixref^0.5
))+((1-Ix./IxFS)/(IxBottom+1/Mw))*SumKjTerm)))^v(p);
    f_Inf =
((IxBottom+(1./Mw))./IxBottom).*(abar0.^(1./v(p))).*Cprod.*K_Inf;  %
Infinite dilution reference state; Mole fraction basis Activity
Coefficient for Dissociating species
end

% Molality basis Inf dilution reference state Activity coefficient (eq.
30)
gamma_Inf = (Cprod./(Mw.*IxBottom)).*((abar0.*K_Inf).^(1./v(p)));

end
```

Appendix E

Copyright Permissions

Parts of Chapter 1, and Chapters 2, 3 and 6 were published in the American Chemical Society (ACS) journals, and are included in this thesis with permission on Apr 18, 2018. The ACS copyright policy states: “Anyone who is doing personal, noncommercial research may view, print material, and temporarily store materials from this site, provided that ACS's copyright notices are not removed and that the reuse of material does not conflict with any of the prohibited uses.”. “Reuse/Republication of the Entire Work in Theses or Collections: Authors may reuse all or part of the Submitted, Accepted or Published Work in a thesis or dissertation that the author writes and is required to submit to satisfy the criteria of degree-granting institutions. Such reuse is permitted subject to the ACS’ “Ethical Guidelines to Publication of Chemical Research”; the author should secure written confirmation (via letter or email) from the respective ACS journal editor(s) to avoid potential conflicts with journal prior publication/embargo policies. Appropriate citation of the Published Work must be made. If the thesis or dissertation to be published is in electronic format, a direct link to the Published Work must also be included using the ACS Articles on Request author-directed link.”

Parts of Chapter 4 were published in the ACS, Copernicus, and Royal Society of Chemistry (RSC) publications, and are included in this thesis with permission from ACS on Apr 18, 2018 and RSC on May 17, 2018. Permission was not required by the Copernicus publications, since the authors retain the copyright of the article. The Copernicus license and copyright agreement states: “All articles published by Copernicus Publications have been licensed under the Creative Commons Attribution 4.0 License since 6 June 2017 or under its former version 3.0 since 2007. Under these licenses the authors retain the copyright. There is no need from the publisher's side to allow/confirm a reproduction. We suggest contacting the authors to inform them about the further usage of the material. In any case, the authors must be given credit.”.

To reprint Figure 5.1a in this thesis, permission was obtained by the RSC under license number 4324990480596 on April 9, 2018.

To reprint Figure 5.1b, permission was obtained by the PNAS executive editor on April 17, 2018, who stated that: “Because this material is published after 2008, a copyright note is not needed.”.

To reprint Figure 5.2, permission was obtained by the AMS Senior Peer Review Support Associate & Permissions Specialist on April 17, 2018, under the conditions stated: “please include the complete bibliographic citation of the original source for each, and please include the following statement with that citation for each: ©American Meteorological Society. Used with permission.”.

To reprint Figure 5.3, permission was not required by the Copernicus publications, since the article was published under a CC BY license and the figure caption does not mention any other licensing.